9-9-2008

Observation of high-lying resonances in the H- ion

Philip G. Harris

LA-11843-T
Thesis

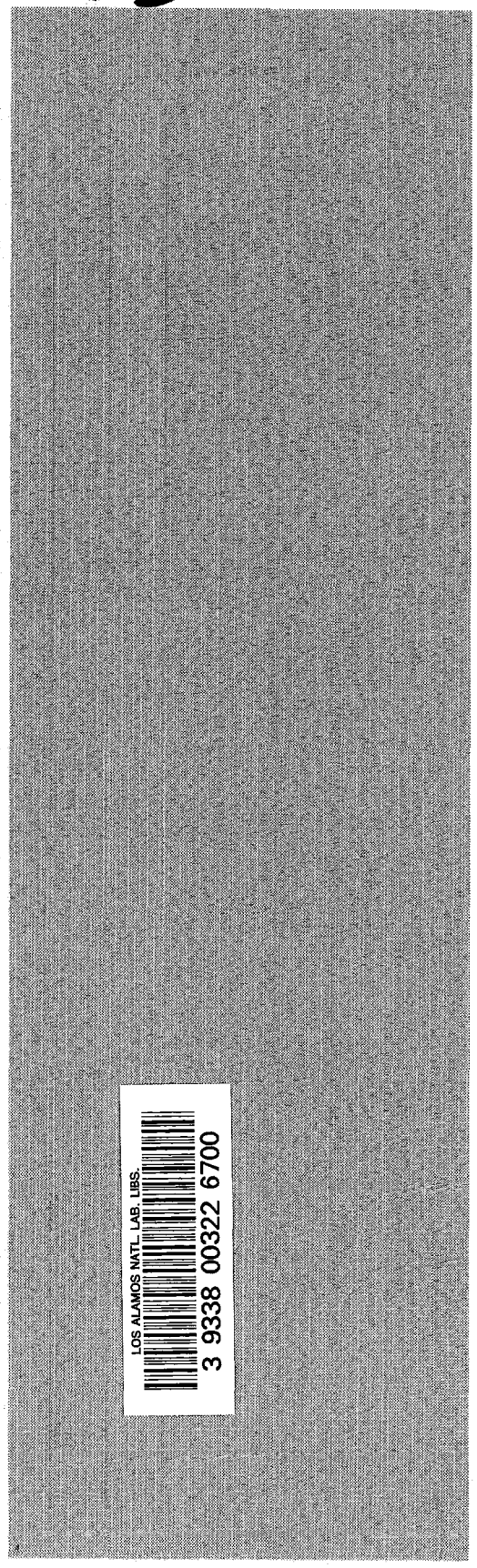

Observation of High-Lying Resonances in the H^- Ion

Los Alamos

Los Alamos National Laboratory is operated by the University of California for the United States Department of Energy under contract W-7405-ENG-36.

D

This thesis was accepted by the Department of Physics and Astronomy, University of New Mexico, Albuquerque, New Mexico, in partial fulfillment of the requirements for the degree of Doctor of Philosophy. It is the independent work of the author and has not been edited by the IS-11 Writing and Editing staff.

This work was supported by the U.S. Department of Energy, Office of Energy Research.

An Affirmative Action/Equal Opportunity Employer

LA-11843-T
Thesis

UC-413
Issued: May 1990

Observation of High-Lying Resonances in the H^- Ion

Philip G. Harris*

*Graduate Research Assistant at Los Alamos. Department of Physics and Astronomy, University of New Mexico, Albuquerque, NM 87131.

Los Alamos National Laboratory
Los Alamos,New Mexico 87545

Acknowledgements

This series of experiments would not have been possible without the support of a great many people. I am indebted most deeply to Professor Howard Bryant, my supervisor on this project and the driving force behind the collaboration since its inception. He has provided invaluable guidance, and shown the way to clear, simple physical insight underlying the solutions to many a problem. On a personal level, he and his wife Mona have provided boundless hospitality and moral support throughout my stay in New Mexico. I consider myself both extremely fortunate and privileged to have been able to work with him.

I also owe a great debt of gratitude to my fellow graduate students Amir Mohagheghi and Chen-Yau Tang. Although each of us had a separate goal — Amir, to study the interactions of the H^- beam with thin foils, Chen-Yau to study the multiphoton detachment process, and myself to investigate the high-lying resonances in H^- — I think it is fair to say that we each contributed to the best of our (usually complementary) abilities on all of the experiments; every one of the experiments was truly a team effort.

Dr. Joey Donahue has also proven himself an invaluable member of the collaboration. He has often championed the cause of these atomic physics experiments at LAMPF, which is primarily a nuclear physics facility; he has, through MP-7, provided both technical and financial support (including the research assistantship under which I myself have been employed); he has a sound knowledge of the accelerator itself, and he is the one best able to provide the special tuning

required for the HiRAB beamline. In addition, I am especially grateful to him for much practical assistance and advice in many matters ranging from data analysis to vacuum hardware.

Dr. Randy Reeder provided a great deal of assistance, particularly in matters theoretical. This was especially appreciated during the past year (1989), during which he was employed by another group but nonetheless gave freely of his own time to assist as and when he could. Likewise, Dr. Bob Quick has contributed greatly, usually in his own free time, and particularly to the multiphoton detachment studies. He is a primary source of expertise in the field of lasers and optics, and has provided much of our optical equipment.

Dr. Stan Cohen has been our mainstay in all aspects of the computing needed for the experiment. He rewrote the "Q" data analysis system several years ago to run on our microvax, and his knowledge of both hardware and software is extensive; he also possesses patience in abundance to explain "computer-speak" to the uninitiated. It is he who provided the initial inspiration for me to become, from the proverbial drawing board, a reasonably competent programmer in Pascal.

My thanks also must go to Dr. Jim Stewart, who helped enormously during my initiation to experimental atomic physics in 1986, when he was completing his own thesis work; to Professor Win Smith, from the University of Connecticut, who visits each summer to help out for a couple of weeks during the runs, and who often has useful suggestions for the future direction of the experiments; to Dan Rislove, and also to Tom Altman, each of whom came to help for an extended period during the 1989 runs (Tom regularly made the necessary hot black coffee at 4 a.m. each morning!); and to Hossein Tootoonchi and Hassan Sharifian, who twelve years ago were the first graduate students to work on this project, and who also came back to help out during 1989.

Discussions with a number of people during the Second International Workshop on the Physics of the Negative Hydrogen Ion, held in Albuquerque in January

1990, were both enjoyable and extremely useful. I would especially like to thank Dr. Hossein Sadeghpour, who did many calculations of the positions of the ^1P resonances, the results of which were presented for the first time at the workshop, and who has patiently explained many of the mysteries underlying the theories of doubly-excited states.

A very great deal of technical support has been provided, both from the University of New Mexico and from Los Alamos National Laboratory; I would like to thank in particular Lawrence Quintana and (prior to his retirement) Afton Kirby in MP-7 at Los Alamos, and Jim Hontas and Jesus Sanchez in the UNM machine shop.

Others who have contributed in important ways are Jim Knudson (who helps with the beam tuning), Vincent Yuan (largely responsible for the Fast Ion Chamber), George Kyrala (assistance with the CO_2 lasers), Bob Sander, Fred Archuleta, John McClelland (who provided truly invaluable assistance in the development of the momentum bunching technique), Bob Hill (for technical assistance with momentum bunching), Olin van Dyck and Kevin Jones (who were largely responsible for controlling the structure of the H^- beam), Vern Sandberg (assistance with PMT base design), Harold Martinez (drafting), Steve Cushing (electrical/technical), Carol Harvey (who helped with taking the 1985 data, used in the "Field-Induced Oscillations" section of Chapter 5), and many more for whose anonymous aid I am nonetheless grateful.

Finally, I would like to show my appreciation to my dissertation committee, including the aforementioned Howard Bryant and Joey Donahue, with Dr. J. Daniel Finley III, Chairman of the UNM Physics Department, who was most helpful in reviewing the theoretical discussions in this dissertation; Dr. Bob McNeil, of the UNM Center for High Technology Materials; and especially to Dr. Bernd Bassalleck, also of the UNM Physics Department, who has concerned himself with my progress throughout my graduate studies.

Acknowledgements

This work was supported by the Division of Chemical Sciences, Office of Basic Energy Sciences, Office of Energy Research, U.S. Department of Energy, and was also funded in part by the U.S. Army Strategic Defense Command.

OBSERVATION OF HIGH-LYING RESONANCES IN THE H^- ION

by

Philip G. Harris

ABSTRACT

This dissertation reports the observation of several series of resonances, for which both electrons are in excited states, in the photodetachment cross section of H^-. These ^1P doubly-excited states interfere with the continuum in which they are embedded, and appear as dips in the production cross section of excited neutral hydrogen.

The experiment was performed by intersecting an 800 MeV H^- beam with a (266 nm) laser beam at varying angles; the relativistic Doppler shift then "tuned" the photon energy in the barycentric frame.

The process was observed by using a magnet strong enough to strip the electrons from the excited hydrogen atoms in selected states n and detecting the resulting protons, which allowed the isolation of the individual n channels. Three resonances are clearly visible in each channel.

The data support recent theoretical calculations for the positions of doubly-excited ^1P resonances, and verify a new Rydberg-like formula for the modified Coulomb potential.

Table of Contents

List of Figures

Chapter 1.

Chapter 2.

Chapter 3.

Chapter 4.

Chapter 5.

List of Tables

Chapter 2.

Chapter 4.

Chapter 1

Introduction and Historical Overview

> The White Rabbit put on his spectacles. 'Where shall I begin, please, Your Majesty?', he asked.
>
> 'Begin at the beginning,' the King said, very gravely,'and go on till you come to the end. Then stop.'

— Lewis Carrol, *Alice in Wonderland*

1.1 Current Interest in H^-.

The H^- ion represents the classic three-body problem in quantum mechanics. It consists of a "core" hydrogen atom, which is polarized by a second electron, allowing that electron to be bound. It is of great interest to theorists (as the simplest Coulombic system beyond the "perfectly" well known hydrogen atom), to astronomers (as a major contributor to the opacity of stellar atmospheres), and to accelerator physicists (as the easiest negative ion to accelerate); but it is only in the last decade or so that study of H^-, both experimental and theoretical, has truly blossomed.

Possibly the most important reason for the increased attention paid to H^- is the availability of new experimental techniques. As will be seen later, there is a great deal of structure in its photodetachment cross section (Figure 1.1) at relatively high photon energies. Although the outer electron is bound by only 0.7542 eV, and there are no excited states below the continuum (*i.e.*, there are no states with just one excited electron, known as *singly-excited* states; Hill, 1976), the region from ten to fifteen eV is extremely rich in (*doubly*-excited)

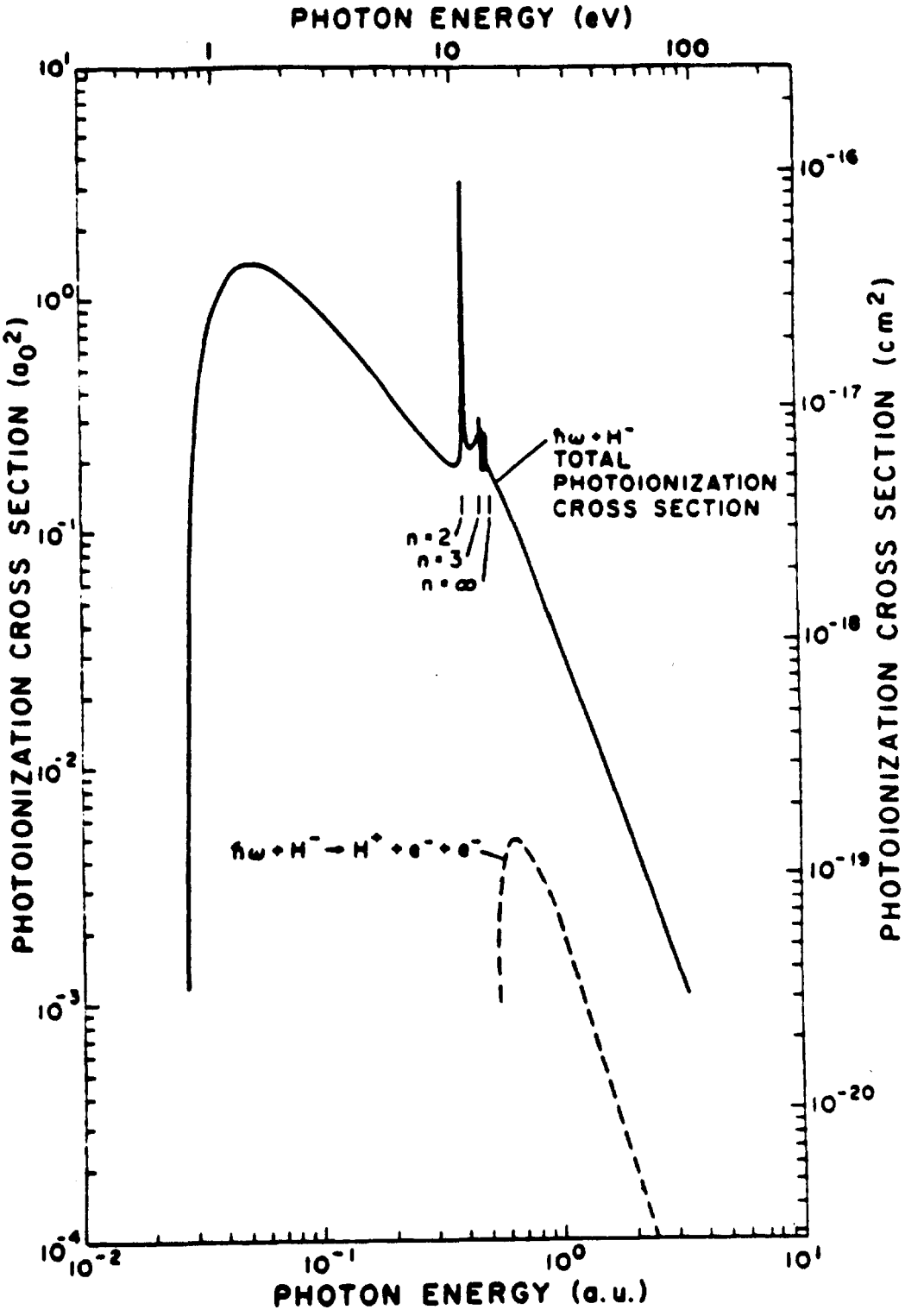

Figure 1.1. Calculated photodetachment cross section of H^-, for both single- and double-detachment. (From Broad and Reinhardt, 1976).

autoionizing resonances. Availability of high-power, short wavelength lasers is at last allowing this structure to be revealed, a century after the spectroscopic structure of hydrogen itself was first investigated. Furthermore, development of computers has paralleled that of lasers; and powerful numerical techniques are at last widely available that allow theorists to tackle this problem. We are thus in the ideal situation of theory and experiment developing alongside, advances in each prompting new investigations and advances in the other.

As studies of three-body, two-electron systems continue, it is perhaps inevitable that comparisons be drawn between H^- and helium. There are, however, great differences; suffice it to say that, because of the doubly-charged nucleus in helium, the electron-electron correlations are much more important in H^-, and H^- is therefore arguably the superior candidate for the study of double excitations, and of the mechanisms by which a pair of electrons may share the energy of a single photon. These correlations, in fact, are so strong that a variational method calculation on an independent particle model, which predicts the binding energy of helium to within about 6% of its true value, predicts that H^- should not be bound at all (Bethe and Salpeter, 1957). It could fairly be said that H^- is as important for the development of the quantum-mechanical three-body problem as was the neutral hydrogen atom for the development of quantum mechanics itself.

The development of high-powered lasers has also spurred the development of a new branch of physics: quantum optics. Interest here often focuses on highly non-linear effects, and in particular, the response of matter to extremely intense radiation fields. Once again, the need is for a simple structure upon which to test theoretical models, the ideal system being a one-electron, two-level atom in isolation. No such system exists, of course, but the H^- ion comes extremely close — there is only one bound state, so the upper of the two levels is at the base of a continuum; and the outer of the two electrons may be viewed almost

in isolation, since the neutral hydrogen atom at the core of the system requires a massive ten eV in order to achieve its minimum excitation, and also only provides a short-range binding potential for the weakly-bound outer electron. Thus, the possibility of observing multiphoton detachment in the H^- ion has provoked a great deal of interest amongst experts in that field. The results of our current multiphoton studies are discussed by Tang (1990).

With regard to technical applications, H^- spectroscopy experiments have been encouraged by those interested in developing neutral particle beam technology, since of course the easiest way to make a neutral particle beam is to accelerate negative ions — again, H^- is the natural candidate, as it has the largest charge-to-mass ratio — and then to neutralize them in a gas target or foil, or by photodetachment. Laser spectroscopy is an excellent diagnostic for relativistic atomic beams, since it can provide an accurate measure of both the direction and the kinetic energy of such beams as well as a monitor of the momentum distribution of the atoms, as described in Appendix E.

It also appears that H^- may be of interest to those developing theories of "quantum chaos". The response of the ion as it passes through thin foils, at relativistic velocities, is not well understood, but the nature of the interaction and the distribution of excited states that result are currently under investigation, and will be covered in some depth in the dissertation of Amir Mohagheghi (1990).

1.2 Relativistic H^- Beam Spectroscopy.

The experiments described here are the latest in a series of studies of H^- that have been carried out at the Los Alamos Clinton P. Anderson Meson Physics Facility (LAMPF), a linear accelerator that provides a beam of H^- ions at energies up to 800 MeV ($\beta = 0.842$). LAMPF is uniquely suited to such studies. The relativistic nature of the beam provides two extremely powerful tools. First, and foremost, is the relativistic Doppler shift. As the H^- ions are moving at

and foremost, is the relativistic Doppler shift. As the H^- ions are moving at relativistic velocities, making them intercept a laser beam of lab photon energy E_0 at a varying angle α changes the barycentric photon energy E according to the formula

$$E = E_0\gamma(1 + \beta\cos\alpha), \tag{1.1}$$

where $\beta = v/c$ and $\gamma = (1 - \beta^2)^{-1/2}$; $\alpha = 0$ when the beams meet head on. The enormous range of tuning — over a decade for an 800 MeV beam — is otherwise totally out of the question for any lasers available either now or in the foreseeable future. Coupling this tuning ability with available lasers, from CO_2 through the various harmonics of a Nd:YAG to an excimer ArF, any photon energy from 0.03 eV up to 21 eV is attainable. This is a perfect match with the energy range of interest for H^-, from well below the single-electron photodetachment threshold, right through the resonance region and up beyond the double-detachment threshold. An H^- beam considerably less relativistic could not provide the necessary tunability; one considerably more so would not survive the magnets needed to steer it, as the fields would tear apart the rather delicate H^- ion.

The second important feature of the LAMPF beam is the relativistic transformation of electromagnetic fields. A modest transverse magnetic field $B_\perp$ in the laboratory becomes a substantial electric field, of strength

$$F_\perp = \gamma\beta cB_\perp \tag{1.2}$$

(SI units), in the rest frame of the ions. (The symbol F is used here for field strength to avoid confusion elsewhere with the photon energy E). It is extremely difficult to apply such strong fields in a normal laboratory environment, especially to charged particles, as the several MV/cm that have been applied here. Thus, this technique allows the study, for example, of the quenching of resonances in

It should be pointed out that there is an alternative method for production and study of doubly-excited states, and this is electron scattering from neutral hydrogen. In fact, the processes are complementary, since the decay of the doubly-excited resonances, H^{-**}, into a neutral hydrogen plus an electron may be regarded as a time-reversal of electron-collision excitation. However, photoexcitation offers two distinct advantages: firstly that the energy resolution is better by typically a factor of ten, because of the difficulty of producing monochromatic e^- and H° beams, and secondly that the final state is well defined — it is always $^1P^\circ$ ($S = 0$, $L = 1$, odd parity) for a single photon process, as opposed to the mixture of states resulting from collisional excitation.

1.3 H^- Photodetachment Studies at Los Alamos.

The photodetachment experiments at LAMPF began in 1977, with the first observation (Tootoonchi Saraf, 1977) of the most dramatic of the high-lying resonances in H^- — the $n = 2$ Feshbach and shape resonances, shown in Figure 1.2. These resonances had been predicted by theory (Broad and Reinhardt, 1976); they are caused by the excitation of the neutral core hydrogen atom into the $n = 2$ state, and its subsequent polarization by the outer electron which is then bound by the resulting dipole potential.

The Feshbach resonance is very narrow, possibly just 30 μeV wide (see, for example, Lipsky and Conneely (1976), and others listed in MacArthur *et al.* (1985)). It also has an enormous peak cross section, possibly as high as 50 a_0^2, although ongoing calculations (Greene, 1990) indicate that it may be an order of magnitude less than this. The shape resonance is much broader, and it had been expected to be visible in stellar spectra; the failure to observe it despite extensive studies (Ott, 1975; Snow, 1975) left its very existence in some doubt until its discovery at Los Alamos. (It was also seen just above background noise levels in

a spectroscopic study by Behringer and Thoma (1978) of ultraviolet discharges from a hydrogen plasma).

Following this initial success, the failure of astronomers to observe the shape resonance was attributed to quenching in the large electric fields near the surfaces of stars. It was decided to test this hypothesis at LAMPF, and it was quickly found that, although the Feshbach resonance did in fact split and quench in moderate fields, the shape resonance was almost unaffected until it eventually broadened and mixed with a ^{1}D resonance when the fields became extremely strong (Butterfield, 1984).

Other landmark experiments in this series have included the discovery of resonances near the hydrogenic n = 3 threshold (Hamm *et al.*, 1979), and the investigation of their behavior in electric fields (Cohen, 1985; Cohen *et al.*, 1989); a survey of the cross section in the region of the double-detachment threshold, which included the initial discovery of three resonances below the hydrogenic $n = 6$ threshold (Frost, 1981; Clark *et al.*, 1980); a test of the special theory of relativity, by looking for discrepancies in the energy level spacing of relativistic neutral hydrogen (MacArthur *et al.*, 1986); the observation of electric-field induced modulations in the photodetachment cross section near the single-detachment threshold (Stewart, 1987; Bryant *et al.*, 1987); and the first observation of multiphoton detachment in H^- (Tang *et al.*, 1989).

This dissertation describes the latest experiments investigating the structure of H^-. It reports the first observation of several series of doubly-excited autoionizing resonances, which appear as structures converging on the threshold energies of excited neutral hydrogen, and it compares the measured energies and widths with theoretical predictions. The analysis reveals that these energies follow a simple and elegant formula, as do the excited energy levels in neutral hydrogen.

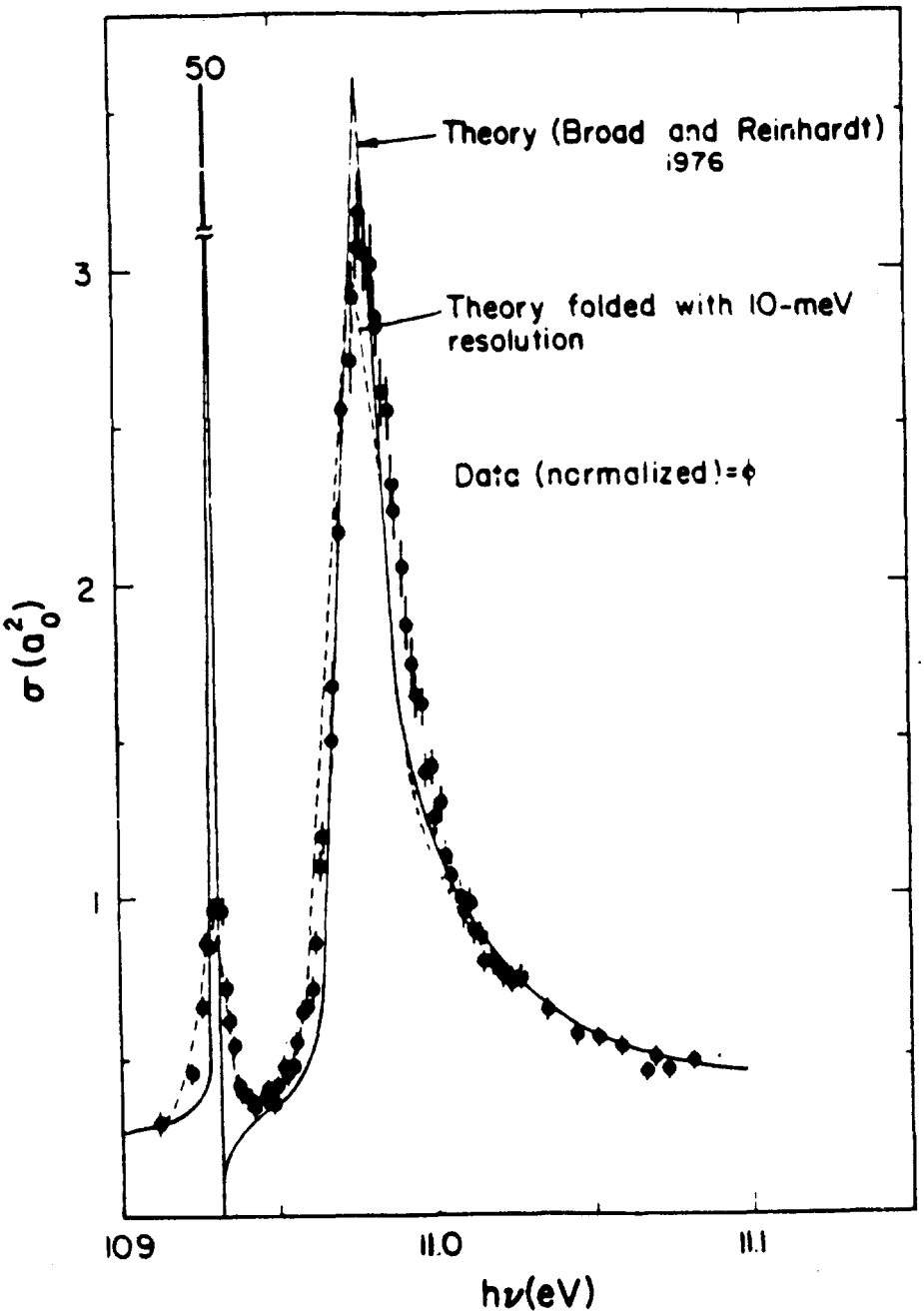

Figure 1.2. The Feshbach and Shape resonances, near the hydrogenic $n = 2$ threshold. (See also Figure E.3 for a high-resolution scan of these resonances).

Chapter 2

Physical Nature of the Resonances

'The truth is rarely pure, and never simple.'

— Oscar Wilde, *The Importance of Being Earnest.*

We have already seen, in Chapter 1, that the photodetachment cross section of H^- has a surprising amount of structure at energies far above that required to detach a single electron (0.7542 eV). One might expect that, once this threshold energy is reached, the free electron would simply carry away any excess energy in the form of kinetic energy, and that the continuum would therefore be structureless; but, as we have seen in Figure 1.1 and again in detail in Figure 1.2, this is clearly not the case. The Feshbach and shape resonances are associated with the $n = 2$ level of neutral hydrogen, and there are likewise many more resonances lying at still higher energies and associated with other hydrogenic thresholds.

In this chapter, we aim to explore the physical principles that lead to the existence of these "bound states in the continuum". We shall see why the resonances are associated with neutral hydrogen, and how they may be classified in various different ways; we shall discuss briefly the nature of the potentials that bind them, and give an approximate (analytic) formula for the expected energy levels; and finally, we shall consider how the resonances would be expected to alter the structure of the continuum cross section.

2.1 Autoionizing Resonances.

One can think of the resonances in H^-, such as the Feshbach and shape resonances, as having a "core" consisting of an excited hydrogen atom which is polarized by a second, outer, electron. This polarization results in a potential, discussed in the following two sections and illustrated in Figure 2.1 for the ^1P resonances near $H^\circ(n = 2)$ (Lin, 1975), which supports one or more bound states. Upon the return of the "core" hydrogen atom to its ground state, the outer electron is ejected — hence the name "autoionizing". (In this case, "autodetaching" would be more appropriate, since a neutral atom is produced rather than an ion; but we shall continue to use the former name). This basic system of a polarized excited core binding an outer electron is sometimes known as a "planetary" resonance.

2.2 Hyperspherical Coordinates and Ridge States.

The non-relativistic Hamiltonian for the two-electron system with fixed nucleus is, in atomic units (see Bethe and Salpeter, 1957),

$$H = -\frac{1}{2}\nabla_1^2 - \frac{1}{2}\nabla_2^2 - \frac{Z}{r_1} - \frac{Z}{r_2} + \frac{1}{r_{12}}, \tag{2.1}$$

where the nuclear charge $Z = 1$ in H^-, r_1 and r_2 are the distances of the two electrons from the nucleus, and r_{12} is the separation between the two electrons.

In discussing the two-electron system, it becomes advantageous to adopt a new set of particle coordinates, the hyperspherical coordinates, defined as

$$\mathcal{R} = \left(r_1^2 + r_2^2\right)^{1/2}, \tag{2.2}$$

$$\tan\alpha = r_1/r_2, \text{ and} \tag{2.3}$$

$$\theta_{12} = \cos^{-1}\left(\hat{r}_1 \cdot \hat{r}_2\right), \tag{2.4}$$

where $\vec{r}_1$, $\vec{r}_2$ are the radius vectors of the electrons.

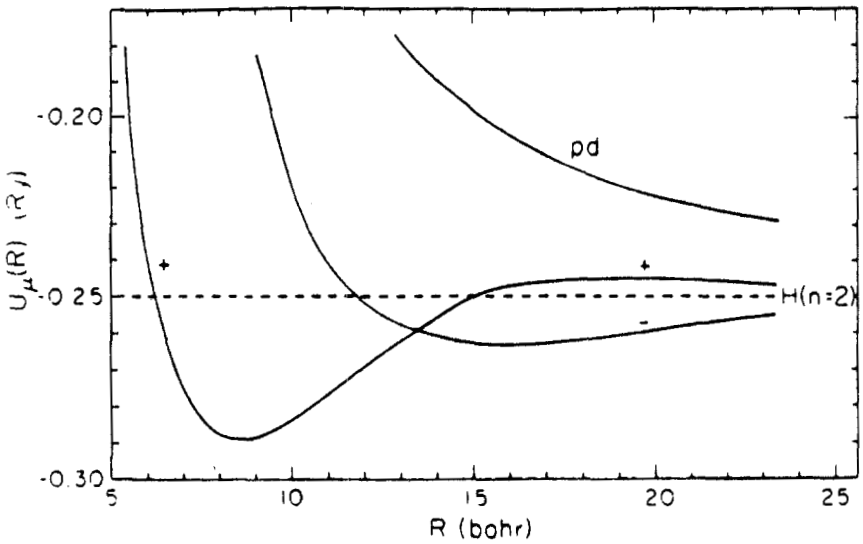

Figure 2.1. Potential curves for ^{1}P channels converging to H°(n = 2). (Lin, 1975).

In these coordinates, and again in atomic units, the Schrödinger equation for the two electrons (with the nucleus fixed) is (Macek, 1968)

$$\left(\frac{d^2}{d\mathcal{R}^2} + \frac{5}{\mathcal{R}}\frac{d}{d\mathcal{R}} - \frac{\Lambda^2}{\mathcal{R}^2} - \frac{2C}{\mathcal{R}} + 2E\right)\tilde{\psi} = 0, \tag{2.5}$$

where Λ^2 is Casimir's operator

$$\Lambda^2 = -\frac{1}{\sin^2\alpha\cos^2\alpha}\frac{d}{d\alpha}\sin^2\alpha\cos^2\alpha\frac{d}{d\alpha} + \frac{L_1^2}{\cos^2\alpha} + \frac{L_2^2}{\sin^2\alpha} \tag{2.6}$$

with eigenvalues $\lambda(\lambda+4)$ where λ is an integer. The potential energy of the system is $V = C/\mathcal{R}$, where

$$\begin{aligned} C &= -\mathcal{R}\left(\frac{1}{r_1} + \frac{1}{r_2} - \frac{1}{r_{12}}\right) \\ &= -\frac{1}{\cos\alpha} - \frac{1}{\sin\alpha} + \frac{1}{(1-\sin 2\alpha\cos\theta_{12})^{1/2}}. \end{aligned} \tag{2.7}$$

This definition of C agrees with that of Lin (1986), but differs by a factor of -2 from that of Macek (1968) and of Lin (1974).

Since the hyperspherical radius $\mathcal{R}$ is simply a scale factor, the potential energy can be represented by C (sometimes known as the "effective charge"), which is a function purely of the hyperspherical angles θ_{12} and α. It may therefore be plotted as a surface, as shown in Figure 2.2. The energy has minima at $\alpha = 0$ and $\pi/2$; these give rise to the "valley states", for which one electron is close to the nucleus and the other is far away; this is a limiting case of the planetary resonances spoken of earlier. Singly-excited states, in a system (such as helium) that supports them, would be valley states.

There is a high maximum when the electrons are coincident, at $\alpha = \pi/4$, $\theta_{12} = 0$. In addition, there is a saddle point at $\alpha = \pi/4$, $\theta_{12} = \pi$, which lies at the back of a broad, flat ridge; some states have a high probability density in this region of hyperspherical space — hence the nomenclature of the "ridge states" (see, *e.g.*, Rau 1987, Lin 1974). At this saddle point, the electrons are equidistant from the nucleus and diametrically opposite one another, and their motion is strongly correlated; they therefore may lose their association with the parent hydrogen atom, and become associated instead with the "grandparent" nucleus.

A whole series of these "ridge" states exists; in the lower limit, they are just the so-called intrashell resonances (both electrons occupying the same shell), characterized as $2s2p$, $3s3p$, $4s4p$... (see section 2.3); in the upper limit, they become the "two-electron ionization ladder" (Nicoliades, 1990), and are eventually responsible for the double-detachment process. The ridge resonance energies obey a Rydberg-type formula which will be discussed at length in section 2.5 and again in Chapter 4.

The Schrödinger equation (2.4) is not completely separable in hyperspherical coordinates. However, substitution of

$$\bar{\psi} = \mathcal{R}^{-5/2}\psi \tag{2.8}$$

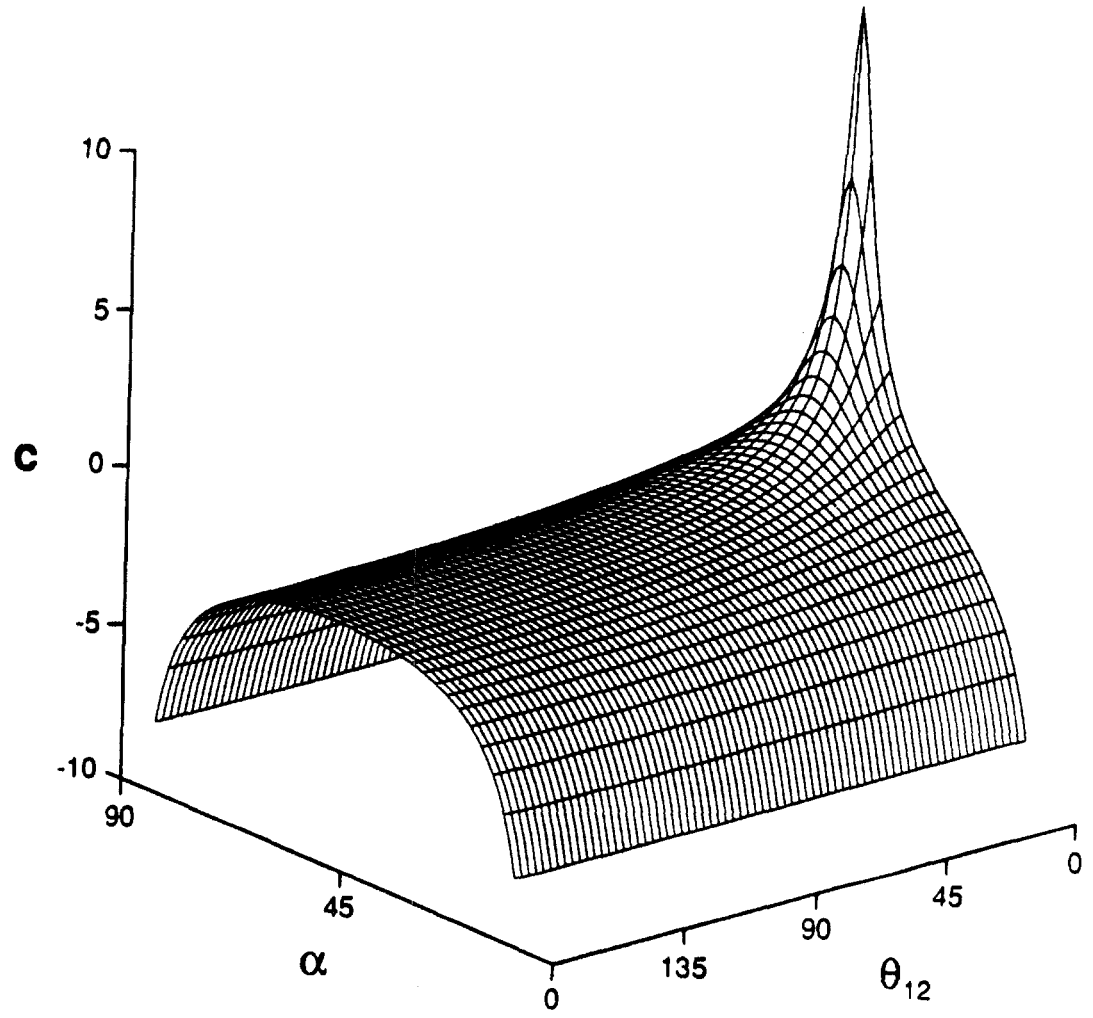

Figure 2.2. Potential surface in hyperspherical coordinates at $\mathcal{R} = 1$ bohr. (Courtesy of J. Knudson; based on a similar figure from Lin, 1974).

reduces it to

$$\left(-\frac{d^2}{d\mathcal{R}^2} + \frac{\Lambda^2 + 15/4}{\mathcal{R}^2} + \frac{2C}{\mathcal{R}} - 2E\right)\psi = 0. \tag{2.9}$$

The wave function ψ can then be expanded (Lin, 1974, 1986) as

$$\psi = \sum_{\mu} \phi_\mu(\mathcal{R}, \Omega) F_\mu(\mathcal{R}) / (\mathcal{R}^{5/2} \sin\alpha \cos\alpha). \tag{2.10}$$

The so-called *channel function* $\phi_\mu(\mathcal{R}, \Omega)$ satisfies the differential equation

$$\frac{1}{\mathcal{R}^2}\left(-\frac{d^2}{d\alpha^2} + \frac{L_1^2}{\cos^2\alpha} + \frac{L_2^2}{\sin^2\alpha} + 2\mathcal{R}C\right)\phi_\mu(\mathcal{R}, \Omega) = U_\mu(\mathcal{R})\phi_\mu(\mathcal{R}, \Omega), \tag{2.11}$$

and the hyperradial function $F_\mu(\mathcal{R})$ satisfies the coupled equations

$$\left\{\frac{d^2}{d\mathcal{R}^2} - U_\mu(\mathcal{R}) + \frac{1}{4\mathcal{R}^2} + W_{\mu\mu}(\mathcal{R}) + 2E\right\}F_\mu + \sum_\nu W_{\mu\nu}(\mathcal{R})F_\nu = 0 \qquad (2.12)$$

where the coupling terms W are defined as

$$W_{\mu\nu} = 2\left\langle \phi_\mu \left| \frac{d}{d\mathcal{R}} \right| \phi_\nu \right\rangle \frac{d}{d\mathcal{R}} + \left\langle \phi_\mu \left| \frac{d^2}{d\mathcal{R}^2} \right| \phi_\nu \right\rangle. \qquad (2.13)$$

At this stage, all of the non-diagonal coupling terms $W_{\mu\nu}$ are usually neglected; the resulting equation,

$$\left\{\frac{d^2}{d\mathcal{R}^2} - U_\mu(\mathcal{R}) + \frac{1}{4\mathcal{R}^2} + W_{\mu\mu}(\mathcal{R}) + 2E\right\}F_\mu = 0, \qquad (2.14)$$

is known as the "adiabatic approximation". The second-order diagonal term $W_{\mu\mu}(\mathcal{R})$ is included in this approximation, although it is usually dropped in the Born-Oppenheimer expansion for diatomic molecules.

Each resonance series and its adjoining continuum are jointly called a "channel", each channel (designated by a set of parameters μ) being characterized by the eigenvalue $U_\mu(\mathcal{R})$ and its eigenfunction $\phi_\mu(\mathcal{R}, \Omega)$. The potential curves illustrated in Figure 2.1 are in fact just the $U_\mu(\mathcal{R})$ for the three channels associated with the hydrogenic $n = 2$ threshold.

2.3. Classification of Doubly-Excited States.

Having seen the origin of the potentials $U_\mu(\mathcal{R})$, we shall next consider the designations of the different channels μ. We begin in sections 2.3.1 and 2.3.2 with the simple "+/−/0" designation (which primarily describes radial correlations), before looking at the more complete K-T-A classification in section 2.3.3.

2.3.1 "+/−/0" Classification.

Following the discovery of autoionizing resonances in helium (Madden and Codling, 1963), Cooper, Fano and Prats (1963) developed a notation to describe

doubly excited states. If the electrons were independent, with, say, one of the pair being in a $2s$ or $2p$ state, a series of excited states would arise from the other being in any of the higher states n. As the electron correlations are very strong, however, single-particle wave functions $u(n,l)$ cannot be used; instead, linear combinations of these states are appropriate. So, for example, the wave functions ψ for the ^{1}P ($S = 0, L = 1$) resonances at the H°($n = 2$) threshold in H^- may be approximated by

$$\frac{1}{\sqrt{2}}(u(2s)u(np) \pm u(2p)u(ns)), \tag{2.15}$$

or more simply as

$$2snp \pm 2pns. \tag{2.16}$$

In this case, the only "+" state supported by the potential is the so-called "shape" resonance (named for the curious shape, with three classical turning points, of the potential curve that binds it — see Figure 2.1), represented by $2s2p$. On the other hand, an entire series of "−" resonances is believed to be supported. The only one of these to have been observed so far (Figure 1.2) is the first in the series, the Feshbach resonance represented by $2s3p - 2p3s$. Its first recursion should occur approximately 1 meV below the $n = 2$ threshold.

In addition to the "+" and "−" channels, Figure 2.1 also illustrates the so-called "*pd*" or "0" channel. ^{1}P states may be formed from linear combinations of np and nd wave functions, but in this case the potential is entirely repulsive, so no bound states are supported.

As we move to higher and higher excited states, more and more such linear combinations become available to form ^{1}P states. The polarization potentials for $n = 2$, 3 and 4 are shown in Figure 2.3 (Sadeghpour, 1990a); those for $n = 4$ to 9 (nicknamed the "spaghetti potentials") in Figure 2.4. Of these, the lowest "+" potentials are isolated in Figure 2.5, which also shows the levels of the first

resonance in each of these channels. According to Greene (1980), two-electron excitations into the "+" channels are expected to occur more strongly than into the "−" channels by one to two orders of magnitude, since the potential curves $U_+(\mathcal{R})$ are more attractive at small $\mathcal{R}$ and allow both electrons to overlap with the ground state far better than do the $U_-(\mathcal{R})$ curves. (Greene's remark was specifically directed towards the $n = 3$ channel, but it should hold equally well for other channels too).

In addition to emphasizing the lowest "+" potential curve in each channel, Figure 2.4 also highlights a potential curve — the fourth 7+ curve — that may support a shape resonance just above the $n = 7$ threshold. At the time of writing, it is not yet certain whether such a resonance is in fact bound here, but if it is it would be very broad, and probably rather weak as it is associated with the fourth "+" series. It may mix with the lowest 8+ Feshbach resonance, which also lies right at the $n = 7$ threshold.

Classifying the wave functions with the "+/−" quantum numbers, which emphasizes whether the two electrons approaching the nucleus are in phase or out of phase — and thus whether the wave function vanishes (for "−") or not (for "+") at $\vec{r}_1 = \vec{r}_2$ (Lin, 1983) — is of course still an approximation. In fact, equation 2.15 should be a sum over all angular-momentum components l_1, l_2 that can add to a total $L = 1$ (Lin, 1975). The hyperspherical calculations, however, treat the different channels ("+", "−" and "*pd*") independently, by omitting the coupling terms $W_{\mu\nu}$ (see section 2.2), and this seems to work well. The potential curves shown in Figures 2.3 and 2.4 illustrate better the real situation; the curves do not in fact cross one another. When they get very close, the coupling strength between them shows a sharp spike, and they repel one another. The region where this occurs is known as an "avoided crossing". From the coupling strength, one can tell if the two curves are decoupled enough to simply assume that they cross,

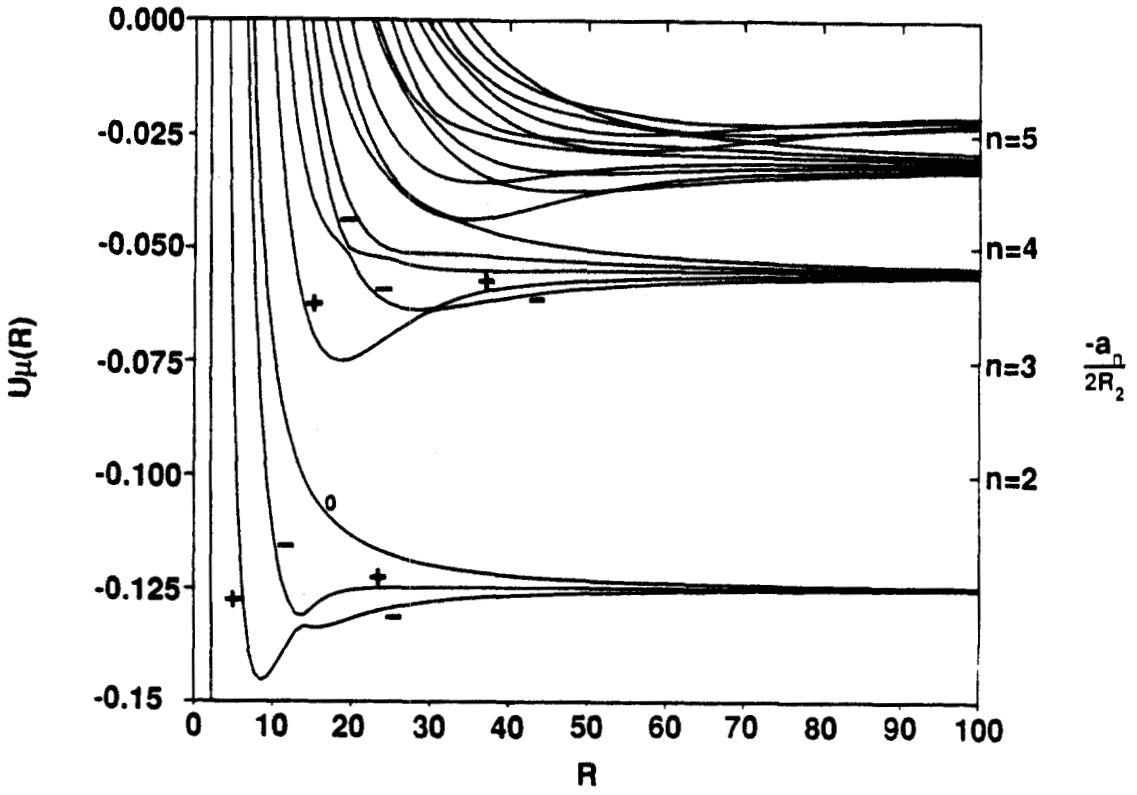

Figure 2.3. Potential curves converging on the $n = 2$, 3 and 4 thresholds of H° (Sadeghpour, 1990a).

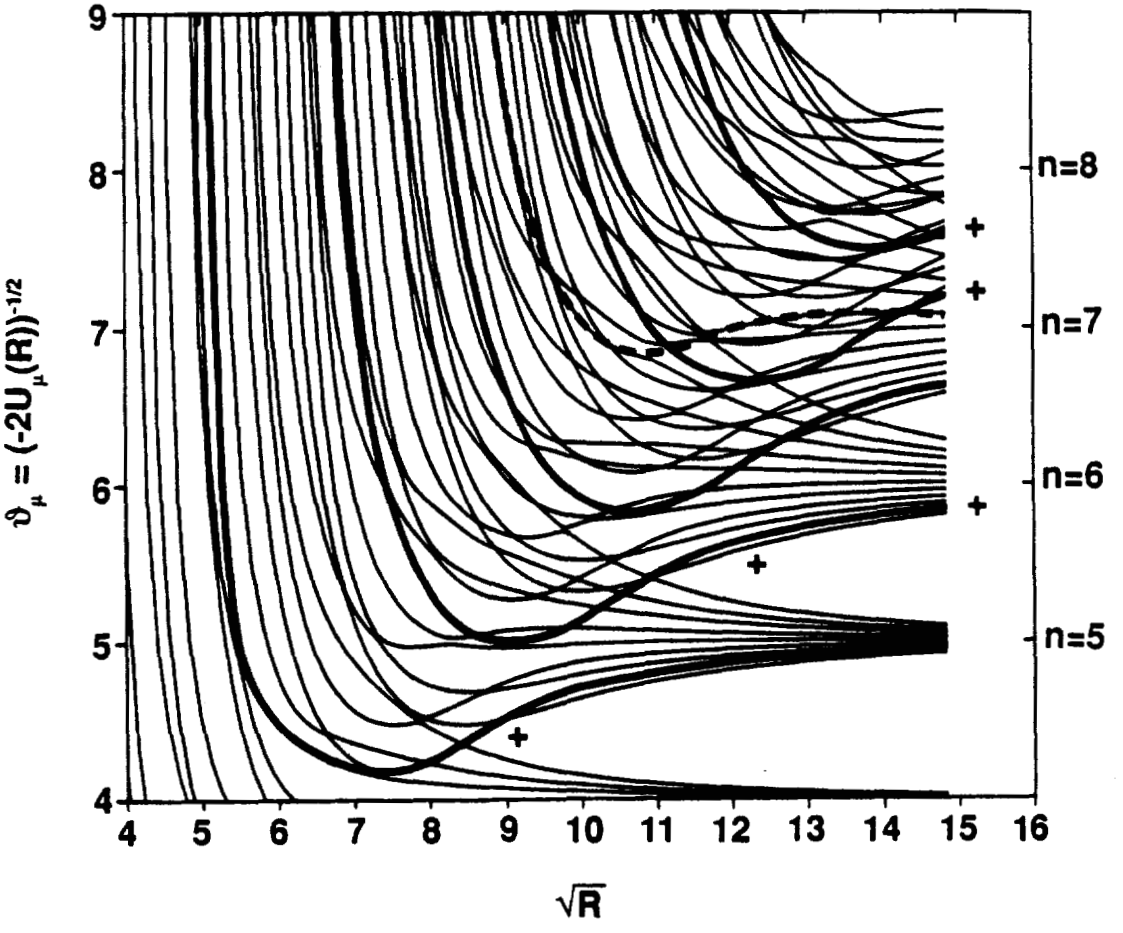

Figure 2.4. Potential curves converging on the n = 4 to 9 thresholds of H° (Sadeghpour, 1990a).

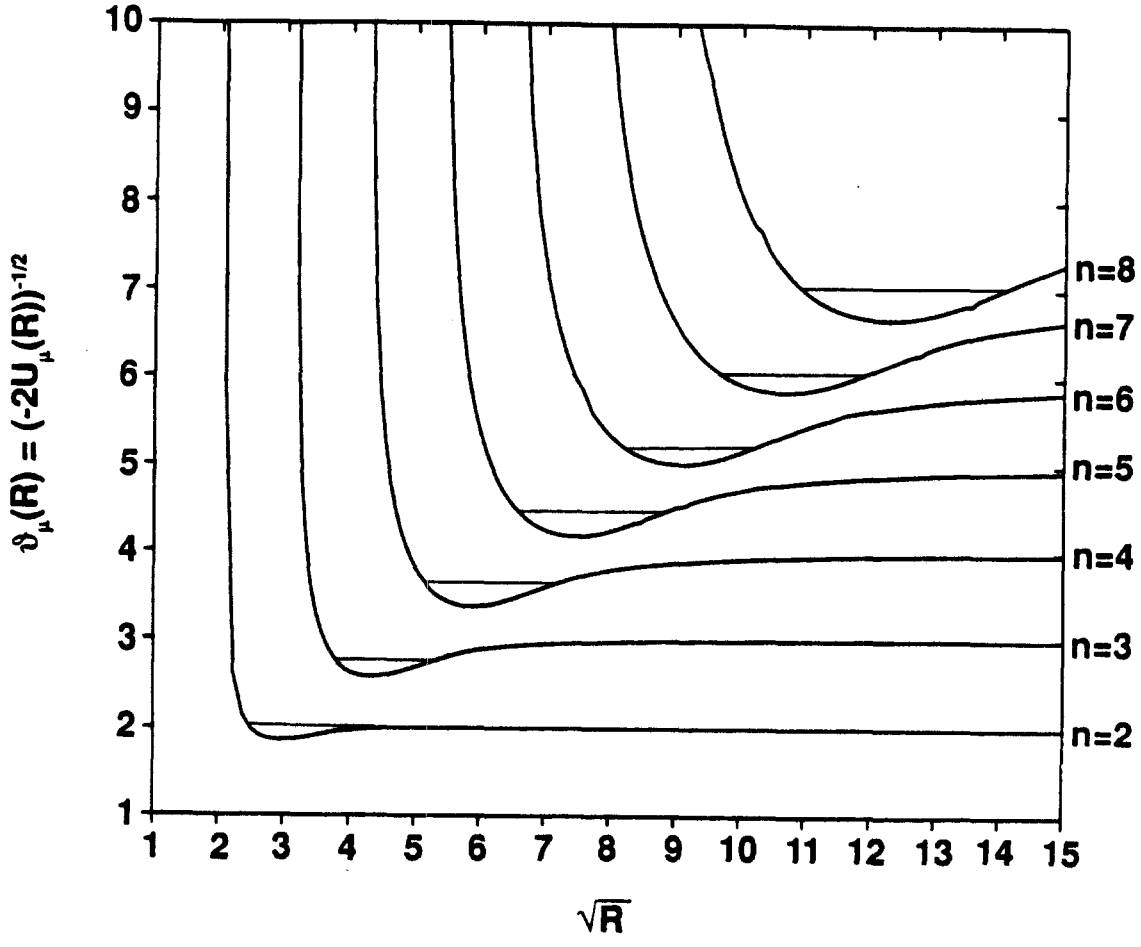

Figure 2.5. Lowest "+" Potential curves converging on the $n = 4$ to 9 thresholds of H°, showing the energy levels of the first resonance in each series (Sadeghpour, 1990a).

as shown in Figure 2.1. In fact, the reason that the 2+ potential is repulsive at large $\mathcal{R}$ (again, see Figure 2.1) is that the "+" and "−" channels interact strongly enough to repel one another, so the "+" channel is pushed up (and supports the shape resonance) and the "−" channel is pushed down. As n increases, the avoided crossings become sharper and sharper, and the approximate "+" and "−" quantum numbers become more and more exact.

2.3.2 Mechanical Analog.

It is helpful to consider a simple classical model to explain the difference between the radial correlations of the electron pair for the "+" and for the "−" types of resonance.

Developing a model suggested by Cooper *et al.* (1963), Bryant proposed a mechanical analog based upon the "Newton's Cradle" — the popular set of steel balls suspended, just touching, in a row, often used to demonstrate resonant behavior in classical mechanics (Bryant *et al.*, 1983). This model consists of just three such balls, the central one being extremely massive (to represent the proton) relative to the outer pair (the electrons), as illustrated in Figure 2.6. There are two resonant modes of oscillation; the outer pair of balls may move either in the same direction (correlated motion), which results in a very long-lived resonance, or their motion may be "anticorrelated", which produces a short-lived resonance that begins to decay immediately, as the balls do not hit the central sphere simultaneously. These represent, then, the Feshbach (−) and shape (+) resonances respectively. This analogy may be carried a stage further, as, in an external field, the outer electron in a "−" type resonance would see a shielded nuclear potential, and so would be more susceptible to detachment, whereas for the "+" type resonance both electrons would see the full nuclear charge when distant from the nucleus. Thus, the shape resonance, normally short-lived (and

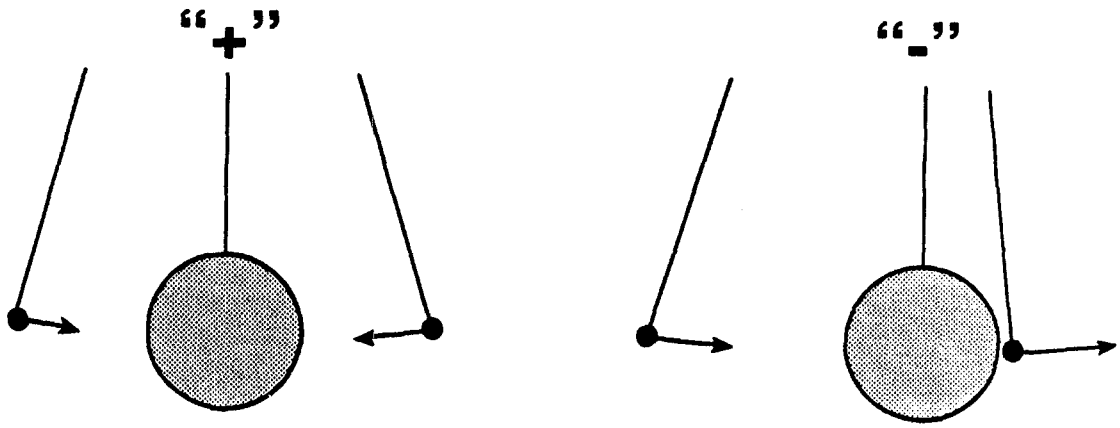

Figure 2.6. "Newton's Cradle" model of two-electron resonances.

therefore broad), remains unaffected until relatively high fields are imposed, and in contrast the long-lived Feshbach resonance is quenched in modest fields.

2.3.3 K-T-A Classification.

An independent-particle model would represent the two-electron wave function as $|n_1 l_1, n_2 l_2, L, S, \pi\rangle$, where L and S are the total angular momentum and spin, respectively, and π is the parity. Herrick and Sinanoglu (1975) introduced mixings of l_1 and l_2 within a given n_1, n_2, and replaced l_1 and l_2 with two new quantum numbers K and T. Each doubly-excited state is then represented by quantum numbers $|nmKTLS\pi\rangle$, where m and n are the principal quantum numbers of the outer and inner electrons respectively. n is therefore the hydrogenic threshold below which the resonance lies. The intrashell resonances, the lowest of any given series, have the two electrons occupying the same shell, so $m = n$.

The numbers K and T arise from group theoretical calculations. K is related to $\langle -\cos\theta_{12} \rangle$, where θ_{12} represents the angle between the radius vectors of the electrons; the larger the positive K, the closer is $\langle -\cos\theta_{12} \rangle$ to unity. K may be considered as a (bending) vibrational quantum number. T, on the other

hand, measures the projection of the total angular momentum L onto the inter-electron axis, and as such describes the orientations between the orbitals of the two electrons; thus, $T = 0$ implies that the orbitals lie in the same plane. T may be considered to be a rotational quantum number. K and T therefore describe the angular correlations of the system (see, for example, Ho and Callaway, 1986). According to Herrick and Sinanoglu (1975), $T = 0,\ 1,\ldots\ \min(L, n-1)$ (although $T = 0$ is forbidden for states where the parity $\pi = (-1)^{L+1}$), and $K = n - T - 1,\ n - T - 3,\ldots, -(n - 1 - T)$.

The lowest $^1P^o$ "+" channels have the maximum possible K within a given n-manifold, namely $n - 2$, and also have $T = 1$.

In addition, Lin (1983; 1990) introduces a quantum number A to describe radial correlations. A is allowed the values $+1$, -1 and 0. A state with $A = +1$ would have an antinode for the hyperspherical angle α (of equation 2.3) at about $\alpha = \pi/4$; a state with $A = -1$ would have a node there. This designation coincides with the "+/−" classification of Cooper, Fano and Prats (1963). States that have neither node nor antinode are assigned $A = 0$, and their characters are similar to singly excited states.

A may also be expressed in terms of the other quantum numbers (see, for example, Lin, 1986). If $K > L - n$, then $A = \pi(-1)^{S+T}$; otherwise, $A = 0$. In addition, states with $L > 2(n - 1)$ must have $A = 0$ (see, *e.g.*, Ho, 1990).

2.4 Recursion Formula.

Having established the nature of the potentials $U_\mu(\mathcal{R})$, let us now consider, in this and the following section, the energies of the bound states that they support.

Gailitis and Damburg (1963a, 1963b) have shown that, as the hyperspherical radius $\mathcal{R} \to \infty$, the potential $U_\mu(\mathcal{R})$ — which is just the interaction energy of an electron in the field of an excited hydrogen atom — takes the form (in eV)

$$U_\mu(\mathcal{R}) \longrightarrow -R\left(\frac{1}{n^2} + \frac{a_n}{\mathcal{R}^2}\right), \tag{2.17}$$

where R is the (reduced-mass) Rydberg energy, 13.5984 eV (not to be confused with the hyperspherical radius $\mathcal{R}$), and the hydrogen atom is in state n. This is the long-range dipole potential that binds series of the so-called Feshbach resonances (of both "+" and "−" character) below the hydrogenic threshold in question, as we have discussed in section 2.3.1. The positions E_k and widths Γ_k of successive resonances within such a series, converging on the threshold at energy $E_n = E_t - R/n^2$ (where E_t is the double-detachment threshold energy, 14.3526 eV) should then obey the simple recursion formula

$$\frac{E_n - E_k}{E_n - E_{k+1}} = e^{\frac{2\pi}{\alpha_n}} = \frac{\Gamma_k}{\Gamma_{k+1}}, \tag{2.18}$$

where $k = m - n + 1$ is the "number" of the resonance in the series, and

$$\alpha_n = (a_n - 1/4)^{1/2}. \tag{2.19}$$

We shall refer to a_n as the *dipole parameter* of the relevant photoionization channel. The values of a_n may be calculated very precisely, and are listed in Table 2.1; they may also be calculated approximately from the formulae (see, for example, Sadeghpour and Greene, 1990)

$$a_n^+ = 3n^2 - \frac{23n}{3} + \frac{2}{3n} + 1 \tag{2.20}$$

for the lowest "+" series, and

$$a_n^- = 3n^2 - \frac{23n}{6} + \frac{7}{6n} \tag{2.21}$$

for the lowest "−" series. These approximations differ from the exact values by less than 0.3%, as shown also in Table 2.1. The series are expected to terminate

Hydrogenic threshold n:	a_n^+ (theory)	a_n^+ (formula 2.20)
3	5.22	5.22
4	18.46	18.50
5	37.70	37.80
6	62.95	63.11
7	94.20	94.43
8	131.45	131.75
9	174.70	175.70
10	223.96	224.40

Table 2.1 Theoretical values of the dipole parameter a_n^+ (Sadeghpour, 1989a). The thresholds in each case are those to which the resonances converge — *e.g.*, the resonances in the $n = 4$ continuum are associated with the hydrogenic $n = 5$ threshold.

only when the resonances are separated from the threshold by an energy equal to the relativistic splitting of the hydrogenic levels.

Calculations (*e.g.*, Sadeghpour, 1990a) have shown that a strong series of "+" type resonances lies below each hydrogenic threshold from $n = 3$ upwards. (The series of Feshbach resonances believed to lie below $n = 2$ is a "−" series). As indicated earlier, the hyperspherical potentials that support these particular series of resonances are illustrated (isolated from their companions) in Figure 2.5, along with the levels of the first resonance in each series. Sadeghpour has to date carried his hyperspherical calculations up to the $n = 12$ hydrogenic level (Sadeghpour and Greene, 1990).

2.5 Recursions of Series: the "2e-Formula".

Since the resonances are associated with the neutral hydrogenic thresholds, which themselves have an (approximate) energy dependence

$$E_n = E_t - R/n^2 \tag{2.22}$$

(where E_t is again the double-detachment threshold energy), it is natural to wonder if the entire series of resonances themselves might obey such a recursion relation. The so-called "modified Rydberg" formula

$$E = E_t - 2R\frac{(Z-\sigma)^2}{(n-\mu)^2} \tag{2.23}$$

for the lowest resonance in each series has been discussed by various authors, for example Read (1982), Rau (1983), and Molina (1989); the form essentially arises from the assumptions (i) that each electron partially screens the other from the charge of the nucleus, reducing the Coulomb potential outside the core from Z/r to $(Z-\sigma)/r$, where σ is a screening parameter, and (ii) that the stronger non-Coulombic potential experienced by an electron that penetrates the core may be parameterized by a quantum defect μ.

The formula may be obtained by considering the energy spectrum produced by the hyperspherical potential (see equation 2.7) expanded about the saddle point (recall from section 2.2 that the lowest resonances in each "+" series, the intrashell resonances, essentially reside at this point). The expansion gives, in atomic units, (Rau 1971, Read 1982)

$$V = \frac{1}{\mathcal{R}}[-Z_0 - Z_\alpha(\pi/4-\alpha)^2 + Z_\theta(\pi-\theta_{12})^2] \tag{2.24}$$

where

$$Z_0 = 2\sqrt{2}(Z-1/4),\ Z_\alpha = 3\sqrt{2}(Z-1/12),\ \text{and}\ Z_\theta = \sqrt{2}/16,$$

and of course $Z = 1$ for H^-. A first approximation to the states localized around $\alpha = \pi/4$, $\theta_{12} = \pi$ is to retain only the "hyperspherically symmetric" part in Z_0. However, because the saddle is so flat, even a small energy level spacing implies a significant extension in α and θ_{12} away from the saddle point; in other words, the wave function does not lie entirely on the ridge, but resides partially in the

valleys. The quantum defect compensates in some ways for this "core" effect. It is introduced, together with the screening parameter, by inclusion of the Z_α and Z_θ terms in the expansion.

Sadeghpour (1990b; see Sadeghpour and Greene, 1990) has fit the screening parameter σ and the quantum defect μ to his own (hyperspherical) calculations of the energies of the lowest "+" ^{1}P resonances in the $n = 3$, 4 and 5 series. By combining the results with the dipole recursion formula and the Rydberg formula, he has produced an analytic expression for the energies of all of the "+" -type ^{1}P resonances in H^- associated with all of the hydrogenic thresholds:

$$E(n,m) = E_t - \frac{R}{n^2} + 2R\, e^{-2\pi(m-n)/\alpha_n}\left[\frac{1}{2n^2} - \frac{0.70784}{(n+0.377)^2}\right], \qquad (2.25)$$

where

n is the principal quantum number of the hydrogenic threshold in question,

$m = n,\ n+1,\ n+2...,$ and

α_n is the dipole parameter belonging to channel n.

The first two terms are the usual Rydberg series for the hydrogenic thresholds, as given by equation 2.22. The term in square parentheses is the difference between these thresholds and the lowest resonance in each series as given by the modified Rydberg formula (2.23). This difference is multiplied by the factor $e^{-2\pi(m-n)/\alpha_n}$ to satisfy the dipole scaling law (2.18).

Notice that the quantum defect μ is unusual in that it is *negative* — this may suggest a different origin than the postulated "core effect".

For future convenience, let us now define

$$\eta = (Z - \sigma)^2, \qquad (2.26)$$

so that in this case $\eta = 0.70784$.

2.6 Cross-Section Structure in the Resonance Region.

So far, we have discussed the nature of the doubly-excited states, the different ways of classifying them and the relationships between their energy levels. We conclude this chapter by considering how the resonances might affect the continuum photodetachment cross section, and what kind of structure we might therefore expect to see as we "tune" the laser through the resonance energies.

If we represent the amplitude of a resonant state as

$$\psi_R(t) = Ae^{-i\omega_0 t}e^{-t/2\tau}, \tag{2.27}$$

a Fourier transform into the energy domain gives

$$\psi_R(E) = \frac{ia\Gamma/2}{(E-E_0)+i\Gamma/2}, \tag{2.28}$$

where $\Gamma\tau = \hbar, E = \hbar\omega$ and $a = 2A\hbar/\Gamma$.

This in turn leads to the usual Breit-Wigner formula for the cross section of a resonance,

$$\sigma = \psi^*\psi = \frac{a^2\Gamma^2/4}{(E-E_0)^2+\Gamma^2/4}, \tag{2.29}$$

where a constant of proportionality is included in the normalization.

If, however, the resonance lies on a continuum, then the total amplitude ψ_t becomes instead (Bryant *et al.*, 1983)

$$\psi_t = b + \frac{ae^{i\phi}\Gamma/2}{(E-E_0)+i\Gamma/2}, \tag{2.30}$$

where b is the continuum amplitude and ϕ is the phase difference between the resonance and the continuum. This leads easily to

$$\sigma = b^2 + \frac{a^2 + 2ab(\epsilon\cos\phi + \sin\phi)}{(\epsilon^2+1)}, \tag{2.31}$$

where $\epsilon = 2(E-E_0)/\Gamma$.

If the resonances overlap one another, it is necessary to add their amplitudes before calculating the intensity $\psi^*\psi$, and thus one obtains

$$\psi_t = b + \sum \frac{ae^{i\phi}\Gamma/2}{(E - E_0) + i\Gamma/2}. \tag{2.32}$$

The continuum background, here represented as b, also may be a function of the photon energy. When fitting to this model, it was assumed that b had a linear dependence on energy.

Equation 2.31 shows that the shape of the resonance depends on the phase ϕ between the resonance and the continuum. The resonances in question here are interesting in that the phase difference with the continuum is close to 180° — they therefore appear as dips rather than peaks! The dips found below $n = 3$ (Hamm *et al.*, 1979), shown in Figure 2.8, are in fact combinations of a dip and a peak, suggesting that the phase difference with the continuum is close to 90°; the $n = 2$ Feshbach resonance appears as a peak (although it is believed to have a dip associated with it), indicating that it is nearly in phase with the continuum in this model.

It is interesting to speculate that if we could somehow separate out the excited states before they were to decay, perhaps by laser excitation to a higher resonant state, the measured partial cross sections would then be from continuum production alone, and the dips should disappear! This is similar to determining which slit a photon went through in a double-slit experiment, which destroys the interference pattern.

With a surprising amount of algebra, equation 2.31 for the cross section may be cast in the more common form (Fano, 1961)

$$\sigma = \sigma_b + \sigma_a \frac{(q + \epsilon)^2}{1 + \epsilon^2}, \tag{2.33}$$

usually known as a Fano lineshape (Figure 2.7). Note that $b^2 \neq \sigma_b$, since as $\epsilon \rightarrow \infty$, $\sigma \rightarrow \sigma_a + \sigma_b$; this would seem to imply that the resonance contributes

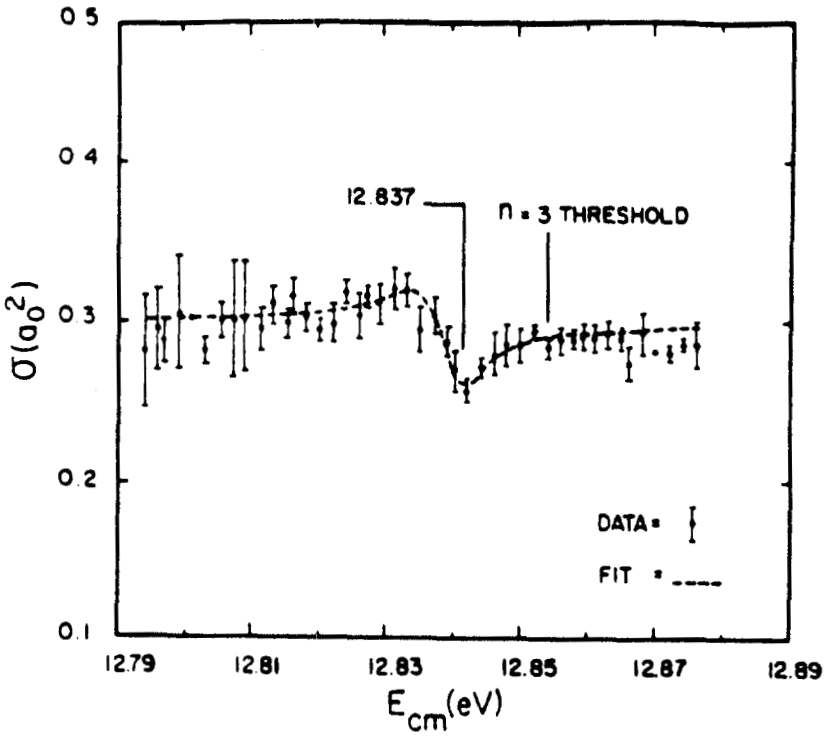

Figure 2.7. Dips in the H^- continuum below $H^0(n = 3)$ (Hamm *et al.*, 1979).

a term σ_a to the continuum background even infinitely far from the energy E_0 of the resonance. Let us therefore redefine σ_b,

$$\sigma_b \rightarrow \sigma_b - \sigma_a, \tag{2.34}$$

so that the continuum amplitude far from the resonance is just σ_b. The resonance is then "decoupled" from the continuum, and the Fano lineshape becomes

$$\sigma = \sigma_b + \sigma_a \left[\frac{(q+\epsilon)^2}{1+\epsilon^2} - 1 \right]. \tag{2.35}$$

A series of such lineshapes that do not overlap would then be represented by

$$\sigma = \sigma_b + \sum \sigma_a \left[\frac{(q+\epsilon)^2}{1+\epsilon^2} - 1 \right], \tag{2.36}$$

where again it is worth emphasizing that the σ_b defined here is slightly different from that defined by Fano.

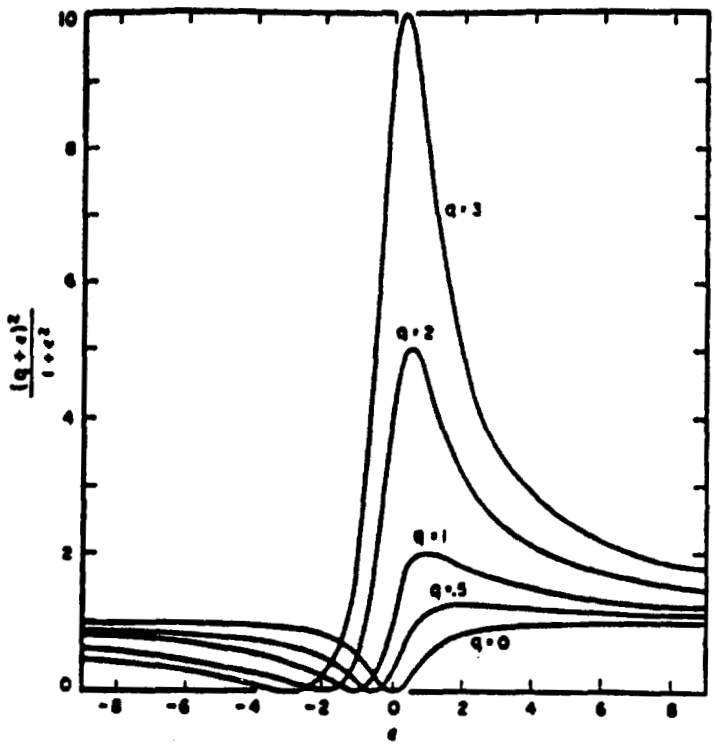

Figure 2.8. Fano lineshapes (Fano, 1961).

The shape of the resonance, determined by ϕ in equation 2.31, is correspondingly contained in the asymmetry parameter q of equation 2.33. This is defined as

$$q = \frac{\langle \Phi | T | i \rangle}{(\pi \Gamma/2)^{1/2} \langle \Psi | T | i \rangle}, \tag{2.37}$$

where $\langle \Phi | T | i \rangle$ is the transition probability from the H^- ground state i to the resonance, and $\langle \Psi | T | i \rangle$ is the transition probability from the ground state to the continuum. Since the overlap of the resonance wave function with the ground state is expected to become very close to zero for high-lying resonances, $q \rightarrow 0$, and the resonances should appear more and more like pure dips.

Early evidence for both the dipole recursion formula and for the dip-like structure of high-lying resonances came from the "survey" double-detachment experiment (Frost, 1981), when dips were found in the $n = 5$ continuum (Clark

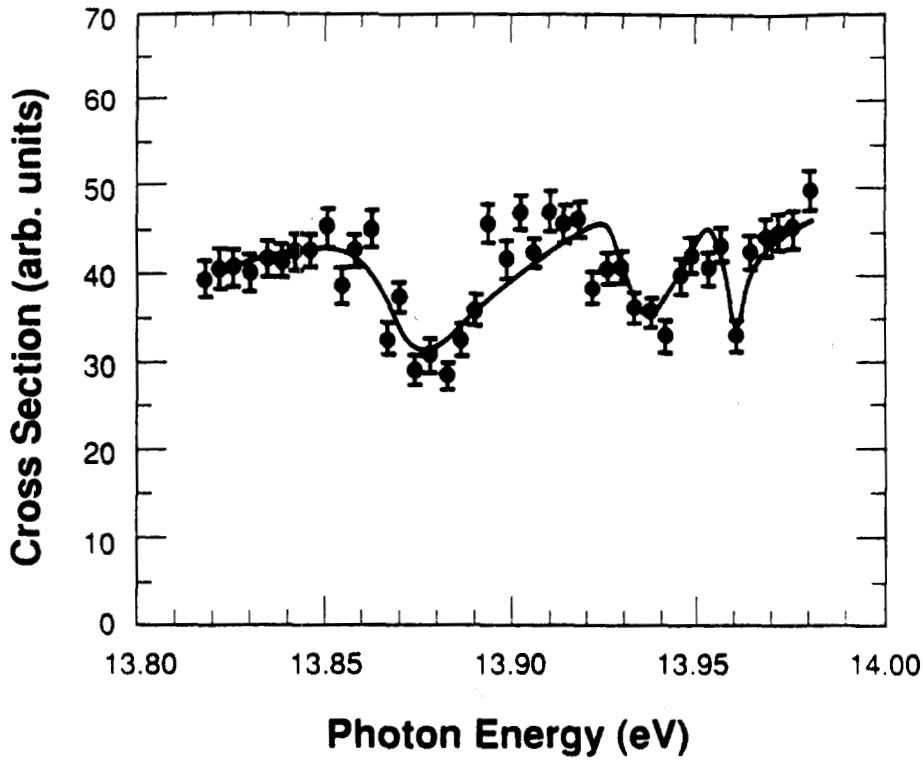

Figure 2.9. Dips in the H^- continuum below $H°(n = 6)$ (Clark *et al.*, 1980). Threshold energies are 13.8084 eV for $n = 5$ and 13.9746 eV for $n = 6$.

et al., 1980), as shown in Figure 2.9. The scan was at coarse resolution, and the third dip was only represented by a single data point.

Chapter 3

Experimental Technique

"Though this be madness, yet there is method in't."

— William Shakespeare, *Hamlet* II: ii: 211.

The experimental apparatus, of which there is a schematic diagram in Figure 3.1, is described in detail in Appendix A. Some familiarity with the material therein is assumed in this chapter, which aims to outline the principles underlying the experiment and the procedures followed during the data taking.

3.1 Overview.

In order to study the high-lying resonances in H^-, which, as has been indicated earlier, lie at energies of 10-14 eV — in the far uv — the fourth harmonic of our Nd:YAG laser ($E_0 = 4.6595$ eV) is Doppler tuned (see Chapter 1) to excite the transition

$$H^- + \gamma \rightarrow H^{0*}(\leq n) + e^-, \tag{3.1}$$

where the principal quantum number n of the hydrogen atom is typically between four and eight, and the "$\leq$" sign indicates that the atom may, instead, be excited to any state lower than n, with the electron carrying off the excess energy. The asterisk (*) indicates that the electron in the atom is excited.

As the angle α between laser and particle beams becomes smaller, and the photon energy correspondingly higher, successively higher n states are produced.

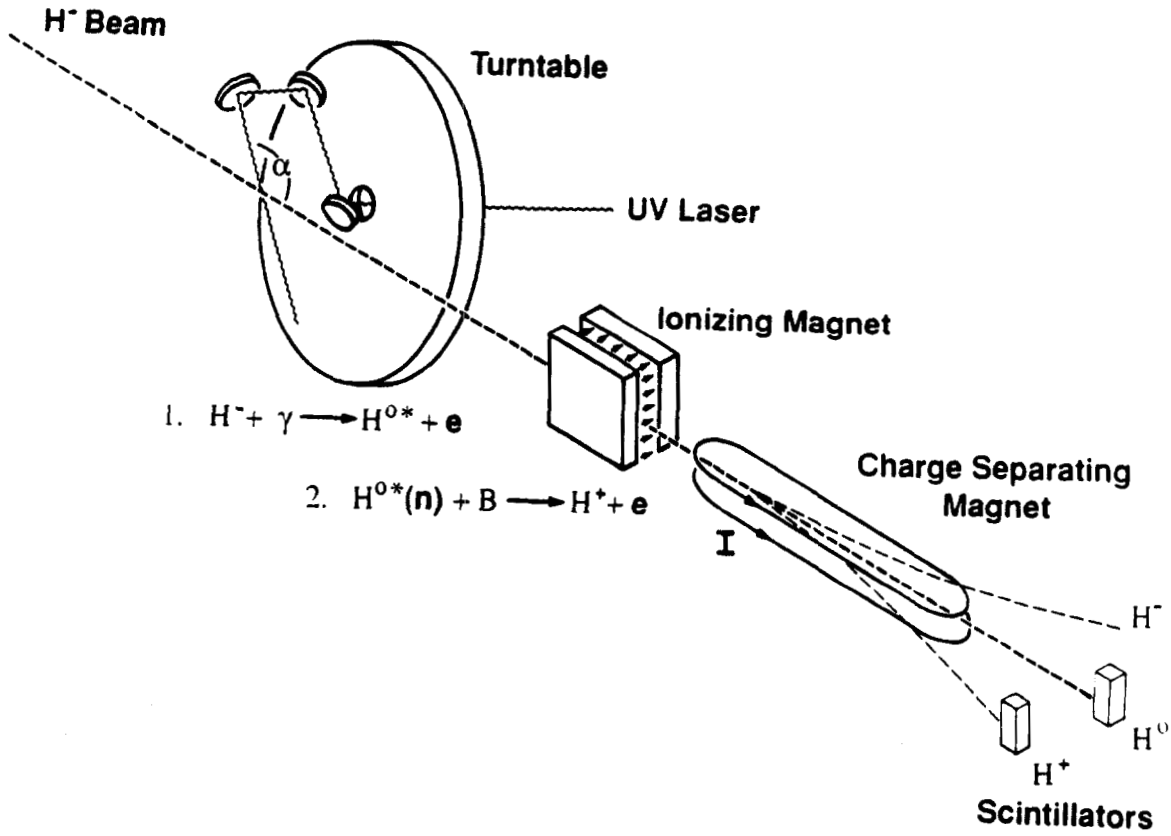

Figure 3.1. Apparatus for High-Lying Resonances Search.

If, however, the photon energy should match that of a resonance in the H^- continuum, then the process

$$H^- + \gamma \rightarrow H^{-**} \rightarrow H^{0*}(\leq n) + e^- \tag{3.2}$$

may also take place. The amplitudes for excitation of the neutral hydrogen atom *via* production of the doubly-excited resonant state H^{-**} (3.2) and that of direct excitation (3.1) will add coherently, resulting in structure on the continuum cross section as discussed in the last chapter.

Let us consider a photon with a Doppler-tuned energy sufficient to detach the second electron from the H^- ion, and to excite the remaining hydrogen atom into the state, say, $n = 4$. There is a large probability that it will, instead, eject the outer electron and leave the neutral hydrogen in $n = 1$, 2 or 3. If we wish to see structure in the $H^0(4)$ production continuum, it is essential that we discriminate against this background.

It is here that the transformation of (lab frame) magnetic fields into (barycentric frame) electric fields becomes important, for, by applying a field of $\sim$ 4000 gauss, the corresponding field of 1.9 MV/cm in the ion's rest frame is sufficient to strip the electron from $H^{0*}(n = 4)$, while leaving unaffected those atoms in $n \leq 3$. The protons resulting from this so-called field ionization (see Appendix H) are then magnetically separated from the remaining neutral and positively charged particles, giving a clear signal of the production of $H^{0*}(n = 4)$.

We might expect, then, that as we increase the barycentric photon energy, starting from that needed to produce $H^{0*}(n \leq 3)$, we should see a staircase-type structure, as shown in Figure 3.2(a), with the onset first of $n = 4$ production, then of $n = 5$, 6, and so on. (This figure also includes a linear dependence with energy of the continuum cross section). In addition, by reducing the magnetic field to the point where it is no longer able to strip $H^{0*}(n = 4)$, but is able to strip

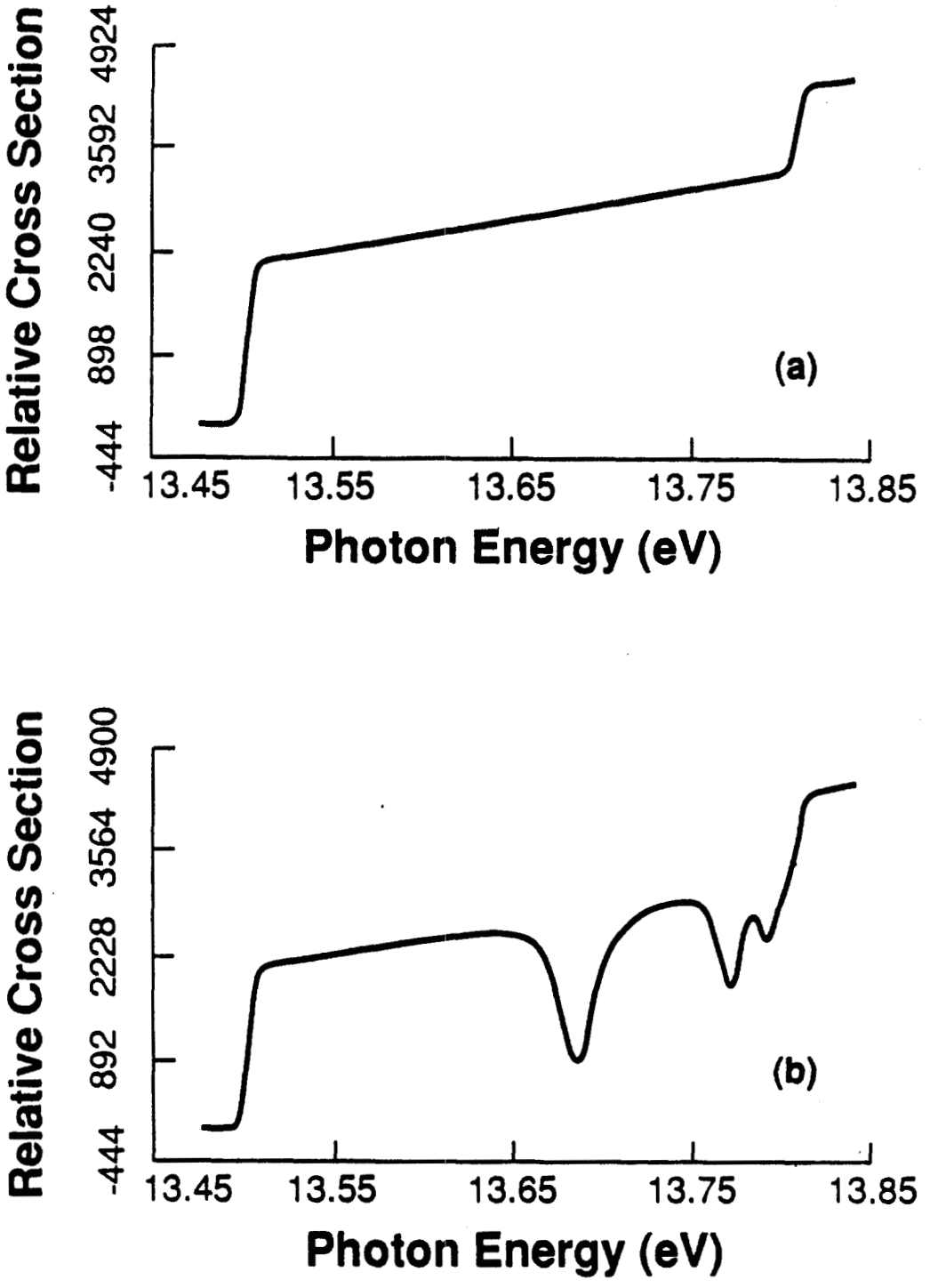

Figure 3.2 Expected "staircase" structure of continuum, (a) without resonances, (b) showing "dip" resonances. A slope has also been included in the continuum cross section.

$H^{0*}(n \geq 5)$, we should again see a staircase structure, but this time beginning with the onset of $n = 5$ production. Thus, we have the means to isolate and study a single channel at a time. This iterative process is repeated for successively higher n states until the signal becomes so small that it is impossible to discern the structure above the background noise.

The interference in the cross section, due to the coherent addition of amplitudes for the production of the H^{0*} continuum and the H^{-**} resonance (see Chapter 2), results in a series of "dips" in each $H^{0*}(n)$ channel, as shown schematically in Figure 3.2(b), becoming progressively narrower and closer together as they converge on the $H^{0*}(n+1)$ threshold. The object of this experiment is to characterize these dips, measuring their positions and widths, and to compare them to the many predicted ^1P resonances in H^-.

3.2 Preparations.

Before data taking can commence, a tuning up procedure must be followed. After the Central Control Room (CCR) has succeeded in steering the H^- beam down the line to our experimental area, the focusing (quadrupole) magnets are adjusted to give the beam spot (as seen on our fluorescent screens) a satisfactory shape (*i.e.*, minimizing the halo around the spot). It is then necessary to set the electronic timing circuits to ensure, firstly, that the laser fires at the right time for the light to intercept the pulse of H^- ions, and secondly that data is taken at the right time — namely, when the signals from the photodetached fragments arrive.

3.2.1 Positioning of detectors.

In order to locate spatially the expected positions of the laser-produced H^0 and H^+ beams, a thin foil, of thickness typically 50 $\mu g/cm^2$, is put into the path of the H^- beam, to produce neutral hydrogen atoms and protons that will follow

the trajectories of the signal particles. With the "skinny" magnet on to separate the charge species, the H° and H^+ detectors are moved to locate their respective beams. The foil may then be removed.

3.2.2 Laser Timing.

The laser flashlamps must be fired 3 ms before the Q-switch allows the release of the laser light. A signal (known as UN02) from CCR tells us approximately when the H^- pulse is expected to arrive, and this permits time for the firing of the flashlamps. The actual arrival of the H^- macropulse is signaled by the "paddle" scintillator; a signal is then sent to the Q-switch to fire the laser in time to intercept the H^- beam while the macropulse is still passing, as illustrated in Figure 3.3.

By setting the "spider" (rotating mirror assembly) to an angle where the photodetachment cross section is high, the large number of H°'s produced give a distinctive laser-related signal in the H° detector. The timing of the laser may then be optimized, ensuring that the interaction takes place well inside the macropulse and away from any parts of the macropulse that may be unsteady in some way.

3.2.3 Setting the Electron Spectrometer.

The calibration of the electron spectrometer must then be determined. By changing the current, and thereby the field, in the spectrometer magnet, it may be tuned until photodetached ("convoy") electrons are detected. The spectrometer is also able to detect highly-excited neutral hydrogen atoms ($n \geq 10$), by field ionization (see Appendix H); its sensitivity to the various excited states may be measured as a function of the magnetic field by putting in a foil (to produce a wide range of excited states) or by using a laser to generate specific excited states

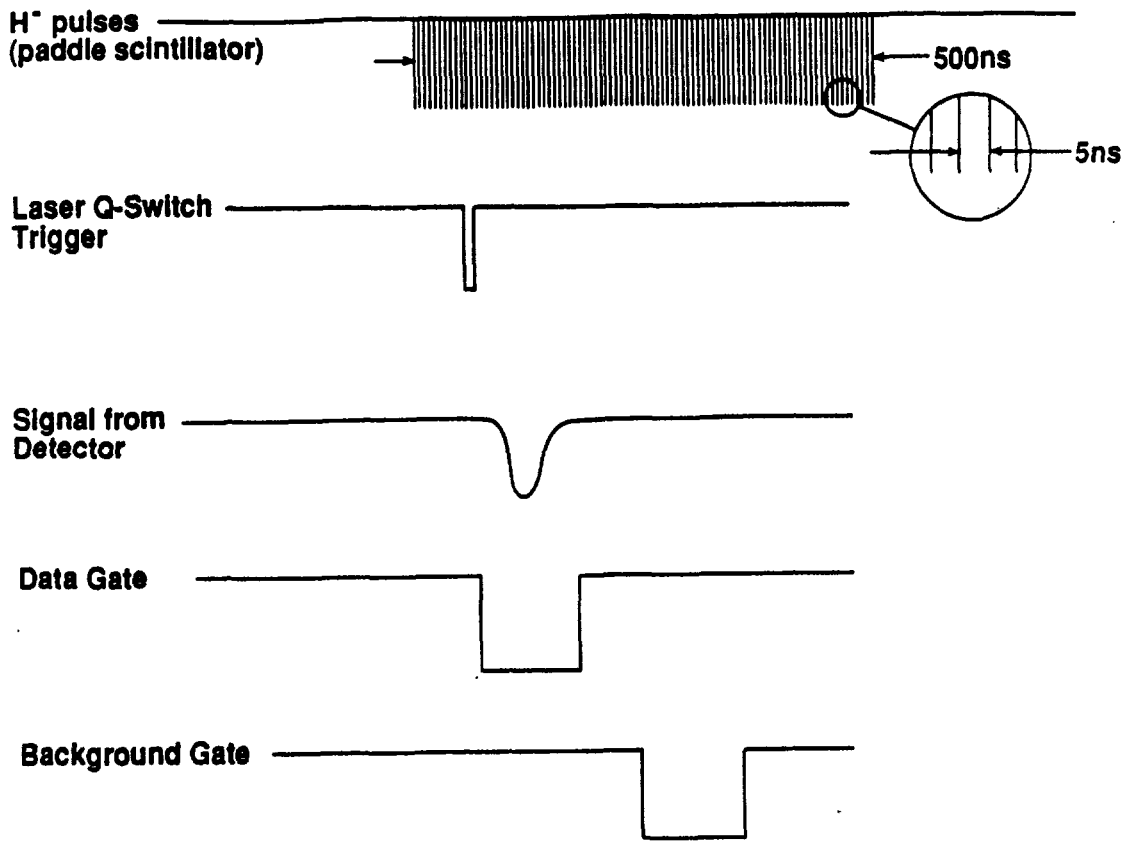

Figure 3.3. Laser-particle beam timing overlap, with relative positions of data and background gates.

(see section 3.3, "Calibration Runs", below), and again scanning the current in the spectrometer magnet to detect the Rydberg atoms thus produced.

3.2.4 Gates.

With all of the detectors receiving photodetachment signals (except possibly the H^+ detector, which may be moved into the H° beam for this purpose), the timing of the data gates must be set. A combination of logic circuits opens the necessary gate for the analog-to-digital converters (ADC's) to digitize the signals under the right conditions (namely that the laser has fired, the H^- beam is on.

and the computer is ready), and delays are inserted into each signal line to ensure that the signals arrive at the right ADC as the gate is opened to receive them. In addition, a background gate of the same duration as the data gate is opened later in the macropulse in order to determine the contribution to the signal pulse of backgrounds that are not laser-related (in particular, from H° and H^+ produced by residual-gas stripping). In a similar way, gates are set for the fast ion chamber (FIC), fast photodiode (FPD) and any other instruments.

3.2.5 Photomultiplier Tubes.

Finally, the photomultiplier tube voltages are optimized to give output pulses as large as possible without saturating either the tubes themselves or the analog-to-digital converters (ADC's). Obviously, these voltages are changed to reflect the needs of the moment as the experiment progresses.

Because the laser pulse has a high intensity, the likelihood is that more than one photodetachment will take place at a time. It is therefore necessary to record the integrated current — the pulse height — of each pulse from each detector. The distribution of pulse heights should show a series of peaks for single, double, triple and other multiple hits, as illustrated in Figure 3.4. The spacing between the peaks, with the offset of the first, allows us to calculate the "slope" and "pedestal" from which the multiplicity of particles may be calculated for any given pulse height, assuming linearity, by the simple relation

$$\text{Number of particles} = (\text{pulse height} - \text{pedestal}) \times \text{slope}. \qquad (3.3)$$

The slopes and pedestals are obviously dependent upon the gains, and therefore the voltages, of the photomultiplier tubes. Unfortunately, the H^+ pulse height distribution did not show the characteristic series of peaks, since its light collection efficiency was so low that individual counts could not be resolved (*i.e.*, the "slope"

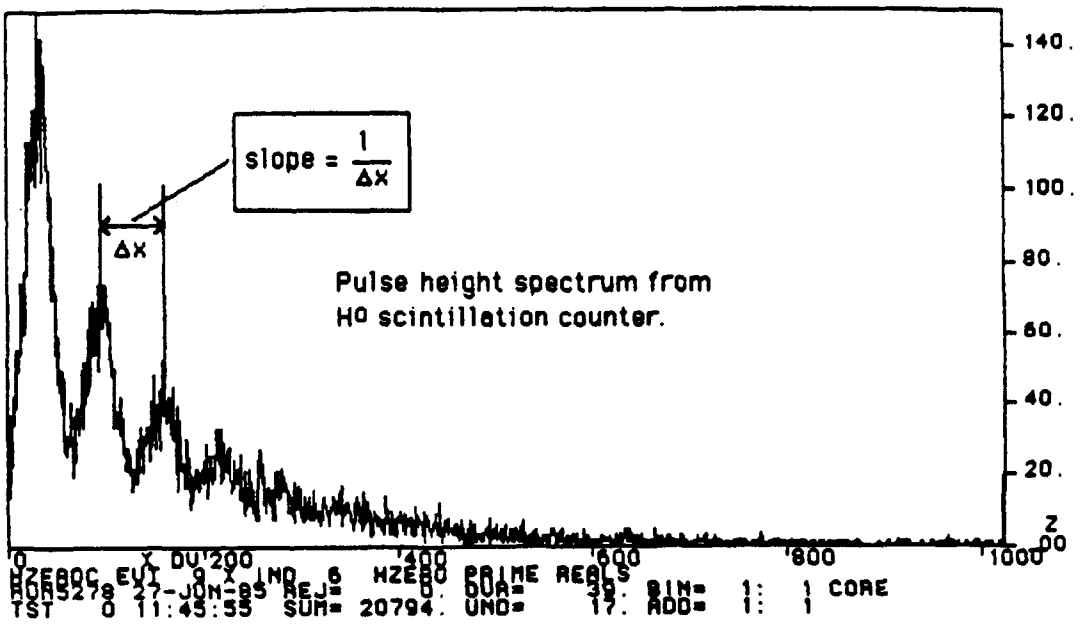

Figure 3.4. Typical pulse height distribution spectrum.

was large); therefore, we had no way of knowing the absolute numbers of protons incident in any pulse, which is actually of little concern anyway for calculation of relative cross sections. The voltage of the H^+ detector was held constant at 1800 V throughout the series of experiments.

Details of the photomultiplier tubes used are to be found in Appendix G.

3.3 Calibration Runs.

Transitions between excited states of neutral hydrogen are used to determine the energy scaling in the data-taking runs. A neutralizing thin foil is used to produce excited H°'s; scanning the magnetic field of the electron spectrometer shows us the distribution of high-lying excited states. If a magnetic field of $\approx$ 130 gauss is then applied just downstream of the foil box (by the sweep, or "Gram" magnet), these high-lying states will be field-ionized, and no longer detectable by

the electron spectrometer. The laser-particle beam intersection angle may then be swept until the spectrometer, set at the appropriate field, once again detects high-lying states, this time promoted from lower excited states by the laser (Figure 3.5). For example, if the spectrometer is tuned to detect, say, $n = 14$, and the sweep magnet has removed all of the foil-produced $n = 14$'s, then the spectrometer will detect nothing until the laser angle is set to the transition from $n = 1$ to $n = 14$ (or $n = 2$ to 14, etc.). The angular spacing between several such hydrogen lines tells us which lines we are looking at, and therefore where to expect other structure. The $n = 2$ Feshbach resonance provides another important energy reference point.

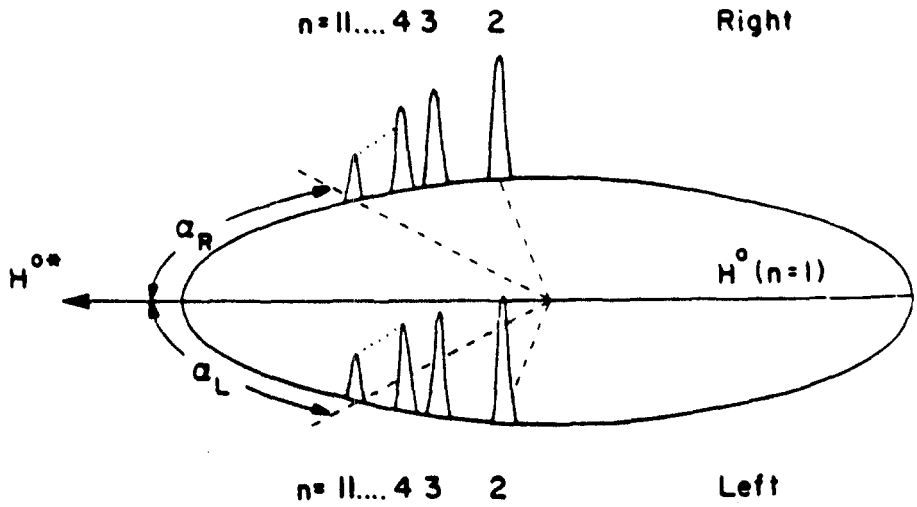

Figure 3.5. Using hydrogen lines for angular calibration. From MacArthur *et al.* (1985).

The angular spacing between these hydrogen lines may appear to vary slightly from that expected for two reasons; firstly, if the laser is not properly aligned, it will "wander" as the spider is turned (see Appendix I); and secondly, runout in the

bearings on the belt drive system will cause a sinusoidal variation from linearity in the encoder readout itself. As the structures under observation here all lie within a very small angular range, however, these are not generally a problem. A longer term drift may be caused by a change in the frequency of the laser itself, by up to a wavenumber. This (systematic) shift in energy scaling is not apparent in any of the data.

3.4 Data-Taking Runs.

During a run, the laser-particle beam interaction will take place at a number (usually 100) of different angles. Signals are collected at each angle for a certain amount of time, determined by a scaler which counts the number of times the Faraday cup has "filled" with 100 pC of integrated primary beam current. (We generally refer to this, with rather imprecise terminology, as the "number of Faraday cups"). At each laser shot, the (integrated) signals (as measured by the ADC's) from the detectors are recorded on magnetic tape; at the end of each angle, the computer calculates the sum, the mean and the standard deviation of the mean of these signals, writes the results to a data file, and records such information as the angle-encoder setting, magnetometer readings and so on. It also generates histograms of signal *vs.* angle number.

3.4.1 Procedure for Taking Data.

A typical run might have the objective of observing the resonances between the hydrogenic $n = 4$ and $n = 5$ thresholds. In this case, the procedure is:

i) to set the number of "Faraday cups", *i.e.*, the total integrated beam current required, for each angle;

ii) to set the step size through which the spider is to move between angles;

iii) to turn on the ionizing (bender) magnets to field-strip H°($n = 4$) and above;

iv) to put the spider at its first angle, for example below the threshold for $n = 4$ production;

v) to apply electric fields if required in the interaction region;

vi) if necessary, to make final checks of spatial and temporal overlaps, the status of magnets in the beamline, photomultiplier voltages etc.;

vii) to make the computer start the run, which is done by following a menu-driven procedure to inform the data acquisition software (the Q system) what data to expect and how to process it;

viii) to monitor the progress of the run by observing the development of the histograms;

ix) to repeat all of the above as necessary.

For successively higher series of resonances, the field in the ionization magnet is successively reduced to strip only states of interest, as described in section 3.1.

Other types of runs — for foil or MPI experiments — are similar in nature; these will be discussed in Chapter 5, and at greater length in the dissertations of Amir Mohagheghi (1990) and Chen-Yau Tang (1990) respectively.

Chapter 4

Results and Analysis

"It is a capital mistake to theorize before one has data."

— Sir Arthur Conan Doyle, *The Memoirs of Sherlock Holmes.*

In this chapter, we discuss the results of the data fitting under various different constraints. Of these results, we shall in particular place emphasis on the fitted energies of the resonances, since several theoretical calculations of these energies are available. We shall find that we are unable to discriminate between the different theoretical approaches at this level of precision, but that the simple analytic "2e-formula" (equation 2.25), with the parameters η (equation 2.26) and μ (from 2.23) determined by a fit to the data, is able to predict the energies as well as any of the more complex calculations.

4.1 Fitting the Data.

All of the data collected and analyzed are displayed in Appendix J; the procedure followed for data reduction is discussed in Appendix D. The data for each hydrogenic continuum channel studied (n = 4, 5, 6, 7) were combined to produce one set of data for each channel, displayed in Figures 4.1(a)-(d). Each contains at least three prominent resonances, which seem to converge on the next higher threshold (n = 5, 6, 7, 8 respectively). These resonances appear primarily as dips (sometimes known as *Fano windows*), although there is still evidence of

some asymmetry — the Fano "q" parameter (equation 2.37) is in each case close, but not equal, to zero. Figures 4.1 also show the results of the fits to sets of Fano profiles.

As explained in Appendix D, the data set for each channel was fit first of all to a set of independent resonances, in which the probability amplitudes ψ_i were added (in case of overlap) before calculating the cross section $\sigma = \psi^* \psi$ (see section 2.6). The amplitude for the continuum background was allowed to be a linear function of energy. When the fitted widths indicated that there was in fact no significant overlap, sets of standard Fano profiles were used for the fitting.

The sets of resonances were then fit to the dipole recursion formula (equation 2.18), both with the dipole moment a_n as a free parameter and with it fixed at the value predicted by theory. This is a direct analogy of the fitting of hydrogen lines to the Balmer formula.

Theoretical considerations suggest that the asymmetry parameter q and the amplitude σ_a of the Fano profiles (as defined in equation 2.35) should be constant (or nearly so) throughout the series of resonances (Greene, 1990). Fits were also performed, therefore, with these constraints.

For each fit, a value is given for chi squared per degree of freedom (χ^2/ν, or reduced χ^2), where the number of degrees of freedom ν is defined as $\nu =$ (number of data points $-$ number of parameters). Confidence levels (CL; defined as the probability of χ^2 exceeding its calculated value) are also given where they exceed 0.01%; however, with $\sim$ 100 data points, the confidence level drops off extremely rapidly for $\chi^2/\nu > 1$.

A gaussian width corresponding to our resolution of 8.3 meV (see Appendices D and E) has been convolved into each fit. Fitted widths significantly less than this value are probably not reliable. The energy scaling was determined independently from the positions and spacing of several hydrogen lines, as outlined in

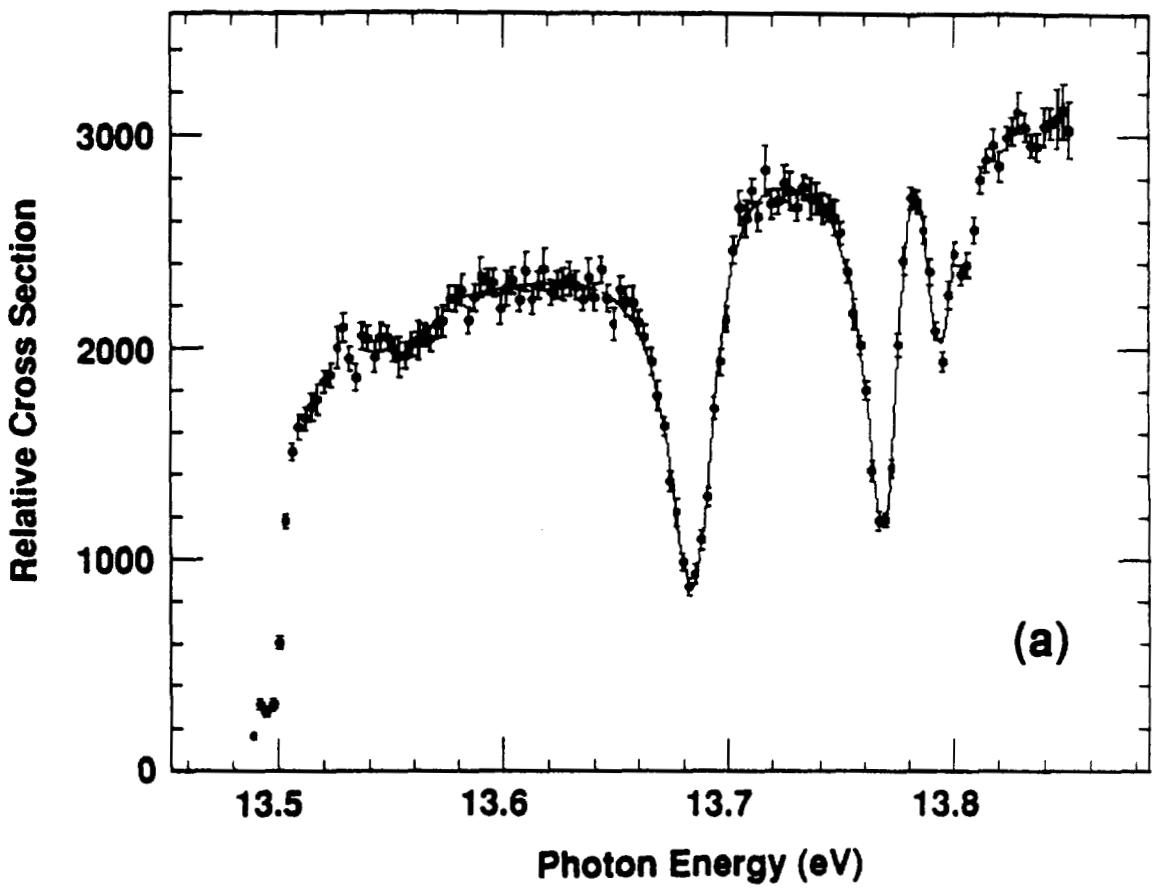

Figure 4.1(a). Resonances in the continuum between the hydrogenic $n = 4$ and $n = 5$ thresholds, appearing as structure in the partial production cross section of $H^{\circ}(n = 4)$. The solid line is a fit to a set of three Fano profiles (see text).

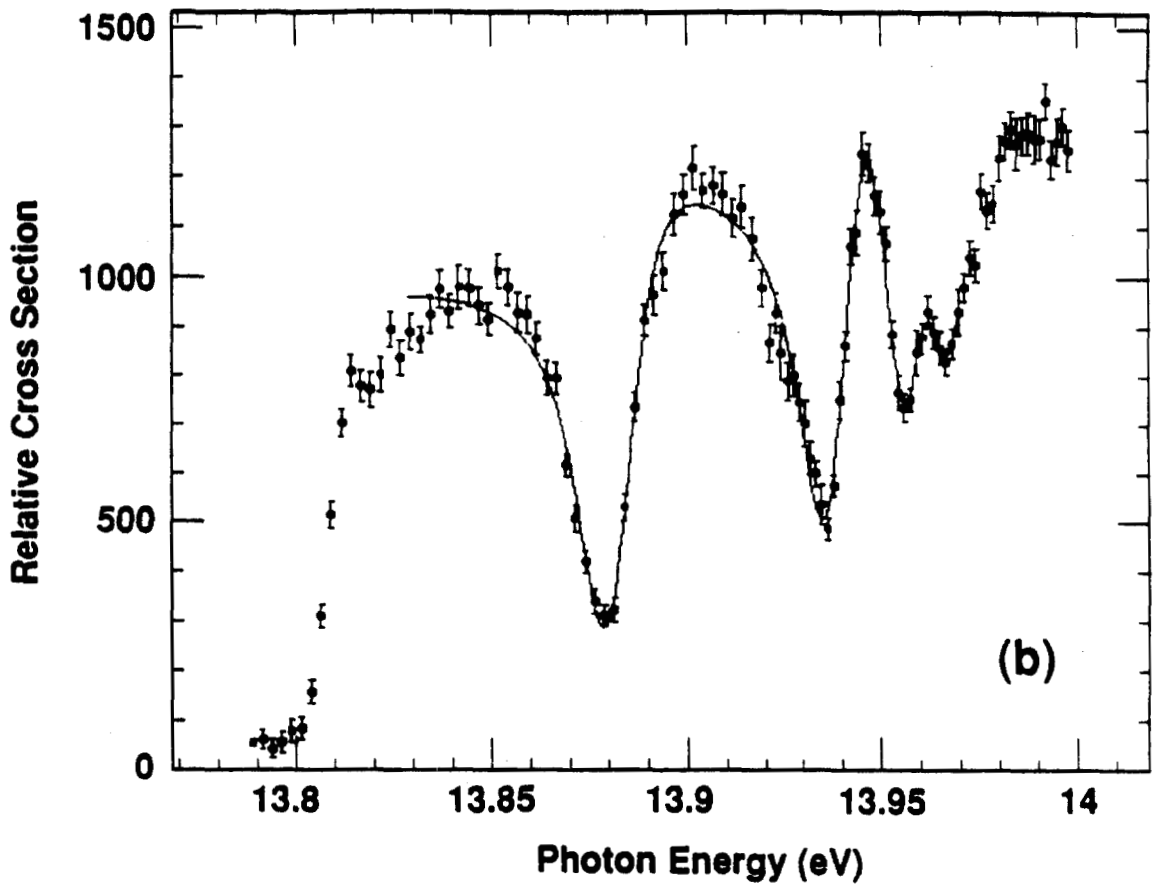

Figure 4.1(b). Resonances in the continuum between the hydrogenic $n = 5$ and $n = 6$ thresholds, with a fit to a set of four Fano profiles.

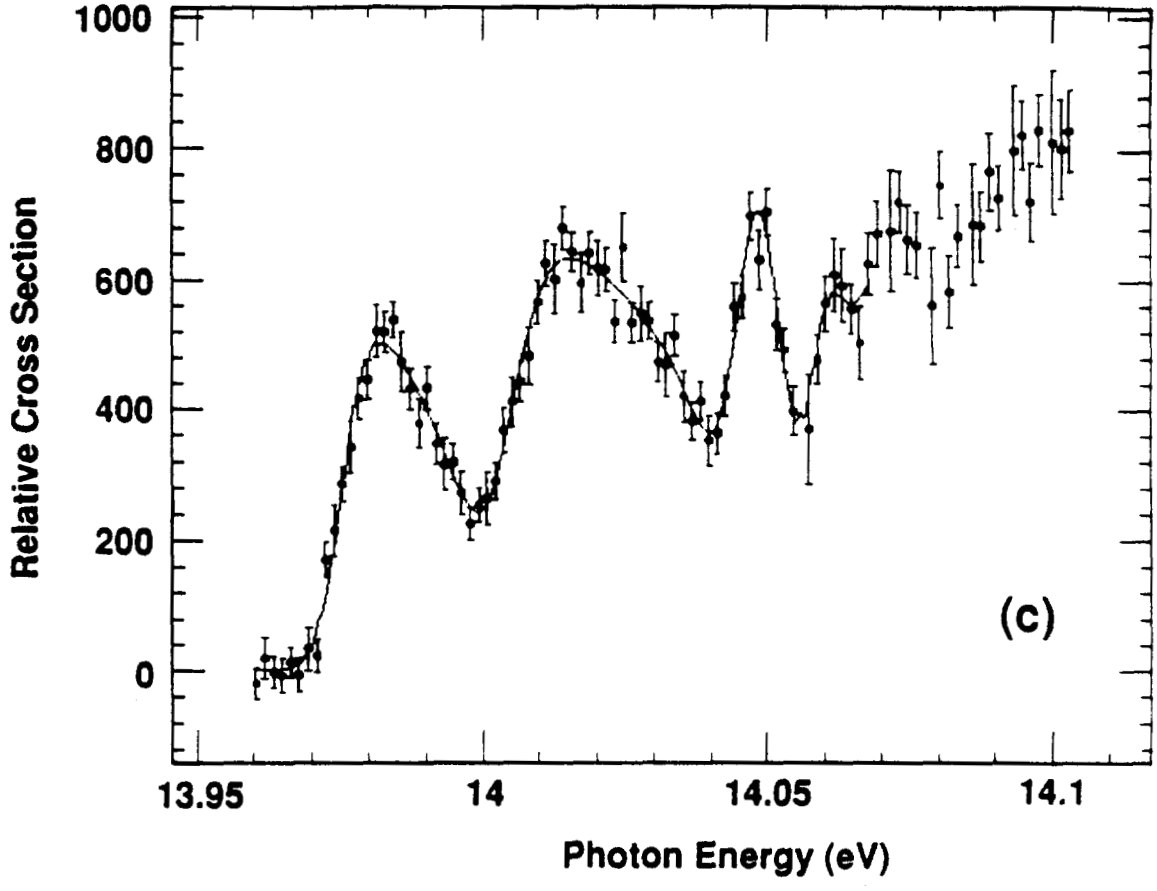

Figure 4.1(c). Resonances in the continuum between the hydrogenic $n = 6$ and $n = 7$ thresholds, with a fit to a set of three Fano profiles.

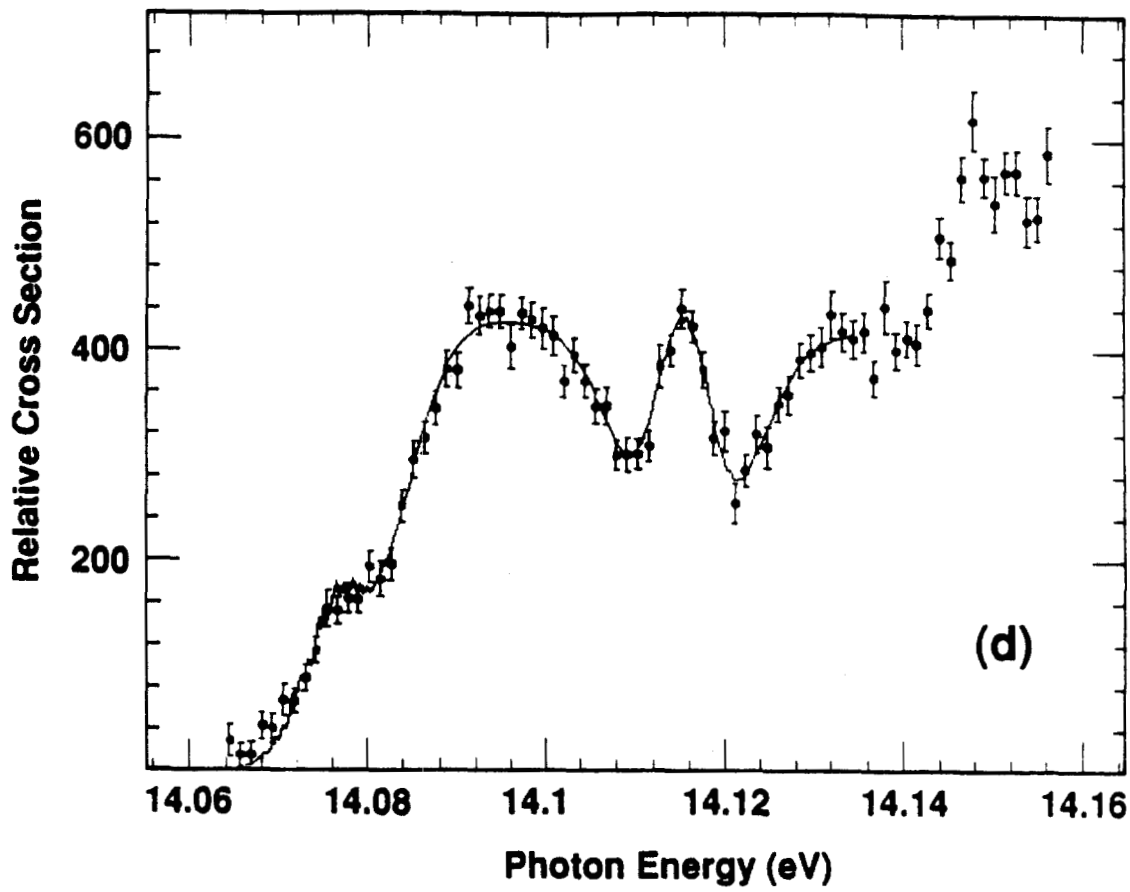

Figure 4.1(d). Resonances in the continuum between the hydrogenic $n = 7$ and $n = 8$ thresholds, with a fit to a set of three Fano profiles.

Chapter 3 and Appendix E, and the absolute uncertainty in energy is less than 1 meV (with a relative uncertainty between points of less than 0.2 meV). This is sufficiently small that no energy uncertainty has been introduced into the fits. Of course, the energies in the unconstrained fits are free to "float", whereas those in the dipole formula fits are tied to the threshold energies; but allowing an energy uncertainty in the dipole fits does not produce a consistent offset — either in magnitude or in sign — for the different channels, and does not bring about a large reduction in χ^2, and so the energy scale was fixed at its independently-measured setting. The number of free parameters is in any case already prohibitive.

4.2 Positions and Widths of the Resonances.

The fitted positions and widths of the resonances are given in Table 4.1. Sets of Fano profiles were used throughout here, the cross section of the continuum background σ_b being assumed to vary linearly with photon energy. The conditions under which the fits were performed are:

a.) Positions of the minima, by eye, read from the data files.

b.) Unconstrained fits; parameters allowed to vary freely.

c.) Fits to dipole series (equation 2.18); dipole parameter a_n allowed to vary as a free parameter. Only the first resonance in each series is given, as the remainder are defined by the recursion formula.

d.) As for c), but with the dipole parameter a_n fixed by theory (see Table 2.1).

e.) As for d), but with the values of the parameters q and σ_a assumed constant throughout the series of resonances.

Uncertainties in the fitted parameters are given in parentheses, and correspond to the change in the last significant digit required to increase the total χ^2 by one. This is a standard approach, although it clearly becomes invalid if χ^2/ν differs significantly from unity.

a. Positions of observed minima, by eye.

Between thresholds:	Position (eV):			
4 and 5	13.682	13.769	13.794	
5 and 6	13.879	13.936	13.955	13.966
6 and 7	13.997	14.039	14.057	
7 and 8	14.076	14.109	14.121	

b. Unconstrained fits.

Between thresholds:	Position (eV)	Width (meV)	χ^2/ν (CL)
4 and 5	13.6858(3)	21.5(5)	0.97(55%)
	13.7708(3)	14.1(7)	
	13.7919(11)	14.3(7)	
5 and 6	13.8812(3)	11.6(8)	1.85(0.01%)
	13.9379(2)	8.2(5)	
	13.9557(1)	5.5(13)	
	13.9628(1)	1.0(4)	
6 and 7	14.0024(7)	12.4(13)	0.88(73%)
	14.0456(7)	4.9(9)	
	14.0558(2)	0.9(2)	
7 and 8	14.0802(10)	3.1(12)	0.98(50%)
	14.1132(2)	1.39(4)	
	14.1171(3)	1.13(6)	

c. Dipole series fits; unconstrained a_n.

Between thresholds:	Position (eV)	Width (meV)	a_n	χ^2/ν (CL)
4 and 5	13.6864(1)	21.4(2)	31.3(2)	2.8
5 and 6	13.8817(1)	13.6(1)	47.5(3)	2.7
6 and 7	14.0016(3)	8.9(1)	73.7(13)	1.5(0.7%)
7 and 8	14.0800(9)	4.0(1)	110.1(46)	1.5(1.5%)

Table 4.1 Positions and Widths of Resonances.

d. Dipole series fits; a_n from theory (Table 2.1).

Between thresholds:	Position (eV)	Width (meV)	a_n	χ^2/ν (CL)
4 and 5	13.6879(1)	21.1(1)	37.70	4.9
5 and 6	13.8815(1)	14.0(1)	62.95	5.6
6 and 7	14.0020(4)	11.6(17)	94.20	1.7(0.06%)
7 and 8	14.0829(8)	4.0(3)	131.45	1.6(0.4%)

e. Dipole series fits; a_n from theory; const. q, σ_a.

Between thresholds:	Position (eV)	Width (meV)	χ^2/ν	q
4 and 5	13.6878(4)	19.8(7)	8.4	0.32(2)
5 and 6	13.8826(4)	11.6(6)	5.9	0.40(3)
6 and 7	13.9995(6)	14.0(14)	2.6	0.10(4)
7 and 8	14.0813(3)	4.0(2)	2.9	-0.09(4)

Table 4.1 (cont.) Positions and Widths of Resonances.

The position of the resonance at the $n = 7$ threshold may be subject to additional uncertainty since it does not appear as a full "dip"; in other words, only half of the profile can be seen. There may also be a shape resonance at the $n = 7$ threshold (see section 2.3.1) interfering with it, although if it is there it should be weak.

4.3 Comparison of Energies and Widths with Theory.

We compare here the fitted energies and widths of the resonances with several theoretical predictions. We begin in section 4.3.1 with the theoretical predictions for the energies of the lowest resonances in several different series, and we compare these numbers with the resonance energies found from the unconstrained fits, to see if we are observing resonances from more than one series in each continuum.

Following this, we compare the fitted energies with the energies expected in a *single* series in each continuum, where we find that the match is considerably better.

Section 4.3.2 discusses the fits to the dipole recursion formula. We then detour briefly in section 4.3.3 to see how well the minima "by eye" match up with the dipole law.

Section 4.3.4 shows a plot indicating the linear dependence of the energy of the lowest resonance in each series (below the double-detachment threshold) on the hydrogenic principal quantum number n (see equation 2.23); values are found for the screening and quantum defect parameters σ and μ. Section 4.3.5 uses these parameters in the 2e-formula, to predict the positions of all (lowest series) "+" resonances from $n = 3$ to $n = 10$.

Section 4.3.6 concludes the discussion of resonance energies with a brief summary.

Section 4.3.7 compares the fitted values of the widths, already touched upon briefly in section 4.2.1, with some theoretical predictions.

4.3.1 Theory *vs.* Unconstrained Fits.

Some theoretical predictions for resonance energies are given in Table 4.2. In each case, these are the energies of the first resonance in each series, the energies of the others following from the dipole recursion formula. The calculated values of Ho and Callaway (1986), Ho (1990), and of Koyama, Takafuji and Matsuzawa (1989), were converted from the published energies in rydbergs (measured downwards from the double-detachment threshold, at 14.35262 eV) by using the *infinite* rydberg $R_\infty = 13.605698$ eV. This should be appropriate for "+"-type resonances, where the nucleus is "stationary" (see the classical analog of section 2.3.2). Conversion to the equivalent energies is simply carried out by adding to

the listed energy E a quantity $\Delta E = 0.000536 \times (14.3526 - E)$; this amounts to no more than 0.4 meV.

The fitted energies (from the unconstrained fits) are also included in the table. It appears that the first resonance in the lowest "+" series of each channel matches fairly well, but no others do, indicating that we are just seeing that lowest "+" series. The calculated widths of some of the other series of resonances are sufficiently large that we might expect to observe them; the fact that we do not do so implies that the resonances are weak, *i.e.*, that σ_a is small.

Between thresholds:	Fitted	Calculated (1)	(2)	(3)
4 and 5	13.6858(3)	13.6846	13.6809	13.6857
	13.7708(3)	13.7574	13.7381	13.7369
	13.7919(11)		13.7675	13.7703
			13.7831	
5 and 6	13.8812(3)	13.8798	13.8794	13.876
	13.9379(2)	13.9202	13.9148	13.9196
	13.9557(1)	13.9710	13.9270	
	13.9628(1)		13.9432	
6 and 7	14.0024(7)	14.0008	13.9991	13.9996
	14.0456(7)	14.0254	14.0245	
	14.0558(2)	14.0544	14.0391	
7 and 8	14.0802(10)			14.0783
	14.1132(2)			
	14.1171(3)			

Table 4.2 Fitted photon energies of resonances (eV), *vs.* calculated values, for lowest resonances in each series, of (1) Ho and Callaway (1986) and Ho (1990), (2) Koyama, Takafuji and Matsuzawa (1989), (3) Sadeghpour (1990). Again, uncertainties in fitted parameters corresponding to $\Delta\chi^2 = 1$ are in parentheses.

Table 4.3 lists the measured resonance energies — again from the unconstrained fits — and compares them with the calculated values of the lowest "+"

resonance series in each channel. The calculations are from Sadeghpour (1990b), and include both precise calculations using quantum defect theory and estimates from the "2e-formula" (equation 2.25), using his values of the parameters η (equation 2.26) and μ as discussed in section 2.5. The match in this case is obviously (qualitatively) extremely good throughout the entire range of energies studied, indicating that the structure that we see is due almost entirely to the lowest "+" series (see Sadeghpour and Greene, 1990).

Between thresholds:	Fitted (1)	Fitted (2)	Calcd. (1)	Calcd. (2)
4 and 5	13.6858(3)	13.6879(1)	13.6857	13.6868
	13.7708(3)	13.7661	13.7730	13.7650
	13.7919(11)	13.7934	13.7963	13.7930
5 and 6	13.8812(3)	13.8815(1)	13.8760	13.8792
	13.9379(2)	13.9326	13.9347	13.9316
	13.9557(1)	13.9558	13.9575	13.9553
	13.9628(1)	13.9662	13.9671	13.9660
6 and 7	14.0024(7)	14.0020(4)	13.9996	13.9989
	14.0456(7)	14.0369	14.0382	14.0352
	14.0558(2)	14.0551	14.0566	14.0543
7 and 8	14.0802(10)	14.0829(8)	14.0783	14.0783
	14.1132(2)	14.1071	14.1064	14.1044
	14.1171(3)	14.1291	14.1217	14.1195

Table 4.3 Fitted photon energies of resonances in eV; (1) unconstrained fits, (2) dipole formula fits, *vs.* calculated values (Sadeghpour, 1990), using (1) quantum defect theory, (2) the "2e-formula" (equation 2.25).

4.3.2 Dipole Recursion Formula Fits.

The fits with energies and widths constrained to the dipole scaling law (equation 2.18; cases c., d. and e. above) have a much higher χ^2, and therefore appear to be considerably poorer descriptors of the data, than the unconstrained fits. However, the fitted energies of the resonances match the unconstrained fits very

closely — within just a few meV in each case, as shown in Table 4.3. The widths do not match as well, as will be seen later.

According to a quantum defect picture, the dipole scaling law holds exactly only if several short-range parameters are constant. One might conclude from the fits that these parameters are not constant, but instead vary weakly with energy. This idea is supported to some extent by the fact that the shapes of the resonances appear to change somewhat — which is itself consistent with the extremely large χ^2 values obtained when q and σ_a are held constant.

It appears, then, that the dipole scaling law is not quite exact. At this level of precision, however, it could be that the background continuum is not well represented by the linear energy dependence of this model, or else that other resonances are altering the cross section, and that the unconstrained fits simply "take up the slack".

It is interesting to note that in each case, when the dipole parameter a_n is allowed to vary, the value obtained is significantly lower (by some 16-25%; see Table 4.1) than the theoretically calculated value. This is consistent with Gailitis's statement (1980) that the lowest resonance in each series is farther from the threshold than one would expect from the dipole scaling law.

4.3.3 Minima "by eye" *vs.* Recursion Formula.

Returning to the top of Table 4.1, we have the positions of the minima of each resonance (as read from the data files) listed. If the parameter q were constant over the range of the series, the resonances would all have the same shape; if, then, the dipole recursion formula holds, we would expect that *any* set of equivalent points on the set of Fano profiles, and not just the centroids, should obey the same recursion formula. Testing this with the calculated values of a_n (Table 2.1), we find a reasonably close agreement; the recursions of the first minima are in

each case not more than a few meV from the observed values. They are, however, outside the uncertainty limits, bearing in mind the 1 meV precision of the energy scale. This again suggests that either q is not quite constant, or that the dipole scaling does not quite work precisely, or both.

4.3.4 Lowest Resonance in Each Series.

According to the modified Rydberg formula (equation 2.23), the energies of the lowest resonance in each series (as measured downwards from the double-detachment threshold) should be proportional to $1/(n-\mu)^2$. Thus, a plot of $(E_t - E)^{-1/2}$ *vs.* n should — and indeed does — yield a straight line, as shown in Figure 4.2. The energies used are those from the unconstrained fits (case b. above). Included in this plot is the first of the dips below $n = 3$ discovered by Hamm *et al.* (1979), at 12.650(4) eV (see Figure 2.7). The $n = 2$ shape resonance is not included since its structure is different from the other lowest "+" resonances, which are all Feshbach-type resonances.

The fitted line is

$$(E_t - E)^{-1/2} = 0.0765(22) + 0.2299(5)n, \qquad (4.1)$$

where as usual the uncertainties are given in parentheses. For this fit, the 1 meV absolute energy uncertainty was added to *each* of the fitted uncertainties listed in Table 4.1; the reduced χ^2 was then 0.78, with a 50% confidence level.

4.3.5 The 2e-Formula.

As discussed in Chapter 2, the 2e-formula (equation 2.25)

$$E(n,m) = E_t - \frac{R}{n^2} + 2R\, e^{-2\pi(m-n)/\alpha_n}\left[\frac{1}{2n^2} - \frac{\eta}{(n-\mu)^2}\right] \qquad (4.2)$$

was fit to calculated energies of the lowest resonance in the hydrogenic $n = 3$, 4 and 5 channels, giving values of 0.70784 and -0.377 for the two parameters

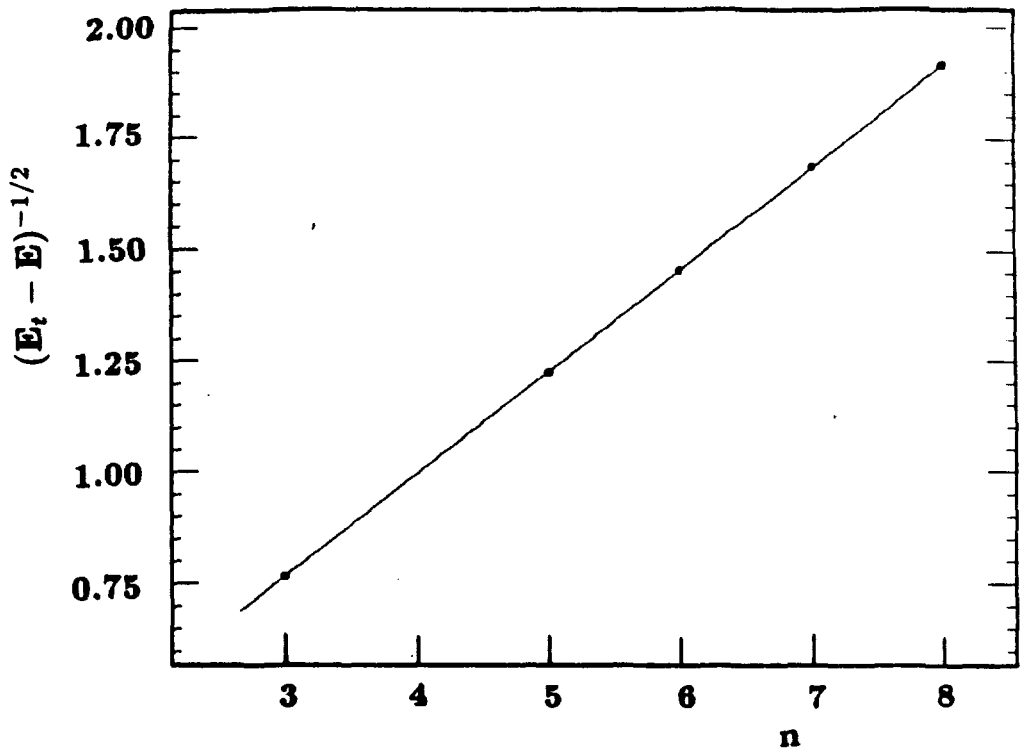

Figure 4.2. A plot of the energy below the double-detachment threshold of the first resonance in each series, $(E_t - E)^{-1/2}$, *vs.* the principal quantum number n.

$\eta = (Z - \sigma)^2$ and μ respectively. We can instead fit it to our measured resonance energies.

The 2e-formula contains *two* assumptions — namely, the modified Rydberg formula for the lowest resonance in each series (equation 2.23), and the dipole scaling law (equation 2.18). Fitting all of the resonances to the combined formula does not tell us *which* of the two formulae, if either, is at fault, and so has no value beyond the fits already performed on the formulae individually. We have already established that the dipole recursion formula is not exact (although it does seem to be a good qualitative predictor of the energies); building it into the fit, without allowing for the fact that it is an approximation (perhaps by increasing the error bars of all resonances beyond the first in each channel to a few meV) just weights

the fit artificially in favor of the channels with more resonances (and therefore against the $n = 3$ dips).

The most sound approach, then, is to fit just the *first* resonance in each channel — which of course we have already done, in the previous section. The fitted line of equation 4.1 translates to values of η and μ of 0.6957(30) and −0.333(10) respectively. Using these values, we may then predict (from the dipole recursion formula) the positions of the resonances; and since we have weighted the $n = 3$ resonance "fairly", along with those of channels $n = 5$ to 8, we may expect that the formula will hold over a wider energy range.

The predictions of the resonance energies are listed in Table 4.4, beside the measured energies. Uncertainties in the calculated energies, which are listed for the first resonance in each series, are from the uncertainties in the fitted parameters η and μ, and so are *not* independent of the uncertainties listed for the measured energies.

Comparison of the measured energies with the 2e-formula predictions reveals that the energy of the second resonance in each series is consistently underestimated by 5-9 meV.

Figure 4.3 shows the 2e-formula predictions and the measured data for comparison. The data points are large enough to include the error bars. The ordinate is $(E_t - E)^{-1/2}$, following the format of Sadeghpour and Greene (1990); this effectively expands the energy scale — the few meV difference between the data and the curve for the second resonance in each series would be almost invisible on a normal scale covering the 1.5 eV range from the lowest $n = 3$ to the highest $n = 8$ resonance. The abscissa indicates the principal quantum number m of the outer electron; $m = n$ for the lowest resonance in each series (the intrashell resonances). Obviously, the curves have no physical meaning between integer values of m. The dashed line, on which the intrashell resonances lie, is exactly equivalent to the line of Figure 4.2.

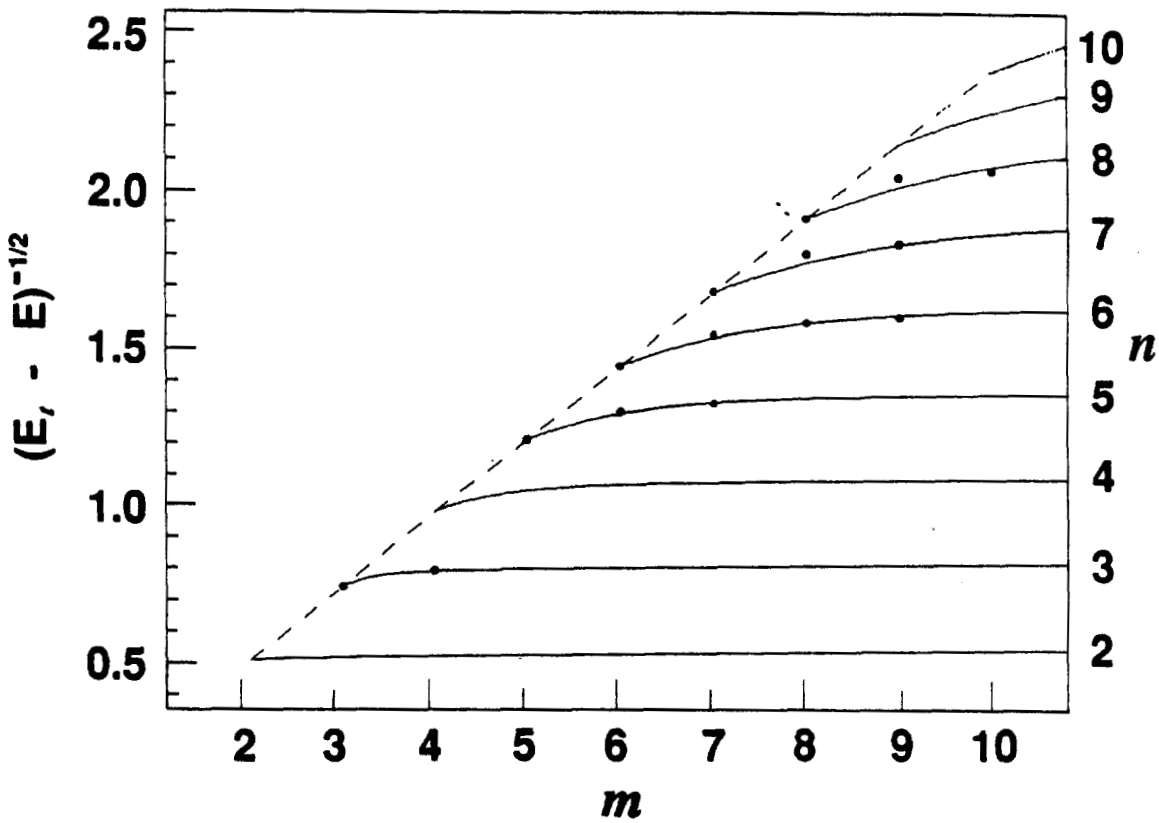

Figure 4.3. The 2e-formula (Sadeghpour, 1990) fit to the energies of the lowest resonance in each series (those lying on the dashed line).

Bear in mind that just *two* free parameters determine *all* of the curves shown!

4.3.6 Summary of Comparison of Energies with Theory.

The energies of the lowest resonances in each series seem to be well determined by a number of different theoretical calculations of varying complexity; disagreements between calculations typically amount to a few meV, and this is of the order of the differences between the calculated values and the experimentally measured values. The dipole recursion formula seems to hold approximately, as expected, within each series. The simple analytic 2e-formula, based on this dipole scaling law and the modified Rydberg formula (equation 2.23), predicts the positions of the resonances just as well as any other calculations.

Bearing in mind that each continuum partial cross section should contain many series of resonances, this remarkably good match seems to indicate that the lowest "+" series dominates every time, since otherwise the overlapping resonances would give a far more complicated spectrum.

4.3.7 Comparison of Measured Widths with Theory.

Table 4.5 shows a comparison of the measured resonance widths *vs.* theoretically calculated widths. The calculated widths are for the first resonance in each series, the remainder being given by the dipole recursion formula.

The width of the first resonance in each channel, from both the unconstrained fits and the dipole law fits, matches the calculated width (to within the error bars) *if* one assumes that the "uncertainty" in the calculated value is 1 in the last digit. Since the first resonance matches, subsequent resonances must match also for the dipole formula fits. Those of the unconstrained fits, on the other hand, seem to bear little relation to the widths expected from the dipole recursion formula, although there is a tendency for them to narrow as the next threshold is approached.

Threshold n:	Fitted (eV)	Calcd. (eV)
3	12.650(4)	12.6494(126)
	12.837(4)	12.8302
		12.8410
		12.8416
4		13.3448(64)
		13.4665
		13.4944
		13.5008
5	13.6858(3)	13.6874(38)
	13.7708(3)	13.7652
	13.7919(11)	13.7931
		13.8031
6	13.8812(3)	13.8809(25)
	13.9379(2)	13.9324
	13.9557(1)	13.9557
	13.9628(1)	13.9662
7	14.0024(7)	14.0008(18)
	14.0456(7)	14.0362
	14.0558(2)	14.0548
		14.0645
8	14.0802(10)	14.0801(13)
	14.1132(2)	14.1055
	14.1171(3)	14.1201
		14.1286
9		14.1354(10)
		14.1541
		14.1657
		14.1729
10		14.1754(8)
		14.1896
		14.1988
		14.2049

Table 4.4 Fitted photon energies of resonances, in eV (from unconstrained fits) *vs.* calculated values from the 2e-formula, using the best fit to the lowest resonance in each channel. The uncertainties in the calculated values arise from the uncertainties in the fitted parameters η and μ, and are therefore *not* independent of the uncertainties in the measured energies. The thresholds n are those to which the resonances converge.

Resonance Widths

Between thresholds:	Fitted (1)	Fitted (2)	Calcd.
4 and 5	21.5(5)	21.1(1)	20
	14.1(7)	7.56	7.2
	14.3(7)	2.7	2.6
5 and 6	13.0(3)	14.0(1)	13
	10.5(3)	6.3	5.9
	8.4(3)	2.9	2.7
	1.4(1)	1.3	1.2
6 and 7	12.4(14)	11.6(18)	11.1
	4.9(9)	6.1	5.8
	0.9(2)	3.2	3.0
7 and 8	3.1(1)	4.0(3)	
	1.39(4)	2.3	
	1.13(6)	1.3	

Table 4.5 Fitted widths of resonances, in meV, (1) unconstrained fits, (2) fits to dipole series, *vs.* calculated values (Ho and Callaway, 1986; Ho, 1990). For the dipole series fits and for the theoretical calculations, widths beyond the first are calculated from the dipole recursion formula. Widths considerably less than the 8 meV resolution may not be reliable.

The third of the resonances converging to $n = 5$ seems to have a rather large width. This may be due to the existence of a fourth resonance in the series, the possibility of which will be discussed in section 4.5.2 below.

With only four channels available for analysis, it is difficult to see any systematic trend of the widths. Those of the first resonances converging on the hydrogenic $n = 5$, 6, 7 and 8 thresholds are 22, 13, 12 and 3 meV respectively (from the unconstrained fits), and no pattern is obvious from these four numbers. Since the dipole recursion formula only appears to hold approximately, precise calculations of widths of higher resonances in each series would be useful, but these do not seem to be available currently.

4.4 Other Parameters.

In this section we give the fitted values of the Fano asymmetry parameter q, the resonance amplitude σ_a, and the amplitudes and slopes of the continuum background.

4.4.1 Asymmetry Parameter q.

For cases b) and d) as outlined above, *i.e.*, with the unconstrained fits and the fits to a series with the dipole moment fixed by theory, the value for the parameter q is given in Table 4.6. These should, however, be treated with some caution, because the apparent shapes of the resonances, which is really what q is measuring, are affected both by the shape of the underlying continuum (which has been assumed to have a linear dependence on energy) and by any other resonances that may be in the vicinity but which are not prominent enough to have been included in the fits. (It should be remembered that several series of resonances, of both "+" and "−" character, are expected in each channel, although the "−" resonances should not be significant, as discussed in Chapter 2 and by Greene, 1980). Except for the first resonance in the n = 5-6 channel, agreement between the different estimates of q is poor.

The values of q for case e), where q and σ_a are held constant, are given with the results in Table 4.1; however, the extremely large values for the reduced χ^2's show that the fits are extremely poor, and therefore that this model fails to represent the true structure. It will not be considered further.

4.4.2 Resonance Amplitudes σ_a.

Resonance amplitudes σ_a are given in Table 4.7, as a fraction of the fitted continuum amplitude A (see the following section, 4.4.3), for the unconstrained fits and for the fits to the dipole recursion formula. There does not seem to be a consistent pattern to these amplitudes, except that they tend to be close to 1.0.

Unconstrained fits (case b. above).

thresholds:	q_1	q_2	q_3	q_4
4-5	0.187(14)	0.323(37)	-1.20(11)	
5-6	0.262(4)	0.406(3)	-0.064(13)	-0.957(54)
6-7	0.456(52)	1.23(21)	0.315(67)	
7-8	-0.09(15)	0.650(15)	-0.660(33)	

Dipole series fits (case d. above).

thresholds:	q_1	q_2	q_3	q_4
4-5	0.292(6)	-0.081(4)	-0.193(21)	-0.863(16)
5-6	0.268(5)	-0.038(8)	-0.206(39)	-0.51(10)
6-7	0.360(32)	0.008(49)	-0.391(49)	-2.00(7)
7-8	0.28(12)	-0.18(7)	-0.317(47)	-2.0(3)

Table 4.6 Fitted values of the asymmetry parameter q, for both unconstrained fits and for fits to dipole series of resonances.

Physically, they cannot be larger than 1.0 if $q = 0$, since this would imply that the dip is *deeper* than the continuum background (neglecting the contribution to the continuum background of the *slope*, discussed in section 4.4.3). This constraint, however, is not built into the fits.

4.4.3 Background Amplitudes and Slopes.

For each series of Fano profiles, the continuum background σ_b (equation 2.36) was modeled by a linear function of energy,

$$\sigma_b = A + B(E - E_n), \tag{4.3}$$

where E_n is the threshold energy (eV) for the continuum channel *in which the resonances are embedded* — in other words, the $n = 4$ threshold for the resonances converging on $n = 5$, and so on.

Between thresholds:	Resonance Amplitudes σ_a. (1)	(2)
4 and 5	0.948(14)	0.717(1)
	1.124(40)	1.036(10)
	0.845(45)	1.016(11)
5 and 6	0.951(12)	0.881(9)
	1.034(8)	1.117(24)
	1.424(6)	1.090(33)
	1.277(5)	0.95(13)
6 and 7	0.621(43)	0.72(6)
	0.517(57)	0.76(10)
	4.4(8)	0.92(21)
7 and 8	1.40(7)	1.02(7)
	2.88(11)	1.26(10)
	3.56(28)	2.20(30)

Table 4.7 Fitted values of the resonance amplitude σ_a, as a fraction of the background amplitude, for (1) unconstrained fits (case b. above), (2) dipole recursion fits (case d. above).

As discussed in Appendix D, an attempt was made to approximate the cross section units to μa_0^2 by using the $1/n^3$ scaling law, and so the quoted units of continuum amplitude are "μa_0^2". Based on the scaling law and on the expected photodetachment cross section into $n = 1$ (see section F.1.2), the expected continuum amplitudes are $\sim$ 2102, 1076, 623 and 392 μa_0^2 for the channels converging on $n = 5$, 6, 7 and 8 respectively. It should be noted, however, that we are really only listing relative cross sections.

Table 4.8 lists the amplitudes A and slopes B of the continuum background. Although the slopes are relatively small, they appear to be essential to the fits, in that the reduced χ^2s increase dramatically if the slopes are fixed at zero. The agreement between the unconstrained fits and the dipole scaling law fits is poor for both the background amplitudes and slopes (except for the background amplitude between the $n = 5$ and $n = 6$ thresholds).

Between thresholds:	Continuum Amplitudes ("μa_0^2"). (1)	(2)
4 and 5	2074(22)	2398(5)
5 and 6	1021(8)	1013(7)
6 and 7	712(25)	608(29)
7 and 8	473(28)	354(17)

Between thresholds:	Continuum Slopes ("μa_0^2"/eV). (1)	(2)
4 and 5	3975(65)	3579(17)
5 and 6	1858(39)	539(15)
6 and 7	-1665(53)	-1075(454)
7 and 8	-538(416)	1676(353)

Table 4.8 Fitted values of the continuum amplitude (in "μa_0^2") and slope ("μa_0^2"/eV) for (1) unconstrained fits (case b. above), (2) dipole recursion fits (case d. above).

4.5. Other Possible Resonance Structures.

We discuss here some structures that appear in the yield curves that may be due to resonances, but which are not as clearly defined as those discussed in the preceeding sections.

4.5.1 The "9+" Candidate.

The fitted "2e-formula" predicts that the first "+" resonance associated with the $n = 9$ threshold will occur at 14.1354 eV, just 4.4 meV below the $n = 8$ threshold. As such, it should decay into the $n = 7$ channel. The $n = 7$ continuum fits discussed earlier were terminated at 14.136 eV, since at this energy (with 8.3 meV resolution) the $n = 8$ production threshold should begin to influence the cross section.

Inspection of the entire energy range, however, shows a dip just before the $n = 8$ onset. It is not a large dip, as the first resonances in each series have been in all other cases, but that may be expected of a "9+" resonance coupling to the $n = 7$ continuum.

Figure 4.4 shows a fit of this entire range up to the $n = 9$ threshold. The parameters representing the first three resonances were held constant at the values previously found in the unconstrained fits. The amplitude and slope of the $n = 7$ continuum were allowed to vary, and the $1/n^3$ scaling law was assumed to hold between the $n = 7$ and $n = 8$ continua. The fitting routine was then asked to find a resonance corresponding to the dip between 14.13 and 14.15 eV. It produced the following parameters, with a reduced χ^2 of 1.9:

$$E_0 = 14.1429(1) \text{ eV},$$

$$\Gamma = 0.9(2) \text{ meV},$$

$$\sigma_a = 1.8(14),$$

$$q = 0.91(8),$$

$$A = 425(6) \text{ “}\mu a_0^2\text{”},$$

$$B = 846(110) \text{ “}\mu a_0^2\text{”/eV}.$$

Again, the amplitude σ_a of the resonance is given as a fraction of the continuum amplitude A.

The centroid of the dip is not quite in the expected place, although there is undoubtedly interference between the $n = 8$ production threshold (which does appear to have a slightly delayed onset) and the resonance itself, in addition to any other resonances in the vicinity (from the 8+ series). It seems quite feasible that this shallow dip is in fact the first 9+ resonance. However, a fit to the 9+ series failed to find resonances in the right place for recursions of this first dip (the best fit had $\chi^2/\nu = 3.6$). Further investigation of this structure, using

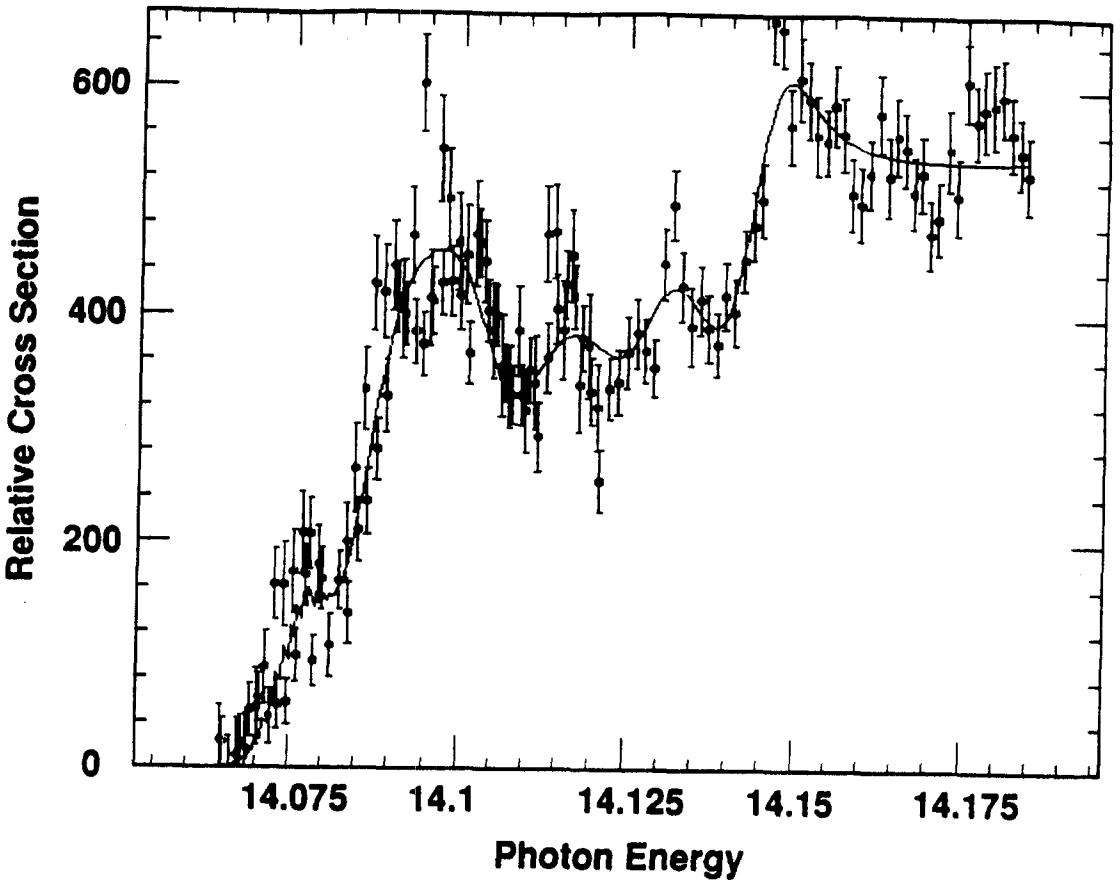

Figure 4.4. H°($n = 7, 8$) continuum production.

a cleaner detection system (the 2-laser experiment discussed in Chapter 6), is highly desirable.

Note that the continuum amplitudes for $n = 7$ and $n = 8$ seem, at least visually, to match the $1/n^3$ scaling law quite well.

4.5.2 $n = 4$ Threshold Dip.

There appears to be a shallow dip just above the $n = 4$ production threshold, centered at about 13.55 eV (see Figure 4.1(a)). This dip is not very well defined, and its shape is not consistent from run to run; however, it does at least appear to be present in all of the runs that cover the appropriate energy range. Its nature is unknown; a shape resonance is possible above $n = 4$, but if it exists it is expected

to be extremely narrow. An alternative possibility is the "tail end" of a broad Feshbach resonance that is expected to lie *below* the $n = 4$ threshold (Ho and Calloway, 1986).

It was not included in this analysis because of its lack of consistency.

4.5.3 Fourth $n = 5$ Dip.

Most of the zero-field runs that cover the range between the hydrogenic $n = 4$ and $n = 5$ thresholds (see Appendix J, Figures J.1-J.8) show a small dip, or at least a plateau, just below the $n = 5$ threshold (at 13.8084 eV). It is generally within the noise, and often represented by a single data point, but it does appear to repeat. It was not included in the fits because, firstly, it is not well defined in any run; secondly, it is too close to the $n = 5$ threshold (bearing in mind that our resolution is 8.3 meV); and thirdly it is not clear that it is a resonance in its own right rather than just a return to the continuum level after a "dip-peak" asymmetric resonance preceeding it. Obviously there would be little meaning to a fit of such a structure to four free parameters.

4.5.4 Peaks Below Threshold.

An interesting structure appears below, in particular, the production threshold for $n = 4$. Although similar features are visible below other thresholds, the phenomenon shows itself most clearly of all in Run 589 (Figure 4.5), which is a high-resolution scan of the region immediately below the $n = 4$ threshold. There are two small peaks at energies of ~ 13.46 and ~ 13.486 eV.

The cross section for production of $n = 3$ excited neutral hydrogen should be more than twice that of $n = 4$ (according to the $1/n^3$ scaling law). Since we are seeing structure below the $n = 4$ production threshold, it must be due to ionization of $H^\circ(n = 3)$; it therefore seems likely that we are seeing a tiny fraction of the $n = 3$ continuum. If we look not at the apparent peaks, but

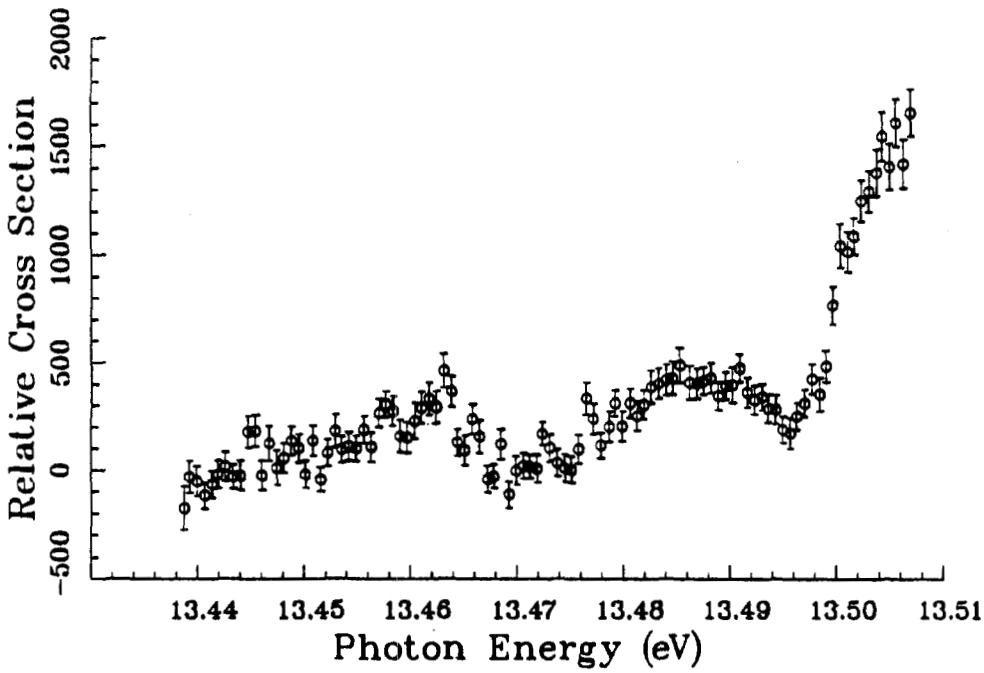

Figure 4.5. Structure below the H°($n = 4$) production threshold.

rather at the dips between them, we see that they are at energies of $\sim$ 13.47 and $\sim$ 13.495; and, indeed, Sadeghpour's "2e formula" (equation 2.25) predicts resonances (converging on the $n = 4$ threshold) at energies of 13.467 and 13.495 eV.

If we are indeed seeing the expected resonances, we must explain the mechanism of the ionization of H°($n = 3$)'s. At a (barycentric) field of 1.9 MV/cm, the lifetime of (all parabolic substates of) H°($n = 3$) is thousands of seconds, and so it is impossible for the magnet to have stripped them. One conceivable alternative is residual gas stripping, although this seems unlikely bearing in mind the small cross sections (see section F.3) and the small number of excited atoms produced. Another possibility is that the laser light is reflecting back from the

"catcher", traversing the interaction region in the opposite direction, and ionizing the H°($n = 3$)'s. The Doppler-tuned photon energy in this case is about 3.6 eV; 1.5 eV is required to ionize $n = 3$. Since 3.4 eV is required to ionize $n = 2$, part of our background may be from this source, although if so another mystery presents itself; there is no drop in background at the angle where $n = 2$ ionization from back-reflection is no longer possible (which corresponds to a forward-directed photon energy of 13.87 eV, in the $n = 5$ continuum). Future experiments should attempt to overcome the back-reflection problem by absorbing the light more efficiently, or at least by directing the reflected light away from the interaction region.

4.6 Effects of Electric Fields.

Electric fields were also applied to the interaction region, to study the quenching of the resonances. The polarization of the light was a mixture (approximately 50% - 50%) of π and σ (parallel and perpendicular to the field). The fields, perpendicular to the plane of interaction of laser and particle beams, were produced by applying a potential difference between a pair of steel discs held 1 cm apart across the interaction region; the electric field F' in the barycentric frame is then γ times the field F in the lab frame. (A fairly weak magnetic field, of strength $B_\perp = \gamma\beta F_\perp/c$, is also produced by the relativistic transformation of the electric field; this amounts to no more than 250 gauss).

The data from the electric field runs are displayed, with the field-free data, in Appendix J. The effects of the fields are twofold; firstly, to quench the resonances; and secondly, to shift the thresholds downward in energy (and to change their shape).

Table 4.9 indicates the resonances that are quenched in given electric fields. Background levels caused problems, and the quality of much of the data is not optimum. Nonetheless, the quenching process is clearly demonstrated for all but

the very strongest resonance (the first in the series below the hydrogenic $n = 5$ threshold). There does not appear to be any appreciable change of shape (or shift in energy) of the resonances, as might have been expected from mixing, prior to the quenching.

Between	Electric Field (kV/cm)			
Thresholds:	12	25	63	87
4-5	3		[2]	2
5-6		3	2	1
6-7	3[2]	2[1]		

Table 4.9 Resonances in each series that are quenched by a given electric field. Square parentheses indicate that a given resonance is significantly suppressed ($\sim 50\%$ reduction in depth of the dip), but not fully quenched.

The threshold shifts, probably due both to field-assisted tunneling from the ground state of H^- and to the changing of the threshold shapes by the linear Stark effect, are also clearly visible. Unfortunately the changing shapes of the thresholds, and the existence of structure below them, makes it difficult to pinpoint the onset of production. From a fairly clear step function at zero field, the threshold smears out into a slope as the linear Stark effect splits the degenerate levels into the different parabolic substates.

Table 4.10 lists the approximate shifts in the threshold energy of $n = 4$, 5 and 6 as the electric fields are applied. These are measured from the base of the (zero-field) step to the base of the (field-induced) slope.

Threshold Shifts (meV)

	Electric Field (kV/cm)		
Threshold:	25	63	87
4	30(5)	45(10)	55(10)
5	35(10)	45(10)	60(20)
6	35(10)		

Table 4.10 Downward shifts in energy (meV) for the various production thresholds of neutral hydrogen.

Chapter 5

Associated Experiments

'Oliver Twist has asked for more!'

— Charles Dickens, *Oliver Twist*.

The study of high-lying resonances in H^- was not performed in isolation; it was one of a number carried out in 1988 and 1989. We detour in this chapter briefly to review the other experiments done en *route*, before returning to the conclusion of the resonance studies in Chapter 6.

5.1 Multiphoton Detachment.

Multiphoton detachment of H^- was first observed by our group in 1988 (Tang *et al.*, 1989), and was studied further during experiments that took place in 1989. The barycentric photon energy of an extremely intense CO_2 laser beam was Doppler tuned between 0.05 eV and 0.32 eV in 1988 (with a 500 MeV H^- beam) and between 0.03 eV and 0.4 eV in 1989 (800 MeV beam). Since H^- is bound by 0.754 eV, and there are no excited states below the continuum, the minimum number of photons required to remove the outer electron was varied from two to twenty two.

A schematic diagram of the experimental apparatus is shown in Figure 5.1. It is the same in principle as the Doppler-tuning equipment already described. Electrons from the multiphoton detachment process were detected in the electron

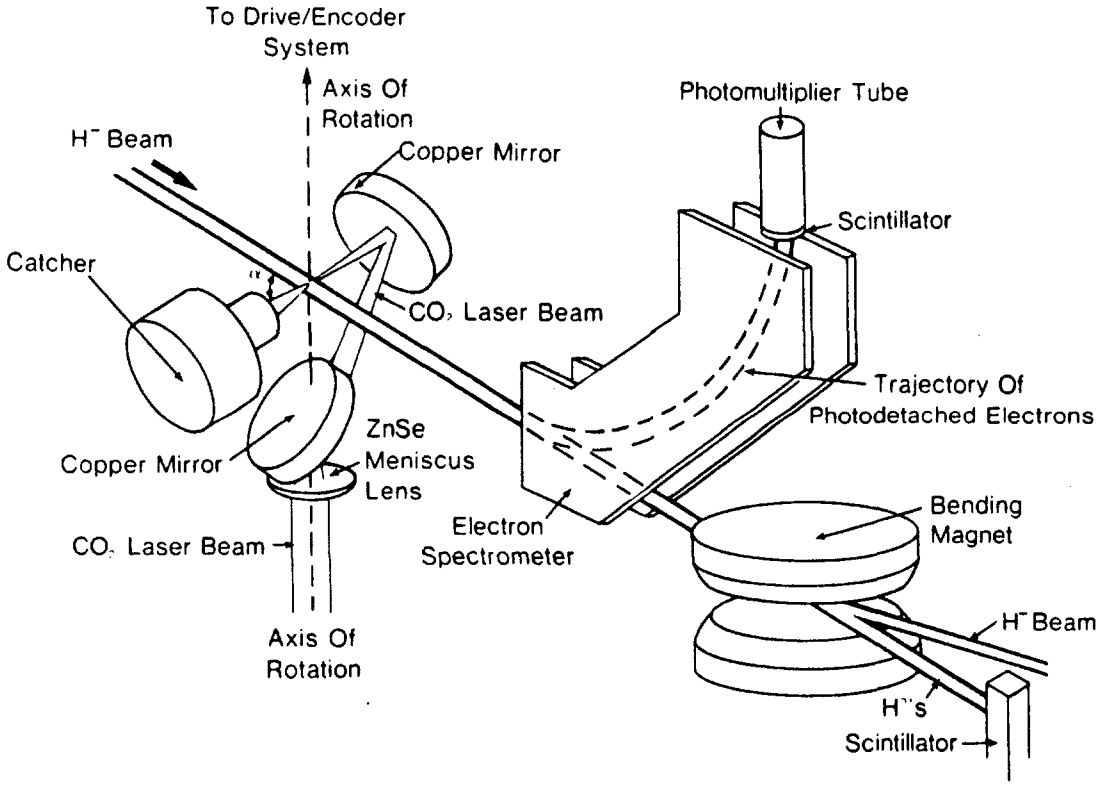

Figure 5.1. Equipment for Multiphoton Detachment of H^-.

spectrometer; the neutral hydrogen atoms were detected in another scintillator, and became a redundant confirmation of the signal.

The preliminary results from the 1988 study have already appeared in the literature (Tang *et al.*, 1989). The primary aim of that experiment was to find a signal for multiphoton photodetachment, thereby justifying a large-scale, thorough investigation, and in that it was successful; however, inherent weaknesses in the design of the equipment meant that certain systematic errors were impossible to overcome. In particular, with the equipment then in use, precision optical alignment was impossible, and the focal spot "wandered" by perhaps 1 mm vertically as the mirror system rotated through 180°. This changed the effective overlap, which was optimized at a particular angle by vertical steering of the (3 mm wide) H^- beam.

For the 1989 experiment, the little chamber was totally redesigned and rebuilt (see Appendix A), as a consequence of which a fairly precise alignment could be performed, thereby eliminating the major uncertainty in the system and allowing quantitative measurements to be made.

The results of the 1989 study will be published in the thesis of Chen-Yau Tang (1990).

5.2 Foil Studies: The Passage of Matter Through Matter.

'Beam me up, Scotty.'

— William Shatner as Captain Kirk, in *Star Trek.*

We have been studying the response of the relativistic H^- ions as they pass through very thin (15-300 $\mu g/cm^2$) foils, composed mainly of vacuum-deposited carbon. Of the ions entering the foil, a sizeable fraction — perhaps 30% for the thinner foils — emerge intact; some — another 30% — are stripped to protons; and the remainder end up in various excited states of H°. The nature of the excitation mechanism is not understood, but it may be chaotic.

The distributions of the highly-excited states ($n \geq 10$) are measured directly with the electron spectrometer; lower-lying states (n = 1, 2, 3, 4...) are first promoted to a higher state — say, n = 13 — by a laser, this higher state then being detected as before by the electron spectrometer.

Many interesting questions arise here. What does the foil environment "look like" to the H^- ion? Presumably, it is an extremely intense radiation field, with field strengths of the order of atomic units, a frequency of 10^{18} Hz (corresponding to the interatomic spacing of the carbon atoms), and a duration of about a femtosecond. How does the H^- ion survive intact, especially as the "orbit" of the outer electron is sufficiently large to contain up to eight carbon atoms? Possibly the electron passes through the foil "independently", and is "picked up" again as it exits. And how is a multiple excitation possible within a femtosecond? Classically, this is of the order of an orbital period for atomic hydrogen; and yet the results suggest that thicker foils produce more atoms in the higher excited states, which implies a diffusive, step-by-step excitation process. These, and other equally interesting questions, will be addressed in the dissertation of Amir Mohagheghi (1990).

5.3 Field-Induced Oscillations.

This section is based upon work accepted for publication in Physical Review A (Harris *et al.*, 1990d).

The recent experimental verification (Bryant *et al.*, 1987; Stewart, 1987; Stewart *et al.*, 1987) of the theoretical prediction (Fabrikant, 1980; Reinhardt, 1985) of electric-field induced modulations in the photodetachment cross section of H^- near the single electron threshold spurred further theoretical efforts to describe more accurately the shape of the cross section, as a function of photon energy, in static electric fields. (An earlier sighting of this effect, in the photodetachment cross section of Rb^- (Frey *et al.*, 1978), was not recognized as such until recently

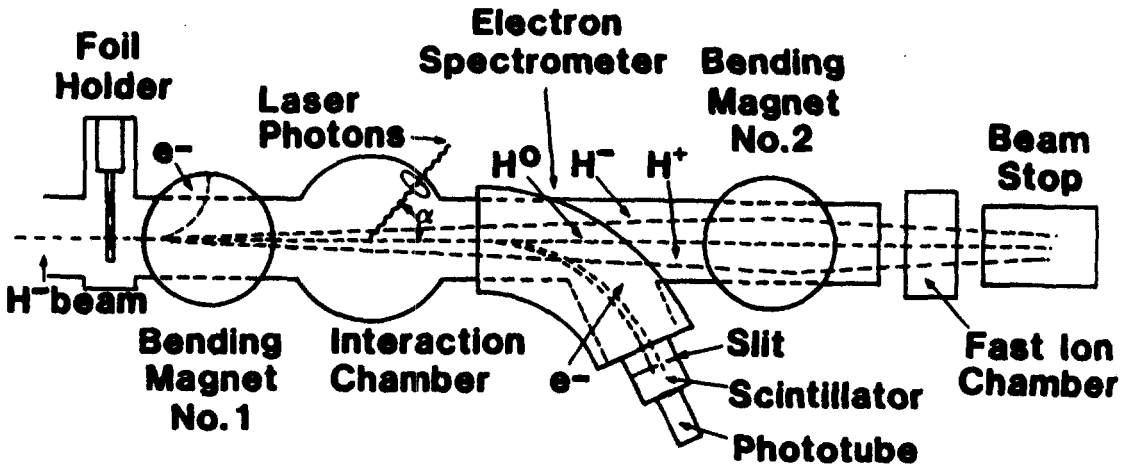

Figure 5.2. Schematic diagram of apparatus for foil studies.

(Greene, 1988)). We give here the results of a further investigation, with two important differences from that reported previously: first, this experiment was carried out in a well-determined electric field; and second, emphasis was focused on the region very close to the zero-field threshold, where any effects due to the residual polarized neutral hydrogen atom should be felt most strongly. These results are fitted to the theory of Rau and Wong (1988). In addition, we present data from an earlier experiment (performed in 1985) in which the field strengths were considerably higher, but the light was exclusively σ polarized.

The experimental method was similar to that described in Chapter 3, with the relativistic Doppler shift once again providing a "tunable" laser, this time in the infrared, the lab photon energy being 1.1649 eV (Nd:YAG fundamental).

In order to produce a uniform electric field, two polished stainless steel plates were mounted, 1 cm apart, on either side of the interaction volume. With a potential difference of up to 60 kV between these plates, barycentric electric fields of up to 96 kV/cm became available. Both π (electric vector of laser light parallel to external electric field) and σ (perpendicular) polarizations were obtainable in this manner. The apparatus is illustrated in Figure 5.3.

This method was in contrast to that used in the previous experiment, where the laser light was passed through the pole pieces of an electromagnet in order to obtain both π and σ polarizations. The relativistic transformation of the magnetic field produced a large electric field in the barycentric frame. The magnetic field, however, was non-uniform, and its strength was not very well known. The electric plates had the additional advantage that their electric field was not angle-dependent, unlike the field produced by the electromagnet, which was fixed with respect to the laser beam. Other differences are that, in the previous experiment, the laser was focused with a cylindrical lens into the plane of the laser and particle beams, primarily in order to let it pass through the pole pieces of the magnet;

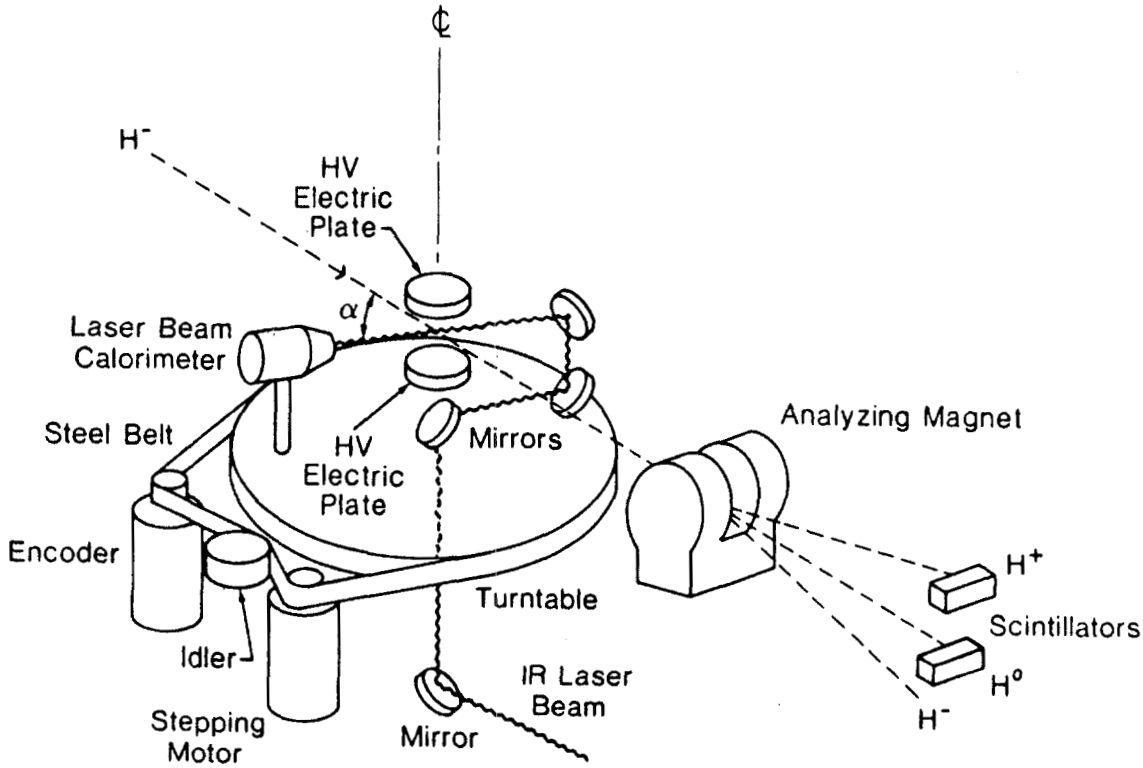

Figure 5.3. Schematic diagram of apparatus for "ripple" studies.

and the laser was not operated in Q-switched mode as was the case in the most recent experiment, so the peak power was much lower.

In the 1985 experiment, the electric field was also produced by the relativistic transformation of a magnetic field; however, the magnet consisted of a pair of Helmholtz coils, which were energized in very short pulses in coincidence with the laser; thus, high fields were obtained for short periods of time, but the geometry of the system permitted only σ polarization of the light.

The neutral hydrogen atoms from photodetachment were separated magnetically from the primary H^- beam and detected, downstream of the interaction region, in a scintillator, also shown in Figure 5.3.

The resulting yields were converted into relative cross sections by applying a multiplicative factor, $\sin\alpha/(1+\beta\cos\alpha)$ (see Appendix F), which allows for the relativistic variation of intensity with angle as well as the change in overlap volume of the two beams. The energy scale for the 1988 (electric field) experiment was calibrated by fitting a series of near-threshold curves at zero field — as shown in Figure 5.4 — to find the angle of the threshold itself; it was also checked by exciting transitions in neutral hydrogen from $n = 4$ to $n = 12$, 13, 14 and 15. The uncertainty in energy is less than 1 meV.

In the absence of any electric field, the photodetachment cross section depends upon photon energy E according to a power law (see, for example, Armstrong, 1963)

$$\sigma = \frac{16\pi}{3(137)} \cdot \frac{E_0^{1/2}(E-E_0)^{3/2}}{E^3} \cdot \frac{1}{1-k_B r_{eff}}. \qquad (5.1)$$

E_0 here represents the threshold energy, 0.7542 eV; $k_B^2 = 2E_0$, and the effective range, r_{eff}, of the potential is 2.646 a_0. Du and Delos (1988) point out that the factor $1/(1-k_B r_{eff})$, numerically equal to 2.65, was absent from the paper, although included in the calculation, of Rau and Wong; it was also omitted from a previous paper published by our group (Stewart *et al.*, 1987).

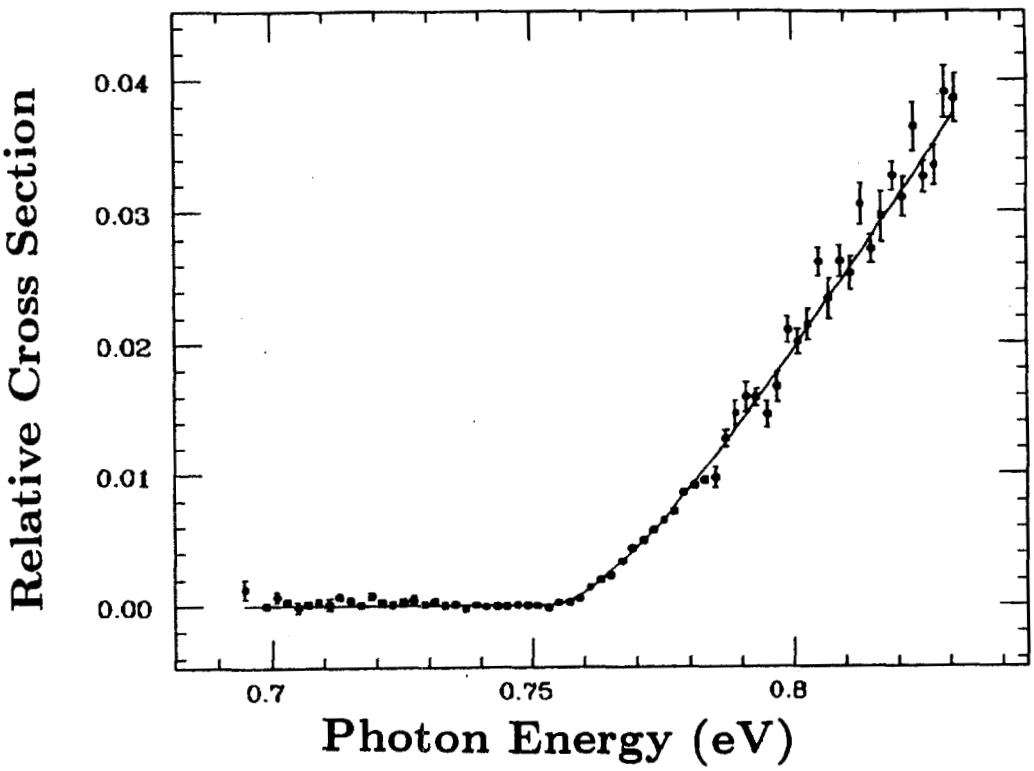

Figure 5.4. Zero-field photodetachment near threshold.

With π-polarized light, "ripples" appear on this cross section. This effect may be understood in a simple way by considering just the wave packet of the ejected electron, spreading preferentially "upstream" and "downstream" in the electric field (σ polarization, in contrast, would produce preferential spreading transverse to the field); the part of the wave packet that spreads "upstream" will reflect from the potential barrier of the external field and will return to interfere with the wave spreading "downstream", thus producing the characteristic interference pattern (Figures 5.5 - 5.8).

The frame-transformation approach of Rau and Wong predicts that the zero

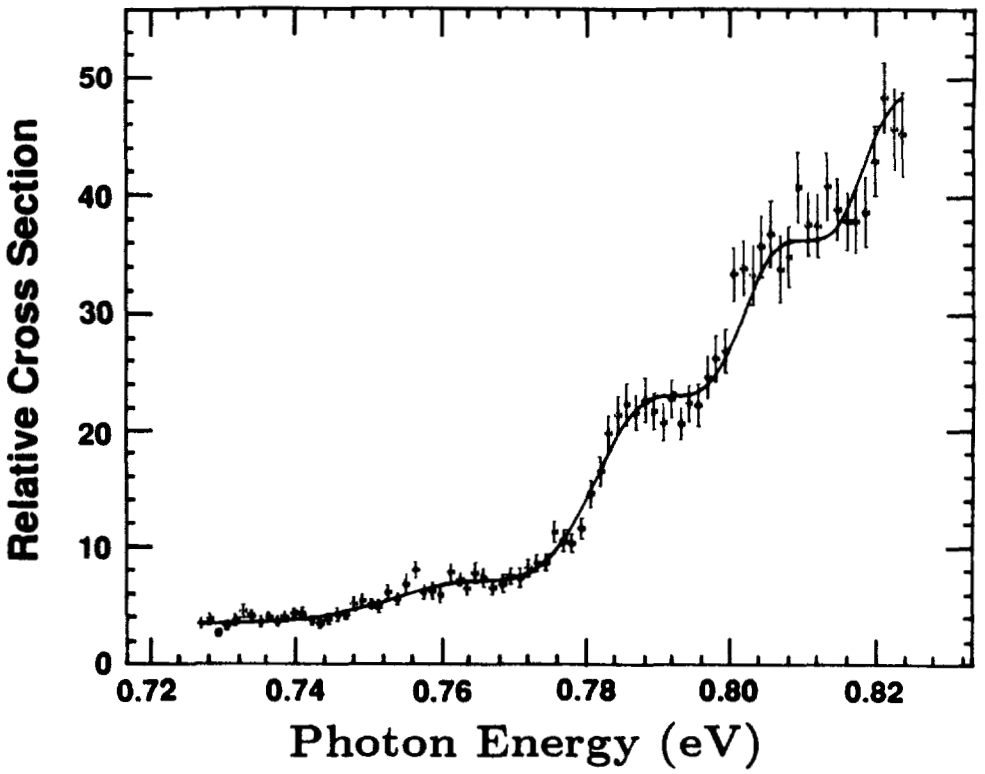

Figure 5.5. Photodetachment in an electric field of 64 kV/cm, with π-polarized light.

field cross section will be modified by a modulating factor $H^F(k)$,

$$\begin{aligned}\sigma^F(k) &= \sigma^{F=0} H^F(k) \\ &= \sigma^{F=0}(k) \int_{-\infty}^{k^2/2} d(q^2/2)|U_{q1}^F|^2,\end{aligned} \tag{5.2}$$

where

$$U_{q1}^F = (3\pi/k^3)^{1/2}(16F)^{1/6}\mathrm{Ai}'[-q^2/(2F)^{2/3}]. \tag{5.3}$$

The expression for the cross section ignores the final state interaction of the electron with the neutral atom (Wong, Rau and Greene, 1988). This is a good approximation, since the electron scattering phase shifts are small ($\delta \leq 0.01$ radians) for H^- in this energy range. The overall effect of δ is to replace $H^F(k)$

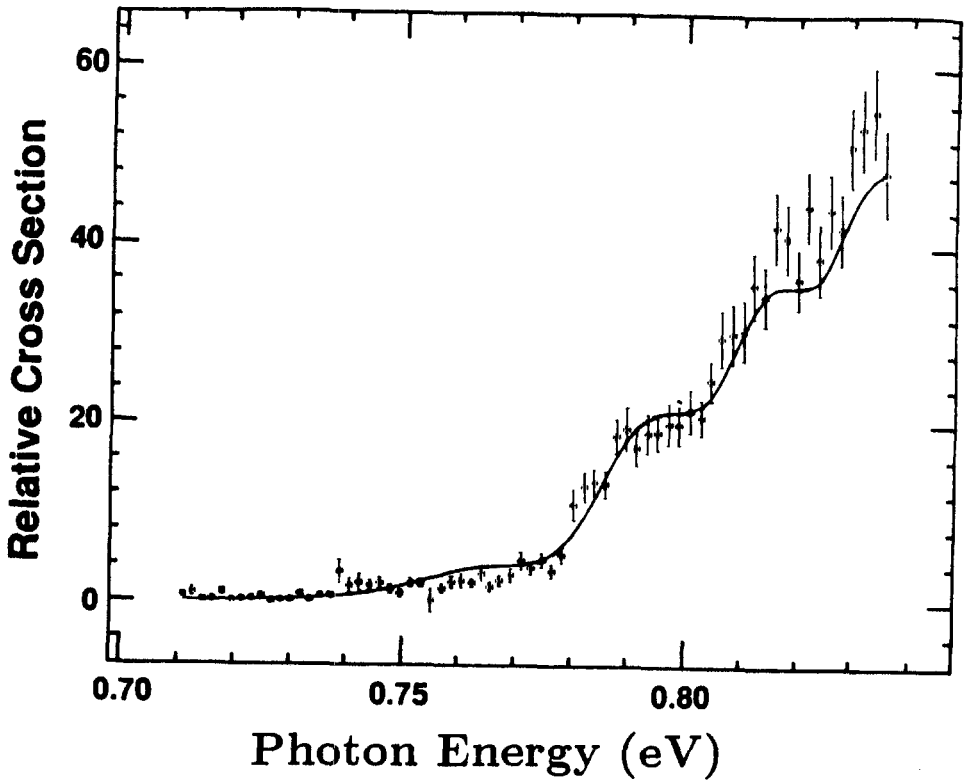

Figure 5.6. Photodetachment in an electric field of 80 kV/cm, with π-polarized light.

by $H^F(k)/(\cos^2\delta + H^F(k)^2\sin^2\delta)$, producing a fractional deviation of the order of 10^{-5}. The simpler formulation has therefore been used in this analysis.

Du and Delos (1988) have produced an equivalent formula that may be closely approximated by a simple analytic function for energies somewhat above the zero field threshold; to be specific, they define a parameter

$$x = \frac{2^{1/3}(E - E_0)}{F^{2/3}}, \tag{5.4}$$

and give as the cross section

$$\sigma = 0.3604\frac{F}{E^3}D(x)a_0^2, \tag{5.5}$$

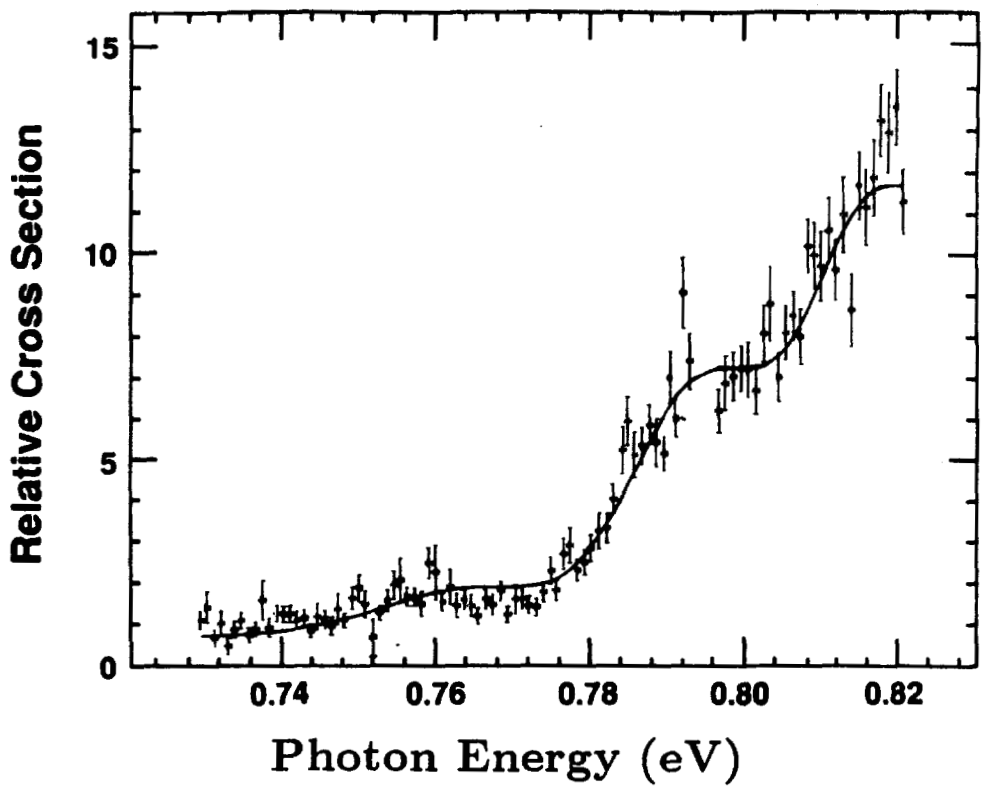

Figure 5.7. Photodetachment in an electric field of 83.2 kV/cm, with π-polarized light.

where

$$D(x) = \int_{-\infty}^{x} \left[\frac{d}{dz}\mathrm{Ai}(-z)\right]^2 dz, \tag{5.6}$$

$\mathrm{Ai}(z)$ being the standard Airy function. For sufficiently large x,

$$D(x) \approx \frac{1}{4\pi}\left[\frac{4}{3}x^{3/2} + \cos(\frac{4}{3}x^{3/2})\right]. \tag{5.7}$$

The difference between the function $D(x)$ defined in equation 5.6 and the analytic approximation (5.7) is 2% for $x = 2$, and 0.2% for $x = 4$ (corresponding to photon energies of 0.78 eV and 0.80 eV respectively at a field of 64 kV/cm). Thus, the analytic formula is extremely good once past the first "ripple".

Figures 5.5 - 5.8 show the results of some typical runs, taken with electric fields of 64, 80, 83.2 and 96 kV/cm. Individual sets of data from all runs are

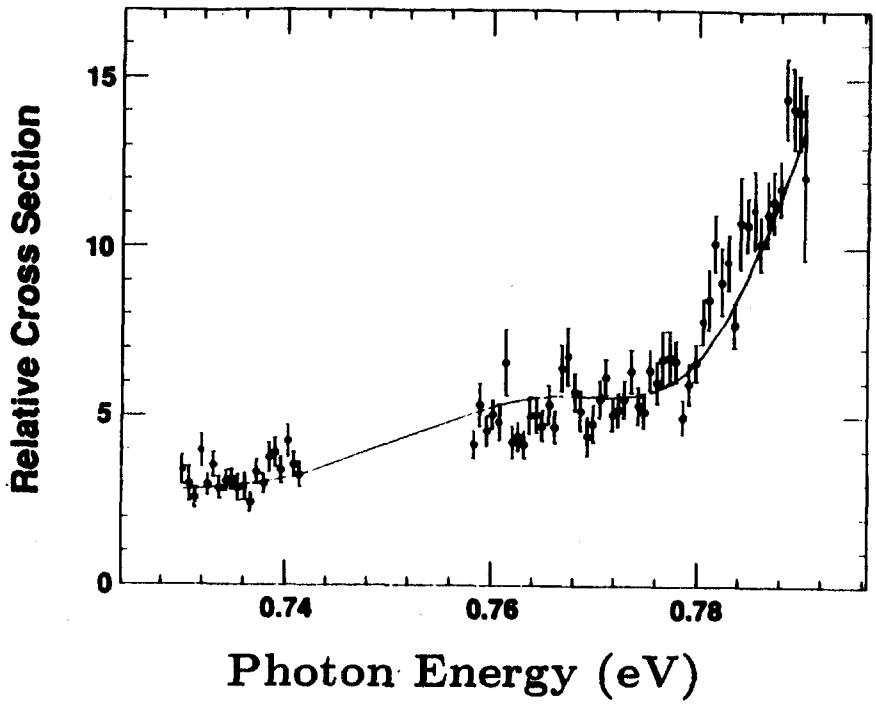

Figure 5.8. Photodetachment in an electric field of 96 kV/cm, with π-polarized light.

tabulated in full in a Los Alamos report (Harris *et al.*, 1989a). The theoretical prediction is represented in each figure by the solid line; the data shown include error bars that are the standard deviation of the mean signal at a given angle (energy). The confidence levels of the fits are low — 29% for the data taken at 64 kV/cm, and $< 1\%$ for the other data; we suspect that this indicates that the error bars are too small, since they do not allow for systematic effects such as changes in the temporal overlap of the laser and particle beams, and a fluctuating background from "spray" associated with the particle beam. However, it is interesting to note a tendency for the theoretical curve to lie above the data in the "toe" region, and to lie below it at lower energies as the cross section tends to zero.

The apparent nonzero cross section below threshold is due in part to back-reflected photons from the laser beam calorimeter, which intersect the H^- beam at a very forward angle and thus have a barycentric energy well above threshold. The cross section at these high energies is, however, relatively flat, and provides a constant background over the small angular range of the near-threshold measurements.

It should be pointed out that magnetic effects cannot be ruled out; the pure electric field in the laboratory produced a magnetic field in the barycentric frame of up to 250 gauss, which, although small, may not be negligible. The Landau levels (resonances due to quantized cyclotron orbits; Landau and Lifshitz, 1965) are unlikely to be the cause of such effects, as their energy spacing is 2.9 μeV at 250 gauss, which is well below our resolution of 0.5 meV.

Figure 5.9 shows all of the above data, for fields of 64, 80, 83.2 and 96 kV/cm, plotted so as to reveal the universal function of Du and Delos; the abscissa, in terms of the function x defined in equation 5.4 above, is

$$X = \frac{4}{3}x^{3/2}, \tag{5.8}$$

while the ordinate is given by

$$y = 4\pi\frac{\sigma E^3}{0.3604F}. \tag{5.9}$$

The solid line in the figure represents the analytic approximation to $D(x)$:

$$y = X + \cos X \approx 4\pi D(x). \tag{5.10}$$

Although Du and Delos do not give a formula for the photodetachment cross section in σ polarized light, Rau and Wong predict that there are once again oscillations on the zero field cross section. These, however, have a considerably smaller amplitude than their π polarization counterparts, and therefore may only be seen

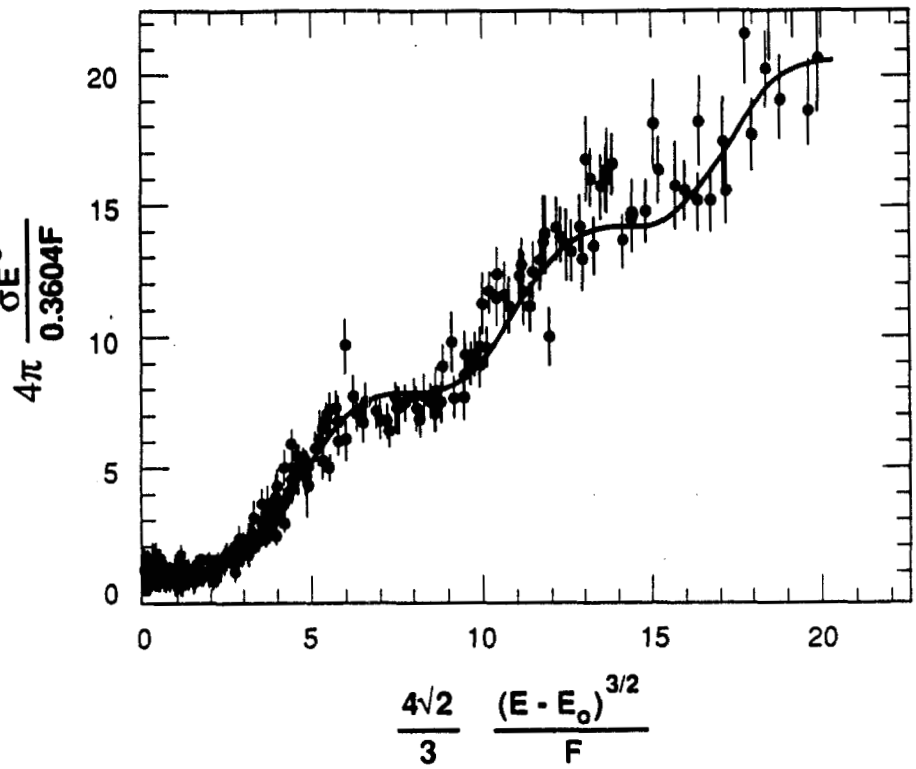

Figure 5.9. Data for fields of 64, 80, 83.2 and 96 kV/cm plotted to reveal the Du-Delos universal function. The solid line is the analytic approximation (see text).

in very strong fields, such as those of our 1985 experiment. The modulating factor in this case is again $H^F(k)$,

$$\begin{aligned} \sigma^F(k) &= \sigma^{F=0} H^F(k) \\ &= \sigma^{F=0}(k) \int_{-\infty}^{k^2/2} d(q^2/2)|U_{q1}^F|^2, \end{aligned} \tag{5.11}$$

where, for σ polarization,

$$U_{q1}^F = (3\pi/2k)^{1/2}(4/F)^{1/6}(1 - q^2/k^2)^{1/2} Ai[-q^2/(2F)^{2/3}]. \tag{5.12}$$

Unfortunately, the oscillation cannot be visualized in a simple manner as can the π polarization ripples, except that the largest effect is a field-induced increase

in the cross section in the threshold region due to the lowering of the potential barrier. Figure 5.10 shows the near-threshold photodetachment cross section as a function of photon energy, for an electric field of 1.32 MV/cm. The solid line is a fit, using the computer routine MINUIT (James and Roos, 1975), to the theory of Rau and Wong; the dashed line is the zero field cross section. Although data above 0.9 eV are available, these were not used as there is a possibility that our detectors may have begun to saturate somewhere above this value. Data below 0.9 eV are believed to be reliable.

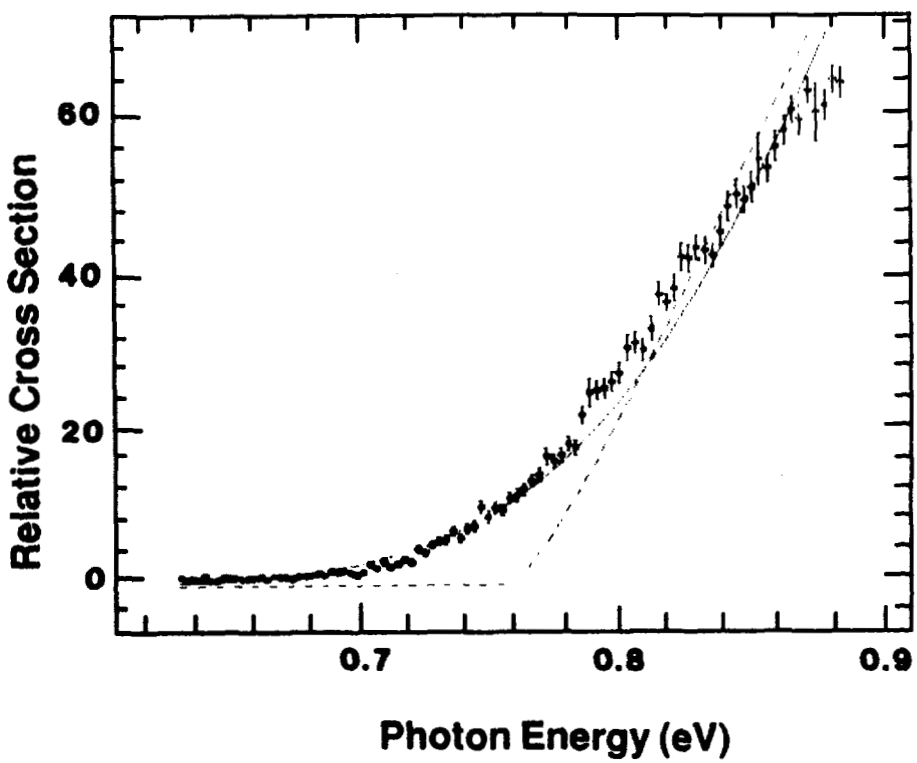

Figure 5.10. Photodetachment in σ-polarized light, in an electric field of 1.32 MV/cm. The solid line is a fit to the theory of Rau and Wong; the dashed line is the zero-field cross section.

The energy scale in the 1985 (Helmholtz coil) experiment is less well determined than for the 1988 runs, and it may be offset by a few meV. This offset was

therefore allowed to vary as a free parameter in the fit, the result indicating that a shift of −8.7 meV was appropriate; the data shown already incorporate this energy shift. The only other free parameters were the amplitude and a background.

It appears that the theoretically predicted shape of the cross section oscillates about the data. This, with the oscillatory nature of the cross section itself, becomes more apparent in Figure 5.11, which shows the difference between the data and the calculated zero field cross section. (The difference between the fitted theory and the zero field cross section is represented by the solid line). Since the fit only had three free parameters, namely the scale factor, the background and a small energy scale offset, we must conclude that the actual shape of the cross section is different from that predicted, although the difference is small. The fit has a chi squared of 6.5 per degree of freedom. As for the π polarized light, the theoretical curve appears to be too high just above threshold, and to be too low at lower energies; in fact, the data does not seem to fall off with the exponential tail that would be expected from a model of field-assisted-tunneling below the zero-field threshold.

Data also exist for lower fields; these are published elsewhere (Stewart, 1987). The effects are seen most clearly in this high-field example.

Fabrikant (1980) also predicts oscillations for both π and σ polarization photodetachment in a field of strength F. He introduces a parameter β,

$$\beta = \frac{2}{3}\frac{m_e^2 v^3}{Fe\hbar}, \quad v = \frac{\hbar k}{m_e}. \tag{5.13}$$

In terms of this parameter, the formulae for the photodetachment cross section are

$$\begin{aligned} \sigma_\pi &= \sigma_0\left[1 + \frac{\cos\beta - 1}{\beta} + O(\beta^{-2})\right], \\ \sigma_\sigma &= \sigma_0\left[1 + \frac{\Gamma(1/3)}{4\beta^{1/3}} - \frac{\sin\beta}{\beta^2} + O(\beta^{-3})\right] \end{aligned} \tag{5.14}$$

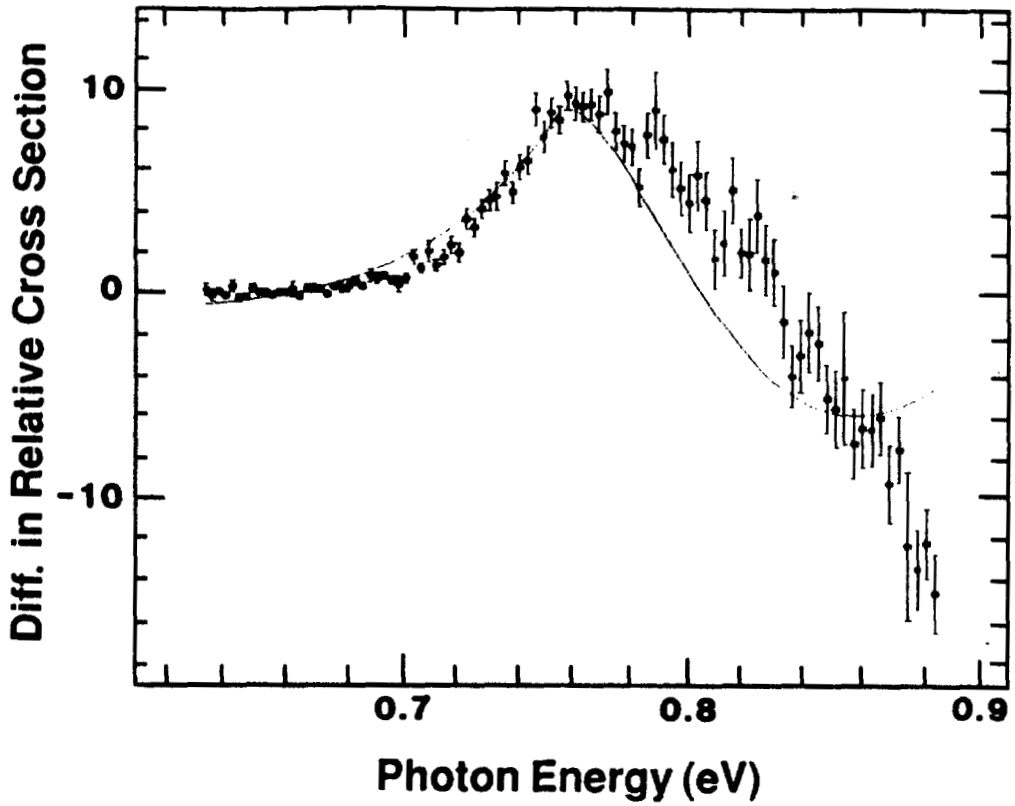

Figure 5.11. Photodetachment in σ-polarized light, in an electric field of 1.32 MV/cm; increase in cross section *above the zero-field level.* The solid line is again the fit to the theory of Rau and Wong.

for π and σ polarizations respectively, with $l = m = 0$. These "ripples" appear to be different in nature from those of Rau and Wong. Unfortunately, Fabrikant's theory only claims to be valid for $\beta > 2\pi$, which, in our case, implies photon energies greater than about 1 eV; in this region, our data may be unreliable due to saturation, and we therefore can make no claims for the validity of either theory. Fabrikant (1990) is pursuing this work further, and is interested in the possibility of a high-precision test in high fields. He has pointed out that prominent oscillations should also appear on the photodetachment cross section near the threshold for production of $H^{\circ}(n = 2)$.

In summary, the theoretical model of Rau and Wong of the threshold photodetachment cross section of the H^- ion in an electric field appears accurate for π polarized light, but the profile seems to fit less well with σ polarized light in much stronger electric fields. The theoretical prediction of Fabrikant differs from that of Rau and Wong, but its range of validity lies beyond currently available data.

5.4 Two-Electron Detachment.

When the photon energy is sufficiently high — above 14.3526 eV for H^- — it is possible for both electrons to escape at once from the nucleus. Figure 1.1 shows the calculated cross section for double detachment, along with that for single detachment, as a function of photon energy.

Determination of this energy dependence of the cross section for two-electron escape is regarded by some as the single most important problem remaining in atomic physics (Temkin, 1979; Reinhardt, 1979). If correlations between the electrons are unimportant, then the cross section would be expected to increase linearly with the energy E above threshold. If, on the other hand, one electron completely screens the other, so that only single detachment occurs, the cross section should rise as $E^{3/2}$ (Wigner, 1948); this has been observed (Frost, 1981; Stewart, 1987) in H^-. For correlated double escape, the energy dependence is more complicated, and lies somewhere between these extremes.

The simplest, classical, calculation for the shape of the two-electron photoionization cross section near threshold (Wannier, 1953) is a modification of the Wigner threshold law. Instead of the (single-escape) 3/2 power law, Wannier predicted that the exponent should become

$$n = \frac{1}{4}\left[\frac{(100Z-9)}{(4Z-1)}\right]^{\frac{1}{2}} - \frac{1}{4} = 1.127... \qquad (5.15)$$

in our three-body case with $Z = 1$.

Rau (1971) introduced quantum mechanics to the Wannier calculation, and verified that Wannier's classical law was correct in its evaluation of the exponent. However, the models of Wannier and of Rau assume that the two electrons escape symmetrically (or nearly so). The double-detachment process is then seen as the "series limit" of the "ridge-state" resonances (see Chapter 2), in which the electrons are on opposite sides of, and equidistant from, the nucleus, and are able to share their energy through their strong correlations. A competing quantum mechanical calculation by Temkin and Hahn (1974), based on the "Coulomb-dipole" model in which one electron leaves slightly ahead of the other (and therefore experiences a dipole potential due to the combination of slow electron and positive nucleus), predicts instead that the cross section obeys a modulated linear law as it increases with energy above threshold. They propose a complicated but analytic function for the threshold behavior. The exact form of this function has undergone a number of changes over the years as their calculations have become more sophisticated; the most recent version,

$$\sigma \propto E[1 - (D/\alpha)\sin(\alpha \ln(E) + \phi)]/(\ln(E))^4, \tag{5.16}$$

(Temkin, 1990) makes allowance for the angle θ_{12} between the radius vectors $\vec{r}_1$ and $\vec{r}_2$ of the electrons, which may not be 180°. Here α, ϕ and D are constants, and the energy E above threshold is in eV; the expected value of the dipole parameter α is ~ 26, and the expected energy range of validity of the theory is $0 \leq E \leq 20/\alpha^2$.

A previous experiment by our group (Frost, 1981; Donahue *et al.*, 1982) was unable to distinguish between the predictions of Temkin and of Wannier; our resolution was at that time inadequate. Competing experiments, in electron impact ionization of H°, are less direct than our own and consequently are extremely difficult to interpret at such low energies. Early results (McGowan and

Clarke, 1968) fitted to a power law produced a value for the exponent of 1.131 ± 0.019, in agreement with our own result of 1.15 ± 0.04 and with Rau's prediction — but again with insufficient resolution to rule out the modulated linear law. Some very recent results, however (Lubell, 1990) do give definite indications of structure above the two-electron threshold. The measurement in this case was of the asymmetry between the scattering cross sections for spin-polarized incident electrons parallel and antiparallel to the spin of the hydrogen target electrons. The Coulomb dipole model did not appear to fit the data very well; nonetheless, its confidence level ($\approx$ 1%) was orders of magnitude higher than that for the straightforward Wannier power law.

5.4.1 Experimental Technique.

The main focus of the experiments covered in this report was intended to be the nature of the double-detachment cross section. This aim was thwarted by high background levels, and the investigation was further diverted by the discovery of the high-lying resonances.

As usual, the primary tool in this investigation was the Doppler tuning, in this case of the fourth harmonic of the Nd:YAG laser (see Appendix A). With the 800 MeV H^- beam, the double-detachment threshold at 14.35 eV corresponds to an angle α of 37.63°.

The products of the interaction are protons (above the two-electron threshold), H° and electrons. These must be separated from the H^- beam and from each other; this can only be done with a magnetic field. There is, however, a problem; the moving atom sees the magnetic field as a strong electric field, and highly excited (Rydberg) states of H° field-ionize (see Appendix H), appearing as signal protons. (This, of course, is the tool that makes possible the study of the doubly-excited resonances). It was therefore necessary to use a long, weak magnetic field to separate the charge species while minimizing the field stripping; as

explained in Appendix A, the magnet employed was the "skinny magnet", which consists of four current-carrying copper rods around the beam pipe.

It was planned to use the high-resolution Nd:YAG laser (in combination with our newly-developed momentum bunching technique, described in Appendix E) in the near-threshold region to search for the structure predicted by Temkin, and then to use the ArF laser (which has a higher photon energy) to scan the higher energy region. A calculation by Broad and Reinhardt (1976) predicts that the two electron cross section will peak at about 18.4 eV; we had hoped to investigate the cross section up to 21 eV (nearly 7 eV above threshold), which should be quite adequate to go "over the bump".

5.4.2 Results.

Although double-detachment was definitely observed, the detector was unfortunately swamped with noise from a source that is as yet unknown, but which appears to have been stray protons traveling down the beamline with the primary beam, or possibly from pinholes in the HiRAB stripper (the thin foil used to collimate our beam). For other experiments, a "dog-leg" in the line will help to reduce such backgrounds; but in this case it was impossible, since the steering magnets would have stripped the highly excited Rydberg atoms. With such a large background (the signal itself being very small in the threshold region), we were unable to match the resolution of the previous "survey" experiment (Donahue *et al.*, 1982). In addition, our ArF laser proved extremely difficult to set up and run; it finally produced a very weak double-detachment signal, but by the time it had done so the optics in the vacuum had degraded very seriously. (The dielectric coatings, being many years old and hygroscopic, had presumably absorbed water which evaporated and caused the coatings to blister and peel off). A very short time later, the laser power supply failed, bringing this measurement to an end.

An example of the double-detachment data is illustrated in Figure 5.12. This shows Run 850, which was probably the very best of the set; nonetheless, it was plagued by noise. The threshold appears at a little over 14.2 eV, instead of the expected 14.35 eV, because the "skinny magnet" had to be kept at a fairly high field in order to separate the proton signal from the beam "spray" , and this high field ionized the Rydberg atoms produced in the interaction. In fact, from the current in the copper rods making up the skinny magnet (about 600 amps), and from their geometry, the field was estimated to be about 100 gauss; this transforms to about 50 kV/cm in the atom's frame, which is adequate (see Appendix H) to strip $n = 10$ and above; since $n = 10$ lies 0.136 eV below the threshold, we should expect the threshold to move down by this amount, and this is consistent with what we observe here. Fits to the Wannier law are so poor that we cannot improve upon the confidence levels set in our survey experiment. The resolution is also rather low here, and since the Temkin theory is only supposed to be valid below a limit of 50-100 meV above threshold, we once again are unable to distinguish between the Wannier and Temkin models.

The ratio of double- to single-detachment cross sections was measured by using the proton detector to detect firstly the protons and then the H°'s in successive runs over the same energy range. The results are shown in Figure 13; again, they are rather noisy. These data appear to be in slight disagreement with earlier published results (Frost *et al.*, 1980), but the detectors used in the earlier measurement were somewhat liable to saturation, whereas our new detectors (see Appendix G) have an extremely wide dynamic range. Saturation in the H° detector in the previous experiment would account for the difference, as the H° signal this time around appears to be larger in comparison with the H^+ signal.

Obviously, much work remains to be done in this area. Following the tantalizing results of Lubell *et al.* (1990), it is more important than ever to determine

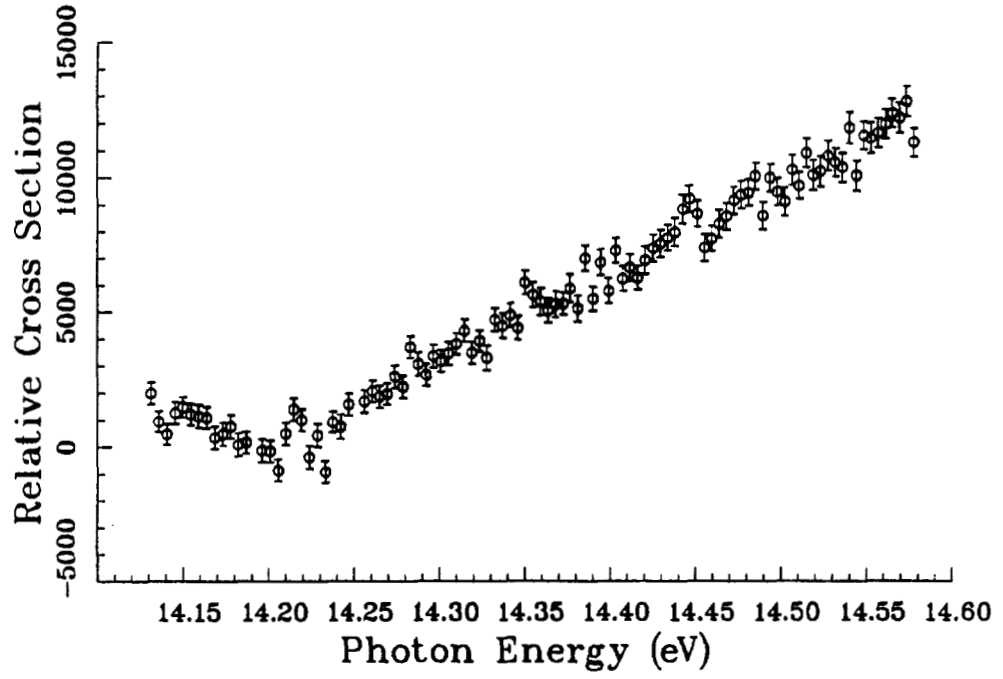

Figure 5.12. Double-detachment cross section as a function of photon energy.

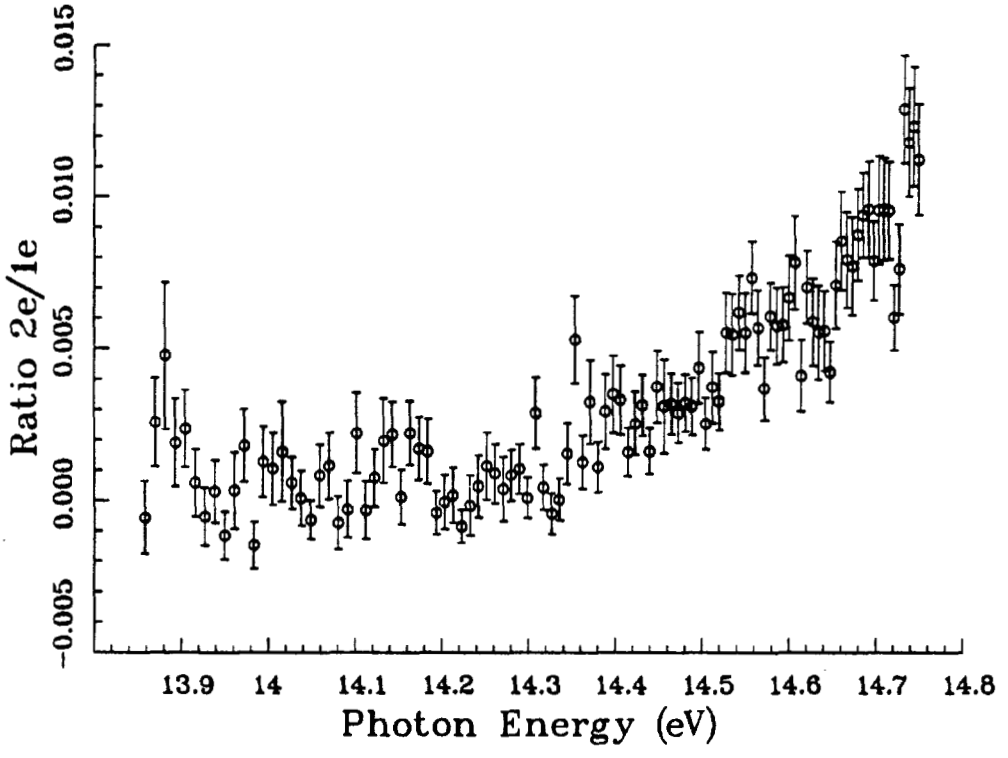

Figure 5.13. The ratio of double- to single-detachment cross sections.

the nature of the threshold law. It would also be a simple matter to apply electric fields to the interaction region to see how they modify this law. In addition, a suggestion that arose from the Second H^- Workshop at the University of New Mexico (January 1990) is to study the two-photon double-detachment process. This would allow access to the ^1S channel, which is believed to have a much larger cross section than the ^1P. Further ideas for the development of this study are presented in the following chapter.

Chapter 6

Conclusion

> 'Would you tell me, please, which way I ought to go from here?', said Alice. 'That depends a good deal on where you want to get to,' said the Cat.
>
> — Lewis Carroll, *Alice in Wonderland.*

6.1 The Outcome of the Resonance Studies.

The introduction to this dissertation included a statement to the effect that a century has passed between the first spectroscopic studies of atomic hydrogen and the current pioneering investigations of the negative hydrogen ion, which consists merely of that same atomic hydrogen with a single additional electron. Balmer discovered a simple recursion formula that predicted almost exactly the energies of the excited states of the hydrogen atom; and now, we are able to confirm a similar simple recursion formula for the energy levels of the doubly-excited states in H^-:

$$E(N,n) = E_t - \frac{R}{n^2} + 2R\, e^{-2\pi(m-n)/\alpha_n}\left[\frac{1}{2n^2} - \frac{0.696}{(n+0.333)^2}\right]. \qquad (6.1)$$

This semi-empirical formula is not a firm theoretical predictor, but it is an extremely good qualitative guide to the energies of the observed resonances. At last, serious inroads are being made in the problem of the quantum three-body system.

The doubly-excited states investigated in this study appear to be, in each case, series of Feshbach-type resonances associated with the hydrogenic thresholds below which they lie. They are due entirely to electron correlations. The good agreement with ongoing theoretical calculations of their energies seems to indicate that we are observing the lowest-lying resonances of "+" character, and their recursions. Calculations of the widths of the resonances are not so abundant, but those that are available also seem to be in good agreement with the data. Calculations of the cross sections, however, appear to be non-existent! This makes fitting the data to theory more difficult, since not only the nature of the resonances, but also the form of the underlying continuum in which they are embedded, is unknown to us.

Figure 6.1 shows the four principal data files analyzed in Chapter 4, combined by adding the continuum background found from each fit to subsequent channels. This models an "ideal" yield from the $n = 4$ threshold all the way up to the $n = 8$ threshold. In reality, structures do not appear as clearly as this over such a wide energy range, due to the large background fluctuations.

Fits of the resonances that are unconstrained yield energies that are very slightly different (a few meV) from those fit to the dipole recursion formula (which is built in to the 2e formula above),

$$\frac{E_n - E_k}{E_n - E_{k+1}} = e^{\frac{2\pi}{\alpha}} = \frac{\Gamma_k}{\Gamma_{k+1}}; \tag{6.2}$$

the quality of the latter fits are, however, considerably worse than those of the former. It is conceivable that the dipole recursion formula is not working precisely, but it also seems quite possible that the shape of the underlying continua are being distorted by the presence of weaker resonances.

The energy range included in this study was from the production threshold of $H^\circ(n = 4)$ up to that of $H^\circ(n = 8)$. (Some data were taken up to the $n = 9$

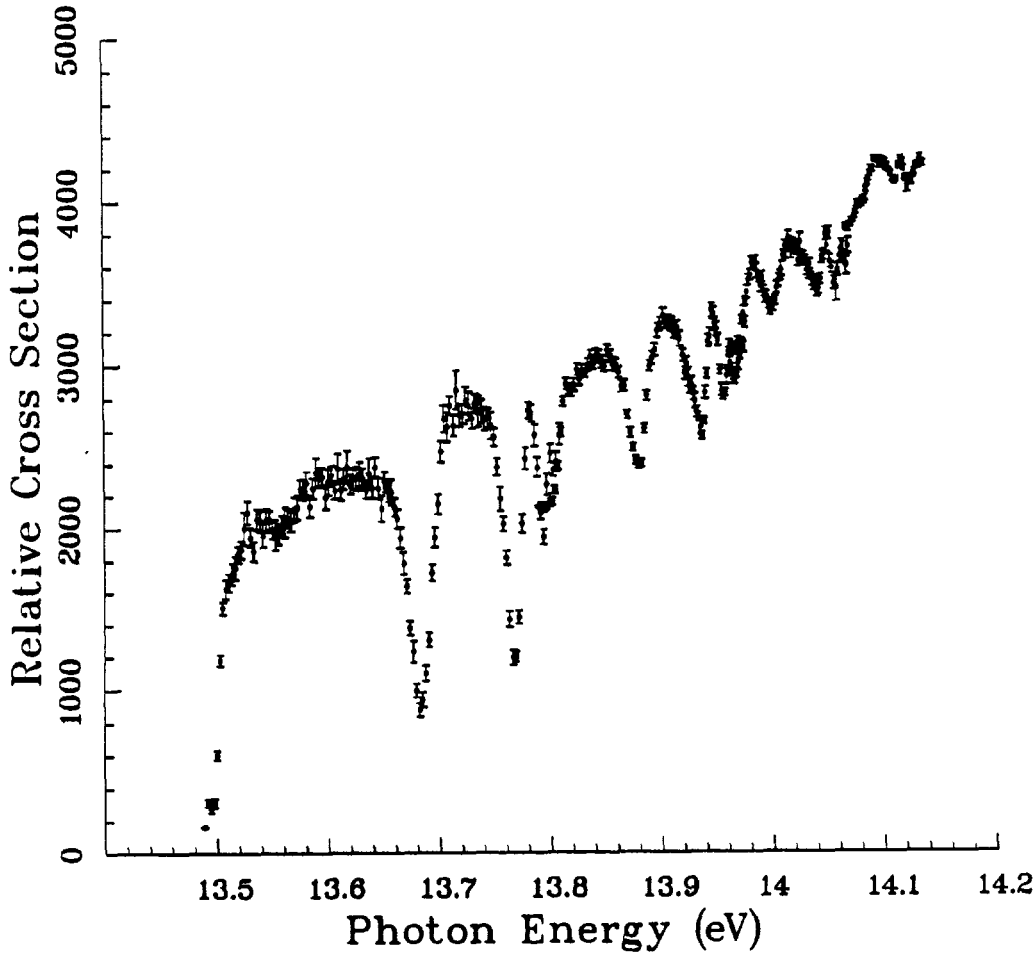

Figure 6.1. A composite picture, showing all of the data files of Figure 4.1 combined. Backgrounds have been added artificially, to show an "ideal" yield curve from the $n = 4$ to the $n = 8$ thresholds.

threshold, but the signals were too small and noisy to observe structure). The region between $n = 7$ and $n = 8$ is of particular interest; the first resonance associated with $n = 8$ lies right at the $n = 7$ production threshold, and so in channels higher than this the first resonance of each series should be "displaced" by a channel. As the high-energy limit of these resonances are the so-called Wannier ridge resonances, which eventually lead to double detachment, it would be extremely interesting to pursue them further in this direction. Future explorations could also make the link with the previously-studied resonances near the $n = 2$ and $n = 3$ thresholds, by investigating the region between $n = 3$ and $n = 4$.

6.2 Future Directions.

> *L'esprit de l'escalier.* [Staircase wit.]
> An untranslatable phrase, the meaning of which is that one only thinks on one's way downstairs of the smart retort one might have made in the drawing room.
>
> — Denis Diderot, *Paradoxe sur le Comédien.*

The clarity of hindsight was amply demonstrated in this series of experiments. With the strong emphasis on the double-detachment process, where magnetic charge separation is necessary, the possible dramatic improvements that can be made (with minimal effort) in the search for the doubly-excited resonances did not become apparent until some time after the last run was over. Instead of using field ionization to detect the excited neutral hydrogen atoms, they should be intercepted by a second laser beam, with the photon energy of this laser tuned to the transition from states n to 13, where n is the low-lying excited state under study. Our electron spectrometer, a well-understood and reliable instrument, could then field-ionize the $n = 13$ state and detect the electron thereby produced, eliminating the need for detecting the (background-limited) proton signal at all. This would have three major advantages:

1.) It would significantly extend the available range of study (in particular, to the region between $n = 2$ and $n = 4$ where the structure of the resonances changes from peak-like to dip-like).

2.) Background levels would be reduced dramatically, possibly even to zero, since the electron detector lies out to the side of the beam line and so does not intercept the heavy background particles.

3.) It would further isolate the individual channels so that, for example, above the $n = 5$ threshold the $n = 4$ channel could still be detected in isolation, thereby allowing the measurement of branching ratios of the resonances into the different channels.

Beyond this, there is also much work to be done in the study of electric field effects, in both π and σ polarized light.

The nature of the double-detachment threshold law remains undetermined, and is still the subject of fierce debate. A new technique could possibly simplify matters here as well. If a long-pulse laser were used (such as, for example, a hollow-cathode copper vapor laser), it could easily be arranged that the probability of single photodetachment above the two-electron threshold was considerably less than unity; this has been done in the past for studies near the single-detachment threshold (Stewart, 1987), when a scaler-counting technique was employed. If, however, the pulse-height distributions of the detached electrons were to be analyzed, pairs of electrons should be visible at photon energies higher than 14.35 eV, from the double-detachment process. The electron spectrometer has perfectly adequate resolution to determine the difference between "convoy" (*i.e.*, laser-detached) electrons and those produced by stripping (in the spectrometer field) of $n \leq 20$; thus, not only would the heavy-particle background that plagues the proton detector be absent, but the "zero-field limit" could be

approached far more closely than with the "skinny" magnet (which, in 1989, had a field strong enough to strip $n = 10$ and above).

This method would also be ideal for a good determination of the ratio of single to double detachment cross sections, since both signals would be detected simultaneously, with the same detector, and since at most one or two particles would be incident during a micropulse there would be no problem with saturation or lack of dynamic range.

The multiphoton detachment investigations, initially a totally new direction for the HiRAB group, may eventually provide a new tool for investigating the structure of H^-. With one photon, only the ^1P states may be reached; a two-photon transition can access both ^1S and ^1D states. This may also be important for further investigations of the double-detachment threshold law; the cross section for double-detachment into an S state is believed to be much higher than that for the equivalent P state.

Other investigations that would be of interest to theorists are, for example:

1.) "Ripples" into $n = 2$. The field-induced oscillations have only been observed at the threshold of the hydrogenic $n = 1$ state, and the structure should also appear at higher thresholds.

2.) High-field ripples. This would involve resurrection, and a little redesign, of the pulsed magnet designed by Butterfield (1984).

3.) Determination of the ratios of production of neutral hydrogen in successively higher n states, to determine the limit of validity of the $1/n^3$ scaling law (see Appendix D).

4.) High-resolution scans of the $n = 2$ Feshbach and shape resonances, to provide data to compare with recent cross-section calculations (Greene, 1990), and to look for recursions of the Feshbach resonance.

5.) A scan of the double-detachment cross section up to 21 eV in photon energy, which should be adequate to see the peak.

6.) Barely within the limits of feasibility is the possibility of using a CCD chip to detect the doubly-detached electrons; if the Wannier model is true, a (transverse) distribution of electrons may just be observable with the correct laser polarization. This technique is similar to that proposed for the study of above-threshold ionization (ATI).

7.) Probably not feasible at all is the idea of catching the elusive $^3P^e$ state (Drake, 1963), on the assumption that it may be produced in thin foils. A laser could scan in angle to promote it to a higher resonant state that could decay into $n = 2$, with an increase in yield of $n = 2$'s being detected by the two-laser scheme outlined above. (The first laser, of course, would have insufficient photon energy to produce $n = 2$'s by any other means). The $^3P^e$ state has long been sought; it is bound just 9.5 meV below $n = 2$, with parity conservation prohibiting its autoionization except through the three-body decay of photon, electron and neutral hydrogen.

It appears that each question answered by the H^- photodetachment studies opens up a range of new and interesting physics that needs to be explored. The ideas outlined above do not even include the future of the multiphoton investigations, which will be discussed by Chen-Yau Tang (1990). The H^- ion still holds many mysteries in the nature of its structure, but this latest in the long series of photodetachment studies has demonstrated most forcefully the power of the relativistic Doppler tuning technique, by confirming the simple and elegant recursive nature of the doubly-excited states and thereby justifying the techniques adopted by theorists in tackling the quantum-mechanical three-body problem. The rôle of accelerators in investigations of fundamental atomic physics seems assured for many years to come!

Appendix A

Hardware

'Give us the tools, and we will finish the job.'

— Winston Churchill.

The beamline equipment, illustrated in Figure A.1, includes apparatus for all of our current experiments. An overview is given here of each component, beginning with the characteristics of the H^- beam itself. The data acquisition hardware (*i.e.*, the computer and the interfacing electronics) will be discussed in Appendix B.

A.1 The H^- Beam and the HiRAB facility.

The half-mile long LAMPF linac consists of a 750-keV Cockcroft-Walton injector, followed by 48 accelerating modules; modules 1 to 4 utilize a 201.25-MHz drift-tube design, and the remaining 44 modules are 805-MHz side-coupled rf cavities. The temporal structure of the LAMPF beam consists of 120 macropulses per second, each lasting for up to 700 μs, and each in its turn consisting of many micropulses spaced a minimum of 5 ns apart. (It gives one pause for thought to consider that a 700 μs pulse of ions traveling at $0.84c$ has a "length" of 59 miles!) The use of choppers allows considerable flexibility in the spacing (and therefore intensity) of the micropulses, depending upon the needs of the users. LAMPF can deliver three types of beam; H^+ and H^- are high-intensity beams (typically 1 mA and 0.1 mA respectively) that normally run at 800 MeV, while

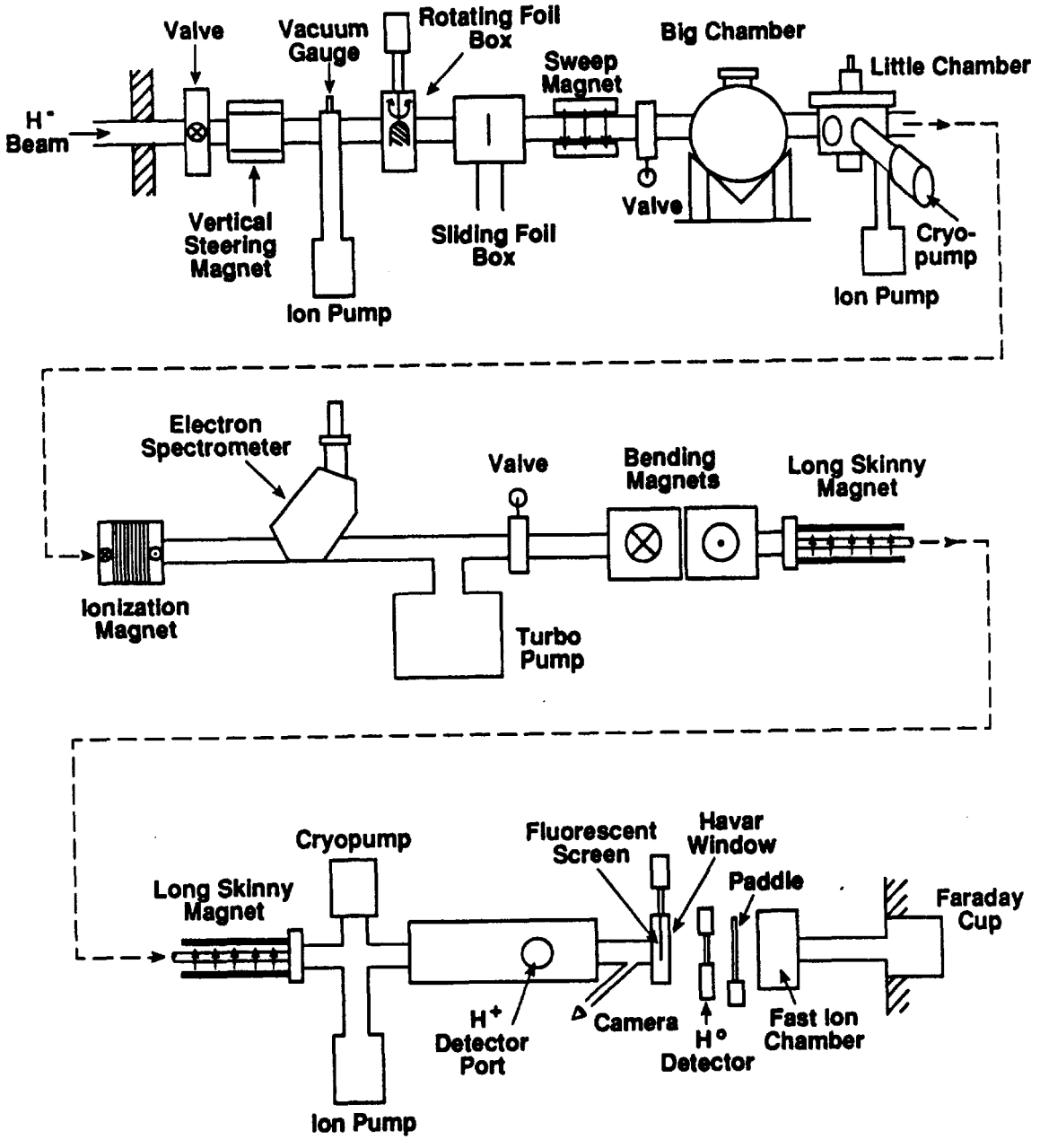

Figure A.1. Schematic diagram of beamline.

the lower intensity (average 10 nA; peak 2 μA) P^- beam (*i.e.*, H^- for which the nuclear spin is polarized) is often used at lower energies (obtained by accelerating only up through the rf module needed for the required energy, and drifting through subsequent modules). The three different beams can be interleaved on different macropulses. Operation of the LAMPF linac is outlined in more detail in McClelland *et al.* (1989).

The High Resolution Atomic Beam (HiRAB) experimental area at LAMPF (see Figures A.2, A.3) is a dedicated atomic physics facility. It normally accepts P^- beam, but, as this was unavailable in the summer of 1989 due to installation of a new optically-pumped polarized ion source (OPPIS), the H^- beam was used instead. Since the cross sections for atomic physics processes are extremely large in comparison with those of nuclear physics, very low beam currents are required. As the primary user, the temporal structure of the beam was tailored to the needs of the HiRAB facility; and so the macropulses were compressed to just 500 ns, instead of the normal 700 μs. The peak intensity of each micropulse was therefore higher, allowing the average current to be held correspondingly lower, typically in the range 1-50 pA. The kinetic energy of the beam was nominally 800 MeV, with our measurements (see appendix E) yielding an actual value of 797.3 ± 0.3 MeV mean kinetic energy, with a momentum spread of $\delta p/p = 5 \times 10^{-4}$.

The divergence of the beam in the vertical direction may be limited, by dedicated strippers, to less than 10 μradians. The necessity for extensive steering prohibits achieving a similar level of collimation in the horizontal plane.

The HiRAB facility includes a large vibration isolation slab, made of concrete on a bed of sand. Studies (McGill, 1989) have shown this to be effective in considerably reducing motion from heavy plant operations going on elsewhere, although the optical tables showed an unfortunate tendancy to resonate at low frequencies. The "clean room" atmosphere specified in the initial building contract has not yet been attained.

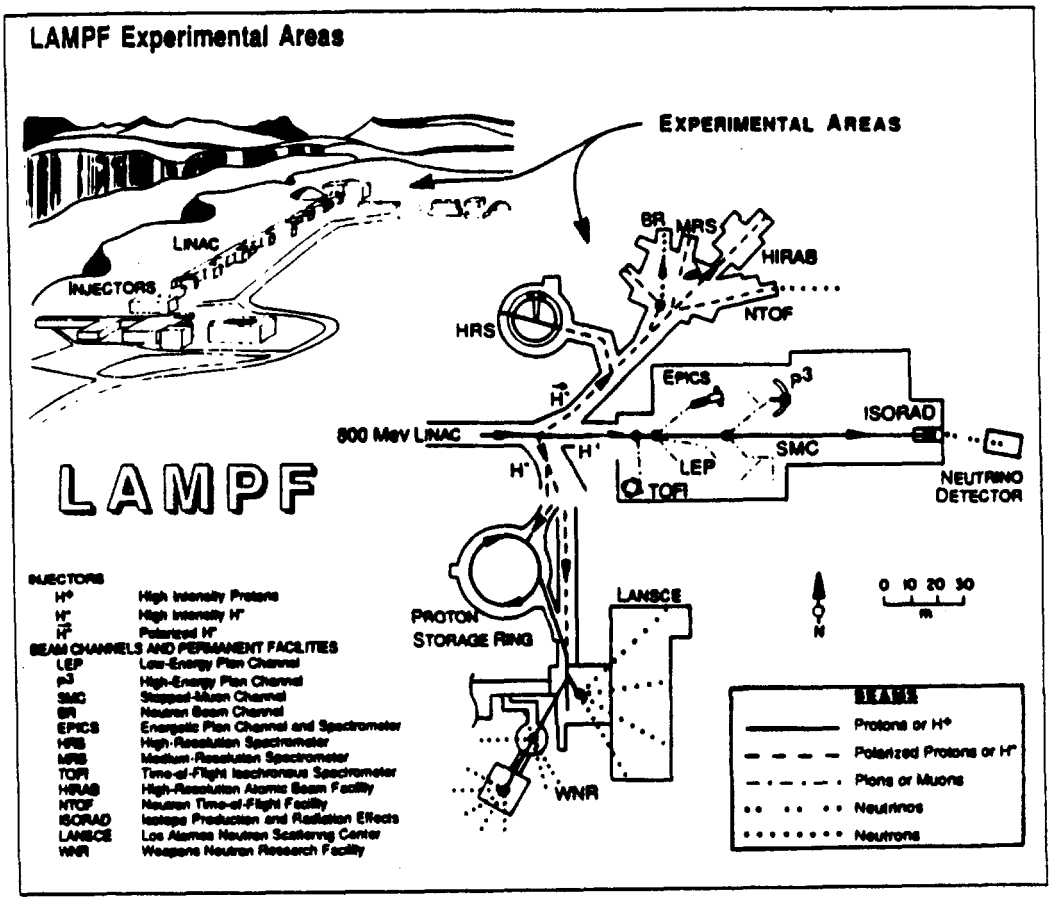

Figure A.2. LAMPF, showing the experimental areas.

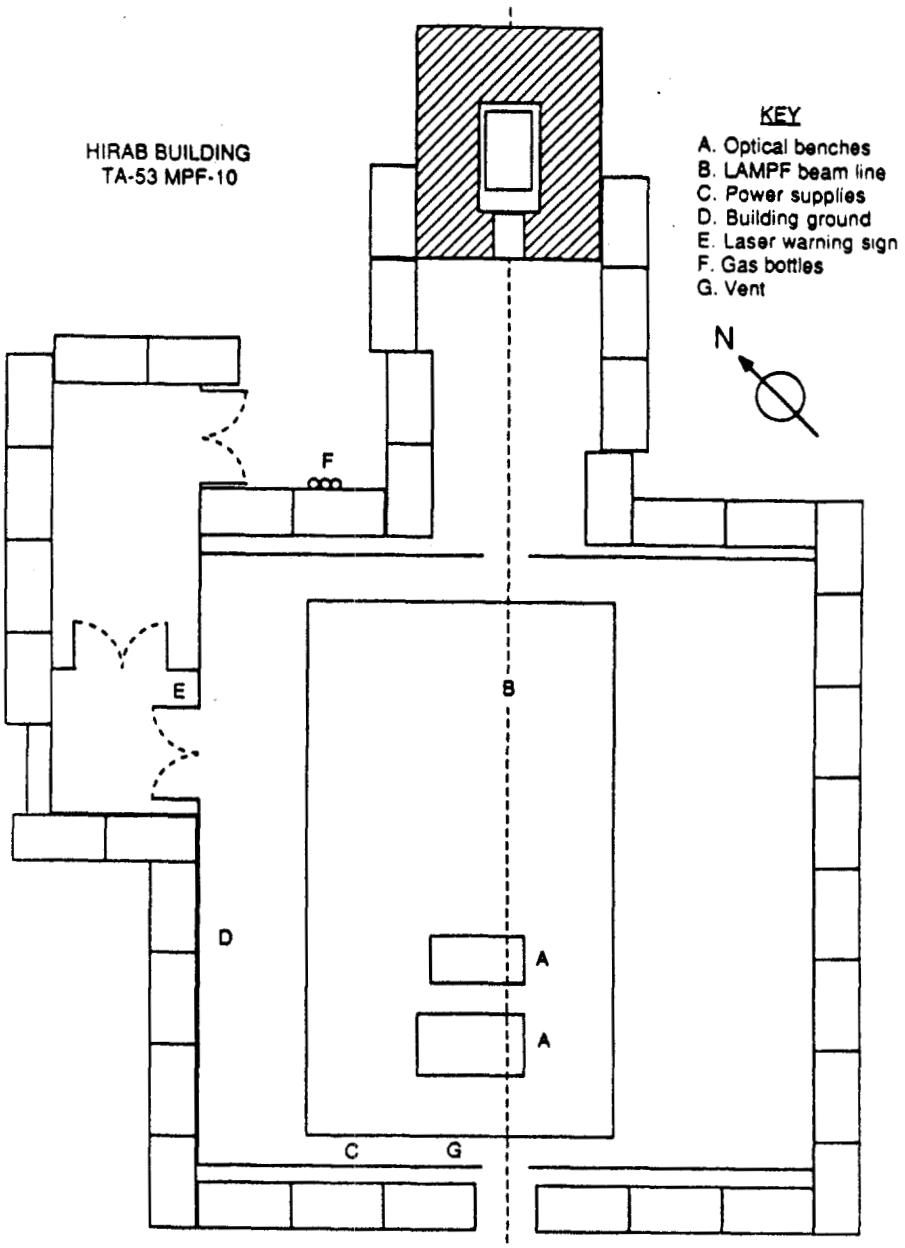

Figure A.3. The HiRAB experimental area.

A.2 Lasers and Optics.

'About light, I am in the dark.' — Ben Franklin.

Three different lasers were used during the 1989 runs — a Nd:YAG laser to look at the high-lying resonances in H^-, a CO_2 laser for the multiphoton detachment studies, and an ArF laser for the two-electron detachment experiment.

A.2.1 Nd:YAG Laser.

The resonant structures in the H^- continuum lie at energies of 10.9-14 eV above the ground state. These high energies mean that, even with the Doppler tuning facility, it is necessary to use ultraviolet photons. We used the fourth harmonic of a Spectra Physics DCR-2A Nd:YAG laser (Figure A.4). The wavelength of the second harmonic was measured (Harris, 1986) some years ago, using a grating monochromator (Perkin-Elmer E-1) previously calibrated by using the known wavelengths of spectral lines from gas discharge tubes, and found to be 532.2002 ± 0.0060 nm; this implies a wavelength of 266.100 ± 0.003 for the fourth harmonic. A long-term drift of about a wavenumber may be expected.

The laser beam is 8 mm in diameter. It has an estimated divergence of 0.5 mrad; an attempt to reduce this by using expansion optics was aborted due to the loss of intensity and consequent loss of signal. The temporal structure of the laser pulse was monitored by a fast vacuum photodiode, the output of which was observed on a fast oscilloscope.

The harmonics were separated by a quartz Pellin-Broca prism on the optical table, the ultraviolet light then following the optical train *via* a succession of dielectric mirrors (from several manufacturers, most commonly CVI) and into the larger of the two scattering chambers. Transmitting optics were all of fused quartz, as the more common glass or plastic optics absorb the ultraviolet light and are quickly damaged.

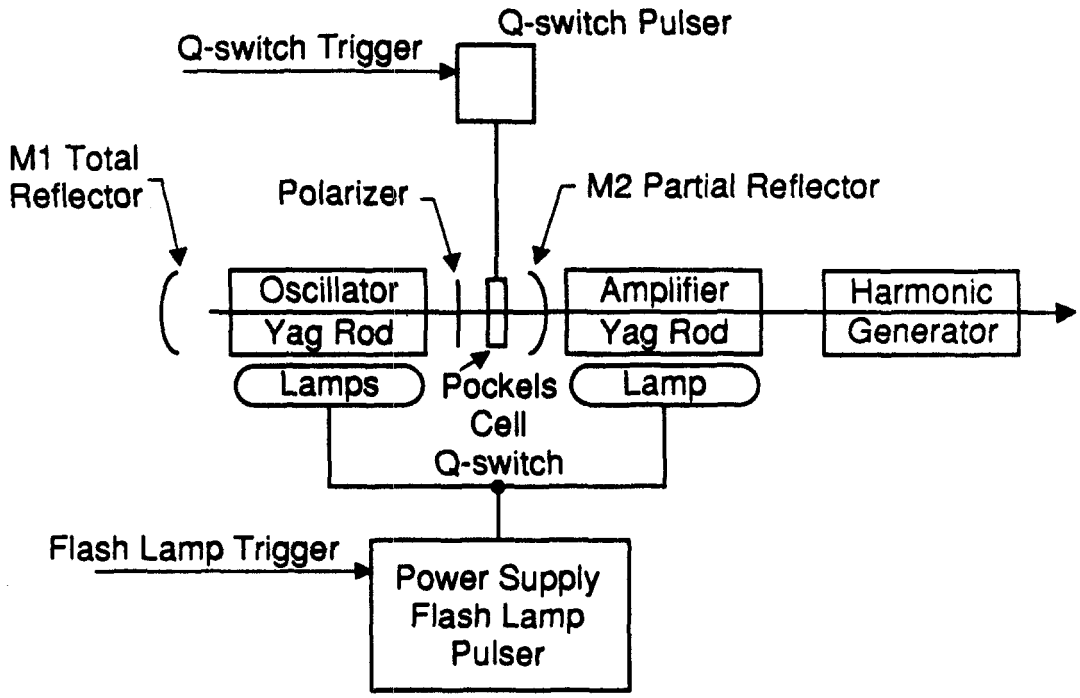

Figure A.4. Quanta Ray DCR-2 Nd:YAG laser.

Because the non-linear nature of the harmonic generation process requires that high intensities be used, the laser had to be Q-switched; this involved pumping the lasing medium with the flashlamps, but reducing the Q-value of the oscillating cavity (and thereby prohibiting lasing) until the gain was optimized (see, for example, Milonni and Eberly (1988)). The Q-switch itself is a Pockels cell, which rotates the plane of polarization of the light away from that favored by the optical cavity (thus acting like a crossed polarizer) while a high voltage is applied to it. This prevents spontaneously emitted photons from "resonating" in the cavity and depleting the gain medium by stimulated emission. Thus, the high voltage is applied to the Q-switch as the flashlamps are triggered, and when, some 3 ms later, the population inversion has reached its maximum, the high voltage is

turned off; the cavity then becomes resonant, and all of the laser light is emitted from the cavity in a short intense burst of duration 8-10 ns. A single-pass amplifier, also consisting of a flashlamp-pumped Nd:YAG rod, boosts the energy of the pulse to 700 mJ for the fundamental frequency, a 10% conversion efficiency giving 70 mJ/pulse in the fourth harmonic.

A.2.1.1 Harmonic Generation.

A crystal of ammonium di-hydrogen phosphate (ADP), with its surfaces cut to Brewster's angle, is used to generate the second harmonic (564 nm). The electrons in the crystal are in an anharmonic potential well, and so the restoring force F that they experience has a term $k_1 x^2$ proportional to the square of their displacement from equilibrium, in addition to the usual linear term $k_o x$. Thus, if the incident wave is represented by $E_0 \cos(\omega t)$, the polarization — the dipole moment per unit volume — will contain terms proportional to $k_1 E_0^2 \cos^2(\omega t) = k_1 E_0^2 (1 + \cos(2\omega t))/2$; in turn, the polarization acts as a source for a contribution to the field E, from the Maxwell equation

$$\nabla^2 E - \epsilon_0 \mu_0 \frac{\partial^2 E}{\partial t^2} = \mu_0 \frac{\partial^2 P}{\partial t^2}. \tag{A.1}$$

Since the polarization P contains terms proportional to twice the frequency of the incident wave, an electric field at this second-harmonic frequency 2ω is generated.

Second harmonic generation is a special case of *three-wave mixing*, in which two waves of frequencies ω_1, ω_2 are added to produce a third wave of frequency $\omega = \omega_1 + \omega_2$ (sum-frequency generation) or $\omega = \omega_1 - \omega_2$ (difference-frequency generation). The third and fourth harmonics are generated in a similar manner, by mixing the fundamental with the second harmonic and by doubling the second harmonic respectively.

The crystals, in particular the fourth harmonic generator, are sensitive to the angle of the incident laser beam, since the incident and second harmonic wave

must be phase-matched; *i.e.*, the refractive index of the crystal must be the same for both incident and generated wave. Since the refractive index is a function of frequency, this is normally a difficult requirement to meet. It is achieved here by making the incident field the extraordinary wave (*i.e.*, polarized parallel to the plane defined by the optic axis and the direction of propagation) and the generated wave the ordinary wave (perpendicular to this plane) in ADP, which is a negative-uniaxial crystal. The refractive index for the extraordinary wave n_e has an angular dependence

$$\frac{1}{n_e^2(\omega,\theta)} = \frac{\cos^2\theta}{n_o^2(\omega)} + \frac{\sin^2\theta}{n_e^2(\omega,\pi/2)}, \tag{A.2}$$

where n_o is the refractive index for the ordinary wave, and phase-matching occurs when θ is chosen such that

$$n_o(2\omega) = n_e(\omega,\theta). \tag{A.3}$$

The tuning of the angle θ was done by turning the ADP harmonic-generation crystals remotely with a pair of stepper motors.

Harmonic generation and three-wave mixing are discussed in more detail in Eberly (1988) and Yariv (1985).

A.2.2 CO_2 Laser.

The CO_2 laser, described fully elsewhere (Tang, 1990), was used for the multiphoton detachment experiments, as its low photon energy (0.1 eV in the lab) lay far below the 0.7542 eV needed to photodetach H^-. It consisted of an oscillator (Tachisto model 215) and an amplifier (Lumonics model TEA-103-2); it was pulsed at 0.5 Hz. To reduce fluctuations in laser intensity, a gain cell (smoothing tube) was incorporated into the oscillator. A salt (NaCl) window was used to admit the light to the Little Chamber, where a ZnSe lens focused it and copper mirrors directed it to the interaction region.

A major problem with this laser that could not have been foreseen was its sensitivity to radiation. The higher the H^- beam current, the more often would the laser misfire; sometimes, more than 50% of the shots did not lase properly, due to radiation-induced breakdown of the high voltage across the electrodes in the lasing medium. Following a survey (Altman, 1989) of the radiation levels in the room, the amplifier was moved to a position in which activity levels were lower, which reduced but did not eliminate the problem.

A.2.3 ArF Laser.

It had been hoped that a comprehensive survey of the double detachment cross section up to 7 eV above threshold might be carried out, and to this end an ArF excimer laser (Lambda Physik model EMG 150 ET; see Figure A.5) was set up. This laser has a wavelength of 193 nm, which is sufficiently small to provide Doppler-tuned photons of energy up to 21.5 eV. (The photo-double-detachment cross section is believed to peak at about 18 eV, as discussed in section 5.4; this has never been observed). However, problems with the laser power supply and degradation of the optics in the vacuum, together with small signals on high backgrounds, prevented this measurement from being carried out at this time.

The name "excimer" is an abbreviation for "excited dimer". The gain medium consists of two gases, one normally inert (argon), the other (fluorine) extremely reactive. When the mixture is excited, by an electrical discharge, molecules may form which are a compound of argon and fluorine in an excited state; there is no ground state, so de-excitation is immediately followed by dissociation. This system has the very useful property that as soon as any ArF molecules are formed, there is a population inversion, and lasing may take place.

The Lambda Physik EMG (excimer multi-gas) 150-ET laser is an oscillator-amplifier pair. The oscillator forms a small, low-power beam that may be tuned to give a narrow linewidth with good characteristics, which is then used to "seed"

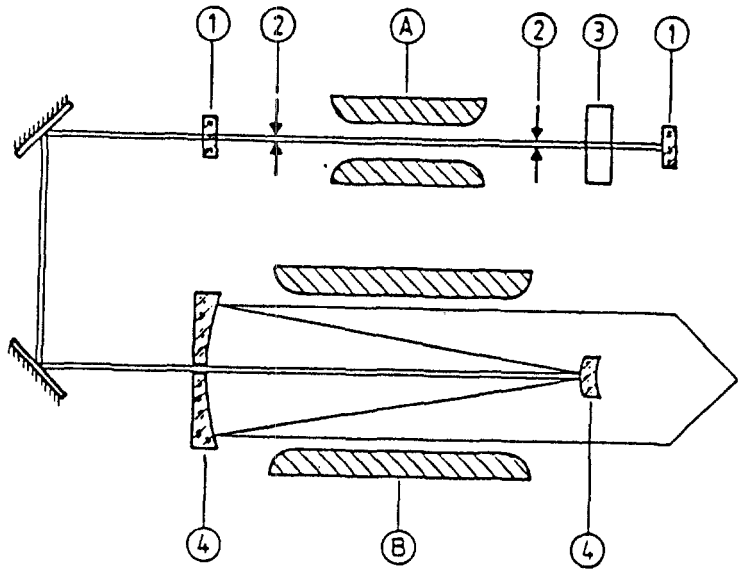

Figure A.5. Lambda Physik ArF Excimer Laser, showing components (A) oscillator, (B) amplifier, (1) oscillator mirrors (the rear mirror being replaced by a grating in our system), (2) apertures for limiting the oscillator diameter, (3) dispersive element (prisms), and (4) amplifier mirrors.

the amplifier. The amplifier itself is a triple-pass cavity that expands the beam to a size of approximately 1 cm × 3 cm, increasing its power correspondingly. The output pulse then has an energy of up to 250 mJ.

The gases have a very limited lifetime; contamination cuts the power by a factor of two within $\sim 10^4$ shots. In order to overcome this problem a cryogenic purifier, consisting essentially of a pump, a filter and a dewar flask filled with liquid nitrogen to freeze out the contaminants, was fitted to the oscillator.

The excimer laser also required a venting system, consisting of an exhaust fan on the roof of the HiRAB building (with a volume of $\geq$ 150 liters/min.) and flexible tubing, eight inches in diameter, connecting the laser head to this fan in order to provide cooling for the thyratron. A similar system was used to vent the cupboard outside the building in which the fluorine cylinder (a 5% fluorine mix with helium) was stored.

It is hoped that at some time in the near future this system may be used successfully to thoroughly explore the double-detachment cross section, especially as the possibility of structure above the threshold now seems less remote (Lubell, 1990; see also the discussion in section 5.4).

A.3 Foils.

Two specially designed vacuum boxes held our neutralizing foils. In the first, the so-called "rotating-foil box", a Formvar foil (of thickness 45 $\mu g/cm^2$, mounted in a stainless steel frame) was attached (*via* a steel shaft and a vacuum feedthrough) to a pair of actuators. This allowed the foil to be put into the beam-line remotely, and, once there, to be rotated through an angle of 30°, effectively varying continuously its thickness as seen by the H^- ions.

The second, "sliding", foil box worked on a principle similar to that of a slide-projector feeding mechanism. It contained eighteen carbon foils of varying thicknesses (from 19 $\mu g/cm^2$ up to 300 $\mu g/cm^2$), a fluorescent screen, and a wire cross hair used for alignment purposes. All were mounted on brass frames, which fitted in a purpose-built aluminum magazine. The entire magazine could be moved to and fro, sliding on a pair of rails and powered by a remotely controlled stepper motor, which was connected *via* a (ferrofluidic) rotary vacuum feedthrough and a worm gear assembly. Once in place, the chosen foil was moved into and out of the beam by a hooked brass arm, actuated by a similar system of stepper motor, feedthrough and gears. A pair of potentiometers measured the positions of the slide magazine and the arm. In addition, a plexiglass window in the top of the box made possible the use of a television camera to view the foils and, in particular, the fluorescent screen.

A.4 Big Chamber.

The "Big Chamber" is the first of the two laser-H^- beam interaction chambers. Inside it, a mirror system known as the "spider", consisting of three (one

inch, 45° angle-of-incidence) dielectric mirrors, is mounted on an optical bench; this in turn is attached to a turntable, allowing rotation in the vertical plane. The laser beam follows the axis of rotation — horizontal, and perpendicular to the H^- beam — into the chamber, where the first mirror deflects it off to one side; the second mirror turns it to become parallel to the axis, and the third turns it in to the point where the axis of rotation intersects the H^- beam. Rotation of the turntable thus changes the angle of intersection of the laser and particle beams, providing the Doppler tuning as illustrated schematically in Figure 3.1.

The turntable is belt-driven. The 0.5 in. wide steel belt, made from 0.005 in. annealed stainless steel 304 shim stock (International Foils) cut to length and laser-welded, passes around a 1.000 in. drive shaft, giving the turntable a 10-to-1 step-down gear ratio. The shaft, coupled to a vacuum feedthrough, is driven by a stepping motor (200 steps per revolution) *via* a 100:1 gearbox. The motor takes a total of 2×10^5 steps per revolution of the spider, which is equivalent to a step size of 31 μradians.

A 14-bit encoder (BEI model 5V 242 BX), also coupled to the turntable by a steel belt, measures the angle with a nominal precision equal to the 31 μradian step size. In 1988, the number of encoder steps for a complete revolution was measured, and found to be 198777.7, by aligning a mark on the spider with the cross-hair in a telescopic sight and turning the turntable until the mark lined up again. This figure implies an average of 552.16 steps/degree, but over any given region there will be some variation from this figure from bearing runout. Because the encoder makes 12.2 revolutions as the spider turns around once, it is also necessary to specify the "sector", as measured with a potentiometer connected to the drive gearbox, to determine the angle absolutely.

The Big Chamber was originally designed for rotation in the horizontal plane. However, the H^- beam at the HiRAB facility may achieve a divergence in the

vertical of better than 10^{-5} radians; by turning the chamber on to its side and allowing the plane of intersection of the beams to be in the vertical also, the low divergence of the particle beam could be used to obtain the optimum resolution. An additional benefit was that the optical alignment was simplified considerably with the chamber on its side.

A pair of polished steel plates with a 1.00 cm separation could be remotely inserted to surround the interaction region. Computer controlled high voltage power supplies were used to provide an electrostatic field (up to 100 kV/cm, barycentric frame). One of the plates also had a small fluorescent screen attached to aid in the alignment of the particle beam.

A.5 Little Chamber.

'We haven't the money, so we've got to think.' — Lord Rutherford.

A small scattering chamber was designed and built specifically for the multi-photon detachment experiment. A large, high-precision chamber had been anticipated, but financial considerations postponed its construction and forced us to build another to take its place. The requirement that the new chamber be ready very quickly and at minimum cost constrained the design to a simple system based on the earliest such scattering chamber in use by the group.

A pair of copper mirrors was mounted on a rotatable frame, supported from the top of the chamber. Laser light from the CO_2 laser entered along the axis of rotation of the mirror assembly through a NaCl window at the bottom of the chamber, and, after passing through a meniscus lens, was reflected by the first mirror off to one side, then making an angle of 65° with the vertical; the second mirror directed the light horizontally back towards the axis, where, in the focal plane of the lens, it intercepted the H^- beam. Rotation of the rigid mirror frame — again known as a "spider", from the appearance of the original version as

it hung from the lid of its chamber — changed the angle of intersection of the laser and particle beams, allowing the Doppler tuning of the photon energy. The system is illustrated schematically in Figure 5.1.

The following are some of the features incorporated in the new "Little Chamber":

i) The spider itself was a rigid aluminum box-section construction, which supported two-inch copper mirrors. It also held the (10 in. focal length, ZnSe) meniscus lens in position so that the laser beam was brought to a focus right at the axis of rotation. The original spider, a brass strip on which two light one-inch mirrors were mounted, had disappeared many years ago.

ii) An optical encoder was obtained for measuring the angles. This had a resolution and accuracy of 1.5 mrad, considerably less than the divergence of the laser beam itself. (A potentiometer had been used in our earlier multiphoton detachment survey experiment).

iii) Most importantly, access was improved. The optical alignment was critical, with the laser beam focused down to a waist of less than 1 mm, and the H^- beam having a diameter of only 2-3 mm. The previous technique involved lifting the lid of the scattering chamber, doing the alignment, and hoping that when the lid was put back down the alignment was still true. The new chamber had six-inch ports, so that all of the optics could be reached when in place, albeit somewhat awkwardly. Along with the improved access came improved visibility; one of the ports was covered with a piece of plexiglass, through which a camera allowed remote viewing, previously impossible.

iv) A small fluorescent screen could be remotely inserted into the interaction region. This greatly facilitated alignment of the two beams. The use of such screens, first introduced just two years ago, has now become a standard time-saving technique in our group.

v) A pair of electro-polished steel plates, of diameter 7 cm and with a 1 cm separation, was supported around the interaction region. Each was electrically connected via a vacuum feedthrough to a high-voltage power supply, so that an electric field of up to 60 kV/cm (100 kV/cm in the rest frame of the H^- ion) could be applied.

The spider was fixed to the axle of a rotary vacuum feedthrough. This was turned by a computer controlled stepper motor, coupled to the feedthrough shaft by a precision 100:1 gear box. Twenty thousand steps of the motor turned the spider through 360°. The computer was programmed to turn a half wave plate, mounted underneath the chamber, at half the rate of the spider, thus keeping the plane of polarization of the laser constant in the interaction region.

Also rigidly attached to the feedthrough shaft was the optical encoder (Renco model 25AE-12CG-7A3-1P6/C3-CCW). This was a 12-bit absolute encoder; its readout was in Gray binary, and it is an interesting exercise to convert this to natural binary. This is discussed in Appendix C.

Although the Little Chamber had some teething problems — in particular, a loose mechanical connection between the spider and the shaft to which it was mounted, and the fluorescent screen not quite passing through the axis of rotation — these were ironed out towards the end of the summer, when it was able to make a significant contribution to the multiphoton detachment studies.

A.6 Electron Spectrometer.

The electron spectrometer (Stewart, 1987) is arguably the most versatile and valuable of our detectors. It consists of a magnet designed to steer electrons out of the ion beam, through a very thin Havar window and into a scintillator. However, sufficiently excited neutral hydrogen atoms are also stripped in the magnetic field (which is perceived as a strong electric field in their rest frame). The electrons

produced are then steered into the scintillator. Thus, by changing the field of the spectrometer, we may detect either free — "convoy" — electrons traveling along with the beam, or excited (Rydberg) H°'s. The range of sensitivity of the spectrometer is from $n = 10$ upwards. If a slit is used to restrict the entrance aperture of the scintillator, the spectrometer may be tuned to be selectively sensitive to a particular excited state, although there is sufficient overlap of the magnetic substates that the peaks for $n = 14$ and above tend to merge. Figure A.6 shows a typical scan of the electron spectrometer field with a foil in the beamline; the "convoy" peak is clearly shown, along with the distribution of excited neutral hydrogen states (see Mohagheghi, 1990). The field in the spectrometer was computer-controlled, and was monitored by a Hall-probe magnetometer.

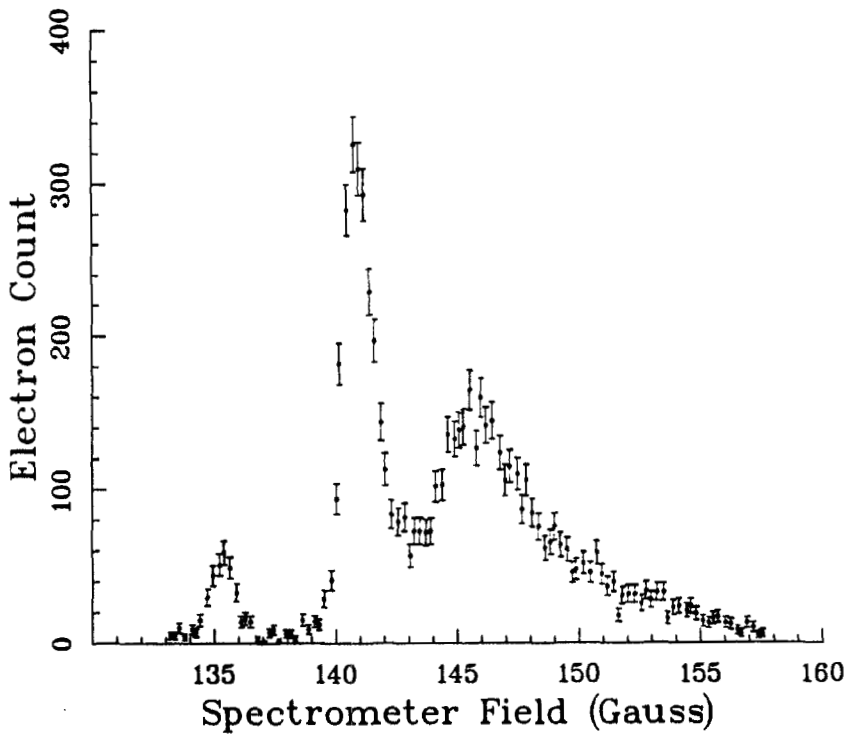

Figure A.6. Electron spectrometer scan, with a 19.3 $\mu g/cm^2$ foil; from the left (low field) are visible the "convoy" peak (free electrons traveling with the beam), the H°($n = 11$) peak and the broad H°($n = 10$) peak. Higher excited states have previously been stripped by the sweep magnet (set at 70 gauss).

A.7 Magnets.

There were a number of magnets present in the beamline; each is listed here with a short explanation of its purpose.

i) HISM2-X and -Y. These steering magnets are in fact just upstream of the HiRAB area; they are controlled from the Central Control Room (CCR), in the first instance to steer the beam down our line during the initial tuning, and thereafter under our direction as required to make small corrections to the steering. The long lever arm between these magnets and the interaction region makes them ideal for displacing the beam while minimizing the angular displacement, to which the Doppler tuning of the lasers is sensitive. (The initials HISM indicate a HiRAB steering magnet; the designation 2 comes from there being another set, HISM1, some way upstream).

ii) Vertical steering magnet. Used in conjunction with HISM2Y, this allowed us to make essentially parallel displacements of the H^- beam. It also provided a much more flexible response to changing vertical steering needs, as it was controlled directly from the HiRAB counting house (as were the remaining magnets in our beamline). Another important function served by this and the "Gram" magnet, together with the HISM2 magnets, was to steer the H^- beam clear of the neutral hydrogen and protons produced upstream by collisions with residual gas.

iii) Gram magnet. This magnet provided horizontal steering, and also separated the H^- beam from the residual-gas stripped background beams; it is often referred to as the *sweep magnet* for this reason. Located downstream of the foil boxes, it is also capable of field-stripping any high Rydberg atoms produced in the foil; so, if the laser is tuned to excite $H^{0*}(n = 4)$ to $H^{0*}(n = 16)$, say, we can be sure that the $H^{0*}(n = 16)$'s we detect in the electron spectrometer are not foil-produced.

iv) Ionization magnet. Designed to produce a strong horizontal magnetic field over a short region of space, i.e. a large **B** with a small $\int \mathbf{B}.\mathbf{dl}$, this magnet could strip the electrons from laser-excited neutral hydrogen atoms of $n = 6$ and above, while minimizing the steering of the beam. It had a compensating pole-piece to offset any steering that did take place; and furthermore, as the field was horizontal, it steered only in the vertical, to which our detectors were not especially sensitive.

v) Bending Magnets. These magnets performed the same function as the ionization magnet, but their higher fields (approximately 4 kG) allowed stripping of $H^{\circ}(n = 4)$. Their residual fields were too large for the higher Rydberg states, and so they were removed from the beamline when necessary and the ionization magnet was used instead.

vi) Long Skinny Magnet. In order to study the double-detachment threshold, a means of separating the signal protons from neutral hydrogen atoms without field-ionizing the highly excited neutrals was required. A long magnet was therefore employed, the weak field of which could gently tease apart the three charge species. This magnet consisted of four copper rods running parallel to the beamline, each on the corner of a square concentric with the beam line as viewed in cross section; each rod, 21 ft. long, carried a current so as to produce a vertical (upward) magnetic field. It resembles an extremely stretched pair of Helmholtz coils, as illustrated in Figure 3.1. In reality, background problems limited the threshold study, and so this magnet was usually run at a fairly high current in order to maximize the separation of the three beams.

As mentioned above, with the exception of the HISM steering magnets, all of these magnets, in addition to the electron spectrometer, were controlled from the HiRAB counting house; this sometimes led to a certain amount of confusion!

The latter two magnets — the long skinny magnet and the bending magnets — were powered by a Dual Transrex high current supply (up to 750 and 500 amps respectively) which, unfortunately, had an unreliable regulator; and so, despite heroic efforts by the power supply technicians, the current in the skinny magnet in particular was prone to sudden jumping at certain current settings, the number of which grew rapidly throughout the summer.

A.8 Detectors.

Photomultiplier tubes in combination with fast organic scintillators were used for detection of electrons, protons and neutral hydrogen atoms. Both the H^+ and H° detectors were on actuators that allowed remote positioning in the transverse horizontal direction; in the case of the H^+ detector, the scintillator itself was in the vacuum, and a light guide passed through the vacuum seal to the photomultiplier.

In anticipation of the need for a wide dynamic range — a single pulse might contain one signal particle, or it might contain a hundred or more — highly linear phototubes (Amperex XP2203B) were obtained. Details of the tube and of the base circuit are included in Appendix G.

The H° detector, which was outside the vacuum (the H° beam had to pass through a Havar window before reaching the scintillator), had a phototube at either end of the scintillator, one being kept at a higher voltage than the other to give a still wider dynamic range.

A.9 Beam Current Monitors.

The photodetachment yield is obviously directly proportional to the current of the H^- beam; it is therefore important to monitor both short- and long-term fluctuations in the beam current. The primary normalization to beam current is done with a Faraday cup (see R. J. Barrett *et al.*, 1975). The absolute charge collection efficiency of this device is better than 1%. A current digitizer (Ortec

model CD 1010) emits a pulse whenever the cup collects 100 pC. During the experiment, the angle of intersection of laser and particle beams was changed whenever the number of such pulses — referred to as the "number of Faraday cups" — reached a preset figure.

The Faraday cup measures integrated current, for on-line normalization; however, it is also important to account for pulse-to-pulse variations in intensity. For this purpose, we employ a fast ion chamber (FIC), which contains three wire grids at high voltage in a hydrogen-filled container (Yuan, 1987); as the beam travels through, the ions produced create a shower, generating a current which passes through a resistive load. A voltage-to-frequency converter then puts out a series of pulses that are counted by a scaler in the CAMAC crate (see Appendix B), to provide a measure of beam current on the timescale of a macropulse.

In addition, a scintillator/phototube combination (the "paddle") allowed observation of individual micropulses. In the end, this latter method proved somewhat unreliable; we believe that the scintillator was unable to respond properly to, and may in fact have been damaged by, the full current of the H^- beam, which was focused to a spot only 2-3 mm in diameter. However, it was still useful for providing timing information, and to confirm the presence of the micropulses.

A.10 Vacuum Pumps and Gauges.

In order to minimize backgrounds from collisional stripping of H^- with residual gas, it was necessary to keep the pressure down to the $10^{-7} - 10^{-8}$ torr range. Unfortunately, the only vacuum gauges available to us were cold cathode gauges, which were not capable of measuring below 10^{-7} torr; however, fairly low currents in the three ion pumps in the line — one by the foil boxes, one on the Little Chamber and one downstream of the skinny magnet — assured us that the vacuum was in fact in the desired range. In addition, two cryogenic pumps were employed, also attached to the Little Chamber and to the beam pipe downstream

of the skinny magnet. As far as possible, only vacuum compatible materials were used in the scattering chambers, although the necessity for providing insulators for the high voltage plates meant that a little plastic was present.

Appendix B

Interfacing Electronics

Fast digital electronics are needed to act as an interface between the computer and the experimental hardware. These electronics fall into two categories; firstly, the Nuclear Instrumentation Modules (NIM) consist of logic units, discriminators, delays, and so on for hardware signal processing and for timing, and secondly the Computer Automated Measurement And Control (CAMAC) system, connected to the computer itself (a DEC microvax II) via a so-called micro-programmable branch driver (MBD). The CAMAC "crate" is a box designed to hold up to 23 modules, including the analog-to-digital converters (ADC's), scalers, and units for computerized control of stepper motors, magnet currents and so on. The crate provides power for these units, and also provides a gateway for data and instructions to flow to and from the computer. The computer itself writes processed output to data files, writes the raw data to magnetic tape (or accepts such data from the tape in REPLAY mode), and interacts with the user through a terminal. Figure B.1 shows the connections between these various components.

Although the details of the NIM circuitry changed according to the needs of the current experiment, the basic "generic" setup is outlined below and illustrated in Figure B.2; the progression of signals and logic gates through this circuitry is illustrated in Figure B.3. A thorough discussion will appear in another dissertation (Mohagheghi, 1990).

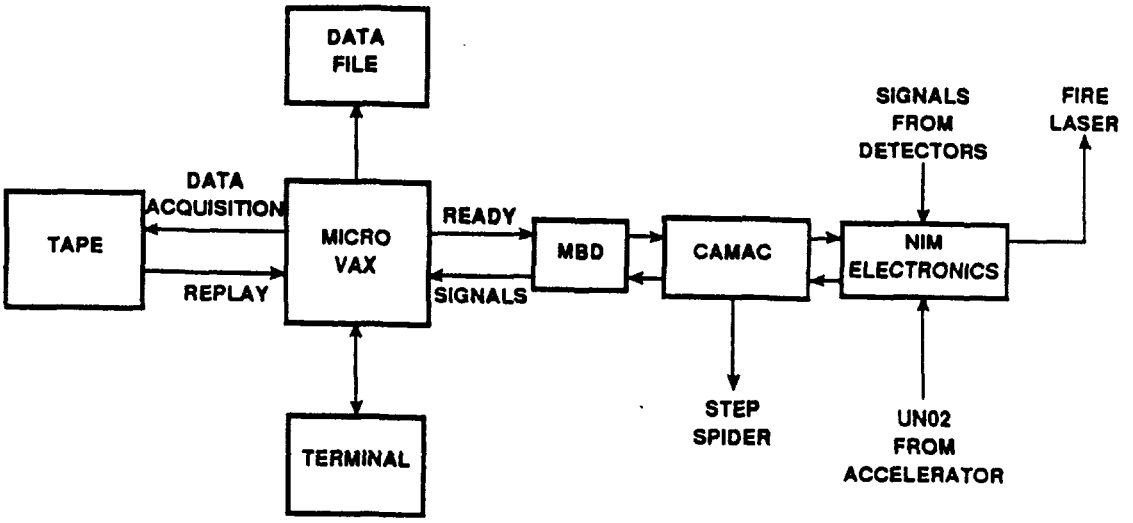

Figure B.1. Block diagram of major components allowing computer control of the experiment.

B.1 Laser timing control.

As discussed in Chapter 3, the timing of the laser pulse is critical, as the laser beam must overlap the H^- beam temporally as well as spatially. A signal — UN02 — from the central control room (CCR) tells us when the macropulse is on its way; the laser flashlamps are then fired 3 ms before the H^- pulse is expected to arrive. With the signal from the "paddle" scintillator telling us that the pulse has reached the experimental area, the laser Q-switch is triggered (after a delay that may be varied by the experimenter), allowing lasing to occur within the macropulse. At times, the H^- micropulses may have a spacing of up to 4 μs; in this case, the delay in the Q-switch trigger is critical, as the (8 ns long) laser pulse must reach the interaction region coincidentally with a specific micropulse. Jitter in the trigger circuitry of up to 5 ns makes this an unreliable mode of operation. A 5 ns micropulse spacing, with a macropulse length of 500 ns, was used throughout the high-lying resonance studies.

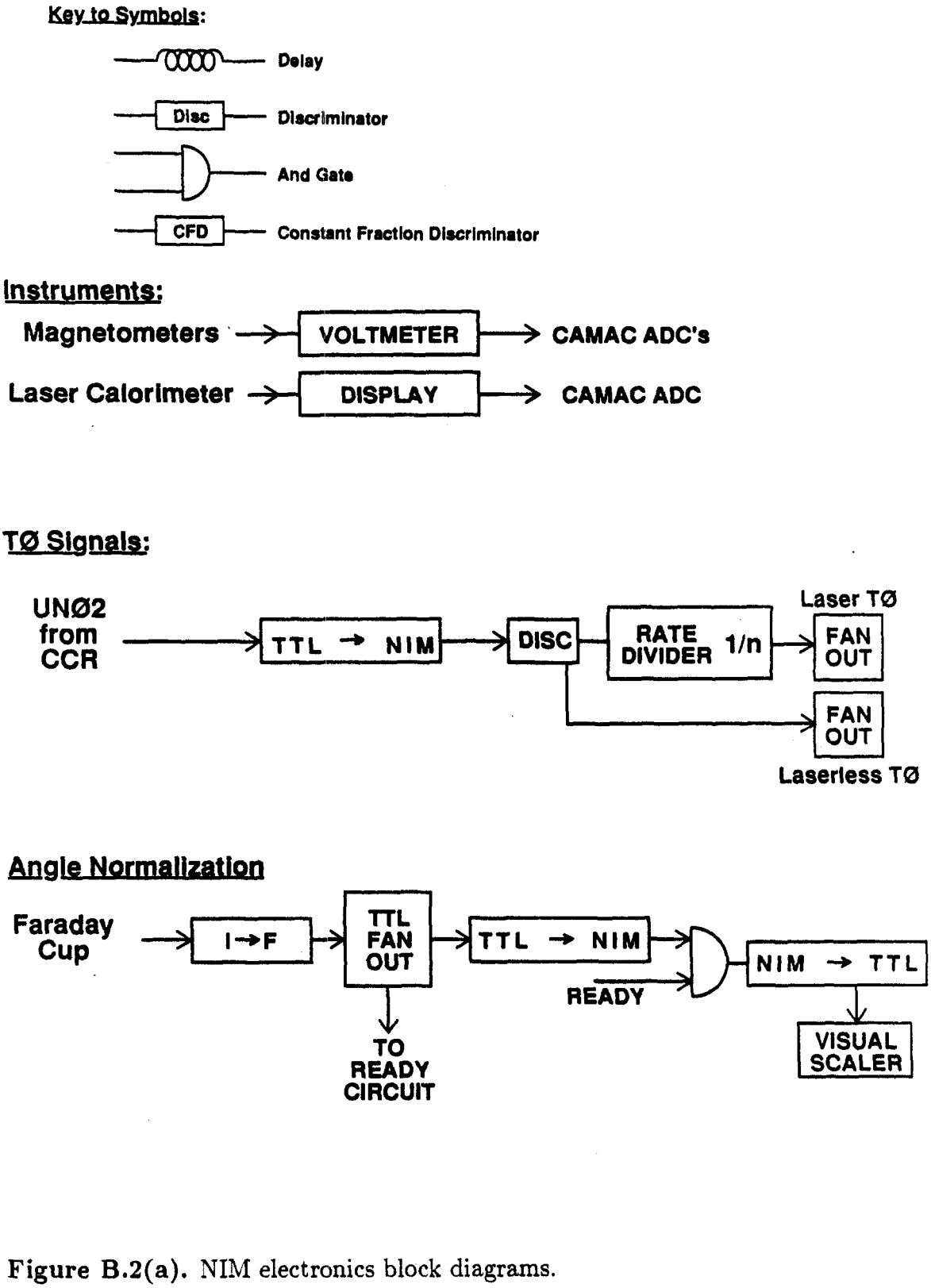

Figure B.2(a). NIM electronics block diagrams.

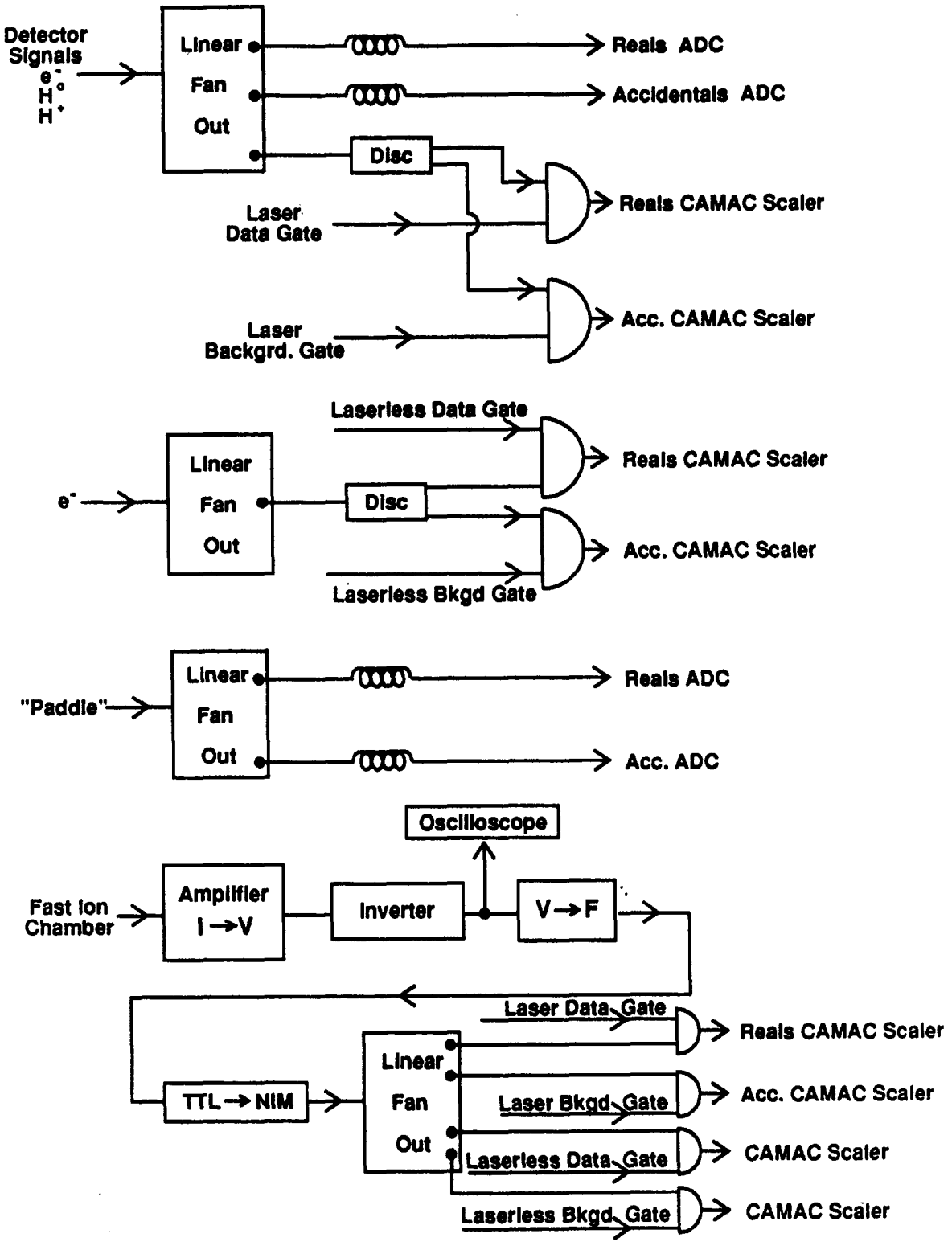

Figure B.2(b). NIM electronics block diagrams (cont.).

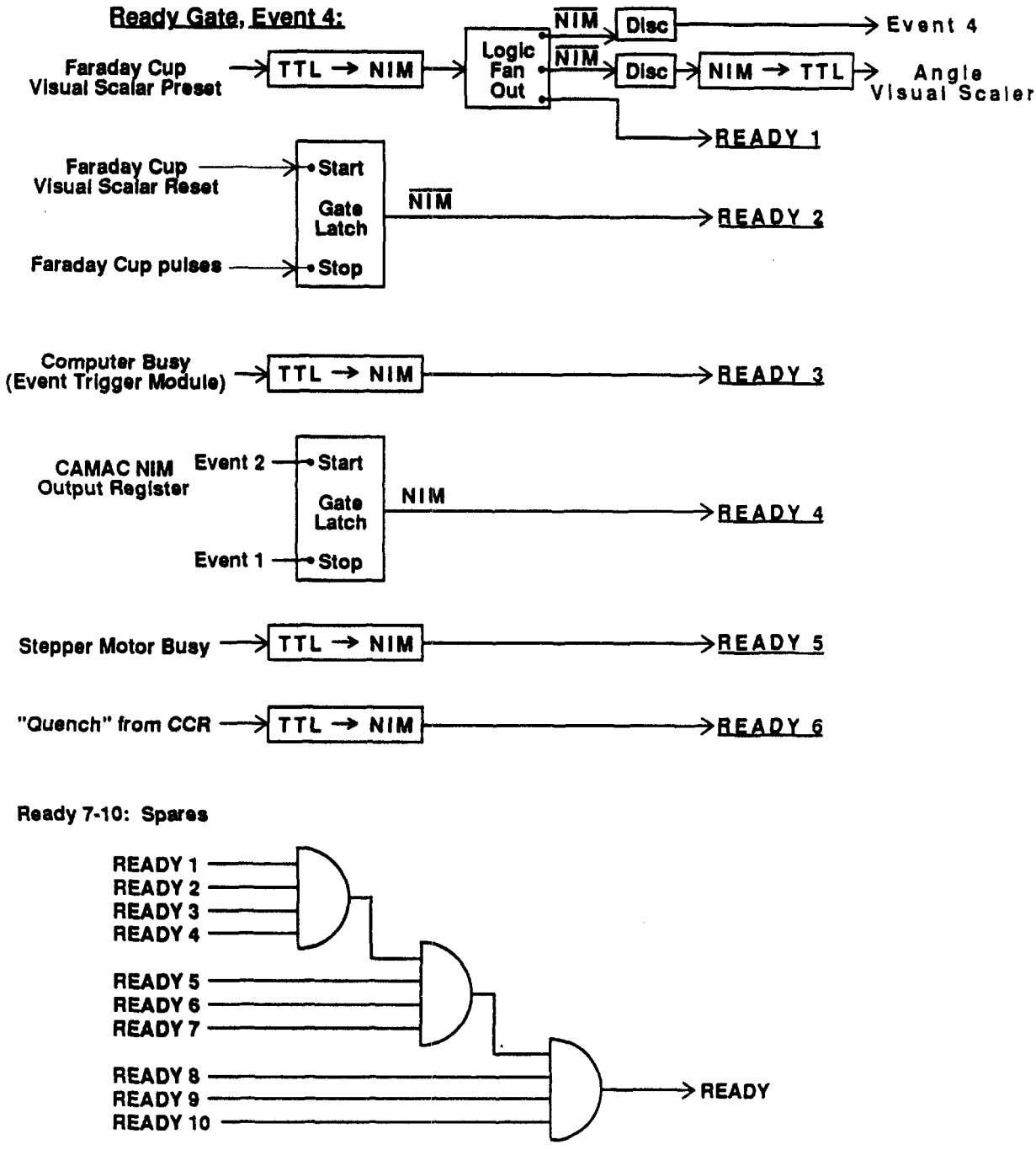

Figure B.2(c). NIM electronics block diagrams (cont.).

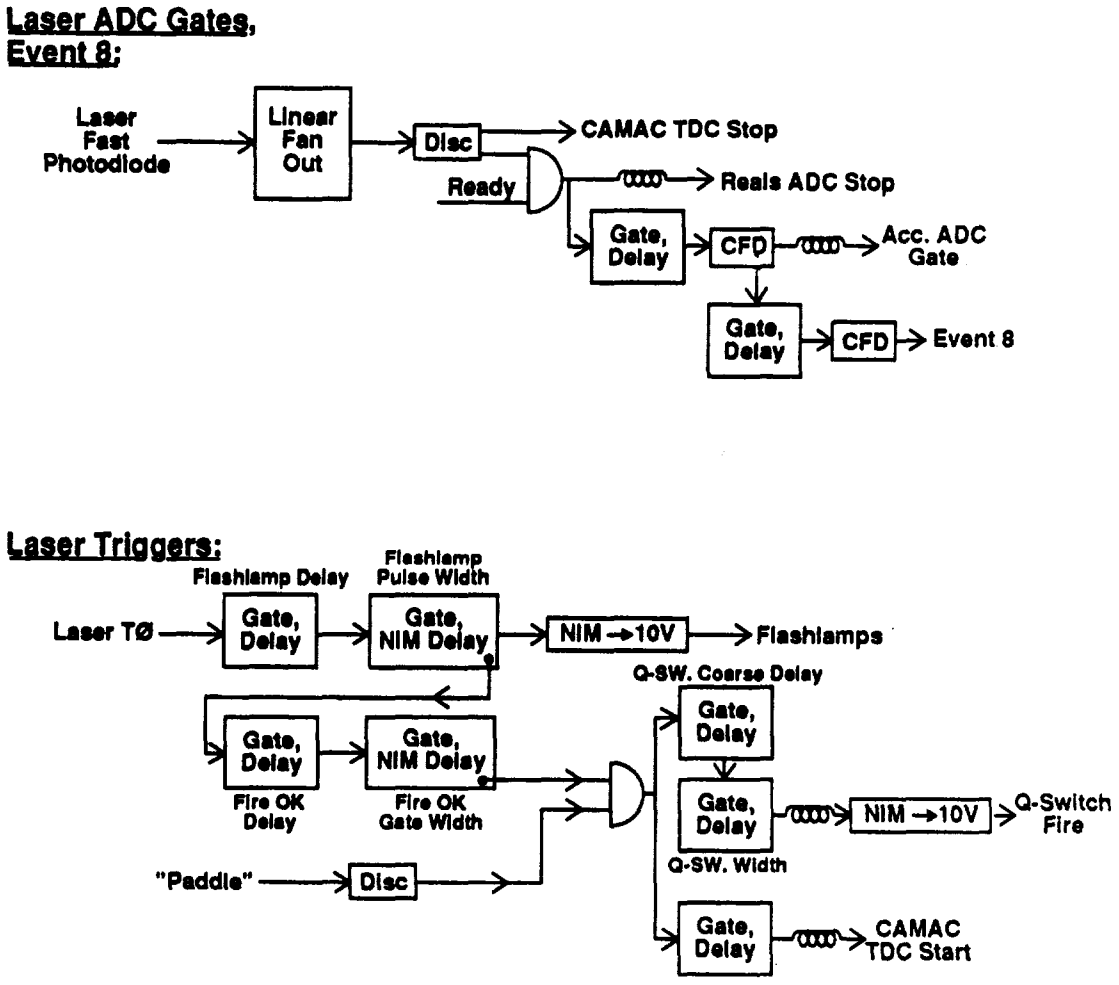

Figure B.2(d). NIM electronics block diagrams (cont.).

Laser Scaler Gates:

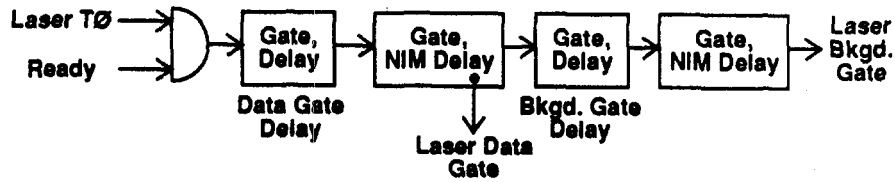

Laserless Scaler Gates, Instrument Gate, Event 9:

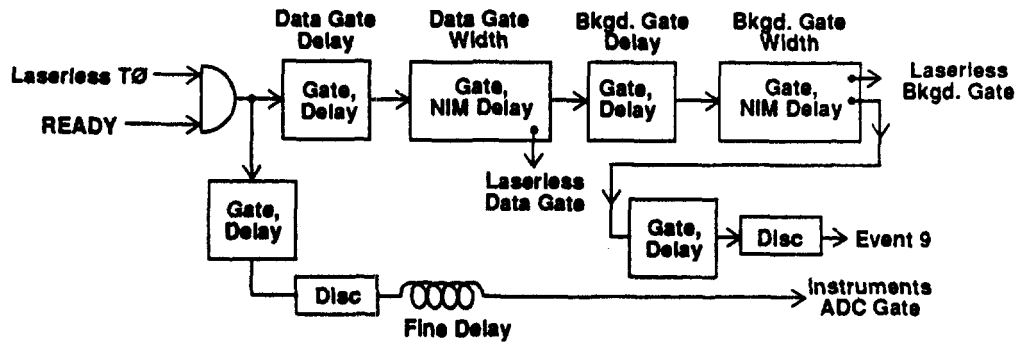

Figure B.2(e). NIM electronics block diagrams (cont.).

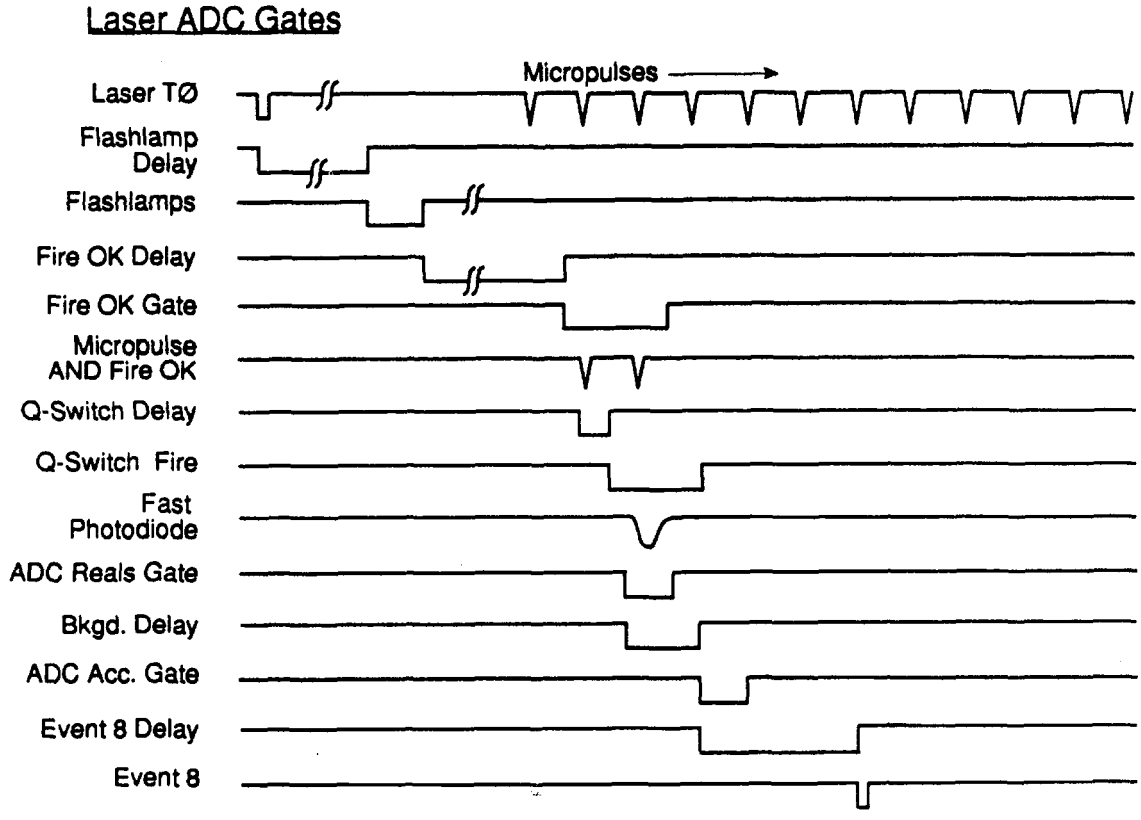

Figure B.3(a). Timing diagram for logic gates.

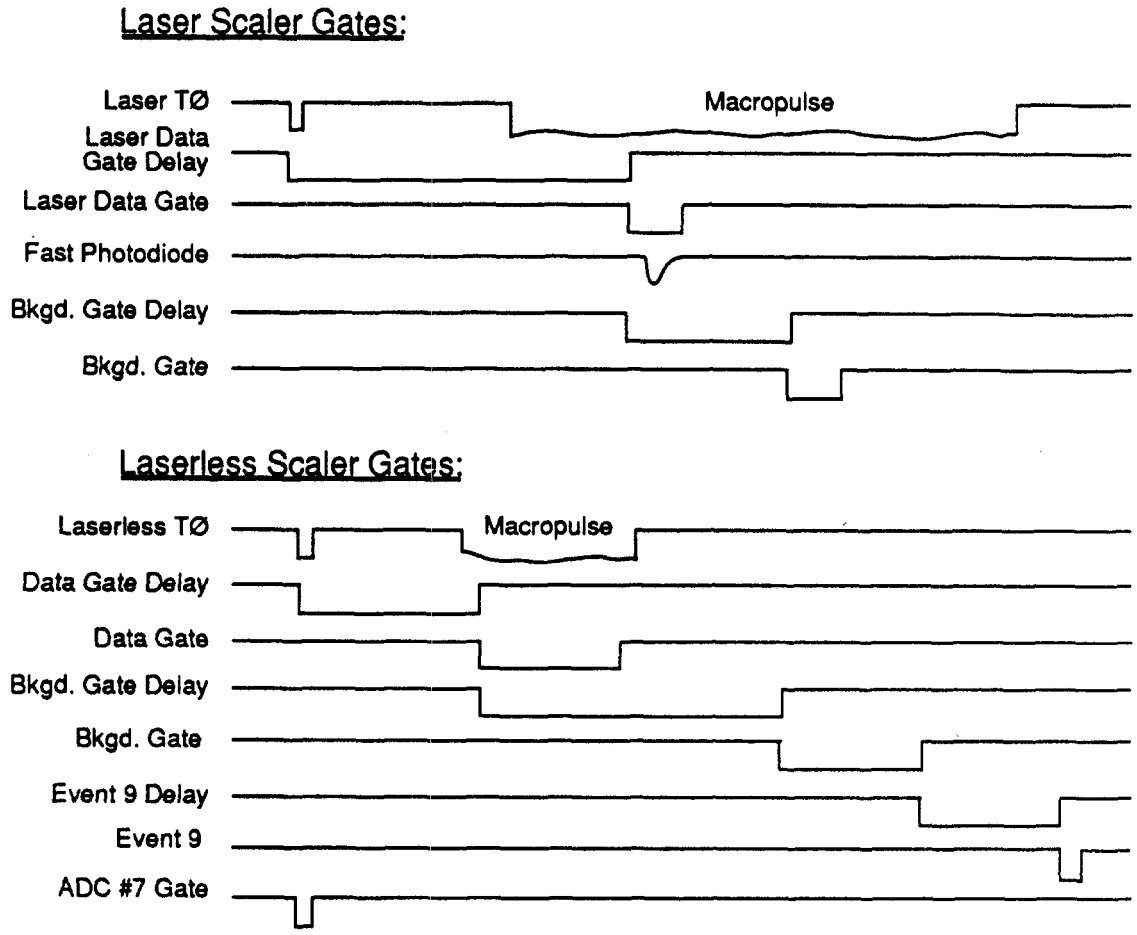

Figure B.3(b). Timing diagram for logic gates (cont.).

B.2 Data acquisition.

The computer may take data when several conditions are met. These are:

i) The laser has fired, as determined by a (discriminated) pulse from the fast photodiode (FPD).

ii) The beam is on, as determined by the beam gate signal (originating at CCR) and a signal from the paddle.

iii) The spider stepper motor has finished stepping.

iv) The Faraday cup counter has not reached its preset maximum.

v) The computer itself is not busy.

Given these conditions, a logic gate called "READY" is generated, and consequently the gates are generated for the ADC's to start integrating their signals. The NIM delays must be adjusted so that the ADC's sample the signals from the detectors for the period (called the data gate) corresponding to the arrival at the detectors of the photodetachment fragments, and again for the same length of time (the background gate) when no laser-related signals are present. The ready gate also allows a scaler to count the integrated current in the Faraday cup, until a predetermined total is reached and the spider moves on to the next angle.

Appendix C

Software

C.1 The Q System.

"Confusion now hath made his masterpiece!"

— William Shakespeare, *Macbeth* II: ii.

Q is the name given to the data acquisition/analysis system developed for use at LAMPF. It controls hardware through the CAMAC interface; it reads data, again through CAMAC, and writes it to tape; it also performs a certain amount of on-line analysis, the results of which it writes to data files. In addition, it controls a histogramming package known as HPL, which allows the data to be presented in graphic form on the screen as it is collected.

It is necessarily modular in structure. As far as the user is concerned, its behavior is governed primarily by a series of procedures, defined in user-written sourcecodes by the name of PROCn.FOR, where n is the procedure number, and is also the number of the EVENT — *i.e.*, the set of circumstances that triggers the execution of the PROC. In our case, there were three important EVENTS, and their corresponding PROCS:

i) EVENT 8 occurred at every firing of the laser, provided that the beam was on and the data gates open. It prompted PROC8 to read the data stored in the ADC's and scalers, and to add these values to the running sums for calculation of average and standard deviation signals.

ii) EVENT 9 was similar to Event 8, except that it occurred at the end of each H^- beam macropulse; PROC9 processed the signals from the fast ion chamber, and also recorded readings of gaussmeters and so on.

iii) EVENT 4 occurred at the end of each angle (for a variable angle experiment — or at the end of each magnetic field setting for a spectrometer run), and prompted PROC4 to carry out the following tasks:

   a. Calculate averages and standard deviations (or sums and square root of the sums) for each of the detectors.
   b. Clear all ADC's and scalers, in preparation for the angle to follow.
   c. Re-initialize all of the running sums to zero.
   d. Read the encoder setting (and convert it to its decimal value).
   e. Write the required data (angle number, encoder setting, averages, standard deviations and so on) to the data files.
   f. Update the histograms.
   g. Step the spider to its next setting, unless the maximum number of angles had been reached.

The Q system maintains in the computer's dynamic memory a list of parameters that controls the nature of the analysis performed. This so-called Dynamic Parameter Array (DPA) contains information on the "slopes" and "pedestals", determined from an analysis of the distribution of pulse heights (see Chapter 3), needed to calculate the number of particles corresponding to a given voltage (pulse height) measured at the detector in question. Other parameters in the array include such information as the type of laser in operation, the scattering chamber being used (whether Big or Little, so as to know which encoder reading to record in the data file), and incidental information such as whether or not a hard copy should be produced of the data during the run.

Data recorded on the tape may be analyzed later, when Q is in its REPLAY (rather than DATA ACQUISITION) mode. If necessary, cuts may be put on the data by means of a test package; for example, a test could be specified that did not allow execution of PROC8 if the signal from the laser photodiode lay outside a certain range, which would restrict the processed data to that taken when the laser power was acceptably steady. In addition, data not written to the data files while the run was in process may be recovered — for example, the correlation coefficients between H^0 and H^+ signals (see Appendix D).

C.2 PS/2 Software.

An IBM PS/2 (model 60) provided a "user-friendly" environment where small calculations could be performed quickly and easily, and independently of the microvax (which was generally occupied with data acquisition). It was especially important to provide simple menu-driven software for the several members of the collaboration who were unused to the microvax "environment". To this end, several programs were written; for example, since many calculations were done on a Lotus-123 spreadsheet, programs were written to transfer data files from the microvax with the aid of a terminal emulator. By simply entering the required filenames, the run data files were transferred, error checking was performed, and the files were loaded into the spreadsheets where macros did background subtraction, normalization and plotting of the data, depending on the type of run in question. A customized menu program was also written to provide an interface for the disk operating system (MS-DOS).

During the 1988 runs, it was found that certain basic calculations wasted much time and resulted in considerable confusion. For example, two series of hydrogen lines ($3 \rightarrow n$ and $4 \rightarrow n$) were found; it was not realized until some time after the run that the lines were, in fact, different from those supposed during the run (so that the line thought to be 4 to 12 was in fact 4 to 13). Occasionally,

we were so uncertain of our calibration that the spider ended up one entire sector (see Appendix A) away from its intended position! Other similar calculations, done on hand calculators, could be extremely time consuming and error prone.

A program — the "Beam Program" — was therefore written in Turbo Pascal (Borland Inc.) to meet these needs in a comprehensive, user-friendly manner. Entirely menu-driven, it included the following utilities:

i) Calculation of angles, including conversion between sector/encoder readings, absolute angles (α) and center-of-mass photon energy. The calibration was performed automatically by simply entering the positions of any two hydrogen transitions.

ii) Electron and proton momenta, and the relativistic parameters β and γ.

iii) Calculation of resolution, and of the minimum step size (in energy) for any given angle.

iv) Calculation of the energies, positions and widths of features such as all hydrogen lines from $n = 1 \rightarrow 2$ through $n = 19 \rightarrow 20$, the $n = 2$ Feshbach resonance and the one- and two-electron photodetachment thresholds.

v) Transformation of laboratory magnetic fields to center-of-mass electric fields, together with calculations of the magnetic fields necessary to strip excited neutral hydrogen in states n from 1 to 20, the angular and spatial displacements of the beam due to passage through a magnet of given length, the radii of curvature of electrons and protons in a magnetic field, and the magnetic field needed to see the "convoy" electron peak in the electron spectrometer — an essential reference point.

vi) Automatic update of all of the above by simply entering new values for any relevant parameters such as beam energy, laser photon energy or wavelength, divergences, momentum spread and so on.

vii) Display of useful constants such as the Rydberg constant, electron and proton masses, $\hbar$ and so on.

In addition to the above, a very useful added feature was that the program was made RAM-resident (see, for example, O'Brien, 1988). This means that it loads itself onto the computer's memory on the initial bootup (*i.e.*, when the machine is first turned on), where it stays dormant, allowing the execution of other programs; it is thus "invisible" to the user, but in fact it intercepts all keystrokes, looking for a particular combination known as the "hot key" (in this case, Alt-Space). Generally, it simply passes on the keyboard characters to whatever program is currently running; but when the user hits the "hot key" combination, it calls the DOS interrupt vectors that activate it — it makes the operating system look at its own instructions instead of those of the other program. This gives it a (deceptively) simple "pop-up" appearance, which avoids the normal (irritating and time-consuming) procedure of leaving the program that is currently running, loading and running the Beam Program, then returning to the original program — spreadsheet, VAX terminal emulator or whatever — just in time to forget what the calculation was needed for in the first place. Exiting the pop-up routine leaves one back in the original program, with the RAM-resident program in its dormant stage once again.

This program proved especially valuable for locating features — an entire series of hydrogen transitions could be mapped out within half an hour, a task that previously could have taken five to ten times as long.

C.3 Gray Binary.

The 12-bit encoder acquired for use on the little chamber had a readout in Gray binary. Although it has no direct bearing on the physics of this experiment, the conversion of Gray to natural binary proved to be an interesting exercise, and is included here for the sake of completeness.

Little used nowadays, Gray binary code has the unique property of only changing one bit at a time as the numbers increment. The need for such a system arises when there may be some ambiguity at the changeover point itself; for example, in natural binary, in changing from 7 (0111) to 8 (1000), all four bits must switch at once, whereas with Gray code, the switch from 7 (0100) to 8 (1100) is defined precisely with the switching of only the fourth bit (where the first bit is the least significant).

The formula for conversion is at once both simple and rather clever. It is

$$B_{n-1} = G_{n-1} \text{ xor } B_n, \tag{C.1}$$

where G represents the Gray code number, B is its natural (base 2) binary equivalent, and "xor" is the "exclusive or" operation. In other words, the $(n-1)^{th}$ Gray bit is compared with the n^{th} natural binary bit; if they are the same, then the $(n-1)^{th}$ natural binary bit is 0; if different, 1. (Note: for an N-bit number, the $N+1^{th}$ bit is effectively zero.) Proof that this does lead to a binary system with the properties described is of academic interest only, and is left as an easy exercise to the reader!

VAX-VMS Fortran contains a function, MVBITS, to move individual bits of a (binary) number; this allows a relatively easy software conversion from Gray to natural binary, as follows:

```
      Subroutine Gray(A,B)
C     This program converts gray code binary to natural binary.
C     A is the Gray code number, B the natural binary.
        IMPLICIT NONE
        INTEGER X,Y,A,B,I
        B = 0
        DO 10 I = 0,31 ! up to 32-bit number
          X = 0
          Y = 0
          CALL MVBITS(B,0,1,X,0)
          CALL MVBITS(A,31-I,1,Y,0)
          B = ISHFT(B,1) + X .XOR. Y
10        CONTINUE
        RETURN

        END
```

In Turbo Pascal (Borland inc.), one may shift whole numbers to the left or right, using the *shl* or *shr* functions; this allows for a rather more cumbersome conversion, as follows:

```
procedure gray(G: word; var B: word);
(*Convert 16-bit Gray number G to natural binary B*)

var c, h : word;
   i : integer;
   x, y, z : byte;

begin
  B := 0;
  for i := 16 downto 1 do
     begin
     c := G shl (16-i);
     y := c shr 15;
     h := B shl (15-i);
     z := h shr 15;
     x := y xor z;
     B := B + (x shl (i-1));
     end;

end;
```

The Fortran subroutine listed above was called by PROC4 to decode the output from the Little Chamber encoder at the end of each angle.

Appendix D

Data Reduction

> "The result of this experiment was inconclusive, so we had to use statistics."
>
> — overheard at an international physics conference.

D.1 Normalization of Signals.

As discussed in Appendix F, in order to obtain the relative cross section from the count rate, the signal must be multiplied by a factor of $\sin\alpha/(1+\beta\cos\alpha)$. However, in the case of the resonances, an alternative form of normalization was available; the cross section for the production of H°'s stays relatively constant over the photon energy range under consideration, and so the H° signal automatically includes the normalizing factor, in addition to any fluctuations that may be related to changes in the laser or in the particle beam.

Before normalization to the H° signal could take place, it was necessary to subtract any backgrounds present in both the H^+ and H° channels. This was sometimes difficult, as, although several runs included signals taken at a few angles with the laser blocked, not all did; it was not obvious at the time that the background levels were changing, sometimes slowly drifting up or down and sometimes jumping. An obvious lesson to be learned from this is that in future all runs should include some data taken with the laser blocked, or better still that data should be taken on alternate macropulses with laser on and laser off.

Each of the two signal channels (H^+ and H°) had a background channel associated with it. By looking at the H° signal for the periods where the laser was blocked, and comparing it with the average value for the H° background (*i.e.*, data taken during the background gate), it was determined that the background count rate needed to be multiplied by 2.4 ± 0.1 in order to make it compatible with the true background levels in the H° signal channel. The uncertainty in this ratio is a systematic error, and so is not included in the error bars, which are purely statistical, as will be discussed later.

A similar subtraction of backgrounds needed to be done from the H^+ signal channel. The cross section here sometimes dropped to zero, in which case the background level could be determined even when the laser was not blocked. The relevant ratio between background levels in the signal and background channels again fluctuated significantly, but the signal-to-background ratio was much smaller (often less than 1), making these fluctuations more important. A different approach was therefore adopted here. First, a particularly "clean" run, where all conditions were stable throughout the run, was chosen for each of the hydrogenic excited state channels studied — $n = 4$, 5, 6, 7 and 8. These runs — respectively 587, 590, 709, 605 and 628 — also had to cover the entire energy range for the relevant channel, including some data points below the threshold, for which the true signals would be zero. (Many runs did not include such regions, and so did not have clearly defined background levels). The background subtraction was done for each of these sets of data as for the H° signals, and the H^+ signals were then normalized to the H° channel for these runs.

The "master" data files produced in this manner were used for scaling all of the other (zero field) runs, so that comparisons could fairly be made between runs taken at different beam currents, with different backgrounds and so on. For this purpose, a program (SCALE) was written that adapted a simplex routine

(Cacechi and Cacheris, 1984) to determine the closest fit (minimum χ^2) of one data file scaled to another. This allowed the background levels to be determined for those runs for which they would otherwise have been unobtainable. With the backgrounds subtracted, each run could then be normalized to its H° signal and scaled appropriately to produce the relative cross section.

D.1.1 $1/n^3$ Scaling.

The actual distribution of excited neutral hydrogen states is expected to obey a $1/n^3$ power law, where n is the principal quantum number. In other words, for every H°($n = 2$), eight H°($n = 1$)'s would be produced; for every H°($n = 3$), 27 H°($n = 1$)'s, and so on. (As the double detachment threshold is approached, however, a Wannier-type power law, $\sigma \propto (E_t - E)^{1.127..}$, where E_t is the double-detachment threshold energy, is believed to become dominant). Although no attempt was made at the time to determine the actual ratios of production of the successive n channels, later analysis shows production of $n = 4$ to $n = 5$ in the ratio of approximately 1.35, and $n = 5$ to $n = 6$ in the ratio of 1.75; these are to be compared with the expected ratios from the $1/n^3$ law of 1.95 and 1.72 respectively. This would seem to indicate that the $1/n^3$ law applies, but that the magnets were not perfectly efficient in stripping $n = 4$; this was to be expected with a 4 kG magnetic field.

The cross section for production of H°($n = 1$) in this energy range is approximately 0.13 a_0^2 (see sections 5.3 and F.1.2). On the basis of this, and the $1/n^3$ law, a multiplicative factor was applied throughout each data file, so that the units labeled "arbitrary" in the figures showing relative cross sections *vs.* energy should in fact be units of approximately $10^{-6} a_0^2$.

D.2 Calculation and Propagation of Uncertainties.

Propagation of error bars was the cause of some concern. Initially, when the backgrounds were subtracted, the uncertainties were added in quadrature; and when the normalization to the H° channel was done, the relative uncertainties were added, again in quadrature. Such is the normal procedure — for data that are independent. However, there are of course strong correlations between the fluctuations in the H^+ and H° signals — it is for this reason that we normalize to the H° channel in the first place! The error bars were therefore too large, and needed to be recalculated.

The mean signal $\bar{x}$ per laser shot is simply given by

$$\bar{x} = \frac{\sum x}{N}, \tag{D.1}$$

where N is the number of laser shots (usually 100-200 for the Nd:YAG laser) per angle. The standard deviation of this mean is

$$\begin{aligned} \sigma_x &= \sqrt{\frac{\sum (x - \bar{x})^2}{N(N-1)}} \\ &\approx \sqrt{\frac{(\bar{x^2} - \bar{x}^2)}{N}}. \end{aligned} \tag{D.2}$$

Although of course the mean signal per laser shot is proportional to the beam current (since the higher the current, the more photodetachments occur in each pulse), normalizing to the H° signal removes this dependence.

Given some function $S = S(x, y)$, the uncertainty in S is obtained from the uncertainties $\delta x = \sigma_x, \delta y = \sigma_y$ by a Taylor expansion (see, for example, Melissinos, 1966) of S evaluated at $\bar{x}, \bar{y}$:

$$\sigma_S^2 = \left(\frac{\partial S}{\partial x}\right)^2 \sigma_x^2 + \left(\frac{\partial S}{\partial y}\right)^2 \sigma_y^2 + 2\left(\frac{\partial S}{\partial x}\right)\left(\frac{\partial S}{\partial y}\right)\sigma_{xy}^2. \tag{D.3}$$

The third term accounts for correlations between the quantities x and y; it is generally close enough to zero to be ignored when x and y are totally independent,

but in our case the signal and background channels will have correlated fluctuations if there are fluctuations in the beam current, and the H^+ and H° signals will also have significant correlations if there are fluctuations in the laser power. The factor σ_{xy} is calculated, in a manner analogous to σ_x and σ_y, by the formula

$$\sigma_{xy} = \sqrt{\frac{\sum(x-\bar{x})(y-\bar{y})}{N(N-1)}}. \tag{D.4}$$

In our case, $S = x - y$, and the uncertainty in the net signal after background subtraction (in both the H^+ and H° channels) is

$$\sigma_S = \sqrt{\sigma_x^2 + \sigma_y^2 - 2\sigma_{xy}^2} \tag{D.5}$$

(where x and y are the values from the signal and background channels respectively). The normalization of the H^+ signal S_+ to the H° signal $S_\circ$, giving a total signal $S_{+/\circ} = S_+/S_\circ$, then requires further propagation of these uncertainties, thus (from equation D.3):

$$\left(\frac{\sigma_{+/\circ}}{S_{+/\circ}}\right)^2 = \frac{\sigma_+^2}{S_+^2} + \frac{\sigma_\circ^2}{S_\circ^2} - 2\frac{\sigma_{+,\circ}^2}{S_+ S_\circ}. \tag{D.6}$$

The resulting error bars represent the true statistical fluctuations in the signals. This method is in contrast to our usual procedure of estimating the number of particles in each pulse from a pulse height analysis (see Chapter 3), and assuming Poisson statistics, where the mean fluctuation in the number of particles is simply equal to the square root of that number. Since the H^+ detector did not give clearly resolved peaks for single, double, triple and other multiple counts (the individual particle signals were too small), it was impossible to calculate the multiplicity of hits.

The error bars do not give any indication of systematic uncertainties. These would tend to smear out all of the error bars by the same amount. Since fitting routines assume that the error bars represent only statistical fluctuations, possible

systematic errors — for example, uncertainty in the overall background levels — have not been included.

Once the data files from the individual runs had been prepared, they were binned together to produce the data sets seen in Figures 4.1(a)-(d). Within each bin, a weighted average (Bevington, 1969) was taken in the normal way, producing a net signal

$$y = \frac{\sum_i y_i/\sigma_i^2}{\sum 1/\sigma_i^2} \tag{D.7}$$

with its standard deviation

$$\sigma = \left[\sum_i \frac{1}{\sigma_i^2}\right]^{1/2}. \tag{D.8}$$

The bin sizes were adjusted so that in each case the energy range covered included about 80-100 data points (just as the angular step size was adjusted during the actual runs for the same reason).

D.3 Fitting.

The fitting routine used here was MINUIT (James and Roos, 1975), a powerful package developed at CERN (Centre Européene pour la Recherche Nucléaire, the European organization for nuclear research), that uses several different methods to minimize a specified quantity; for this analysis, the quantity used was χ^2, defined as

$$\chi^2 = \sum \left(\frac{f(x) - d(x)}{\sigma_x}\right)^2, \tag{D.9}$$

where $d(x)$ are the data points with uncertainties σ_x, and $f(x)$ is the function (with up to 30 parameters, up to 15 of which may be varied at once) to which the data are being fit.

D.3.1 Fitting Techniques.

The fitting techniques employed by Minuit are:

i) A Simplex routine. Developed by Nelder and Mead, this technique uses a figure defined by $n+1$ vertices in the n dimensional parameter space, and continually approaches the minimum by reflecting the worst of the vertices in the hyperplane defined by the other vertices. "Worst" in this sense means that having the largest χ^2.

ii) Migrad. This is a gradient method, which uses information from the derivatives of the variables at a point to predict a good trial point relatively far away. Unlike the Simplex method, Migrad will calculate a covariance matrix.

iii) Seek. This is a Monte Carlo method that consists of testing points chosen randomly according to some distribution. It can be useful to provide a starting point (or to look for deeper minima than one already found) for the simplex routine, but it becomes very inefficient when searching a multi-dimensional parameter space.

iv) Improve. This "fills" a local minimum found by the simplex routine and then proceeds to search for a deeper minimum elsewhere. It requires the covariance matrix to have been calculated, and so is only called after the Migrad routine has been run.

D.3.2 Fitting to Resonances.

In the case of the resonances on the continuum background, each resonance has an amplitude (see Chapter 2)

$$\psi_R(E) = \frac{ia\Gamma/2}{(E-E_0)+i\Gamma/2}, \tag{D.10}$$

and a phase difference ϕ with the continuum on which it lies. The amplitude of the continuum was modeled as linearly increasing with photon energy. Thus, the total amplitude for a series of n resonances is

$$\psi_t(E) = b + cE + \sum_{k=1}^{n} \frac{ia_k e^{i\phi_k}}{i + 2(E-E_{0_k})/\Gamma_k}, \tag{D.11}$$

where the factor of $\Gamma/2$ in the numerator of equation D.10 has been included in the constant a_k. The function $f(x)$ is then given by the cross section (or intensity),

$$f(x) = \sigma(x) = \psi^* \psi. \tag{D.12}$$

Usually, three resonances were used to model the data; as each has an amplitude, a phase, a width and a centroid, there would be twelve free parameters together with another two for the continuum background and slope. When Minuit had made reasonable estimates of the parameters of the continuum and of the largest of the resonances, these could be "fixed" and a fourth resonance added in for "fine tuning". In no case were more than four dips visible in one channel.

It emerged that the resonances were narrow enough (in comparison with their spacing) that there was little danger of their overlapping; in this case, the intensities could be added directly (rather than adding the amplitudes), and so they were also fit to sets of the more standard Fano profile (see section 2.6),

$$\sigma = \sigma_b + \sum \sigma_a \left[\frac{(q+\epsilon)^2}{1+\epsilon^2} - 1 \right]. \tag{D.13}$$

The σ_b here is a little different from that of the usual Fano profile, since an extra σ_a has been subtracted from it (see Chapter 2 for further discussion of this point), and it is also assumed to have a linear energy dependence. Note that there is a slight difference here from the "coherent amplitude" model, in which the *amplitude* of the background continuum was assumed to be a linear function of the photon energy ($b + cE$ in equation D.11).

In addition, the widths and energies of each series of resonances (in each hydrogenic n continuum channel) were fit to the recursion formula (see section 2.4)

$$\frac{E_n - E_k}{E_n - E_{k+1}} = e^{-\frac{2x}{a}} = \frac{\Gamma_k}{\Gamma_{k+1}}. \tag{D.14}$$

Chapter 4 contains additional discussion of the fits carried out, together with their results.

A gaussian resolution of 8.3 meV (FWHM) was assumed in each fit. This resolution was determined by an analysis of the linewidths of the $n = 2$ Feshbach resonance and of several hydrogen lines, as outlined in Appendix E.

Appendix E

Energy Resolution and Momentum Bunching

This appendix is based upon work accepted for publication in Nuclear Instruments and Methods A (Harris *et al.*, 1990c).

E.1 Resolution Limits.

The energy resolution in these Doppler-tuned spectroscopic experiments is determined by three factors: the laser linewidth (normally negligible), the combined divergences of laser and particle beams, and the momentum spread of the particle beam. The effect of each is found by a Taylor expansion of the Doppler shift formula (equation 1.1)

$$E = E_0\gamma(1+\beta cos\alpha) \tag{E.1}$$

yielding

$$\frac{\delta E}{E} = \left[\left(\frac{\delta E_0}{E_0}\right)^2 + \left(\frac{\beta sin\alpha}{1+\beta cos\alpha}\delta\alpha\right)^2 + \left(\frac{\beta^2+\beta cos\alpha}{1+\beta cos\alpha}\cdot\frac{\delta p}{p}\right)^2\right]^{\frac{1}{2}}, \tag{E.2}$$

where higher-order terms are ignored, and δE_0, $\delta\alpha$ and δp are assumed to be Gaussian distributed independent variables, allowing the sum in quadrature.

The $n = 2$ Feshbach resonance lies at a center-of-mass photon energy of 10.9264 eV (MacArthur *et al.*, 1985). Because it is narrow, with a predicted width of the order of 30 μeV (Lipsky and Conneely, 1976; however, estimates

range as high as 1 meV; see Broad and Reinhardt, 1978), a measurement of its width provides an excellent measure of instrumental resolution. The linewidths of the transitions between excited states of neutral hydrogen are likewise dominated entirely by instrumental resolution, since the natural linewidths are of the order of 10^{-8} eV. As these features occur at different energies, and therefore different angles (e.g. 71.5° for the Feshbach resonance, 47.8° for $n = 1$ to 12 and 137.1° for $n = 2$ to 12), equation E.2 will produce three (or more) simultaneous equations which may be solved for the three unknowns $\delta E_0, \delta\alpha$ and the momentum spread $\delta p/p$.

Measurements of the positions of a number of spectroscopic features of well-known energy (for example, whole series of hydrogen lines) may be fit to the Doppler-shift formula of equation E.1 to yield a precise value of β, and thus of the beam energy; the accuracy in this case can be better than 0.3 MeV.

For small angles, i.e., high blueshifts, the momentum spread tends to dominate the resolution, and it therefore is desirable to reduce it. As outlined in Appendix A, the H^- beam is often used at energies lower than 800 MeV, which are obtained by accelerating only up through the rf module needed for the required energy, and drifting through subsequent modules. We describe here the use of the last two of these modules to reduce the momentum spread, in a rather unusual technique.

E.2 Momentum Bunching.

Following the success of McClelland *et al.* (1989) in longitudinally focusing, or "spatially bunching", the beam at LAMPF, it was decided to use a similar approach to "momentum bunch" the beam. The aim of the longitudinal (or temporal) focusing was to make all of the ions in a beam pulse arrive at a target simultaneously; momentum bunching, on the other hand, may be regarded instead

as a collimation process — longitudinal focusing on a target at infinity, thereby giving all of the ions in a beam pulse the same energy.

We follow here the "thin lens" formalism of McClelland. A bunching cavity should slow down the fast ions, while accelerating the slow ones; it is able to make the distinction because the micropulse has had time to spread out since the final accelerating cavity prior to the buncher, and the faster ions therefore arrive at the buncher ahead of the slower ions. A "thin" buncher cavity will increase the energy of a given ion (relative to the central ion) by

$$\delta E = -eV_0 \sin(\omega \Delta T) \approx -eV_0 \omega \Delta T \tag{E.3}$$

where e is the electronic charge, V_0 is the peak cavity voltage, ω is 2π times the cavity frequency and ΔT is the time by which the ion precedes the center of the bunch. It should be noted that this approximation requires that the micropulse pass through the cavity during the "linear" part of the sine wave; for the 805-MHz cavities at LAMPF, a "window" of approximately 400 ps gives a deviation of up to 20% from linearity.

The energy change δE is measured with respect to the central ion. If the micropulse does not pass through the buncher at zero field on average, there will of course be an average change in energy, in addition to the relative change in energy of each of the ions within the micropulse.

If the distance from the last accelerating cavity to the bunching cavity is S, then, assuming that all ions leave the cavity simultaneously, an ion that has energy ΔE greater than the central ion will arrive at the buncher at a time

$$\Delta T = \frac{S}{c}\left(\frac{\sqrt{1-\beta^2}}{\beta}\right)^3 \frac{\Delta E}{mc^2} \tag{E.4}$$

earlier than the central ion, and will therefore leave the buncher with an energy

$$\Delta E' = \Delta E - eV_0 \omega \Delta T \tag{E.5}$$

greater than the central ion. For momentum bunching, we require that

$$\Delta E' = 0, \tag{E.6}$$

from which we obtain

$$\frac{1}{S} = \frac{eV_0\omega}{mc^3}\left(\frac{1}{\beta^2} - 1\right)^{3/2}. \tag{E.7}$$

(This is equivalent to $1/S' = 0$ in McClelland's equation (8) — *i.e.*, longitudinal focusing on a target at infinity). Within the constraint of this equation, a balance must be struck; the drift length S must be great enough that the bunching will work effectively — the micropulse must have time to spread out — but it must not be so great that the pulse length exceeds the acceptance of the bunching cavity. An additional constraint on our experiment was that, with the last few cavities turned off to perform the bunching, the beam energy should still be adequate to allow the Doppler-shifted photon energy to reach 15 eV.

The ray-tracing program SIMALAC (Crandall, 1970), given the design parameters of the LAMPF linac, predicted that the momentum spread at 716 MeV, which is normally about the same as that at 800 MeV, could be reduced by a factor of approximately 5 by using the last two modules as bunchers. Results from this program are shown in Figure E.1. The horizontal phase-space ellipse of Figure E.1(a) indicates the tightly-bunched (temporally) beam with a significant energy spread as it exits the last acceleration cavity (module 43). The micropulse then spreads out in time as it drifts, as shown in Figure E.1(b); modules 47 and 48 then act together to rebunch the beam momentum. Figure E.1(c) shows the beam as it exits the buncher, with the momentum spread reduced considerably.

It is obviously necessary that the bunching cavities should have the right phase and amplitude. On the other hand, it is important that the accelerator should continue to function normally for the beams that do not require bunching. In order to operate the buncher only on the part of the rf cycle that would affect

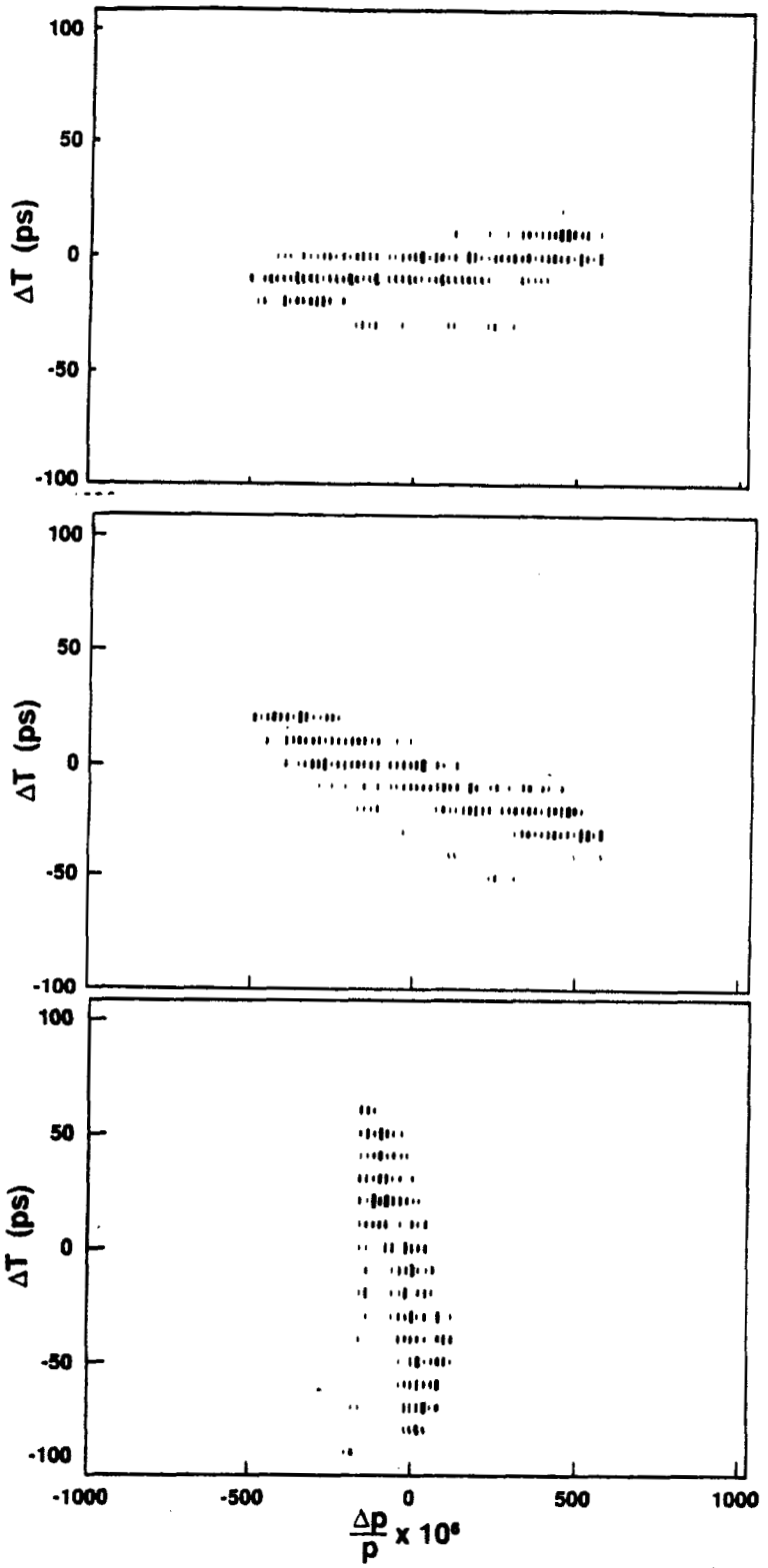

Figure E.1. Results from the SIMALAC ray-tracing program, showing the phase space of the particle beam (a) as it exits the last accelerating cavity, (b) as it enters the bunching cavity, (c) as it exits the buncher.

their beam, McClelland's group installed special controls on module 48, allowing them to vary the effective phase and amplitude of that module for P^- only (or, as used in our case, for H^- only). Module 47 has no capability for adjustment.

The prediction of the SIMALAC program was, rather fortuitously, that modules 47 and 48 should be operated at full amplitude and with no change of phase. In fact, it was found that a phase change in module 48 was necessary, principally to compensate for the last cavity having been tuned to optimize the beam for the group using the H^+ beam, and further, it was found that the necessary phase change drifted over time.

E.3 Results.

Figures E.2(a) and E.2(b) show fine scans of the Feshbach resonance, respectively at our normal resolution (typically about 7 meV FWHM), and at the increased resolution (2 meV) made possible by momentum bunching and by expansion of the laser beam to reduce its divergence. Figure E.3 shows a high resolution scan of the Feshbach and shape resonances. Measurements of the fitted widths of hydrogen lines ($n = 1$ to 12 and $n = 2$ to 13) combined with those of the Feshbach resonance show that the momentum spread, $\delta p/p$, has been reduced from its initial value of approximately 5×10^{-4} to about 1×10^{-4} (a factor of 5, as predicted by SIMALAC). However, small errors in the measured linewidths produce large uncertainties in the calculated energy, angle and momentum spreads, and can easily produce physically unreal results. These initial estimates, which were made by assuming that the uncertainty in the laser linewidth was negligible, should therefore be treated with caution. It should be a relatively simple matter, if higher precision measurements are required in the future, to reduce the laser divergence to the point where its contribution to the resolution becomes negligible (at small enough angles α), and the measured linewidth is dependent almost entirely on the momentum spread, thus simplifying the calculations considerably.

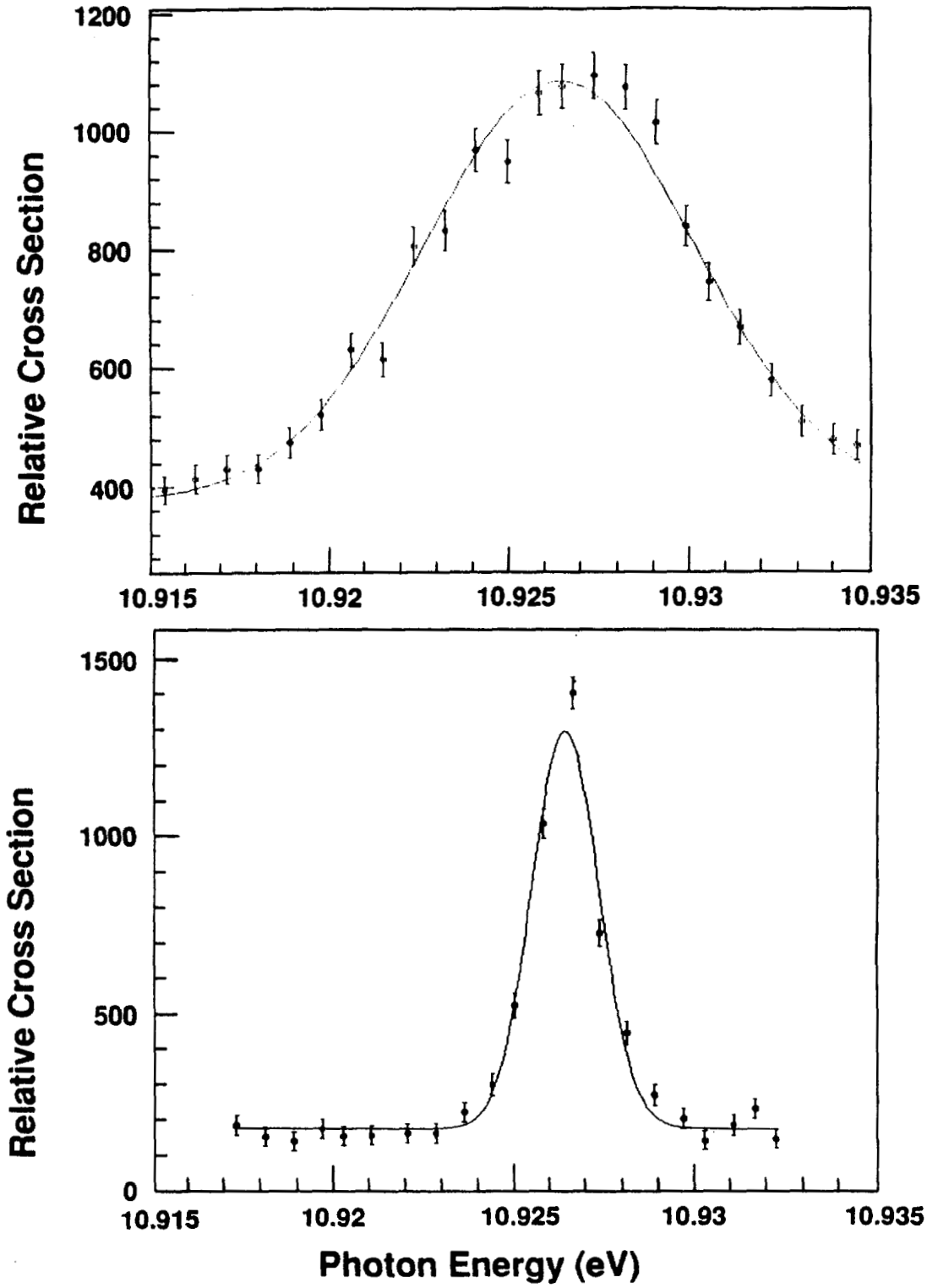

Figure E.2. Fine scans of the Feshbach resonance, (a) without momentum bunching, (b) with momentum bunching (and a slight reduction in laser beam divergence).

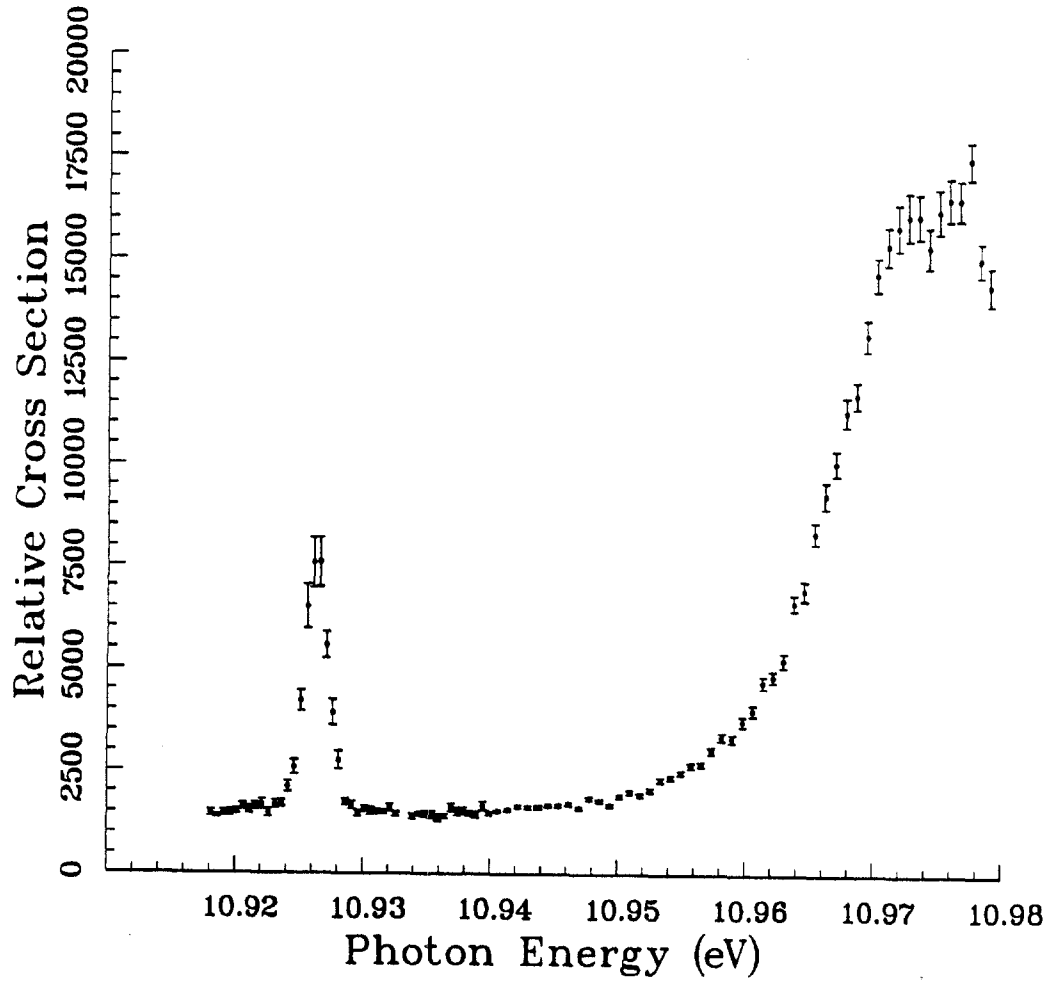

Figure E.3. High resolution scan of the Feshbach and shape resonances, made possible by momentum bunching. See Figure 1.2 for comparison.

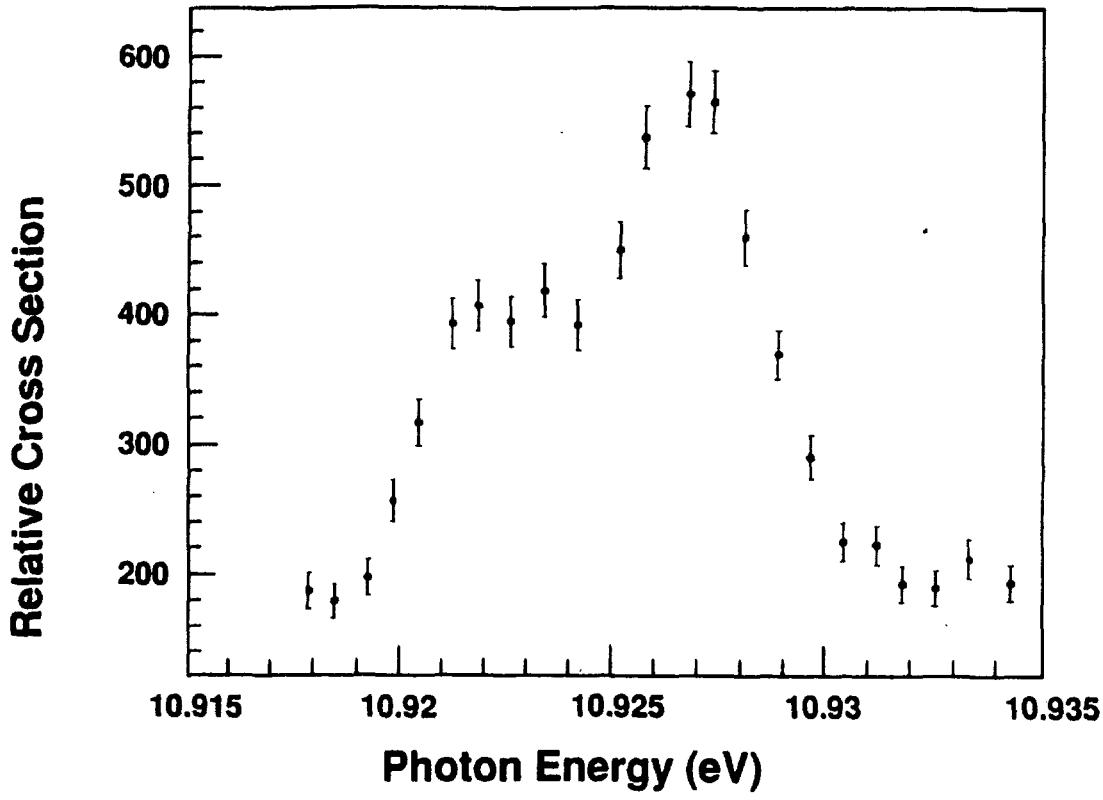

Figure E.4. Fine scan of the Feshbach resonance, with the bunching cavity out of phase; the momentum profile of the beam is reflected in the lineshape.

The buncher cavities also produced an overall change in energy, from the nominal 716 MeV to 714.3 MeV. This change was of no concern to our experiment; it simply changed slightly the angles of intersection α at which the spectroscopic features were seen.

It is interesting to note that when the momentum spread dominates, the lineshape mirrors the momentum profile of the beam; this is shown quite clearly in Figure E.4, which is also a scan of the Feshbach resonance, but with the phase of the final bunching cavity not optimized. There are obviously two components to the beam, one having a slightly higher momentum than the other.

Laser spectroscopy has provided an important diagnostic tool for the LAMPF H^- beam. This technique gives not only an excellent measurement of the beam

momentum, but also allows monitoring of the momentum profile and spread. We have demonstrated the feasibility of using the linac cavities to reduce the momentum spread, and it is hoped that further significant progress may soon be made in this direction. The possibility of using laser spectroscopy to measure energy spread to an accuracy of a few keV is discussed by Holtkamp and Quick (1990).

Appendix F

Cross Section Calculations

F.1 Normalization of Yield to Cross Section.

The calculations in this section and in section F.2 were carried out jointly with Chen-Yau Tang, and appear (somewhat compressed) in Tang *et al.* (1989).

For a cross section σ (cm^2) and a photon flux Φ (per second, per cm^2) the instantaneous count rate is

$$R' = \sigma\Phi' \tag{F.1}$$

per atom. (The prime indicates the rest frame of the ion). The total count rate during the interaction is therefore

$$R' = \int dV'\sigma\Phi'\rho', \tag{F.2}$$

where the integral dV' is over the volume of interaction of the particle and laser beams, and ρ is the number density of ions.

The total number of counts in a micropulse of the H^- beam is a relativistic invariant; *i.e.*,

$$\int R'dt' = \int R\,dt, \tag{F.3}$$

where the time integrals extend over the duration of a micropulse. However, $dt' = \gamma dt$, and so the rates in the barycentric and the lab frames are related by the equation $R' = R/\gamma$. The photon flux Φ transforms like the photon energy,

$$\Phi' = \Phi\gamma(1 + \beta\cos\alpha), \tag{F.4}$$

since the intensity $P = \Phi\hbar\omega$ transforms (Landau and Lifshitz, 1965, p. 424) as does $(\hbar\omega)^2$. In addition, $dV' = dV/\gamma$ and $\rho' = \rho/\gamma$.

We therefore arrive at the instantaneous rate as measured in the lab frame,

$$R = \int dV\, \sigma\Phi\rho(1 + \beta\cos\alpha). \tag{F.5}$$

If an average count rate is to be used instead of the instantaneous rate R, a duty factor should be included.

The volume integral is dependent upon the angle α of intersection of the two beams. Generally, the angular dependence is simply given by

$$\int dV = \frac{1}{\sin\alpha} \int dV_0, \tag{F.6}$$

where the subscript 0 indicates that the integral is over the interaction volume for $\alpha = 90°$. (This does not hold under certain circumstances; for example, a) if there are hot-spots in the laser beam which move around as the mirrors rotate, b) if either beam is very tightly focused so that the cross-sectional profile changes significantly over the (few mm) interaction region, or c) the photodetachment rate is high enough for the micropulse to become significantly depleted, in which case the ion density ρ will effectively acquire an angular dependence).

Therefore,

$$R = \sigma \frac{1 + \beta\cos\alpha}{\sin\alpha} \int \Phi\rho\, dV_0, \tag{F.7}$$

from which we obtain our final result

$$\sigma \propto R \frac{\sin\alpha}{1 + \beta\cos\alpha}, \tag{F.8}$$

with the constant of proportionality k given by

$$k^{-1} = \int \rho\Phi\, dV_0. \tag{F.9}$$

F.1.1 Evaluation of k.

Let us consider the somewhat unrealistic case where ρ and Φ are constant over the interaction volume (they will typically have a Gaussian distribution instead), and the particle and laser beams are cylinders of radii a, b respectively. If we take "horizontal slices" of the interaction region, each slice having depth dy, length $2\sqrt{y^2 - a^2}$ and width $2\sqrt{y^2 - b^2}$, we find that equation F.9 becomes

$$k^{-1} = \rho\Phi \int_{-r_<}^{r_<} y(a) \cdot y(b)\, dy, \tag{F.10}$$

where $y(x) = 2\sqrt{x^2 - y^2}$, and $r_<$ indicates the smaller of a and b. This integral would normally need to be done numerically. We shall, however, consider two special cases; firstly, if $a = b$, it reduces to

$$k^{-1} = 4\rho\Phi \int_{-a}^{a} (a^2 - y^2)dy = \rho\Phi\frac{16a^3}{3}, \tag{F.11}$$

and secondly, if $b \gg a$, so that over the range of integration $b^2 - y^2 \approx b^2$, we obtain

$$k^{-1} = 4\rho\Phi b \int_{-a}^{a} \sqrt{(a^2 - y^2)}dy = 2\rho\Phi b\pi a^2. \tag{F.12}$$

Since

$$\rho = \frac{I}{\pi a^2 \beta c} \tag{F.13}$$

and

$$\Phi = \frac{J}{\pi b^2}, \tag{F.14}$$

where I and J are the *instantaneous* ion and photon currents respectively, the absolute cross section for laser and particle beams that are cylinders of equal diameter is given by

$$\sigma = R\frac{\sin\alpha}{1 + \beta\cos\alpha}\frac{3\pi^2}{16}\frac{ac\beta}{IJ}. \tag{F.15}$$

On the other hand, if one of the beams is considerably larger than the other, we obtain

$$\sigma = R\frac{\sin\alpha}{1 + \beta\cos\alpha}\frac{\pi}{2}\frac{r_< c\beta}{IJ}. \tag{F.16}$$

These results are in fact very similar, since $3\pi/16 \approx 1/2$. In the experiments with the Nd:YAG laser, the laser beam was typically 1 cm in diameter, in comparison with the 2-3 mm H^- beam; the CO_2 laser, on the other hand, was focused down to a few hundred microns, again intersecting an H^- beam of 2-3 mm diameter. In each case, then, the latter formula (equation F.16) is more appropriate.

Of course, neither equation F.15 nor equation F.16 is strictly accurate, since each assumes that the density of ions ρ and the photon flux Φ are constant over the interaction region.

F.1.2 Absolute Cross Section Estimate.

In the absence of any electric field, the photodetachment cross section depends upon photon energy E according to a power law (see discussion in section 5.3)

$$\sigma = \frac{16\pi}{3(137)} \cdot \frac{E_0^{1/2}(E-E_0)^{3/2}}{E^3} \cdot \frac{1}{1-k_B r_{eff}}. \qquad \text{(F.17)}$$

E_0 here represents the threshold energy; $k_B^2 = 2E_0$, and the effective range, r_{eff}, of the potential is 2.646 a_0.

We may make an estimate of the absolute cross section from, for example, the 1988 near-threshold studies (Chapter 5). If we use our estimated typical values of 30 counts per pulse at a c.m. photon energy of 0.82 eV, with $V_0 = 6 \times 10^{-2}\text{cm}^3$, $T_0 = 10^{-9}\text{s}$, $\rho = 500\text{H}^-/\text{cm}^3$, $\alpha = 140°$, and a photon flux of $\Phi = 1.6 \times 10^{27}/(\text{cm}^2 \cdot \text{s})$, we obtain

$$\sigma = 10^{-18}\text{cm}^2, \qquad \text{(F.18)}$$

in comparison with the expected value of 7 x 10^{-18}cm^2. This discrepancy is a cause of minor concern; however, the volume of overlap, the particle density and the photon flux have only been estimated approximately, each perhaps within a factor of two. It should be possible to make a more precise measurement of the absolute cross section, perhaps to within 20%, in future experiments.

F.2 Multiphoton Cross Section.

The above normalization calculation holds true for a single-photon process. For an n^{th} order multiphoton process well below saturation, the transition rate per atom is given by (see references in Tang *et al.*, 1989)

$$W'_n = \sigma_n(\Phi')^n, \tag{F.19}$$

where Φ is the photon flux, σ_n is the so-called generalized cross section (which is independent of the laser intensity) and the prime indicates the rest frame of the ion. If higher order processes also contribute, we may write the transition rate as

$$W' = \sum_{m \geq n} \sigma_m(\Phi')^m = \sigma\Phi', \tag{F.20}$$

where σ is the total cross section:

$$\sigma = \sum_{m \geq n} \sigma_m(\Phi')^{m-1}. \tag{F.21}$$

Comparing equations F.1, F.8 and F.19, we may again write

$$\sigma \propto R\frac{\sin\alpha}{1+\beta\cos\alpha}. \tag{F.22}$$

However, σ here is no longer a "cross section" in the usual sense of the word, in that it is not independent of the rate of the process, which depends on the order n. But if, in fact, the lowest order process is dominant, we have, in terms of the generalized cross section,

$$\sigma = \sigma_n(\Phi')^{n-1} = \sigma_n\Phi^{n-1}\gamma^{n-1}(1+\beta\cos\alpha)^{n-1}, \tag{F.23}$$

and so

$$\sigma_n \propto \frac{R\sin\alpha}{[\Phi\gamma(1+\beta\cos\alpha)]^n}, \tag{F.24}$$

where the constant of proportionality now contains one more factor of γ than in equation F.21. In this case, then, equation F.16 would be modified to yield a generalized cross section for a dominant nth order process,

$$\sigma = \sigma_n = R\frac{\sin\alpha}{(1+\beta\cos\alpha)^n}\frac{\pi}{2}\frac{r_< c\beta}{IJ^n}\left(\frac{\pi b^2}{\gamma}\right)^{n-1}. \qquad \text{(F.25)}$$

F.3 Background Count Rates.

In all of our experiments, the backgrounds are expected to arise from two sources; residual gas stripping and field ionization. The following calculation of the background rates for gas stripping is based on a similar calculation by Dr. Joey Donahue.

The upstream bending magnet sweeps out gas-stripped electrons and protons produced upstream of the chamber. This leaves a distance of approximately 1000 cm of residual gas at about 5×10^{-8} torr to produce background protons.

The gas stripping cross sections (per atom) are (Bentley, 1974)

$$\begin{aligned} \sigma_{-1,0} &= 8.76 \times 10^{-19}\ \text{cm}^2, \\ \sigma_{0,1} &= 3.98 \times 10^{-19}\ \text{cm}^2, \text{ and} \\ \sigma_{-1,1} &= 0.4 \times 10^{-19}\ \text{cm}^2. \end{aligned} \qquad \text{(F.26)}$$

The notation $\sigma_{i,f}$ denotes the cross section for an ion of initial charge q_i to be gas stripped to a final charge q_f.

The number of scatterers at 5×10^{-8} torr is

$$\begin{aligned} N_T &= \left(\frac{6.022 \times 10^{23}\ \text{molecules/mole}}{22400\ \text{cm}^3/\text{mole (STP)}}\right)\left(\frac{5 \times 10^{-8}\ \text{torr}}{760\ \text{torr}}\right)\left(\frac{273\text{K}}{300\text{K}}\right)\left(\frac{2\ \text{atoms}}{\text{molecule}}\right), \\ &= 3.22 \times 10^9 \text{atoms/cm}^3. \end{aligned} \qquad \text{(F.27)}$$

The number of ions of each charge surviving after a distance x is

$$N_{q_i}(x) = N_{q_i}(0)\exp\Big[-\sum_f \sigma_{q_i,q_f}\, N_T\, x\Big]. \qquad \text{(F.28)}$$

The number of protons produced by stripping from H^- per second in the 1000 cm region is then

$$\begin{aligned} N_{+1} &= \int_0^{1000} N_{-1}(x)\, N_T \sigma_{1,-1}\, \mathrm{d}x \\ &= \left[N_{-1}(0) \left(\frac{\sigma_{-1,1}}{\sigma_{-1,1} + \sigma_{-1,0}} \right) \left(1 - \exp\left[-(\sigma_{-1,1} + \sigma_{-1,0})\, N_T\, x \right] \right) \right]_0^{1000} \\ &\approx \left[N_{-1}(0)\, \sigma_{-1,1}\, N_T\, x \right]_0^{1000} . \end{aligned} \tag{F.29}$$

The number of H^- ions/sec for a 10 pA beam is

$$\begin{aligned} N_{-1}(0) &= \left(\frac{10 \times 10^{-12}\mathrm{C/s}}{1.602 \times 10^{-19}\mathrm{C/H^-}} \right) \\ &= 6.24 \times 10^7/\mathrm{s}, \end{aligned} \tag{F.30}$$

giving a background count rate of

$$\begin{aligned} N_{+1} &= (6.24 \times 10^7/\mathrm{s})(0.4 \times 10^{-19}\ \mathrm{cm^2})(3.22 \times 10^9/\mathrm{cm^3})(1000\ \mathrm{cm}) \\ &= 10.0\mathrm{H^+/s}. \end{aligned} \tag{F.31}$$

We demand time coincidence between the scintillator and the laser pulse. With pulses of 500 ns duration at 10 Hz, the number of protons in a 30 ns gate is

$$\begin{aligned} N_{+1} &= 10.0 \left(\frac{20 \times 10^{-9}}{10 \times 500 \times 10^{-6}} \right) \\ &= 6 \times 10^{-2}\mathrm{protons/gate}. \end{aligned} \tag{F.32}$$

In fact, this background was exceeded considerably because of a "halo" associated with the beam, the source of which has not yet been identified.

Appendix G

Scintillators and Photomultiplier Tubes

G.1 Scintillator calculations.

An estimate may be made of the light levels expected from a scintillator. For a thin absorber (in the Landau regime; see Landau, 1944), the most probable energy loss for 800 MeV protons traveling through 1 cm of organic scintillator may be calculated (see, for example, Rossi) to be approximately 1.8 MeV. (In fact, the distribution of energies from particles that deposit very little of their energy — and this defines a "thin" absorber — tends to be smeared by a high-energy tail, known as a Landau tail). Typically, a photon will be produced for every 100 eV deposited; so, with 100 protons incident in a micropulse, we would expect $\sim 1.8 \times 10^4$ photons to be produced in the scintillator.

The collection efficiency of the light guide system is unknown, but may be as low as 5%. The quantum efficiency of the photomultiplier tubes varies with wavelength as (Fernow, p. 161)

$$QE = 123.95 \frac{S_k}{\lambda}, \tag{G.1}$$

where S_k is the sensitivity, here 65 mA/W at 450 nm giving a quantum efficiency of 12%. We would therefore expect about 10^4 photoelectrons to be emitted from

the cathode in these circumstances, which, if released in 1 ns, would give a cathode peak current of 1.7 μA.

G.2 Amperex 2203B Photomultiplier Tube and Base.

The Amperex 2203B phototube (see the Amperex manual) was chosen for its high degree of linearity over a wide dynamic range. The trialkali (SbNaKCs) photocathodes deliver pulse linearity up to 10 μA, as opposed to the more common bialkali cathodes for which departures from linearity have been observed for currents as low as 10^{-10} A. The ten box-and-grid type linear focused stages provide a gain of 3 x 10^5 at 1700 V.

The circuit used for the base of the tube is illustrated in Figure G.1. The following features are included:

i) High current. The potential divider chain contains relatively low resistances throughout, in order to maintain a high current — in this case, 2 mA at 1700 V. In pulsed operation, the average divider current should be at least 100 times the maximum integrated anode current, which in our case would amount to approximately 100 x 200 mA x 25 ns x 10 Hz, giving 5 μA; 2 mA is therefore a very "stiff" base.

ii) Reservoir capacitors. Since we are operating in a pulsed mode, rather than drawing a continuous current from the tube, it is possible that the anode current can reach high instantaneous values; the capacitors, which recharge between pulses, are able to supply the necessary charge in order to avoid any significant change in the potentials of the last few dynodes. The capacitors are individually connected to ground so that if one stage is overloaded it does not "pull down" the next.

iii) Damping resistors. With the tube operating in the pulsed mode, a high frequency stray oscillation superimposed on the anode pulses may be observed

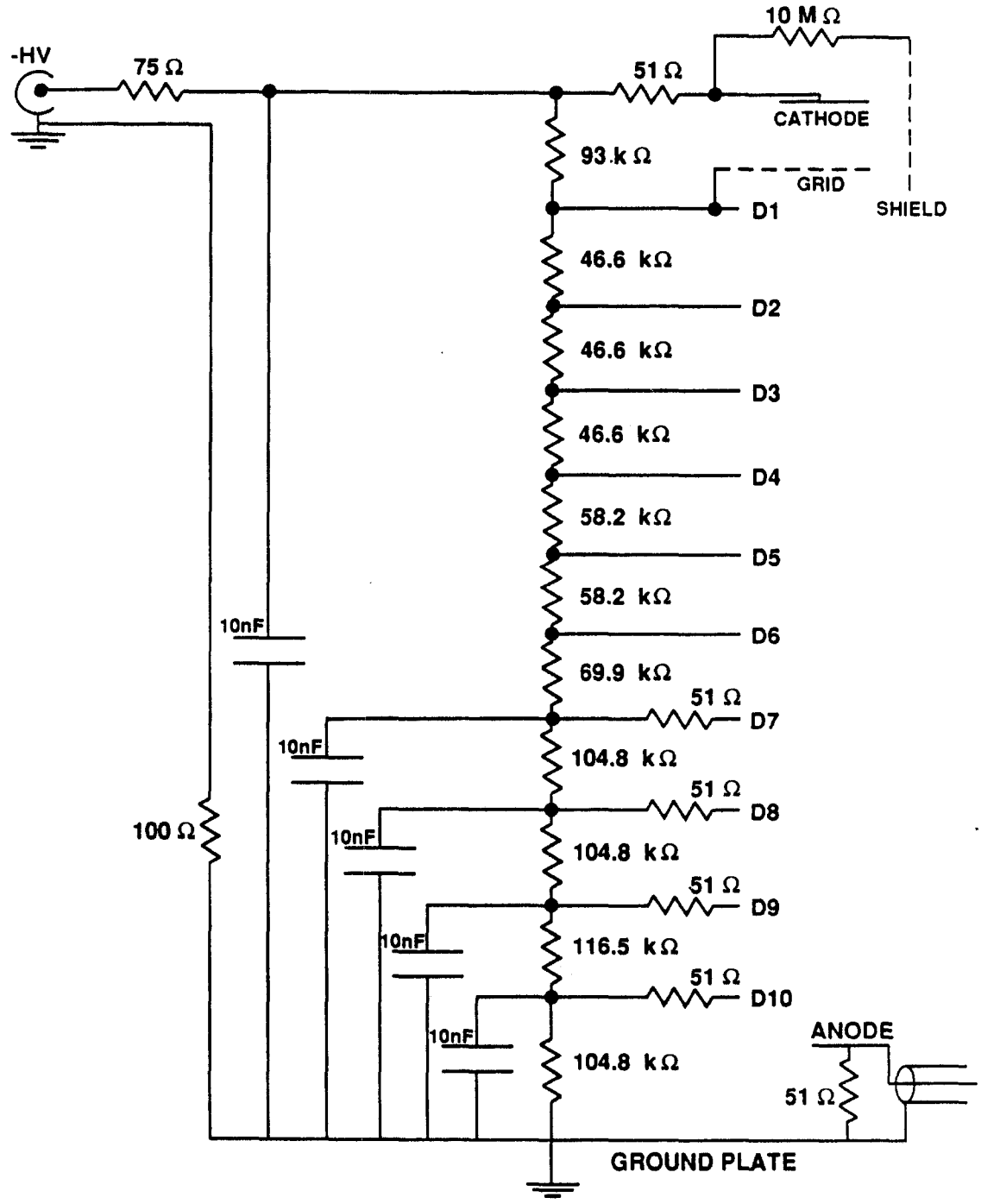

Figure G.1. Circuit diagram of PMT base.

when the anode current exceeds a certain level. The 51 Ω resistors in series with the last four dynodes helps to overcome this effect.

iv) Isolated HV ground. In order to prevent ground loops, a 100 Ω resistor is included between the ground lead of the high voltage cable and the case/signal ground. Likewise, the leads on all resistors were kept as short as possible to avoid creating inductive loops.

v) Electrostatic shield. Aluminum foil is wrapped around each tube, and maintained at the cathode potential to prevent any detrimental stray field effects. This shielding is itself wrapped in Mylar to prevent accidental grounding, and a 10 MΩ resistor lies between it and the cathode in case of such an occurrence. The electrostatic shielding is in addition to the usual magnetic shielding (of mu-metal).

The capacitance needed on the $(n+1)$th dynode may be approximated by assuming that the charge Q_c to be supplied by C_{n+1} is much greater than the charge Q_a carried by the pulse,

$$Q_a = \int I_a dt, \tag{G.2}$$

where I_a is the anode current pulse amplitude. Therefore,

$$C_{n+1} = \frac{Q_c}{V_{dn}} >> \frac{Q_a}{V_{dn}} = \frac{1}{V_{dn}} \int I_a dt. \tag{G.3}$$

Typically the voltage V_{dn} between dynodes is of the order of 200 V, and the integrated current for a pulse is at most a few nC; thus, the charge stored by each of the 10 nF capacitors is 500 times that required for the pulse. The charging time constant for the capacitors is the RC of the circuit, in this case somewhat less than 1 ms, which allows plenty of time for recharging between pulses.

Zener diodes are sometimes used to maintain a constant voltage across given stages; however, this has the disadvantage that the tube must be run at one voltage only in order to maintain the "taper" specified by the tube manufacturer.

Boutot, Nussli and Vallat (1983) contains an extremely useful review of photomultiplier technology and techniques.

Appendix H

Field Ionization

Great use has been made during this experiment of the phenomenon of field ionization, and it is worth exploring it in a little more depth. Strong magnets are used to tear the electron from excited neutral hydrogen atoms; as discussed in Chapter 1, the (transverse) magnetic field $B_\perp$ appears in the rest frame of the atom to be an electric field (also transverse) of strength (equation 1.2)

$$F_\perp = \gamma\beta c B_\perp. \tag{H.1}$$

This electric field lowers the potential barrier that binds the electron to the nucleus. An approximate formula may be obtained, from a classical model, for the critical field necessary to strip a given excited state. I am indebted to Dr. Randy Reeder (1989) for much of the material presented here.

For a hydrogen atom exposed to an external electric field $\mathbf{F} = F\hat{z}$, the potential seen by the electron is

$$V(r) = -\frac{e^2}{r} + ezF. \tag{H.2}$$

The potential barrier will be lowest in the $-\hat{z}$ direction (and highest in the $+\hat{z}$ direction). Since

$$\frac{\partial V}{\partial z} = \frac{e^2 z}{r^3} + eF, \tag{H.3}$$

there exists a saddle point at $(0, 0, -\sqrt{e/F})$. At this saddle point the potential energy is

$$\begin{aligned} V(r) &= -\frac{e^2}{\sqrt{e/F}} + e\left(\sqrt{e/F}\right)F \\ &= -e^{3/2}\sqrt{F} - e^{3/2}\sqrt{F} \\ &= -2e^{3/2}\sqrt{F}. \end{aligned} \tag{H.4}$$

Assuming that an electron with energy E greater than or equal to the potential energy at the saddle point can escape, we have

$$E = -2e^{3/2}\sqrt{F_c} \tag{H.5}$$

where F_c is the critical electric field. Thus,

$$F_c = \frac{E^2}{4e^3}. \tag{H.6}$$

If we use the Bohr energy levels,

$$E_n = -\frac{\mu e^4}{2n^2\hbar^2}, \tag{H.7}$$

we obtain a critical field of

$$\begin{aligned} F_c &= \left(\frac{\mu e^4}{2n^2\hbar^2}\right)^2 \cdot \frac{1}{4e^3} \\ &= \frac{\mu^2 e^5}{\hbar^4} \cdot \frac{1}{16n^4} \\ &= \frac{5.14 \times 10^9}{16n^4}\text{V/cm}. \end{aligned} \tag{H.8}$$

We may also take account of the first-order Stark effect. The energy of a Stark state labeled by the parabolic quantum numbers n_1, n_2 and m, where $n_1 + n_2 + |m| + 1 = n$, is (in atomic units)

$$E = -\frac{1}{2n^2} + \frac{3}{2}n(n_1 - n_2)F - ..... \tag{H.9}$$

The maximum shift occurs when $|m| = 0$, *i.e.*, when $n_1 - n_2$ is greatest. For states with $n_2 = 0$, $n_1 = n - 1$ (its largest value) and the states are called

extreme blue-shifted Stark states. When $n_1 = 0$, so $n_2 = n - 1$, the states are *extreme red-shifted Stark states.* One can show that the red-shifted states are confined to a region near the saddle point. For these states, then, the critical field for ionization is (to first order, in atomic units)

$$\begin{aligned} F_c &= \frac{E^2}{4} \\ &= \frac{1}{4}\left(\frac{1}{2n^2} + \frac{3}{2}n(n_1 - n_2)F\right)^2 \\ &= \frac{1}{4}\left(\frac{1}{2n^2} - \frac{3}{2}n(n-1)F\right)^2. \end{aligned} \tag{H.10}$$

Therefore,

$$\frac{1}{4n^4} + 2\frac{3n(n-1)F_c}{4n^2} - 4F_c + \frac{9}{4}n^4F_c^2 = 0. \tag{H.11}$$

This is a quadratic equation in F_c, which has the solution

$$F_c = \frac{\pm\sqrt{16n^2 + 30n + 9} + 5n + 3}{9n^5}; \tag{H.12}$$

for large n, where $n \approx n - 1$, this becomes

$$F_c = \frac{1}{9n^4}. \tag{H.13}$$

Although the extreme blue-shifted states have a lower critical field

$$F_c = \frac{\pm\sqrt{112n^2 - 66n + 9} + 11n - 3}{9n^5}, \tag{H.14}$$

which, for $n \approx n - 1$, becomes

$$F_c = \frac{1}{21.6n^4}, \tag{H.15}$$

they are not as susceptible to ionization as they are spatially localized away from the saddle point.

In each case, to obtain the field in V/cm, these results should be multiplied by the atomic unit of electric field,

$$F_a = 5.14 \times 10^9 \text{ V/cm}. \tag{H.16}$$

These results ignore tunneling, the rate of which increases exponentially with field. They are, however, in fairly good agreement with experiment.

Appendix I

Effects of Small Laser Misalignments

As the laser beam is sent through the system of three rotating mirrors known as the "spider" (see Appendix A), any slight angular misalignment of the laser will cause the spot to wobble at the interaction region. (A spatial displacement will also cause wobble, but if the beam enters the scattering chamber parallel to the axis of rotation then there will be no angular wobble, which is the important factor in determining the Doppler tuning). This appendix aims to discuss the consequences of an angular misalignment upon the interaction angle α of the two beams. It is assumed that the mirrors in the spider system itself are perfectly aligned — perhaps an unjustified assumption, but modifications to the derivation presented here may easily be made should it be discovered that this is not the case.

The main use of this work may be in fine scanning near the "magic" or Doppler-free angle, at which the barycentric angle α' is 90°. At this angle, defined by $\beta = -\cos\alpha$, the momentum spread does not contribute to the resolution (to first order — see equation E.2), and the resolution is therefore optimized. In order to observe structure at or near this angle, it may be desirable to take steps smaller than those currently possible in the Big Chamber (31 μrads); this may be done by using the last mirror prior to the chamber to make small changes in the angle at which the beam enters the chamber, and calculating the resulting

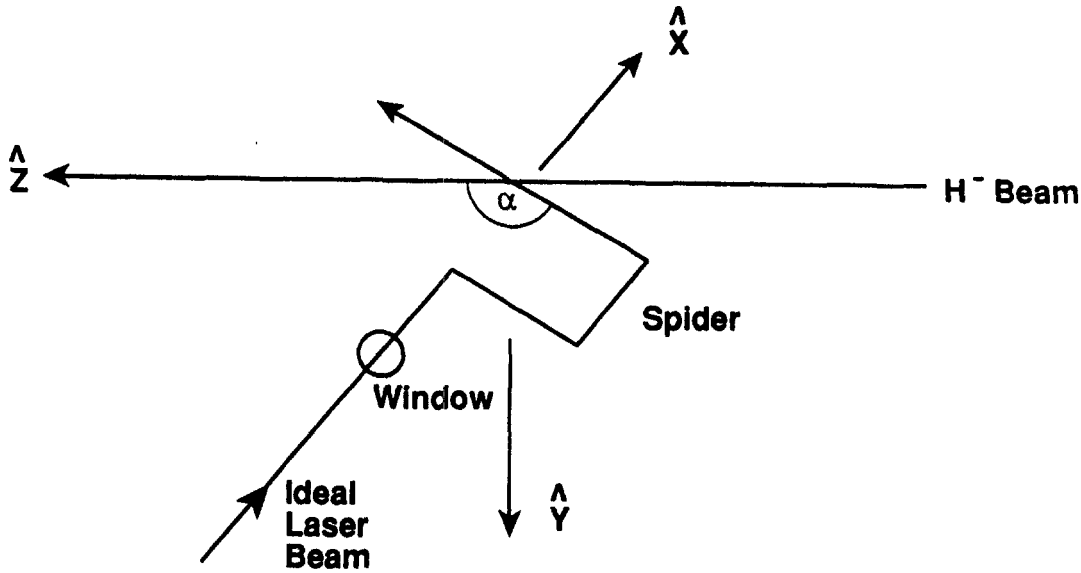

Figure I.1. Ideal path of laser beam through "spider" mirror system.

change in α. Mirror mounts are available that take the necessary steps of just a few microradians.

I.1 Definitions.

Let us define the direction of propagation of the H^- beam — from South to North in the HiRAB building — as the $\hat{z}$ axis, and the horizontal direction perpendicular to the H^- beam and in which the laser enters the scattering chamber — from West to East in HiRAB — as the $\hat{x}$ axis. To complete a right-handed coordinate system, the (downward) vertical direction becomes the $\hat{y}$ axis. This is illustrated in Figure I.1, which shows the ideal path of the laser beam through the spider.

If we use vectors consisting of direction cosines to define the direction of propagation of laser light, then the input and output beams, of directions $\vec{a}$, $\vec{b}$ respectively, are related by

$$\vec{b} = \underline{\mathbf{S}}\vec{a}, \tag{I.1}$$

where $\underline{\mathbf{S}}$ is a transformation matrix, and in the ideal situation

$$\vec{a} = \begin{pmatrix} 1 \\ 0 \\ 0 \end{pmatrix}, \vec{b} = \begin{pmatrix} 0 \\ -\sin\alpha \\ -\cos\alpha \end{pmatrix}. \tag{I.2}$$

I.2 The Transformation Matrix $\underline{\mathbf{S}}$.

The transformation matrix $\underline{\mathbf{S}}$ may be derived by first considering reflection from a mirror. If an incident ray has direction $\hat{\imath}$ and the normal has direction $\hat{n}$, then the reflected ray will be in direction

$$\hat{r} = -(\hat{n}.\hat{\imath})\hat{n} + (\hat{n} \times \hat{\imath}) \times \hat{n}. \tag{I.3}$$

The spider is effectively a mirror with

$$\hat{n} = -\frac{1}{\sqrt{2}} \begin{pmatrix} 1 \\ \sin\alpha \\ \cos\alpha \end{pmatrix}. \tag{I.4}$$

Using in turn the three basis vectors

$$\vec{a} = \hat{\imath} = \begin{pmatrix} 1 \\ 0 \\ 0 \end{pmatrix}, \begin{pmatrix} 0 \\ 1 \\ 0 \end{pmatrix}, \begin{pmatrix} 0 \\ 0 \\ 1 \end{pmatrix}, \tag{I.5}$$

we find

$$\underline{\mathbf{S}} = \begin{pmatrix} 0 & -\sin\alpha & -\cos\alpha \\ -\sin\alpha & \cos^2\alpha & -\sin\alpha\cos\alpha \\ -\cos\alpha & -\sin\alpha\cos\alpha & \sin^2\alpha \end{pmatrix}. \tag{I.6}$$

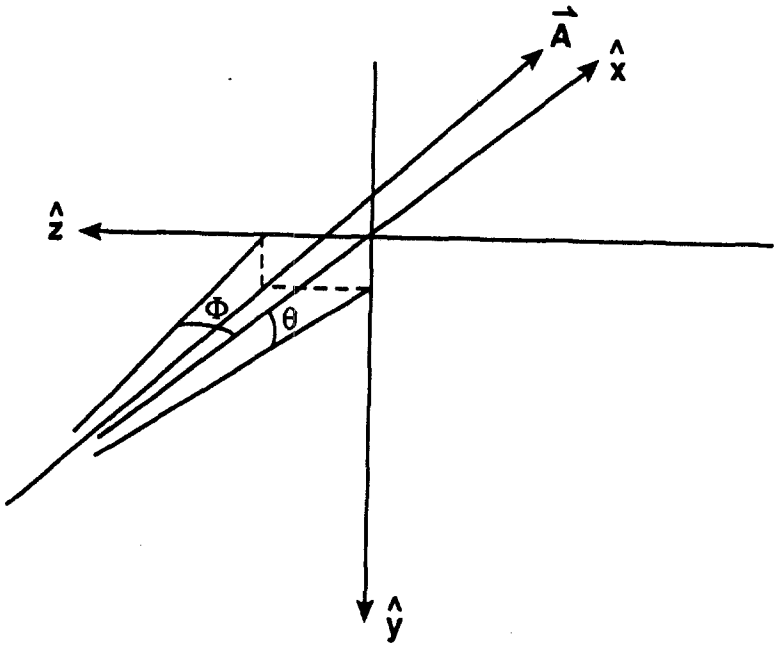

Figure I.2. Angular displacements from $\hat{x}$ are θ in the $+\hat{y}$ direction, ϕ in the $+\hat{z}$ direction.

I.3 Off-Axis Input Beam.

Let the angular displacements from the ideal input beam be θ in the $+\hat{y}$ direction and ϕ in the $+\hat{z}$ direction, as shown in Figure I.2. Then the vector representing the input beam direction becomes

$$\vec{a} = \begin{pmatrix} \cos\theta\cos\phi \\ \sin\theta \\ \sin\phi \end{pmatrix}, \tag{I.7}$$

whence the transformed output beam direction

$$\begin{aligned} \vec{b} &= \underline{S}\vec{a} \\ &= \begin{pmatrix} -\sin\alpha\sin\theta - \cos\alpha\sin\phi \\ -\sin\alpha\cos\theta\cos\phi + \cos^2\alpha\sin\theta - \sin\alpha\cos\alpha\sin\phi \\ -\cos\alpha\cos\theta\cos\phi - \sin\alpha\cos\alpha\sin\theta + \sin^2\alpha\sin\phi \end{pmatrix}. \end{aligned} \tag{I.8}$$

For small angles θ, ϕ this becomes

$$\vec{b} \approx \begin{pmatrix} -\theta\sin\alpha - \phi\cos\alpha \\ -\sin\alpha + \theta\cos^2\alpha - \phi\sin\alpha\cos\alpha \\ -\cos\alpha - \theta\sin\alpha\cos\alpha + \phi\sin^2\alpha \end{pmatrix}. \tag{I.9}$$

The angle of intersection of the laser and particle beams will then be α', where

$$\cos\alpha' = -\vec{b}\cdot\hat{z} \approx \cos\alpha + \theta\sin\alpha\cos\alpha + \phi\sin^2\alpha. \tag{I.10}$$

If we wish to constrain the angles θ, ϕ such that no angular displacement takes place out of the plane of rotation, then, as the angle θ is changed, the angle ϕ must be changed also such that $\vec{b}\cdot\hat{x} = 0$. This gives

$$\theta\sin\alpha = -\phi\cos\alpha \tag{I.11}$$

(where θ and ϕ are still small angles). If this is the case, the angle of intersection α' is then given by

$$\cos\alpha' \approx \cos\alpha - \phi. \tag{I.12}$$

Thus, at a nominal angle α, very small steps may be taken to adjust the angle at which the laser beam enters the scattering chamber, resulting in well-determined small changes in the actual angle of intersection α'.

Appendix J

Data

This appendix contains plots of all analyzed runs containing data pertaining to the high-lying resonance studies, both in zero field and with applied electric fields. The graphs show relative cross section *vs.* photon energy (eV). The units of relative cross section should be close to $10^{-6}a_0^2$.

J.1 Zero Field Data.

J.1.1 Resonances Converging on $n = 5$.

The following data show the production of H° in $n = 4$ (and above) as a function of photon energy.

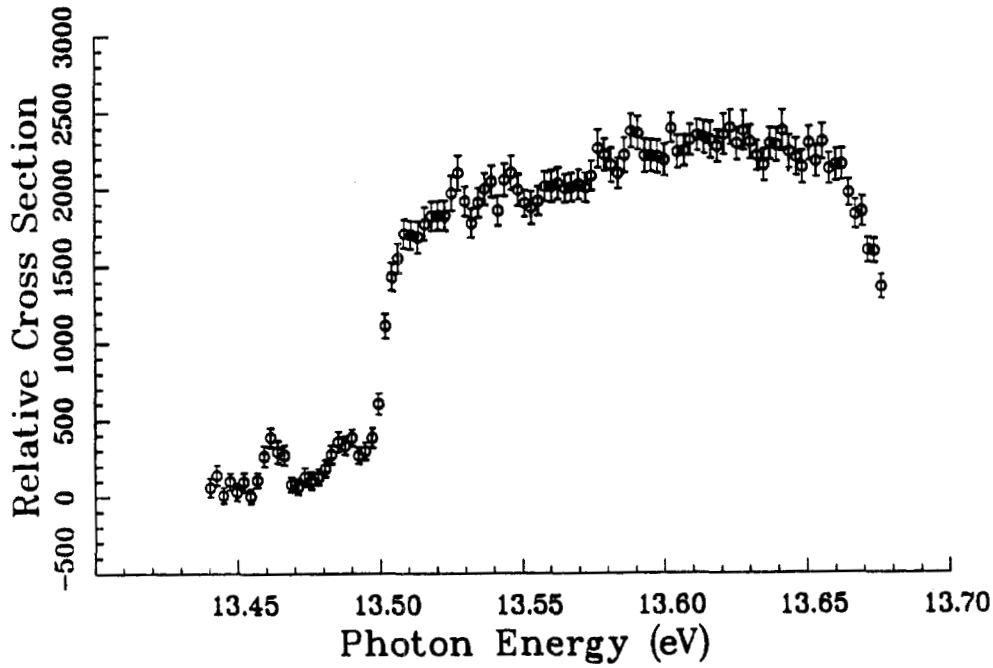

Figure J.1. Run 584.

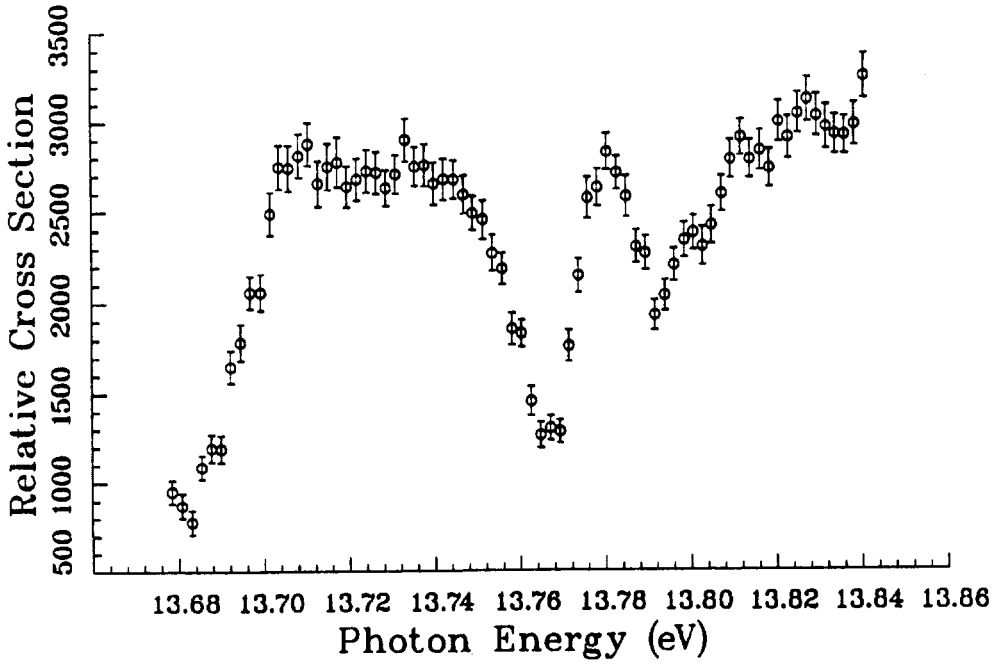

Figure J.2. Run 585.

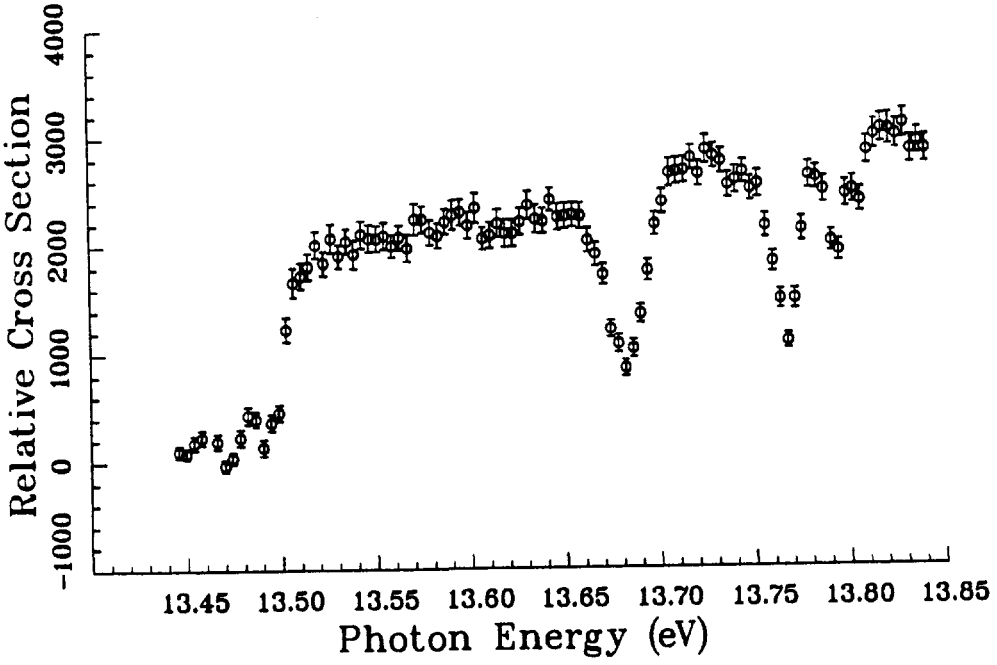

Figure J.3. Run 587.

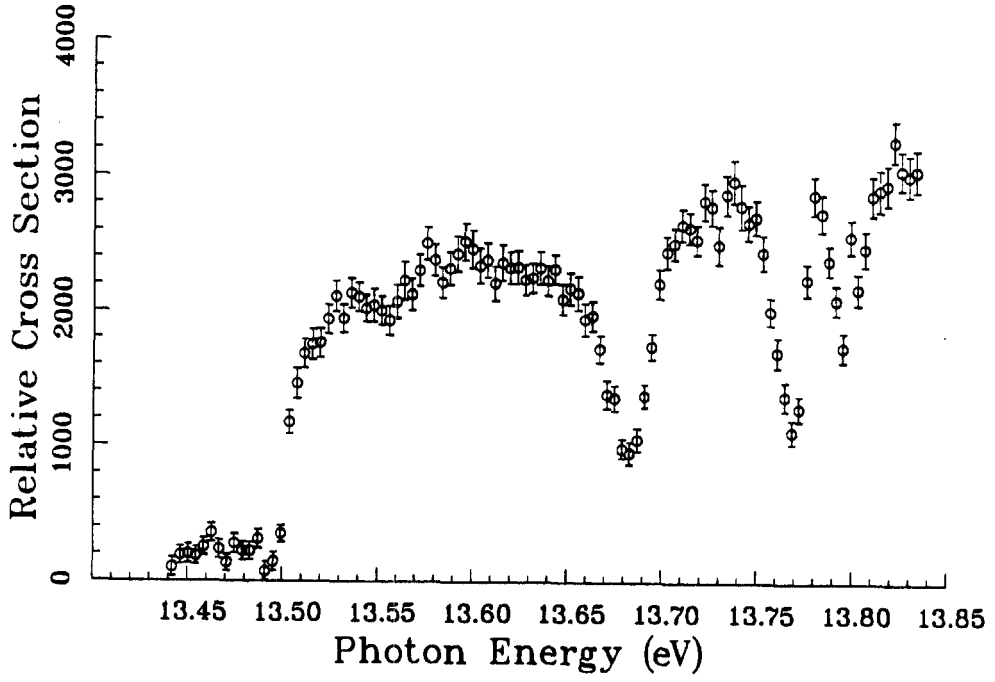

Figure J.4. Run 588.

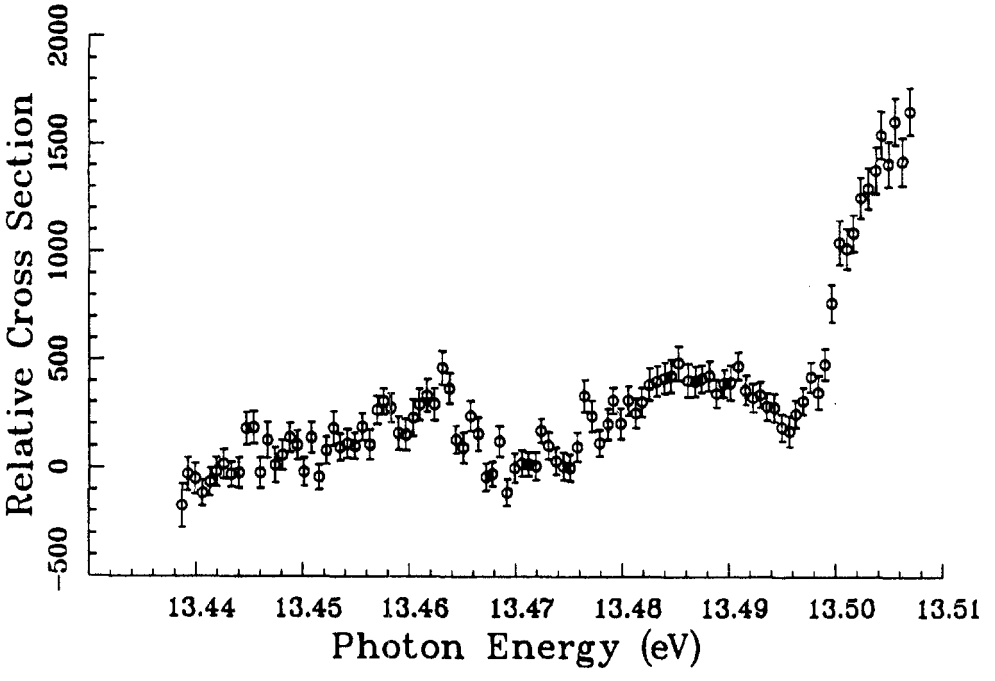

Figure J.5. Run 589.

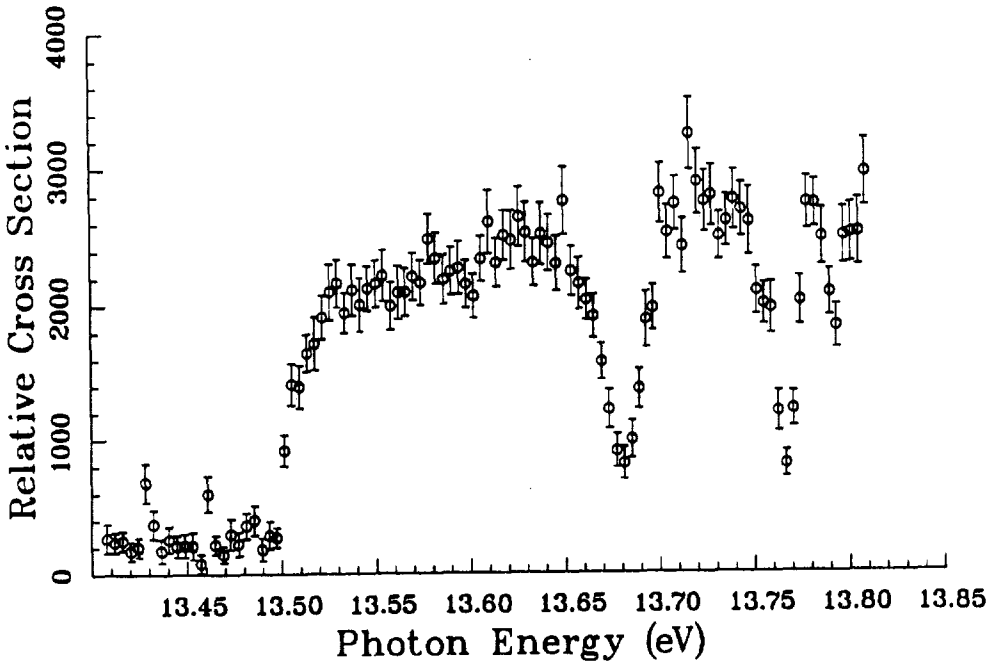

Figure J.6. Run 643.

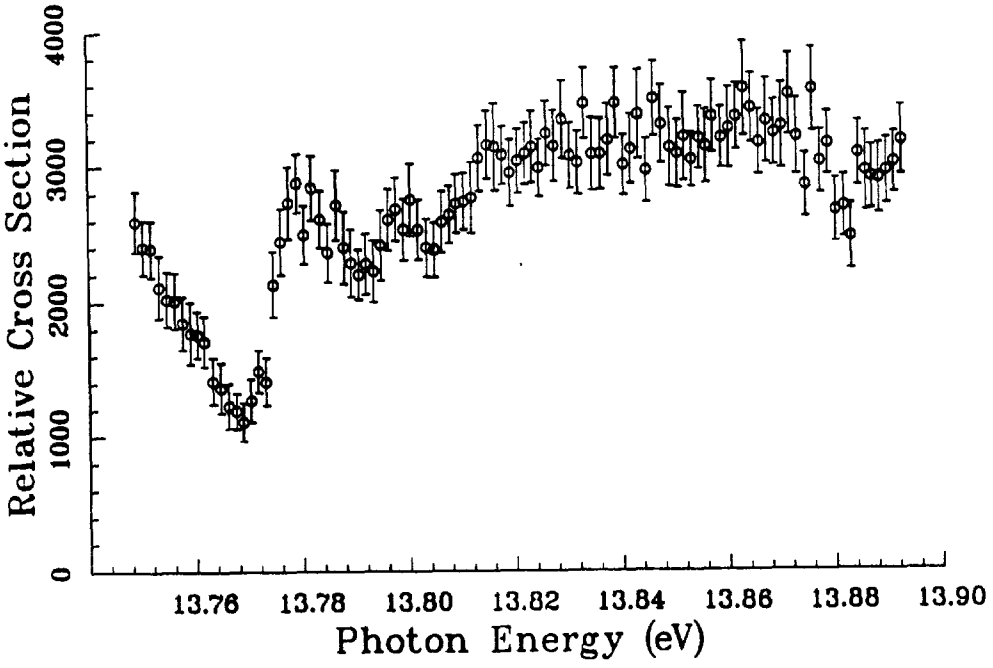

Figure J.7. Run 657.

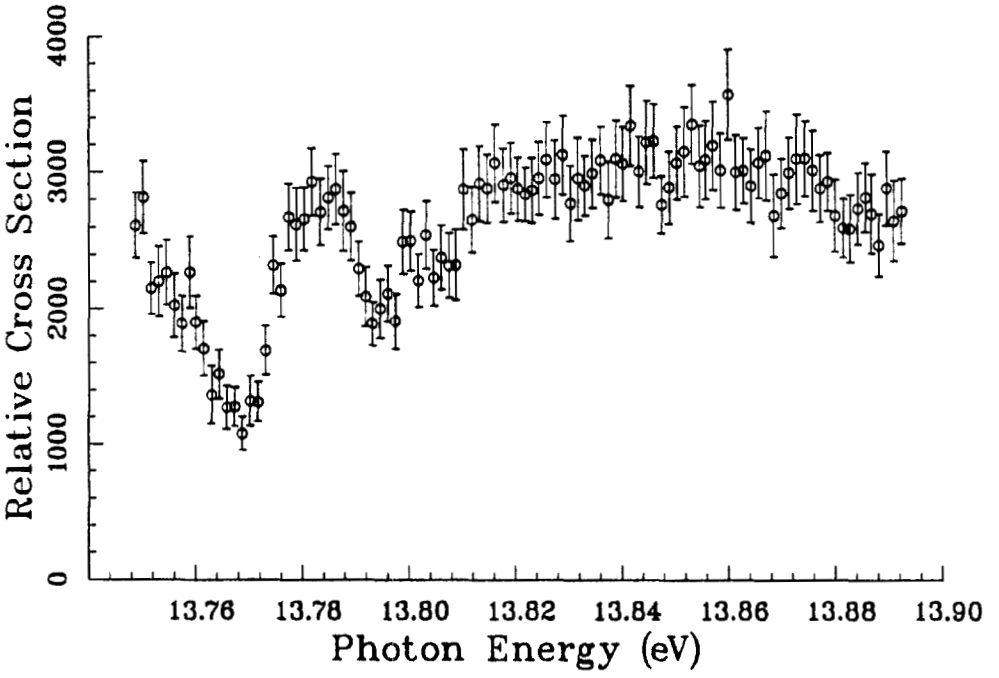

Figure J.8. Run 658.

J.1.2 Resonances Converging on $n = 6$.

The following data show the production of H° in $n = 5$ (and above) as a function of photon energy, with no applied electric field.

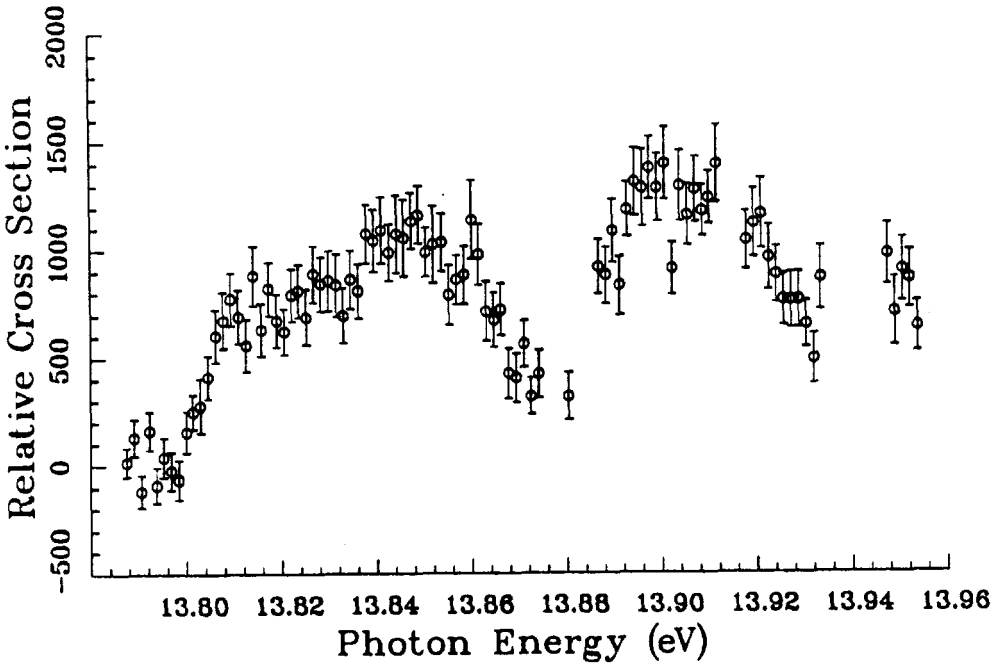

Figure J.9. Run 543.

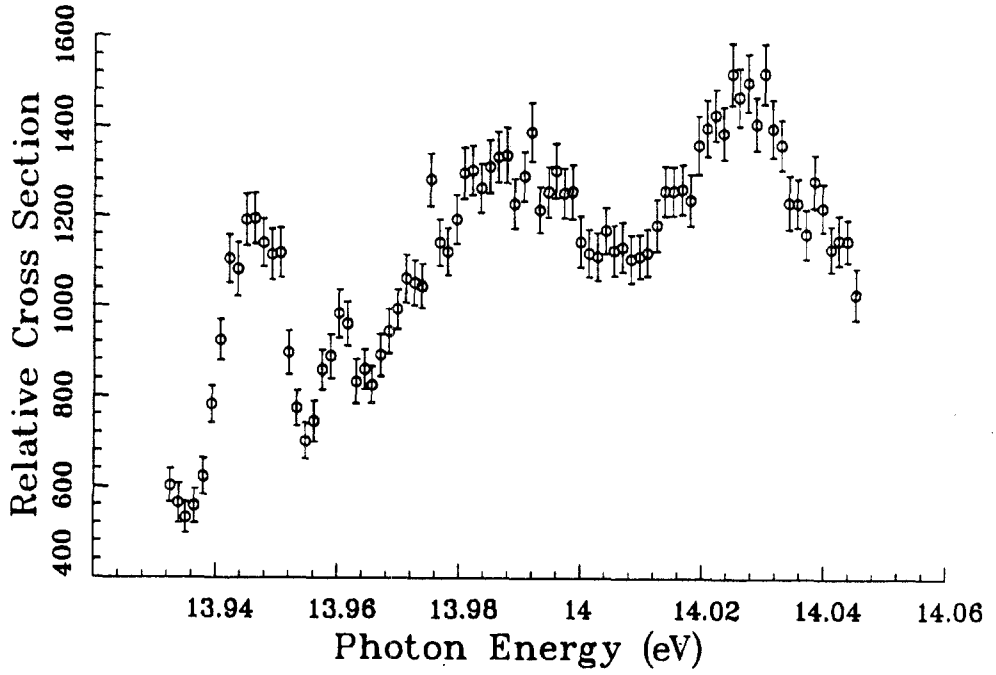

Figure J.10. Run 569.

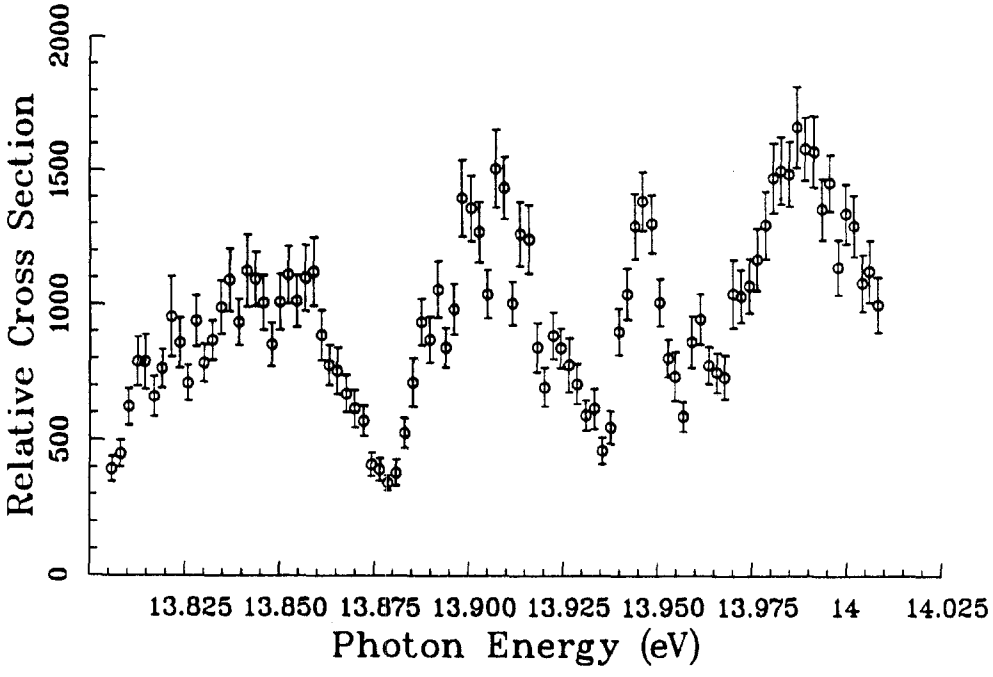

Figure J.11. Run 572.

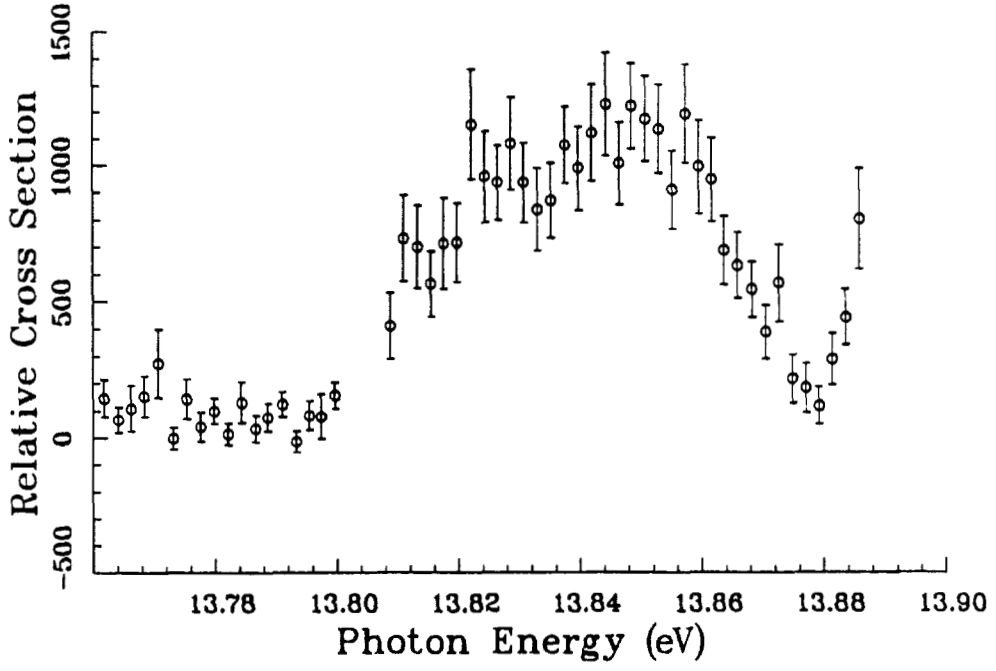

Figure J.12. Run 573.

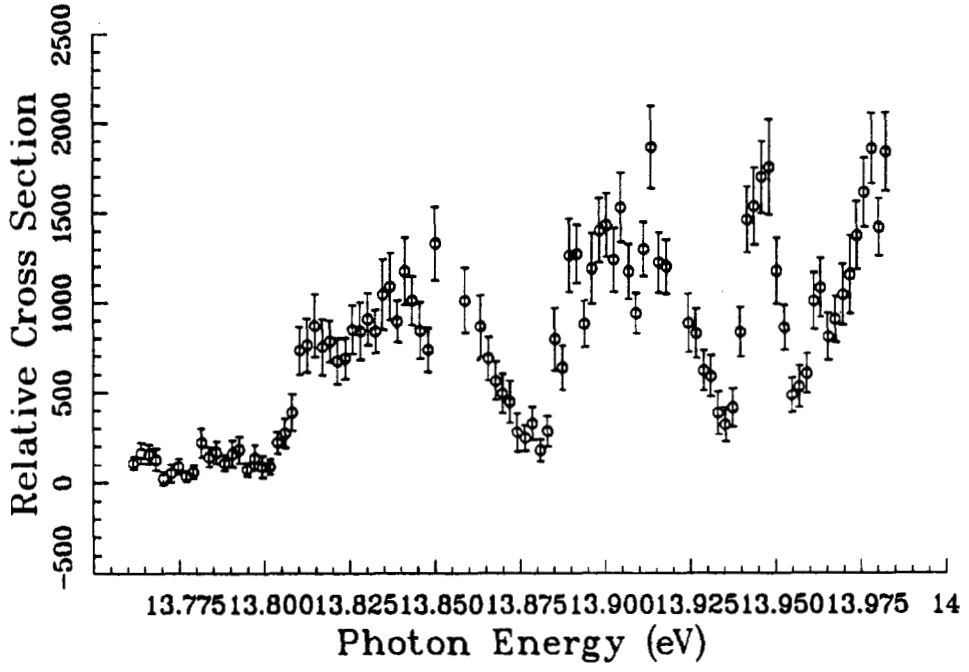

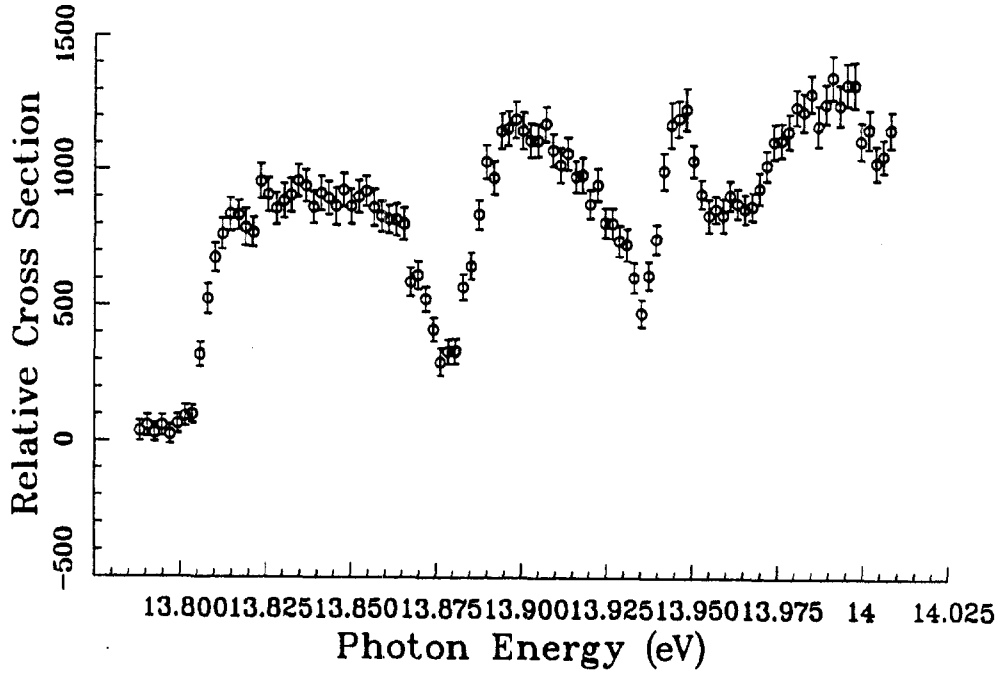

Figure J.14. Run 590.

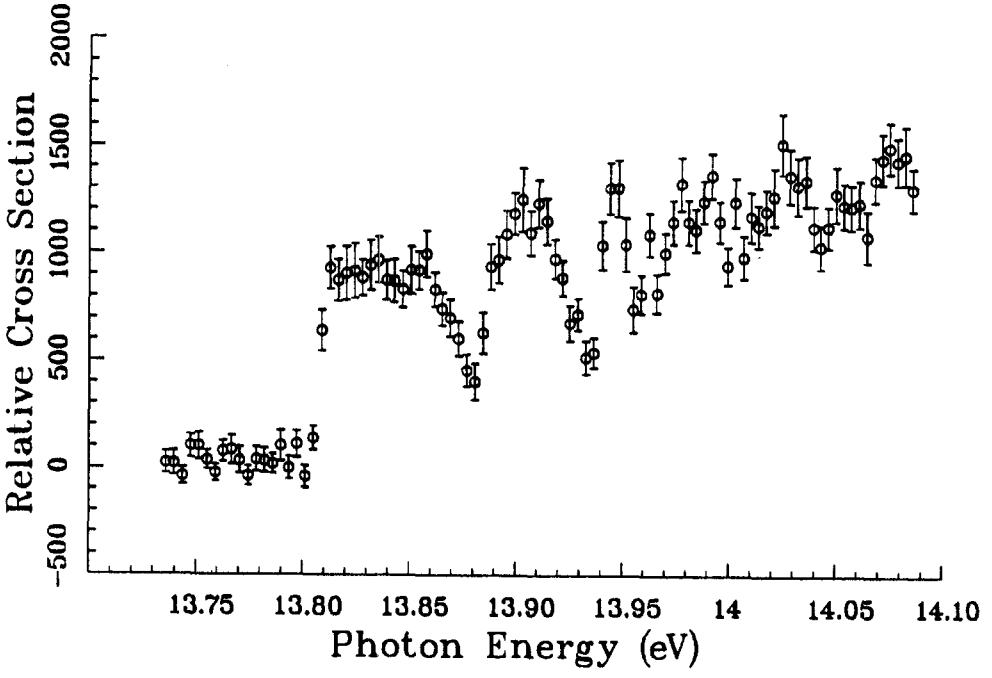

Figure J.15. Run 640.

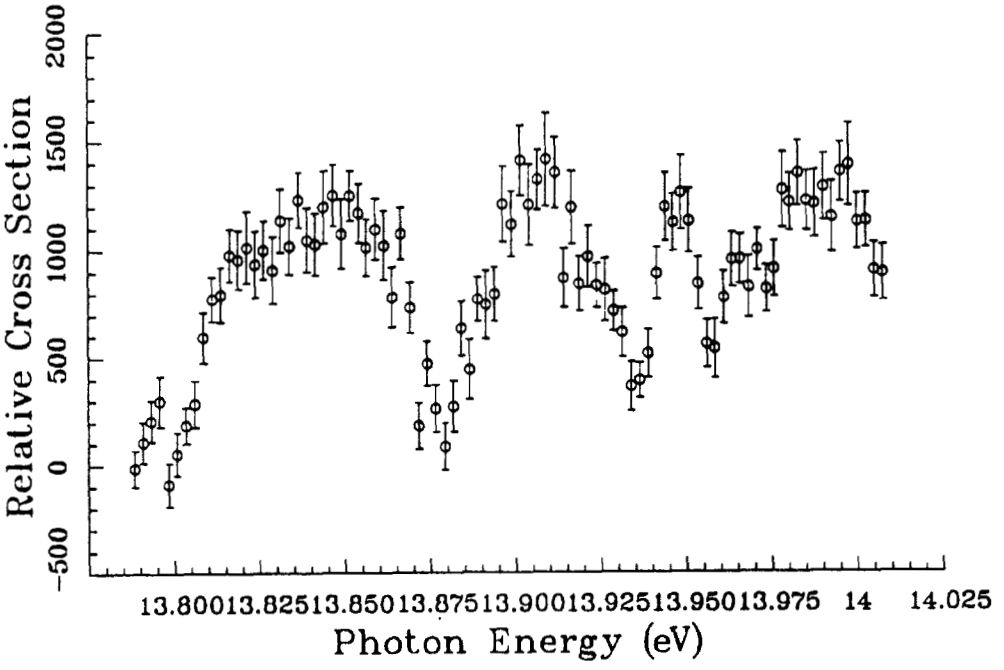

Figure J.16. Run 670.

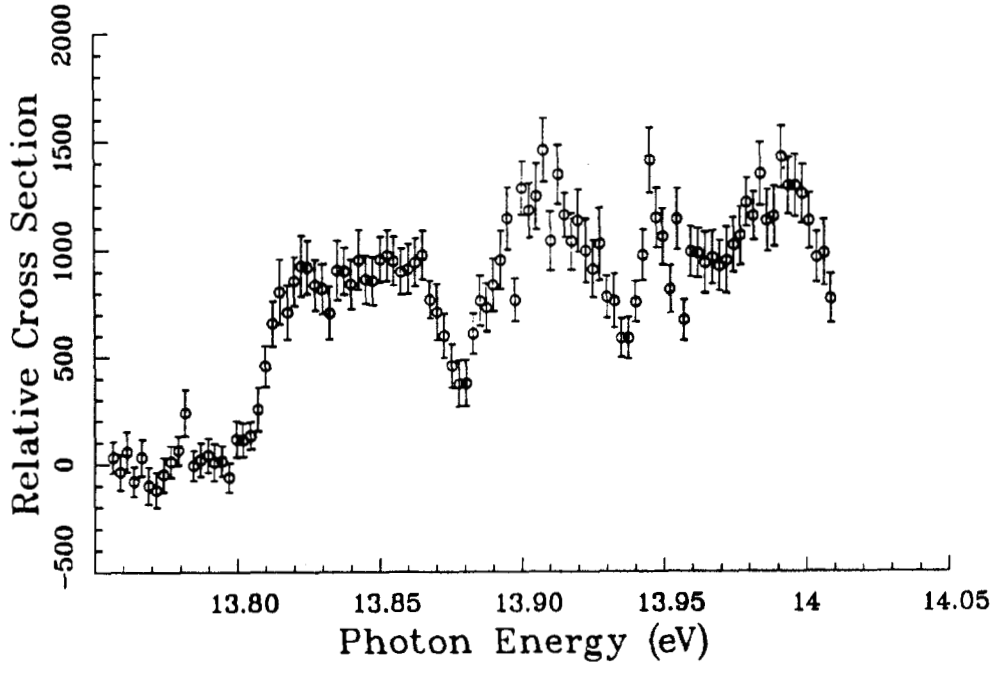

Figure J.17. Run 671.

J.1.3 Resonances Converging on $n = 7$.

The following data show the production of H° in $n = 6$ (and above) as a function of photon energy, with no applied electric field.

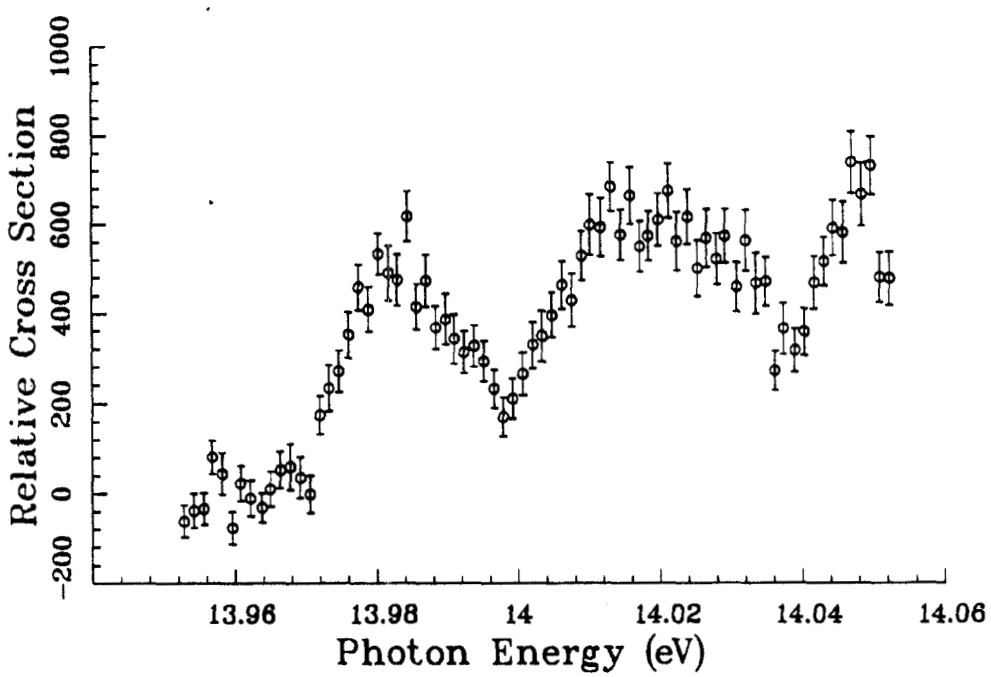

Figure J.18. Run 591.

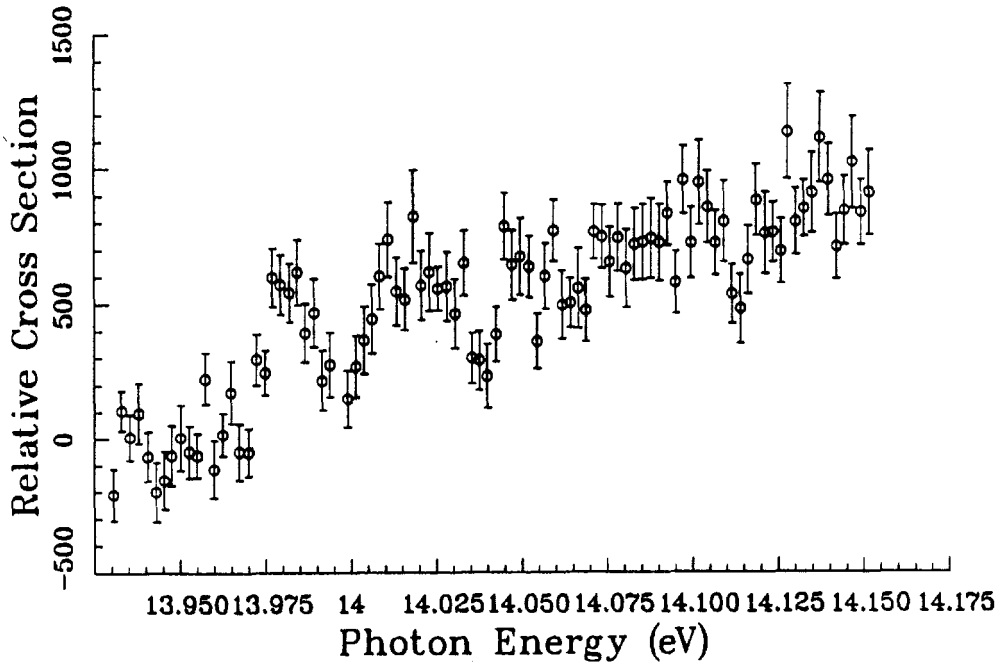

Figure J.19. Run 697.

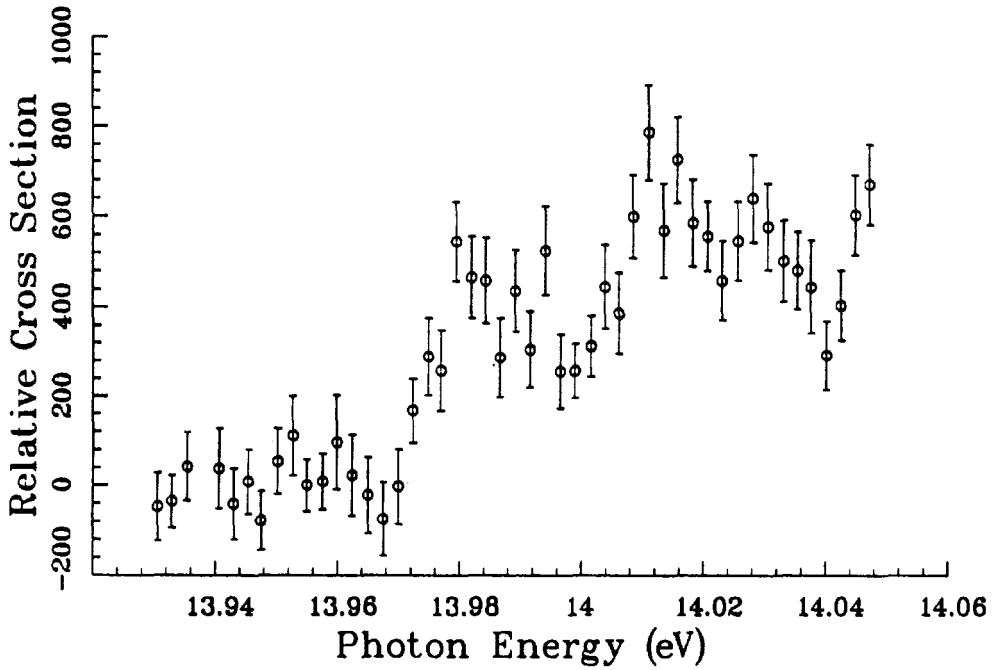

Figure J.20. Run 703.

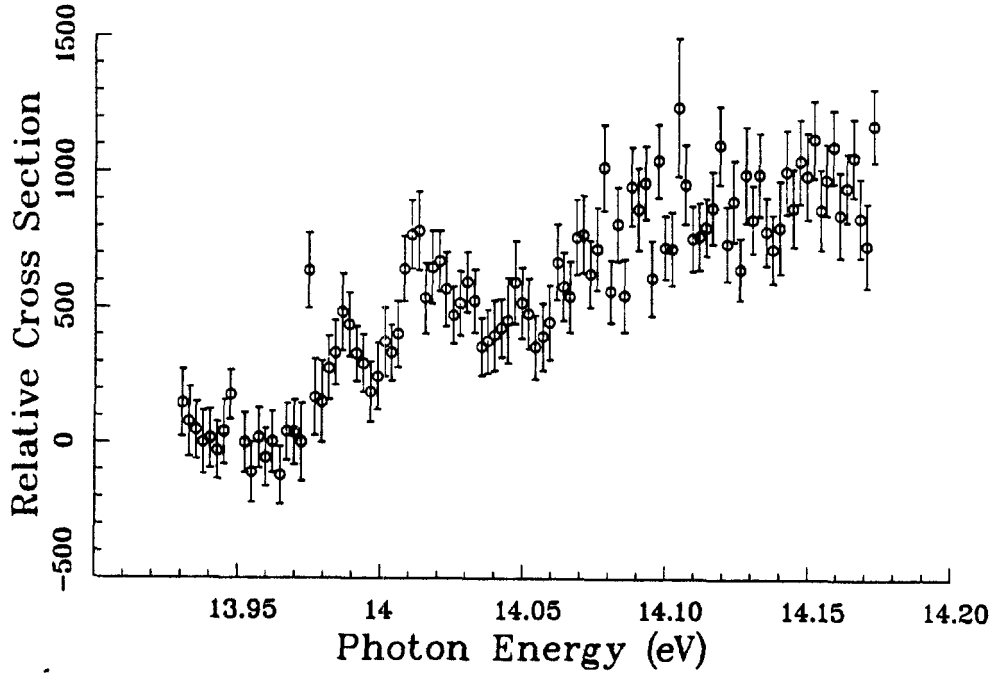

Figure J.21. Run 704.

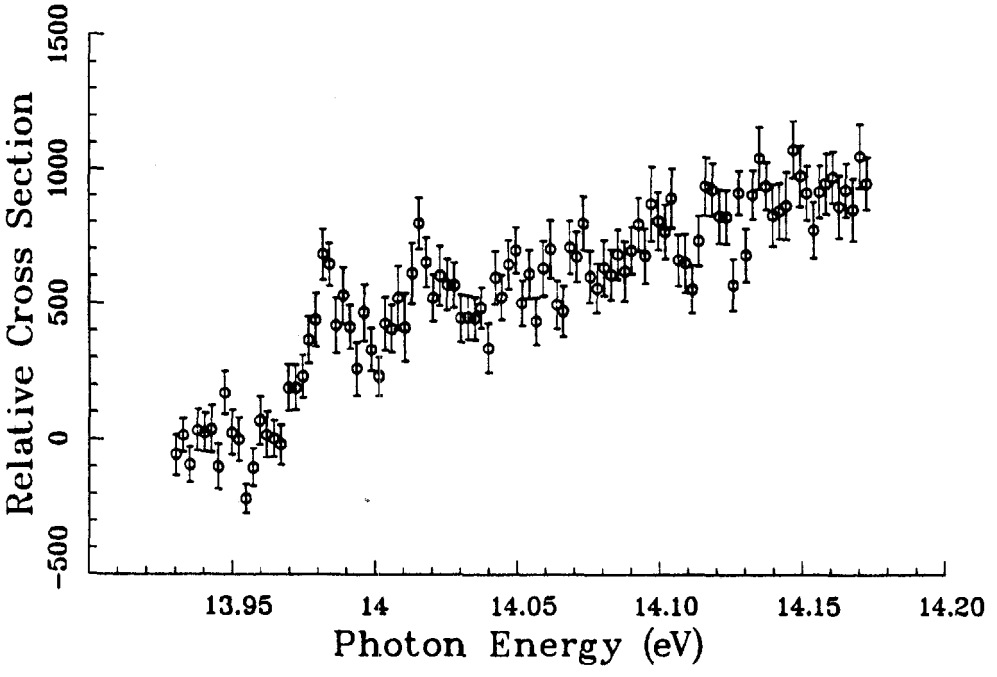

Figure J.22. Run 705.

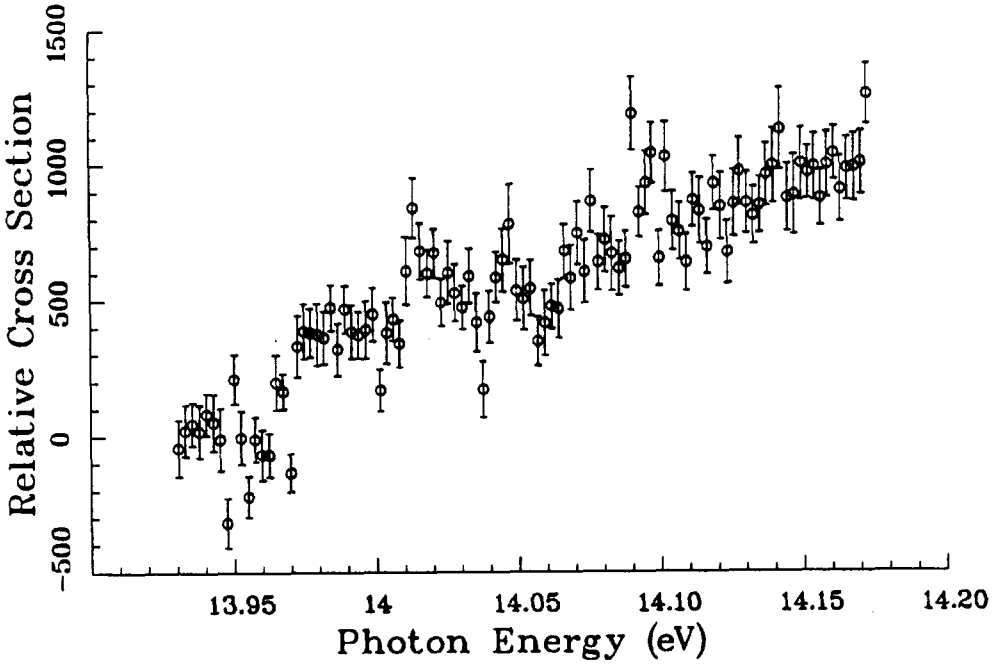

Figure J.23. Run 706.

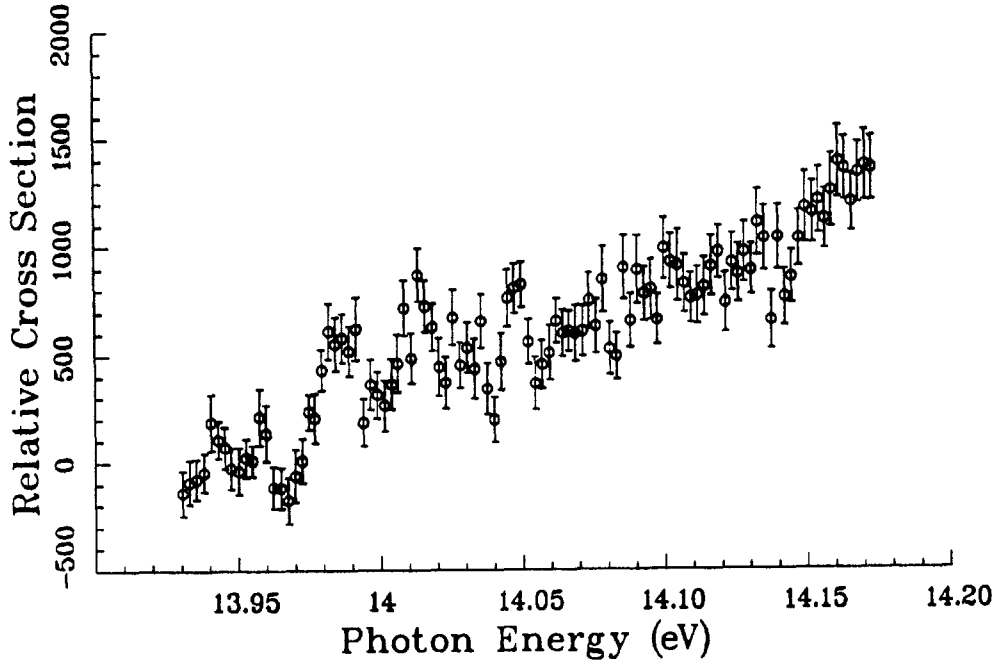

Figure J.24. Run 707.

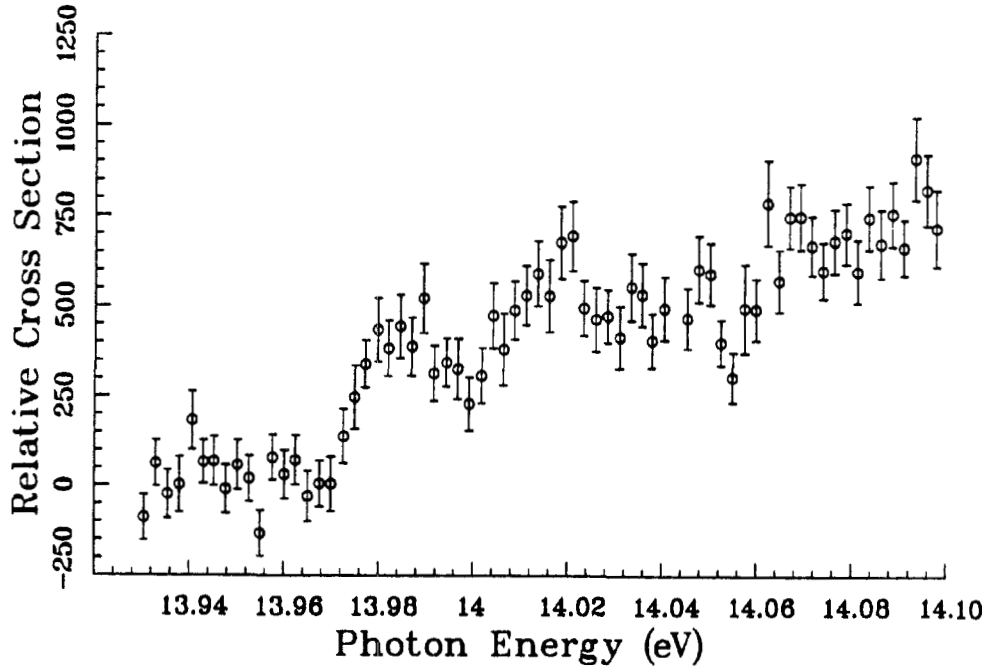

Figure J.25. Run 709.

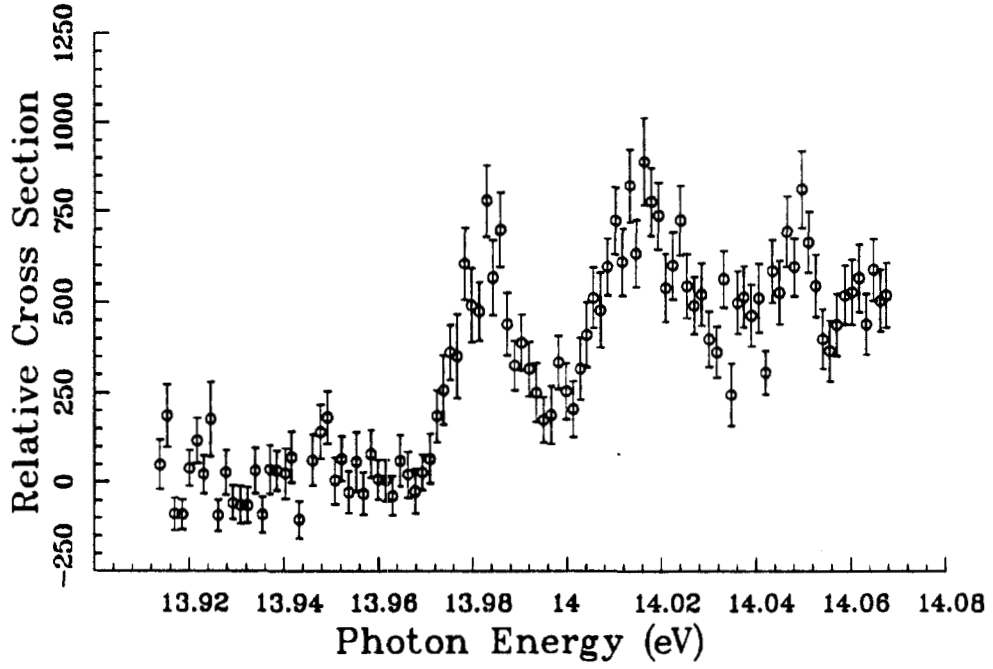

Figure J.26. Run 723.

J.1.4 Resonances Converging on $n = 8$.

The following data show the production of H° in $n = 7$ (and above) as a function of photon energy, with no applied electric field.

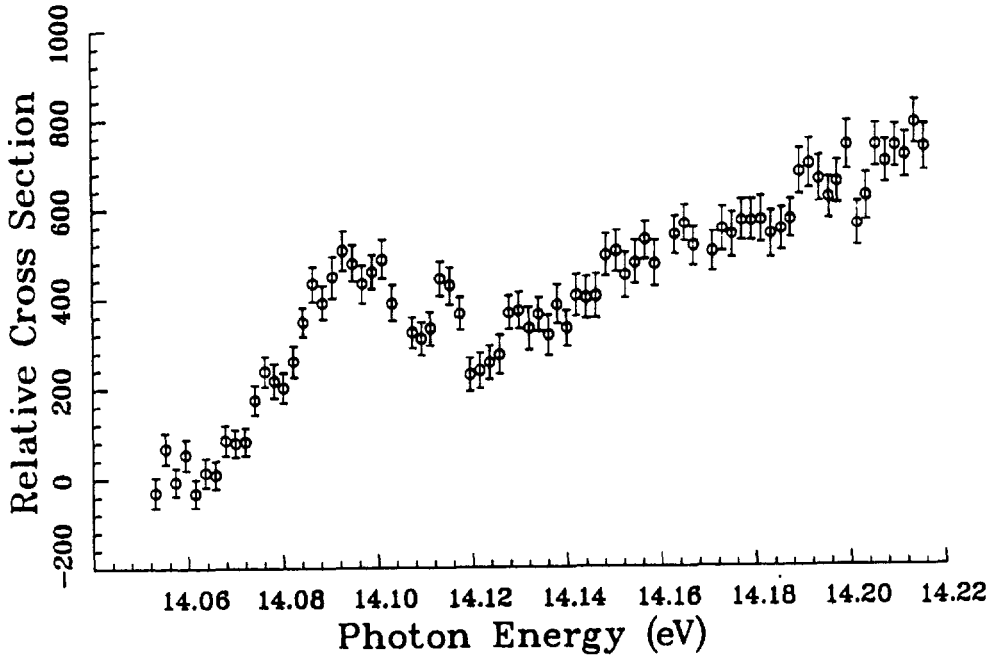

Figure J.27. Run 605.

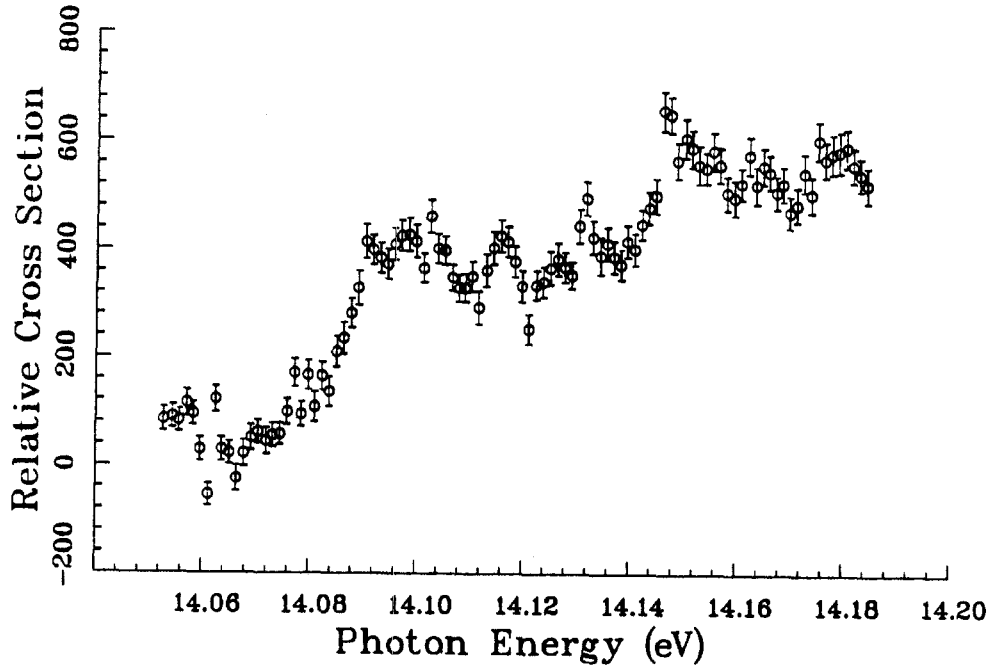

Figure J.28. Run 606.

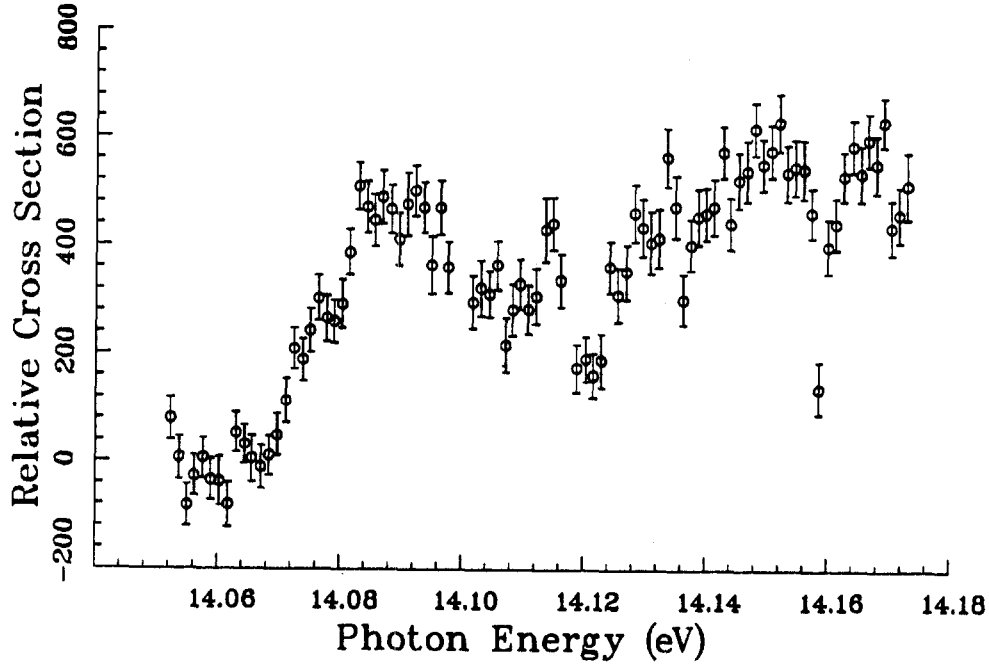

Figure J.29. Run 607.

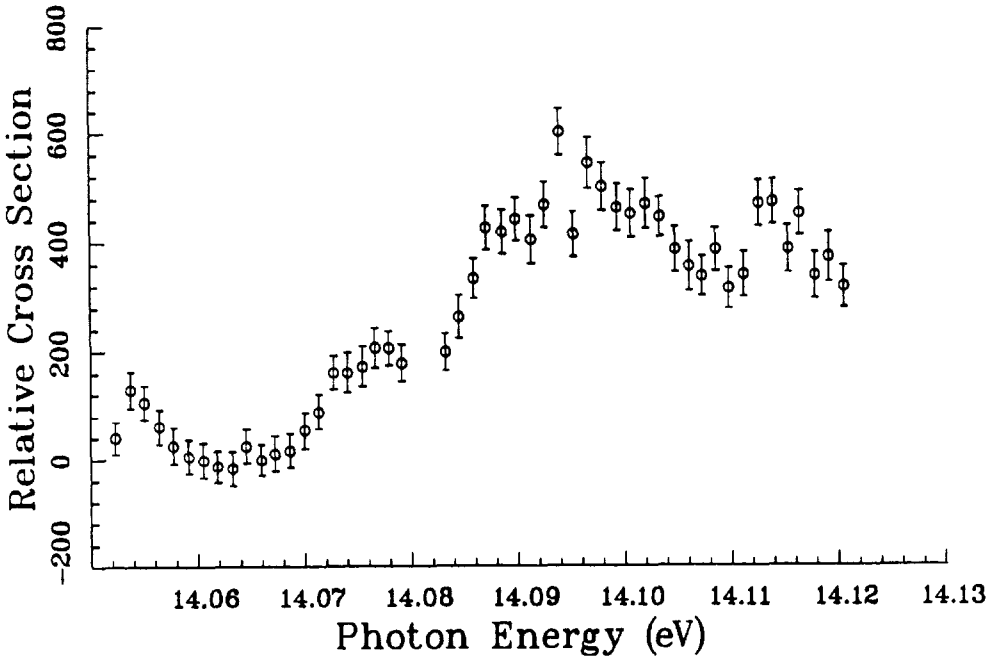

Figure J.30. Run 608.

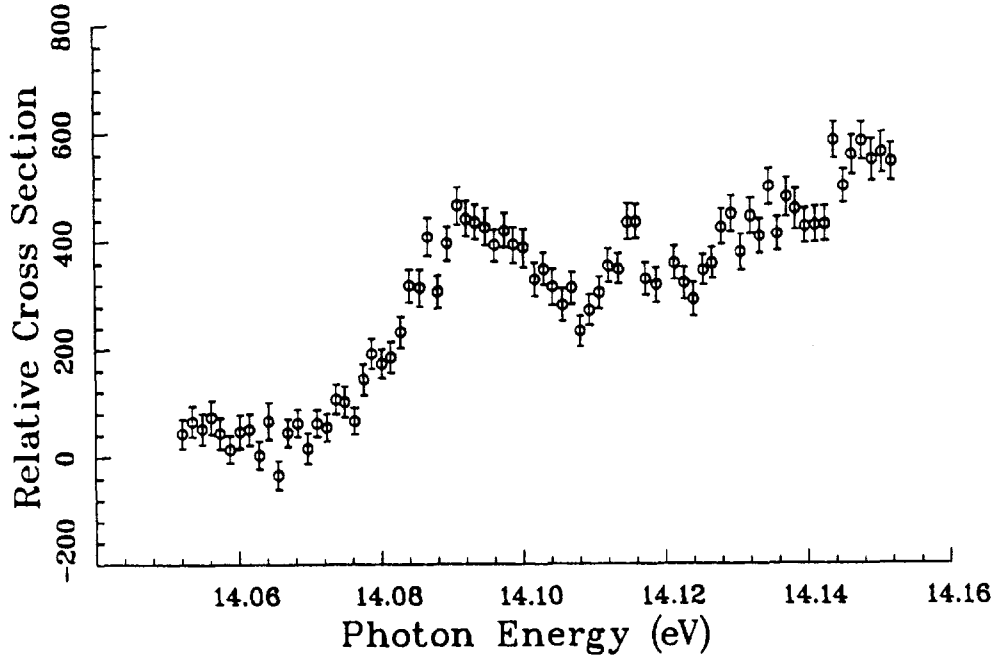

Figure J.31. Run 609.

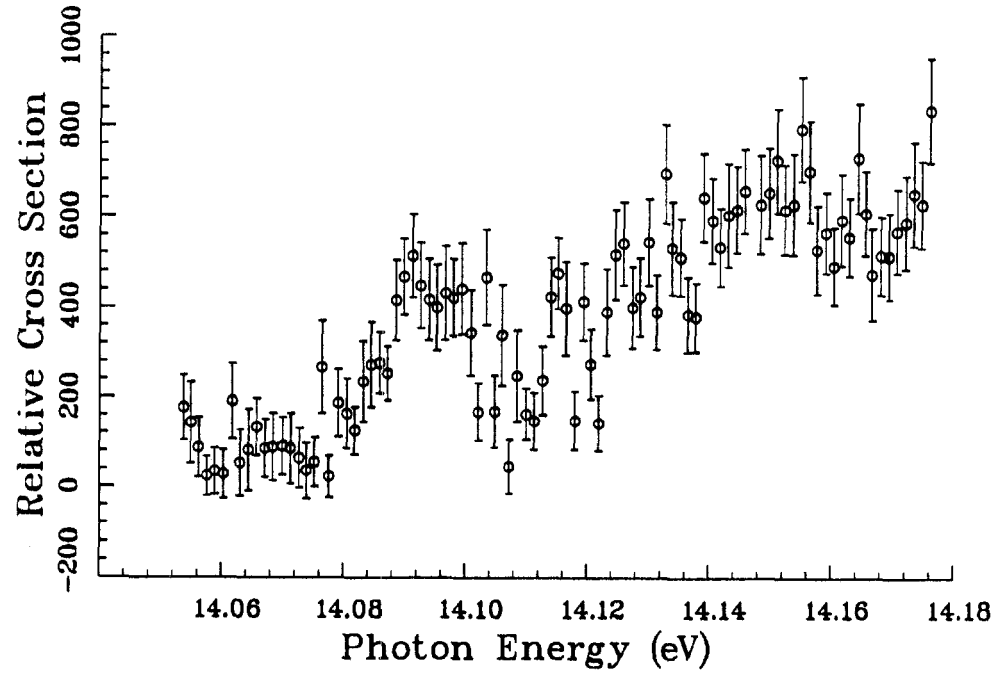

Figure J.32. Run 616.

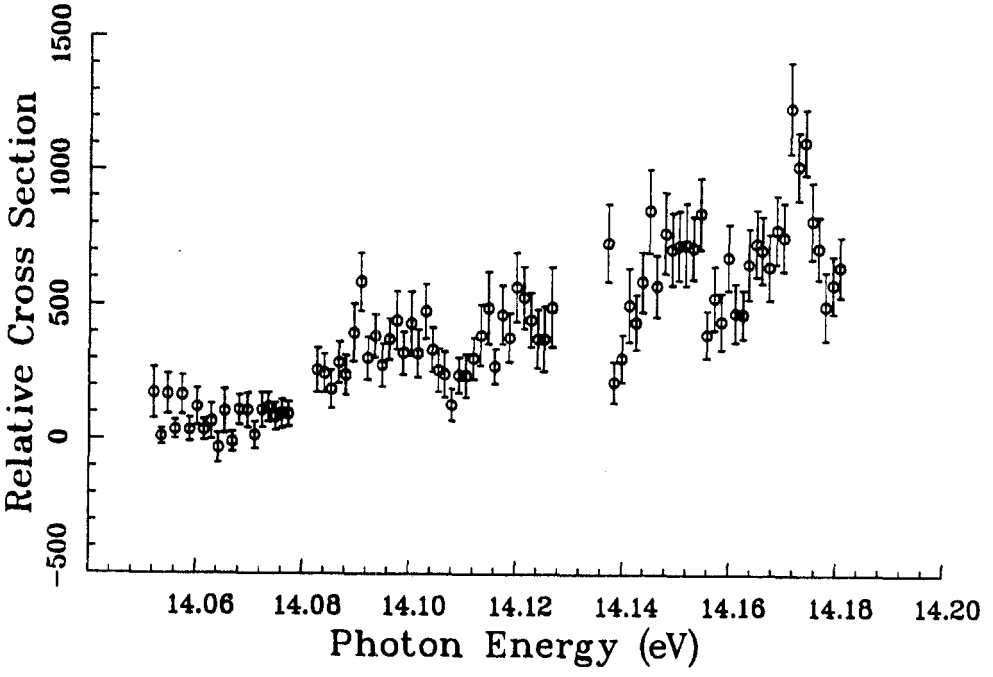

Figure J.33. Run 617.

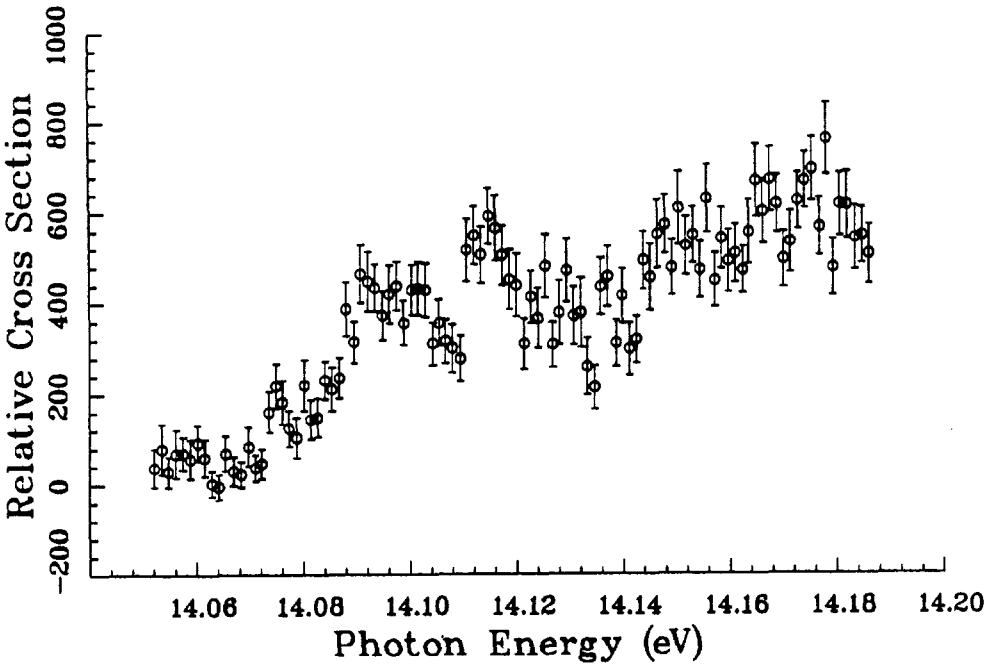

Figure J.34. Run 623.

J.1.5 Resonances Converging on $n = 9$.

The following data show the production of H° in $n = 8$ (and above) as a function of photon energy, with no applied electric field.

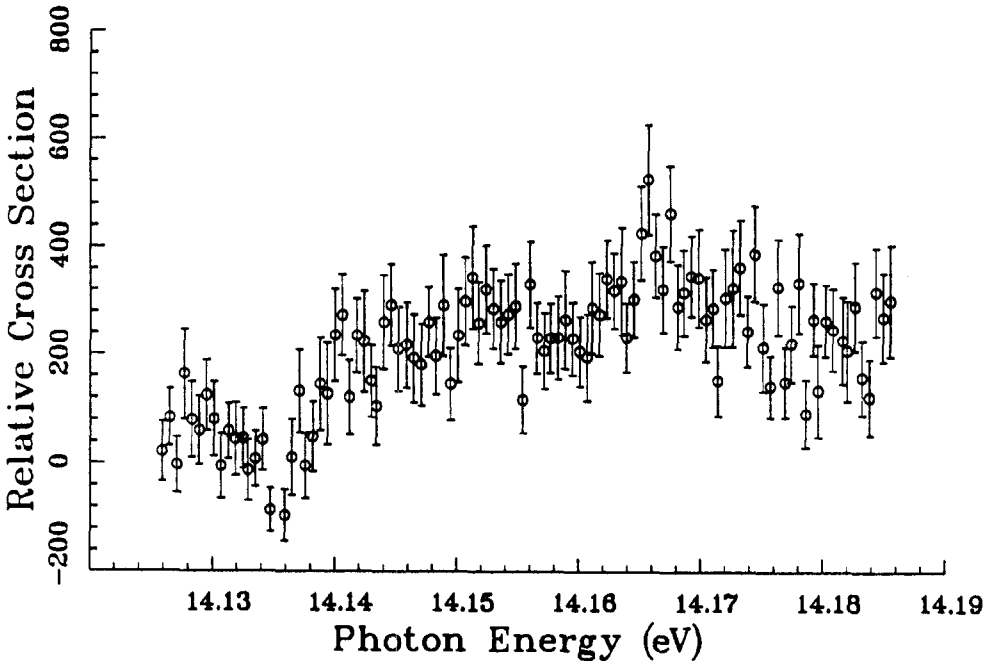

Figure J.35. Run 624.

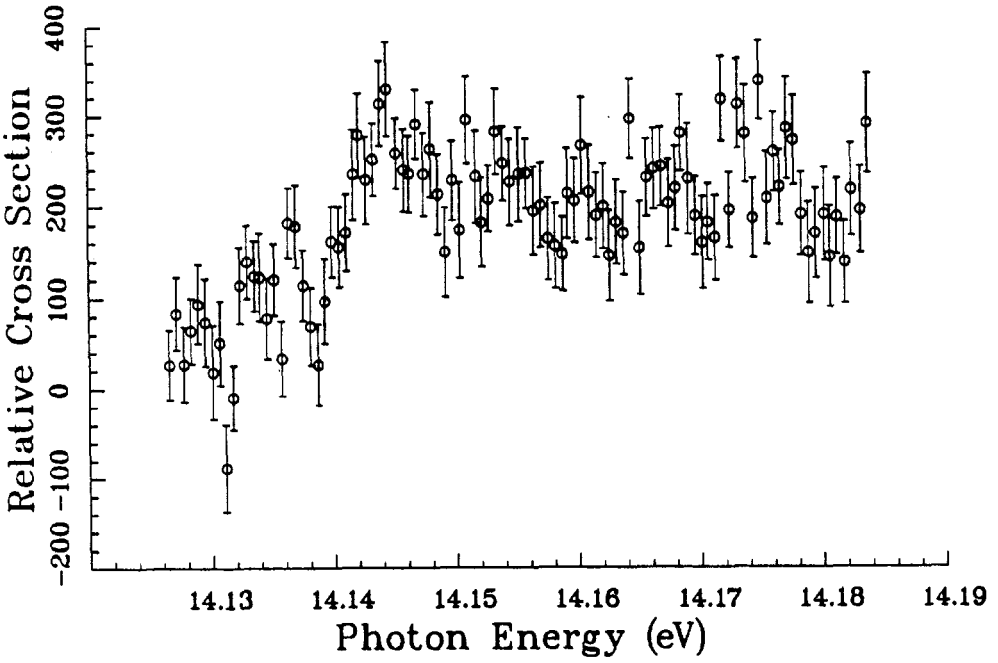

Figure J.36. Run 628.

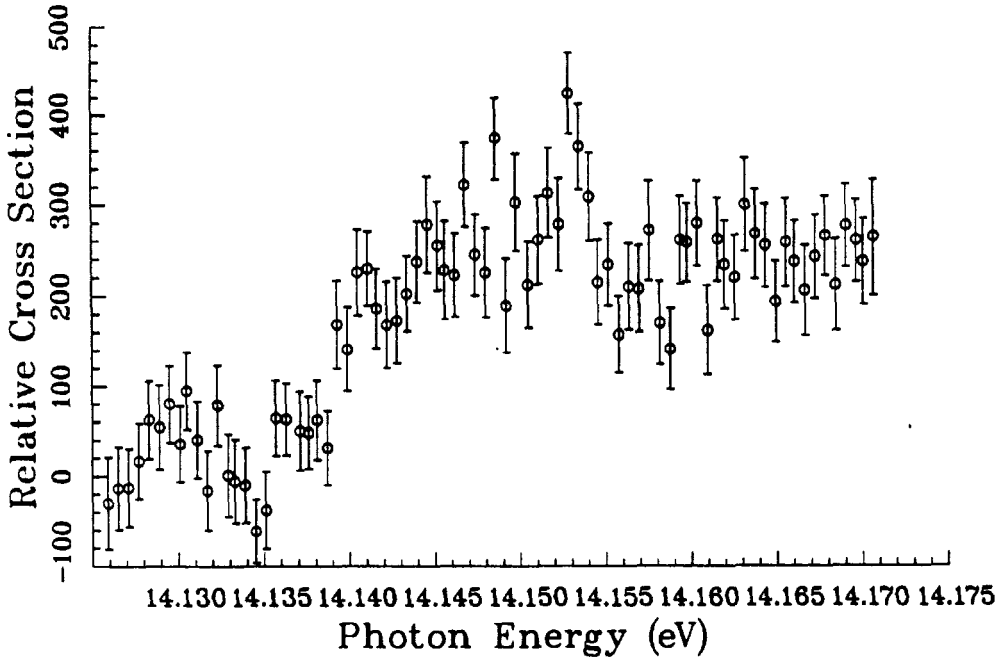

Figure J.37. Run 629.

J.2 Applied Electric Field Data.

J.2.1 Resonances Converging on $n = 5$.

The following data show the production of H° in $n = 4$ (and above) as a function of photon energy, with various applied electric fields. The light was approximately 50% π polarized.

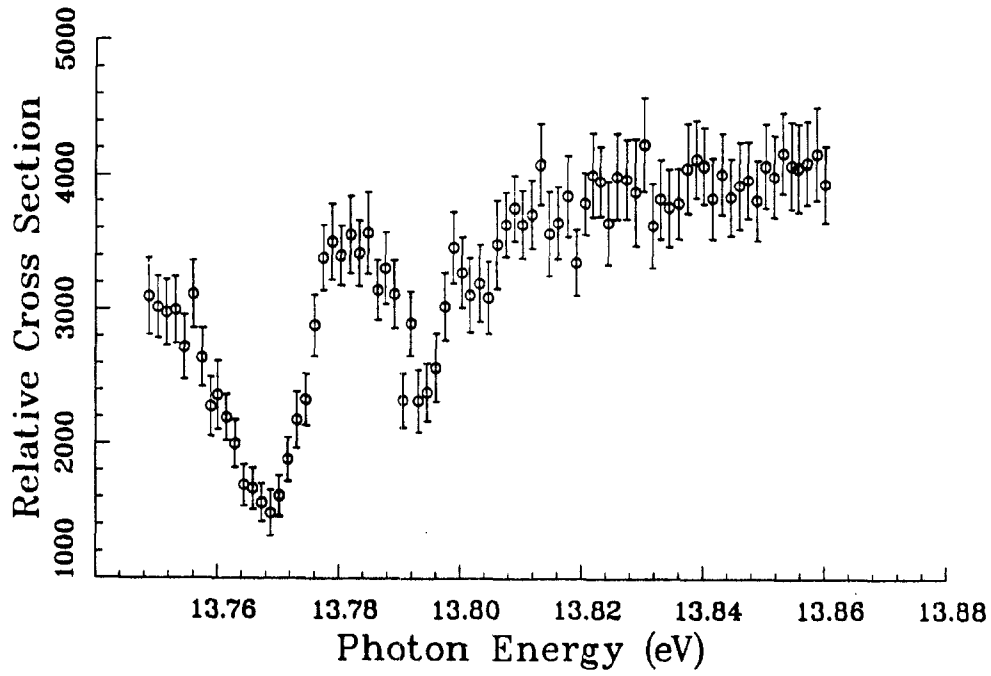

Figure J.38. Run 659: 2.5 kV/cm.

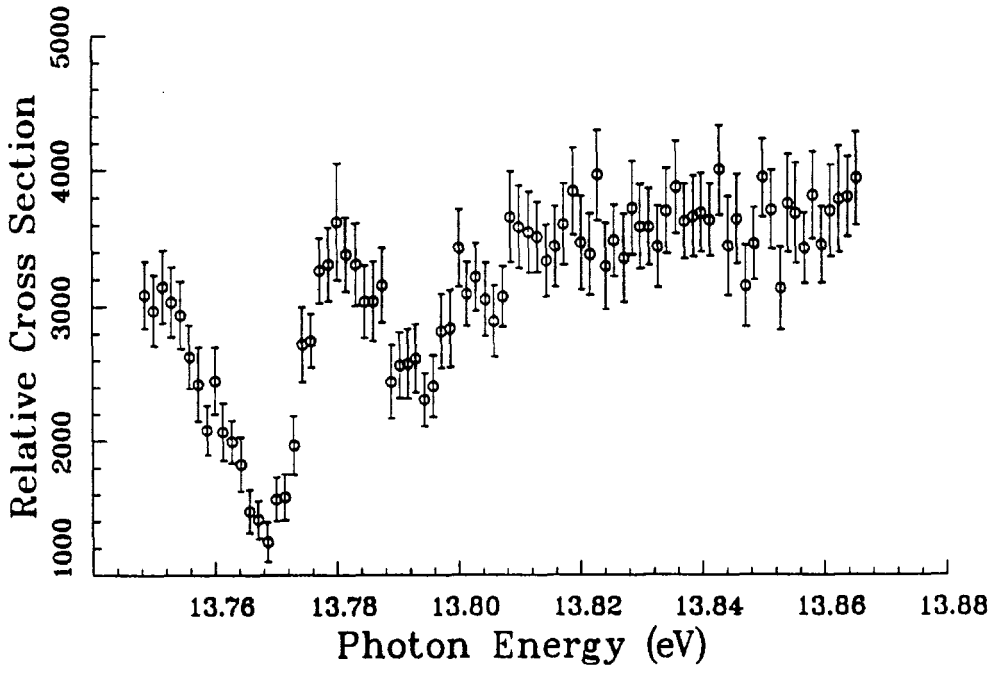

Figure J.39. Run 660: 2.5 kV/cm.

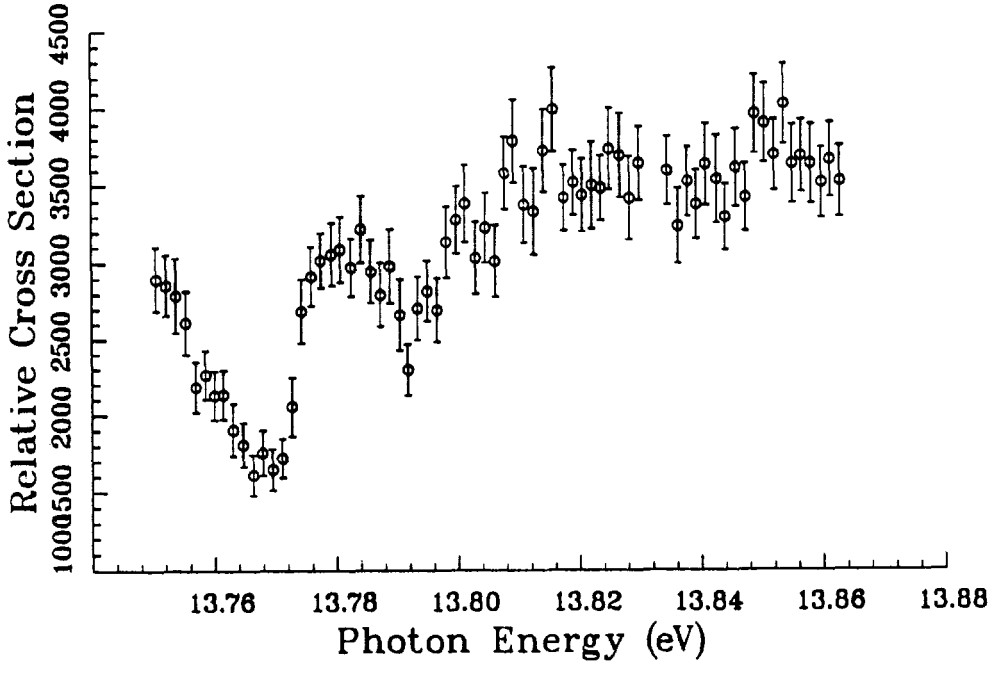

Figure J.40. Run 661: 5 kV/cm.

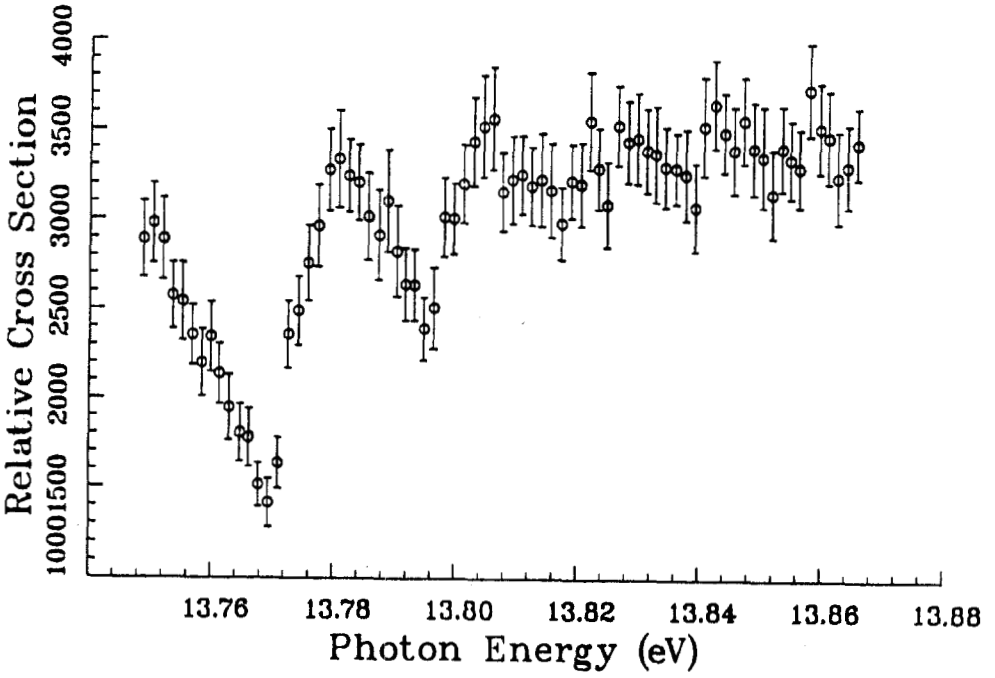

Figure J.41. Run 662: 5 kV/cm.

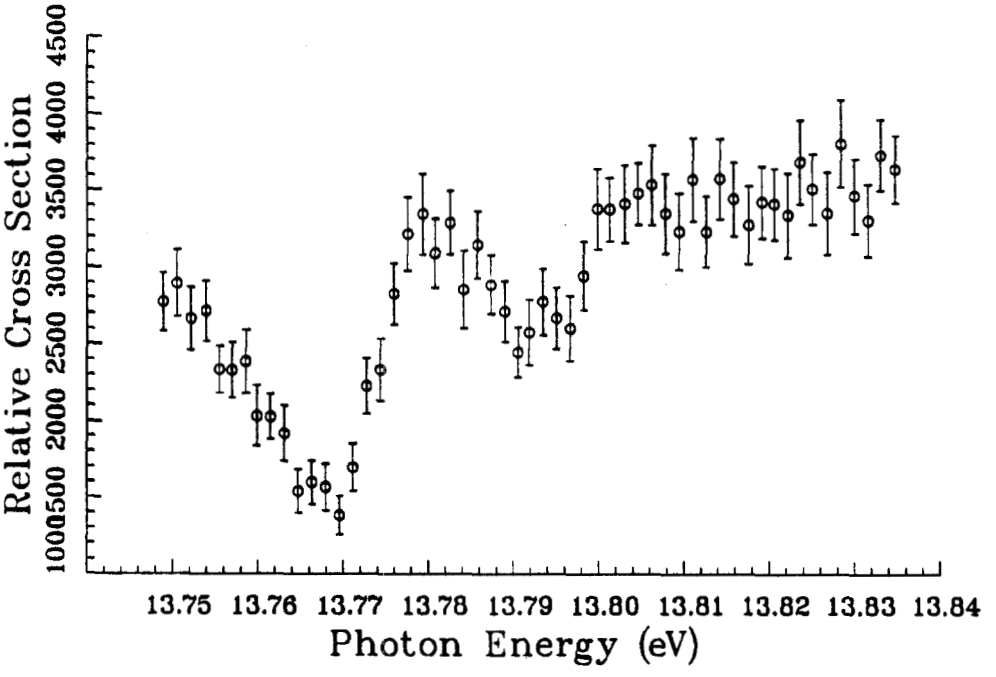

Figure J.42. Run 663: 7.5 kV/cm.

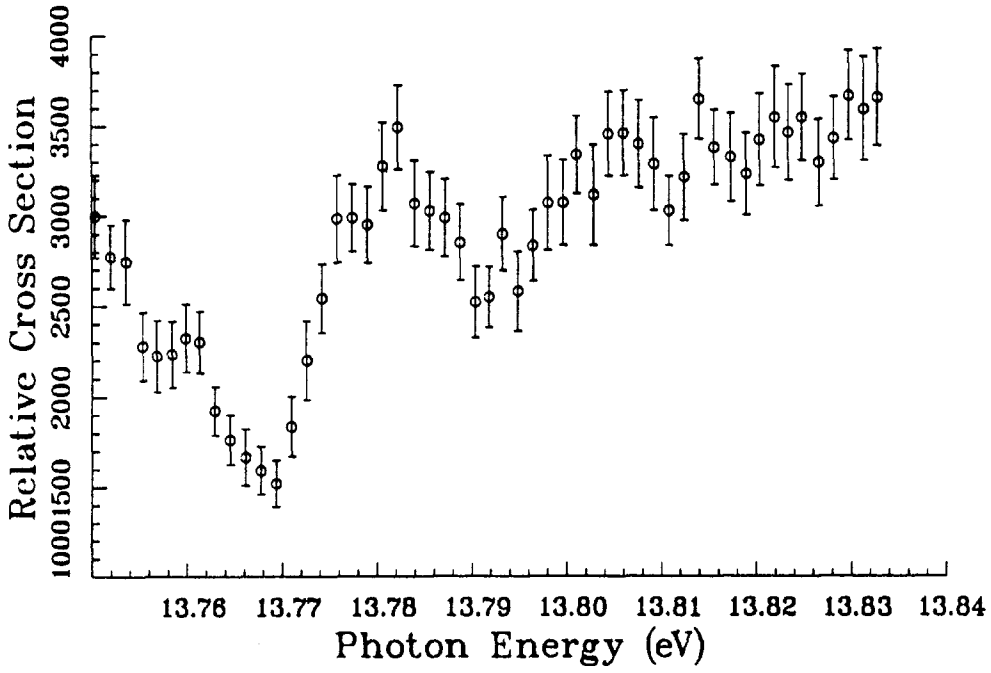

Figure J.43. Run 664: 7.5 kV/cm.

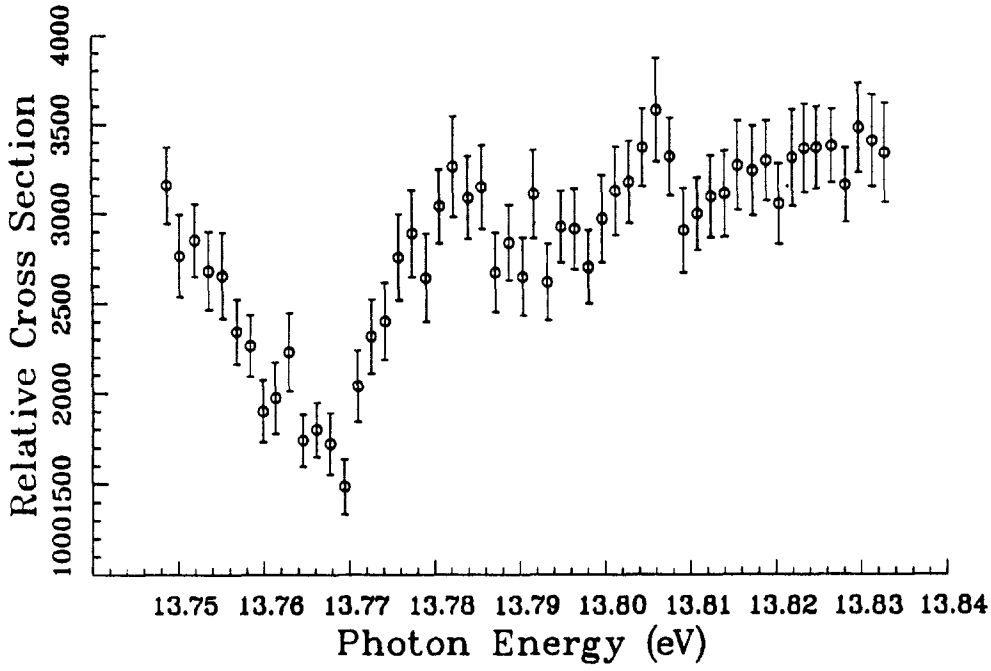

Figure J.44. Run 666: 10 kV/cm.

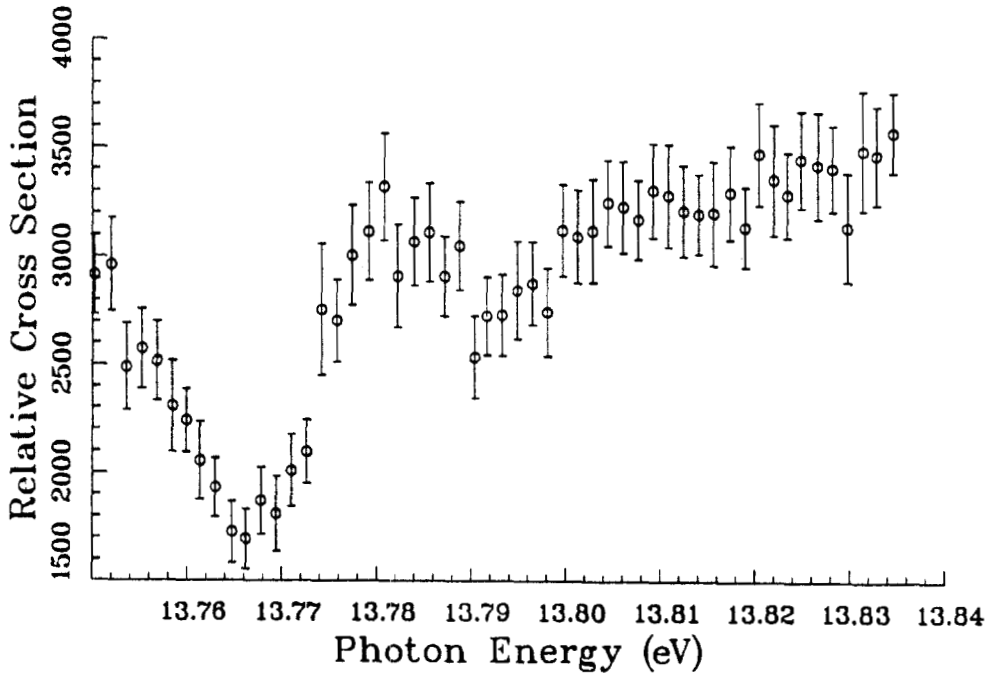

Figure J.45. Run 667: 10 kV/cm.

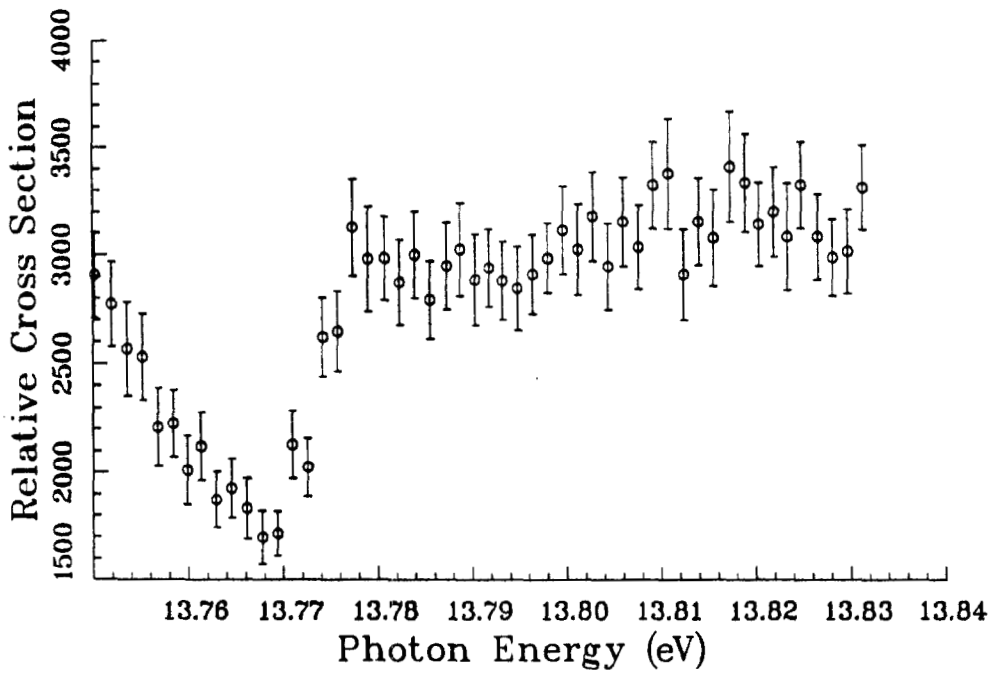

Figure J.46. Run 668: 11 kV/cm.

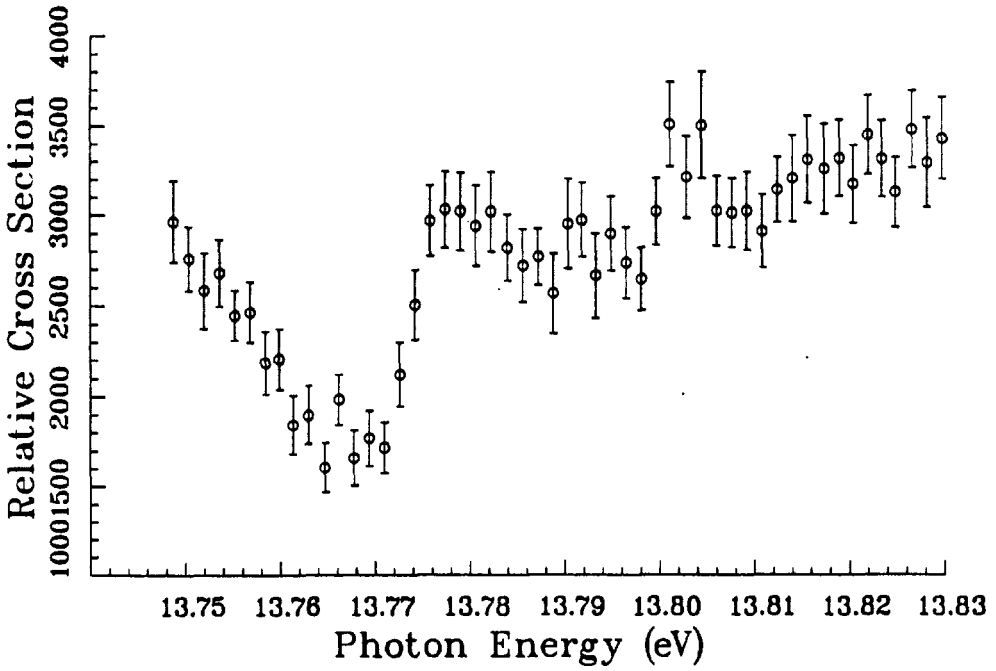

Figure J.47. Run 669: 11 kV/cm.

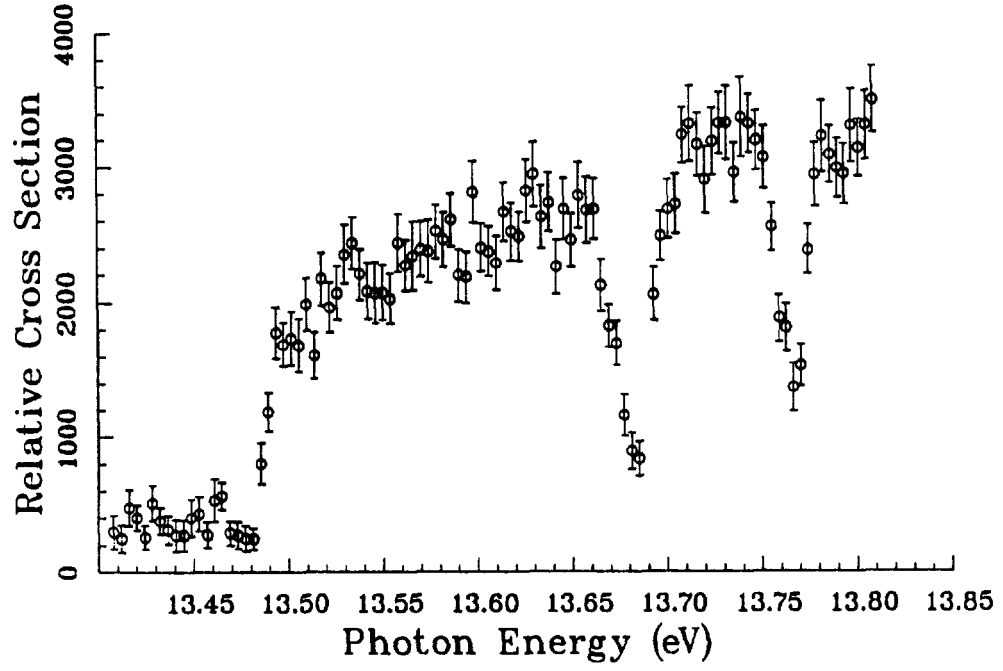

Figure J.48. Run 644: 13 kV/cm.

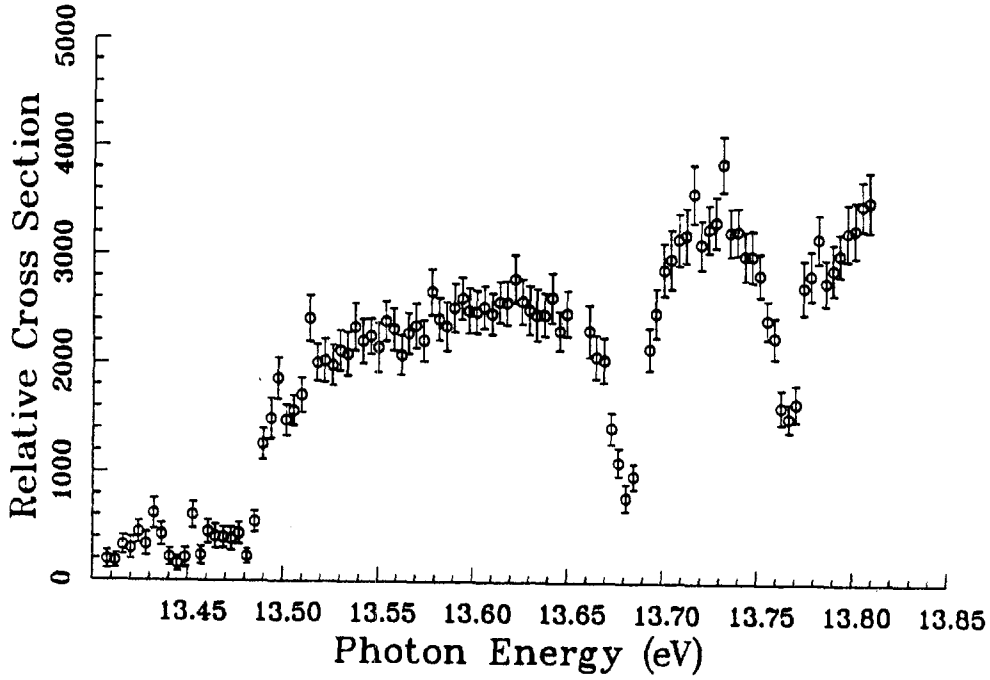

Figure J.49. Run 645: 13 kV/cm.

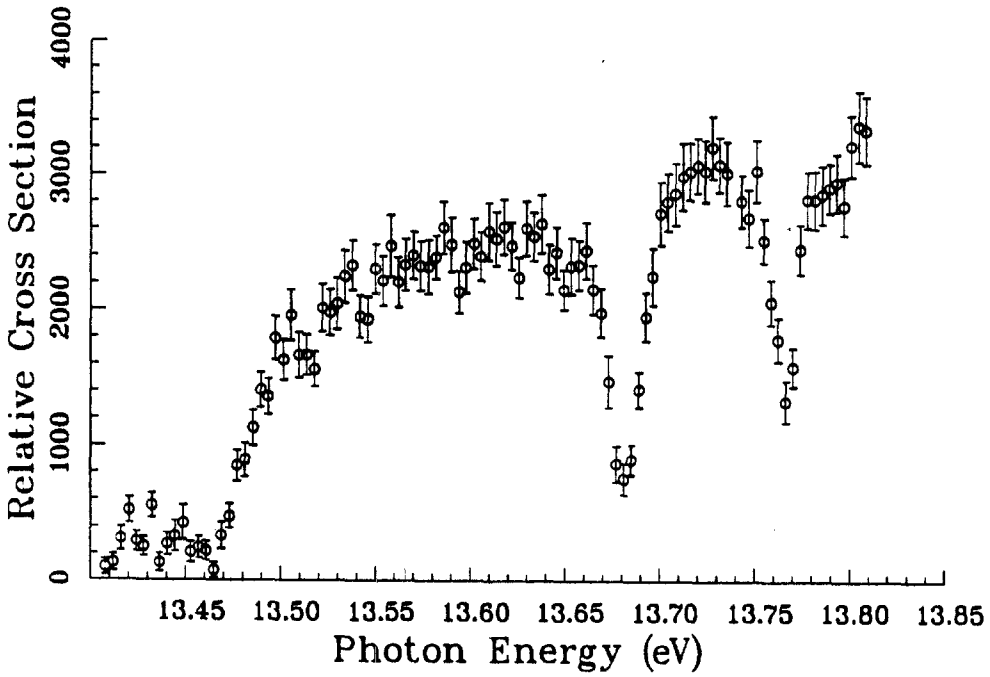

Figure J.50. Run 646: 25 kV/cm.

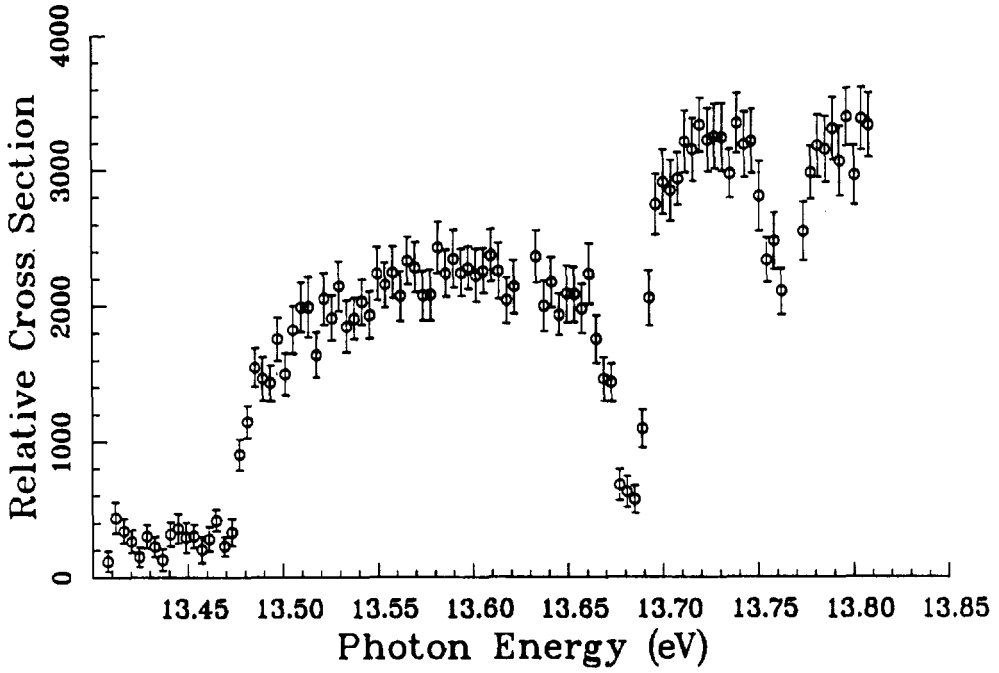

Figure J.51. Run 647: 25 kV/cm.

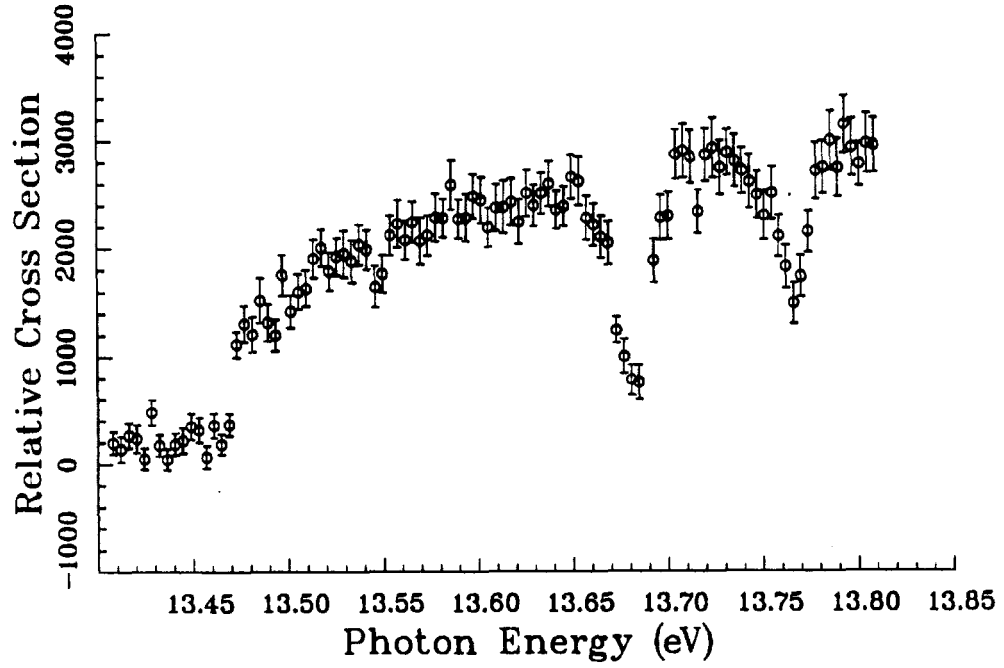

Figure J.52. Run 648: 38 kV/cm.

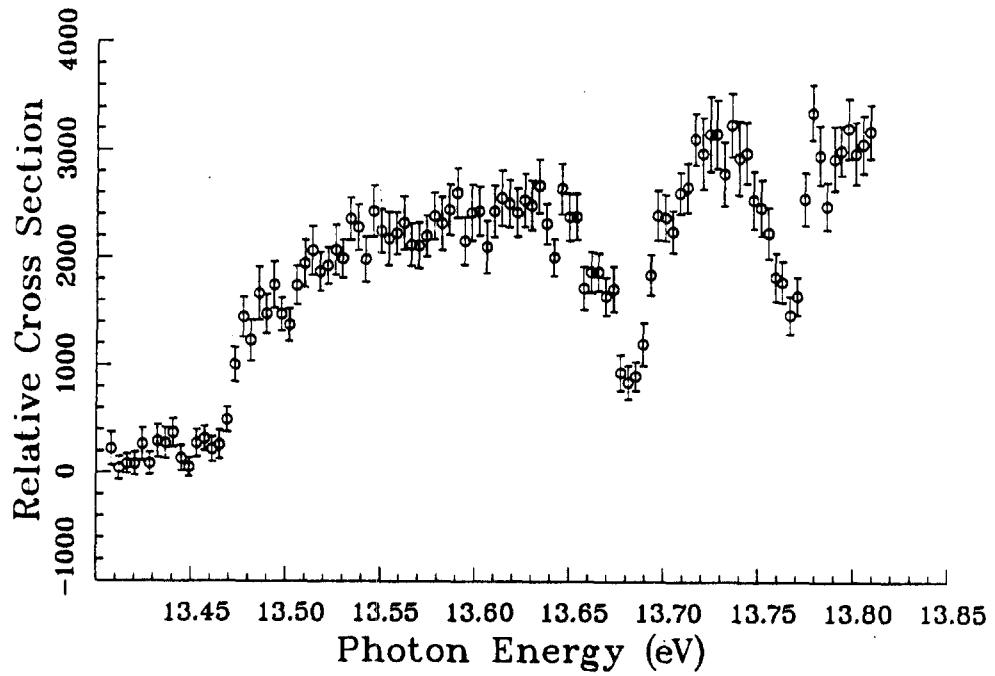

Figure J.53. Run 649: 38 kV/cm.

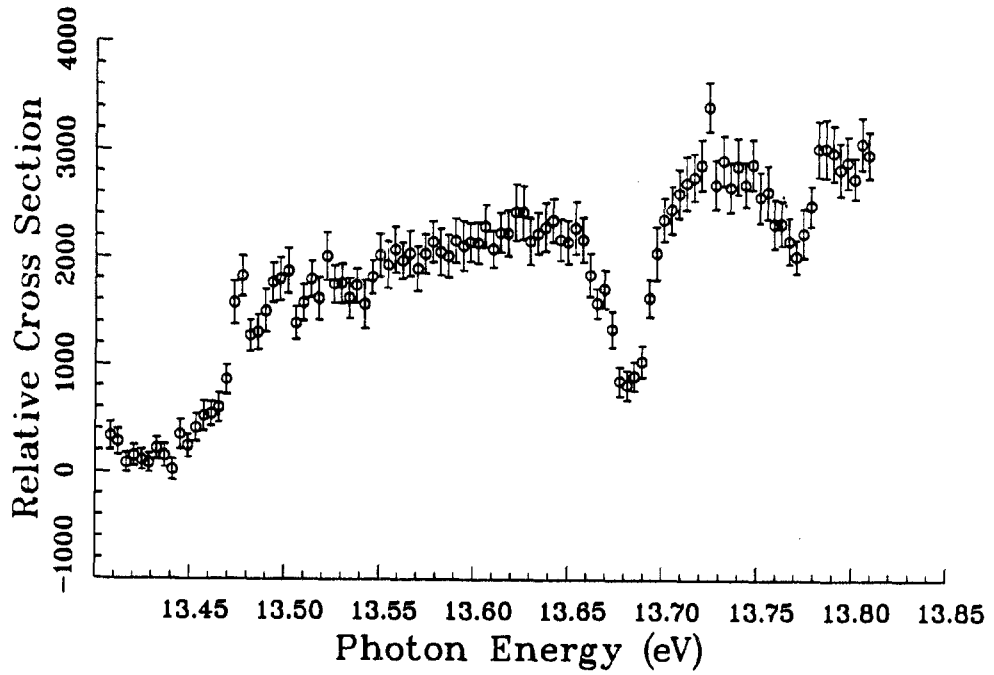

Figure J.54. Run 650: 63 kV/cm.

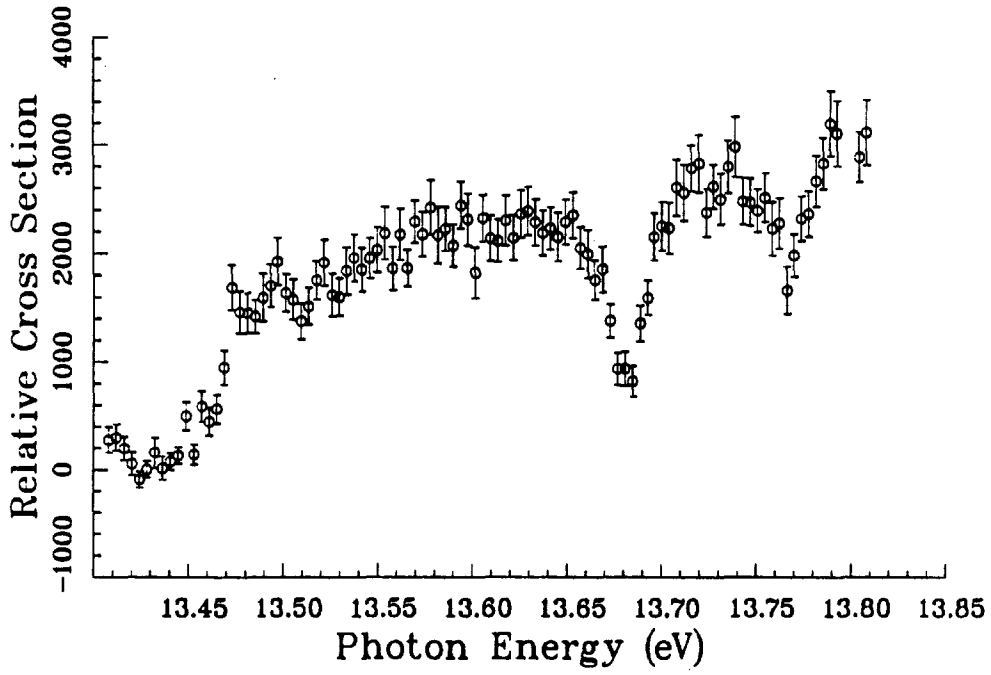

Figure J.55. Run 651: 63 kV/cm.

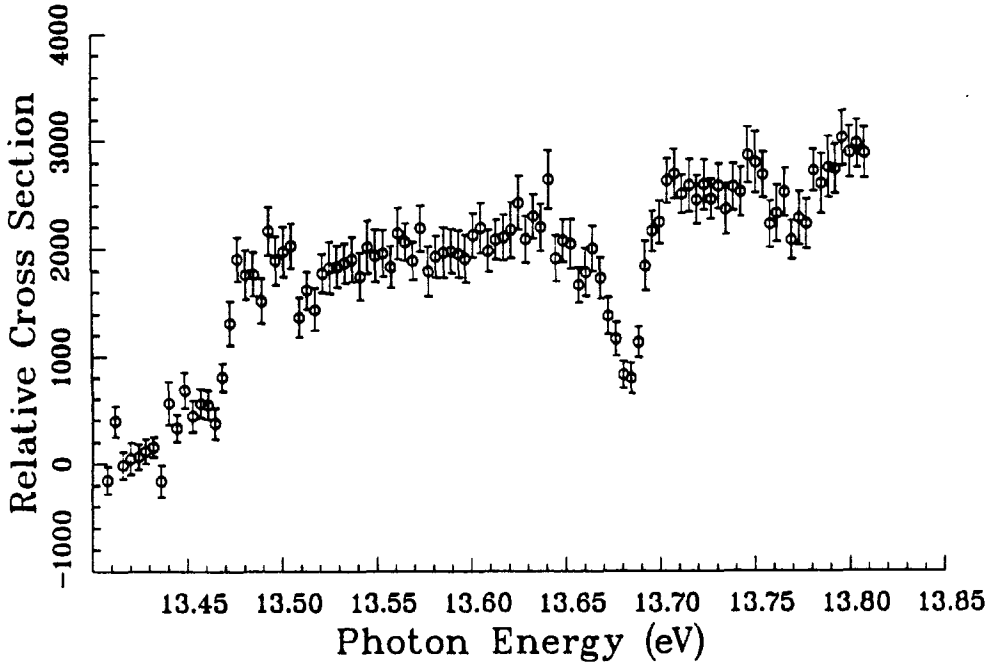

Figure J.56. Run 652: 87 kV/cm.

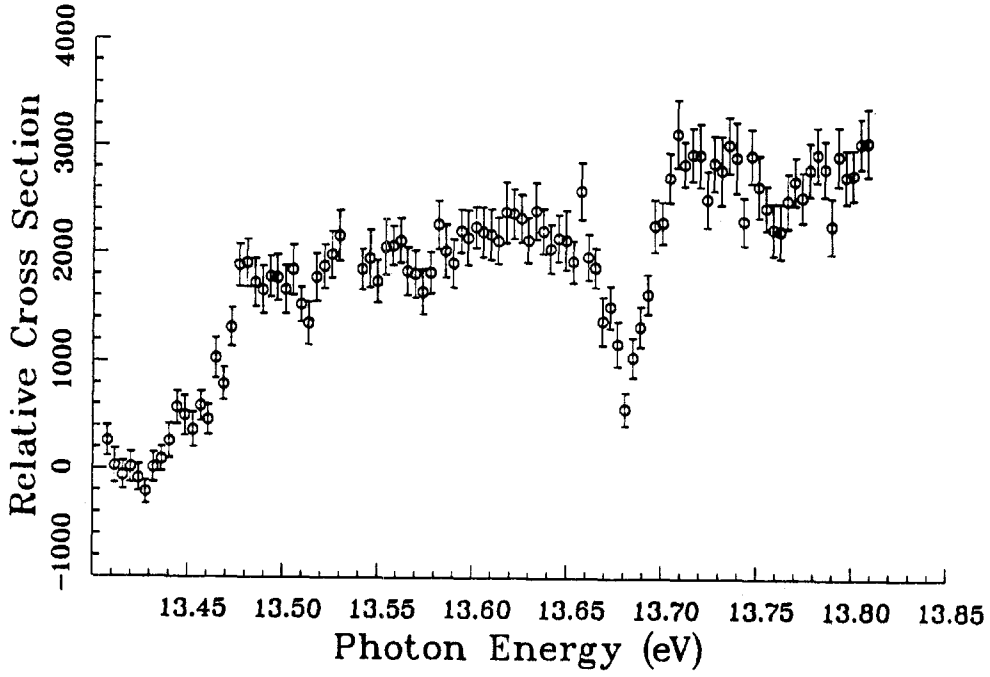

Figure J.57. Run 653: 87 kV/cm.

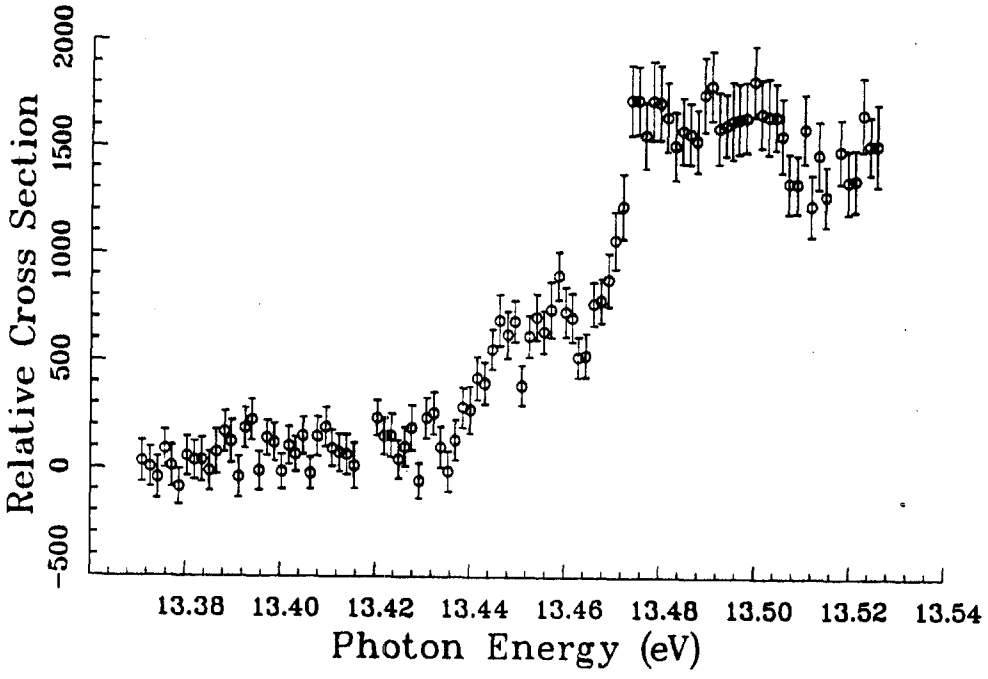

Figure J.58. Run 654: 87 kV/cm.

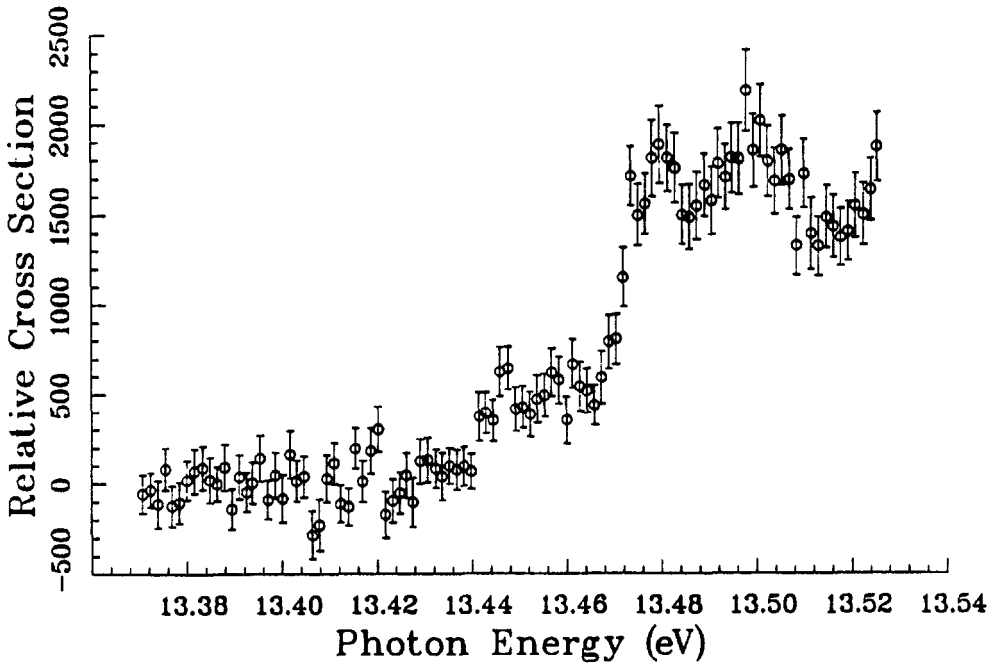

Figure J.59. Run 655: 87 kV/cm.

J.2.2 Resonances Converging on $n = 6$.

The following data show the production of H° in $n = 5$ (and above) as a function of photon energy, with various applied electric fields. The light was approximately 50% π polarized.

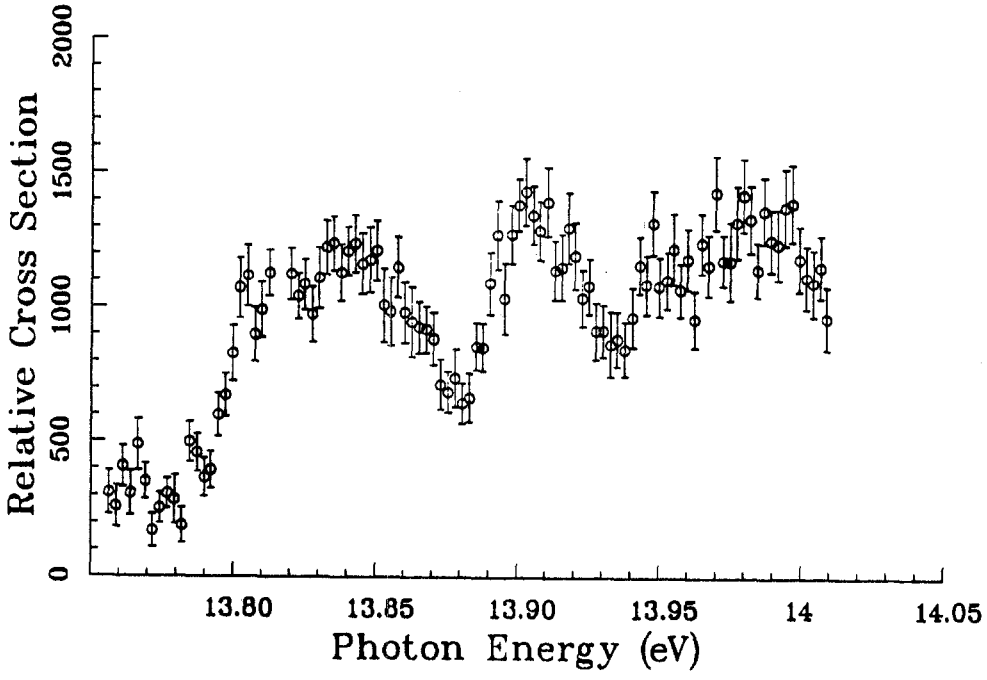

Figure J.60. Run 673: 13 kV/cm.

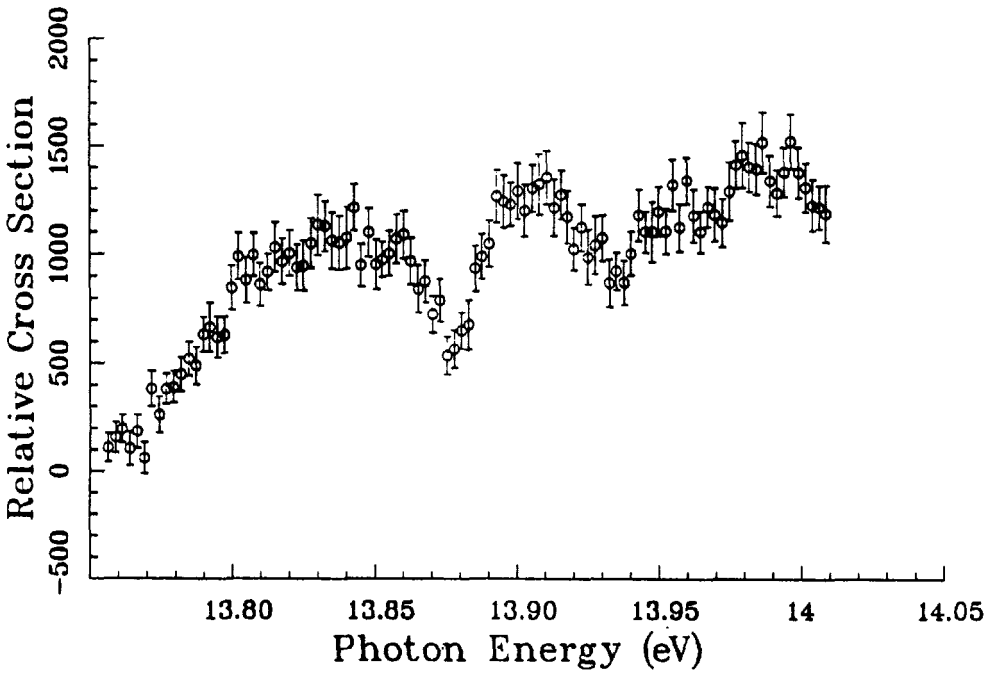

Figure J.61. Run 674: 25 kV/cm.

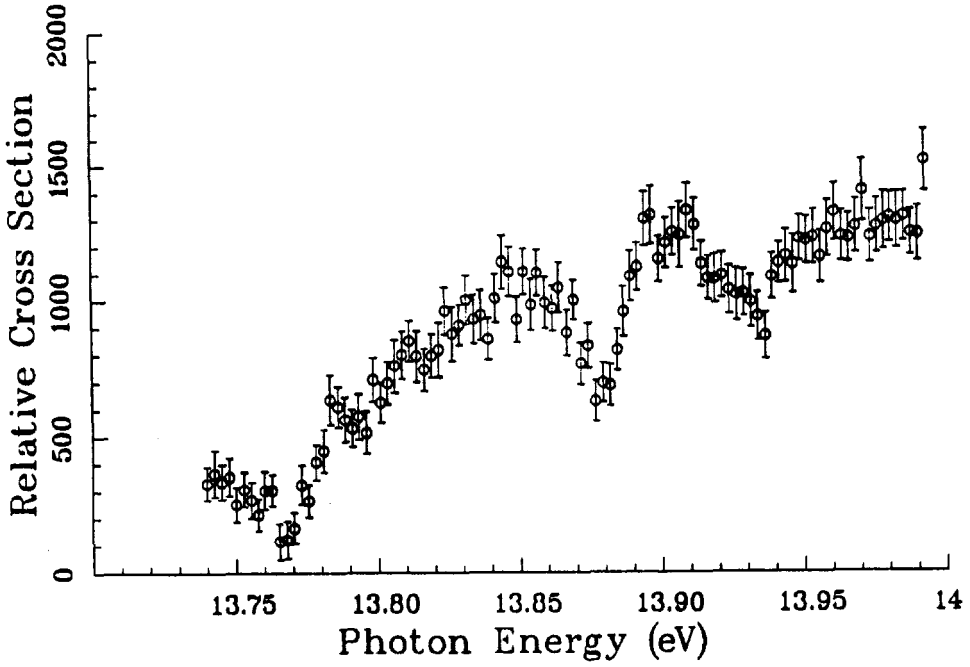

Figure J.62. Run 675: 25 kV/cm.

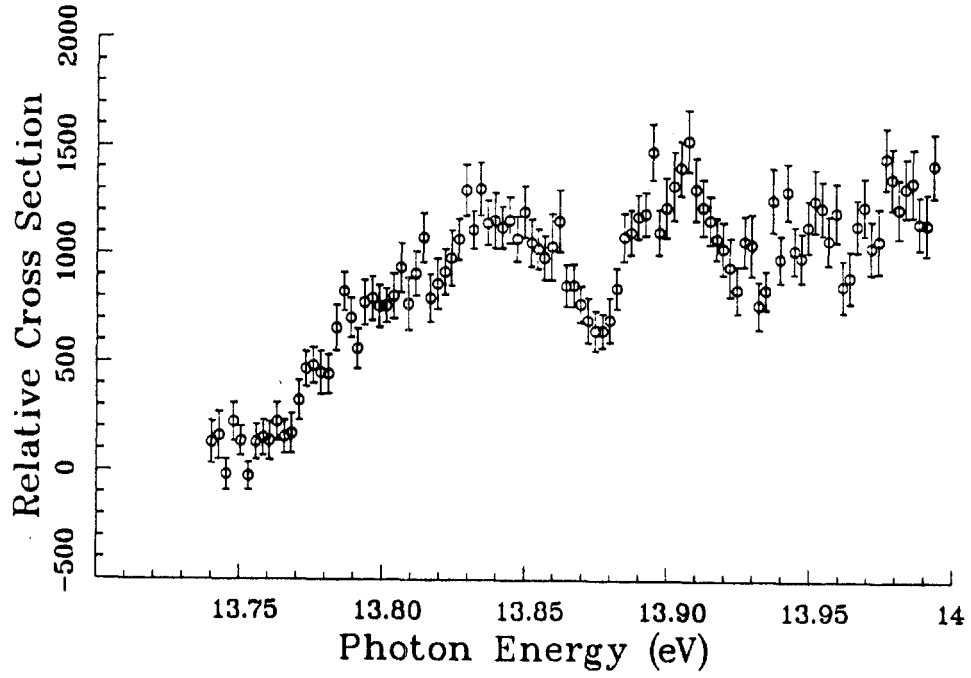

Figure J.63. Run 676: 38 kV/cm.

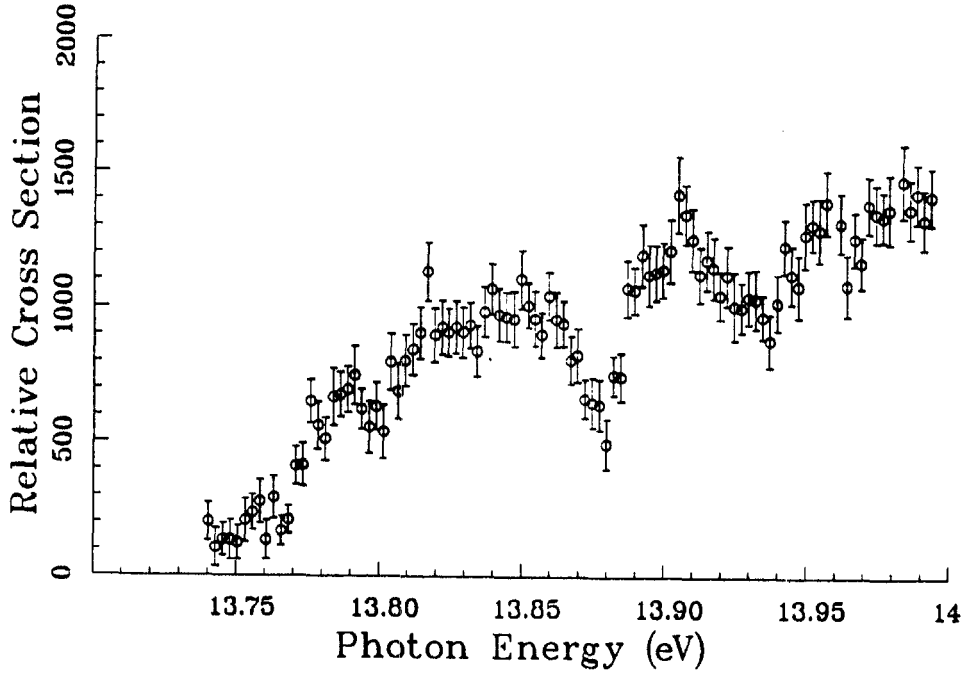

Figure J.64. Run 677: 38 kV/cm.

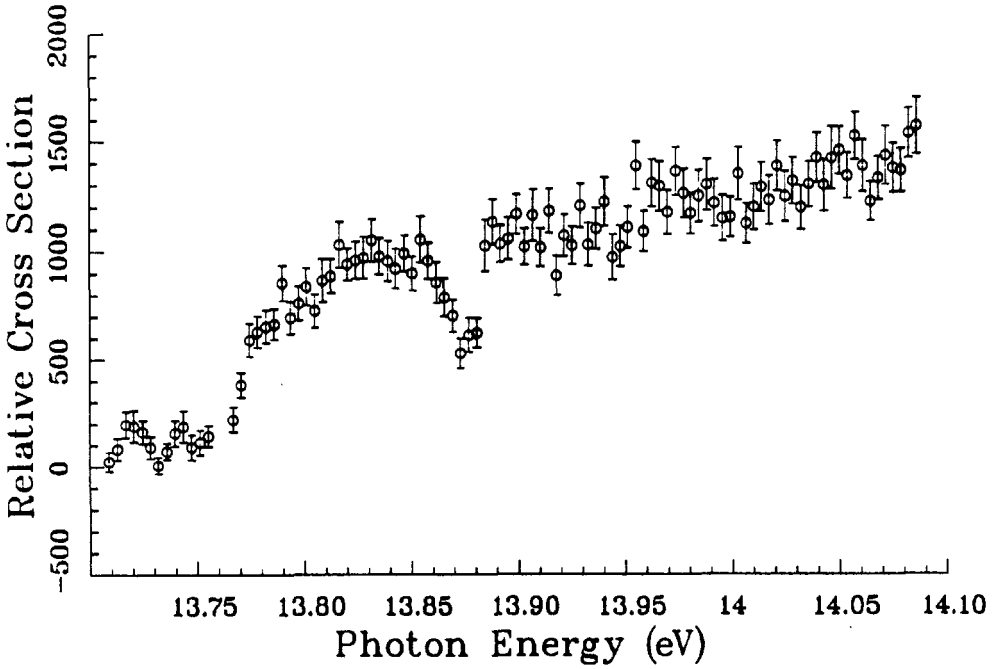

Figure J.65. Run 642: 50 kV/cm.

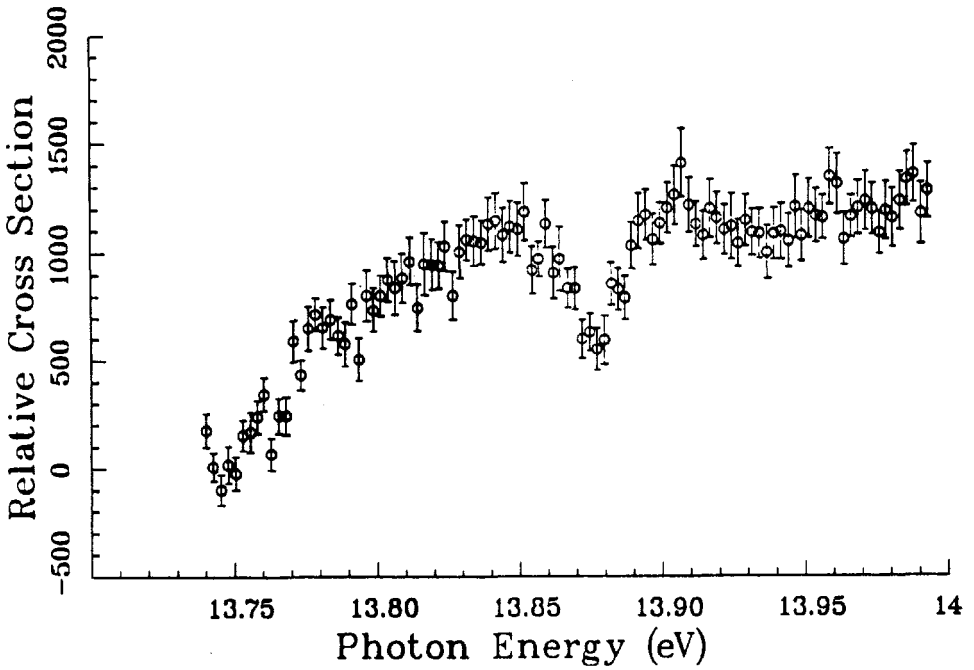

Figure J.66. Run 679: 50 kV/cm.

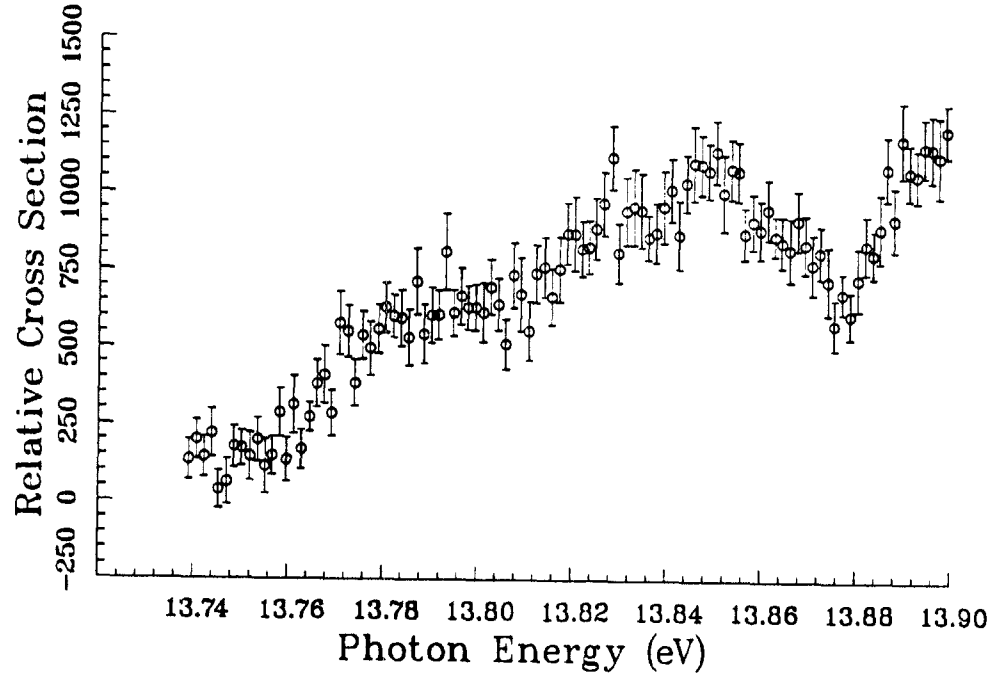

Figure J.67. Run 680: 50 kV/cm.

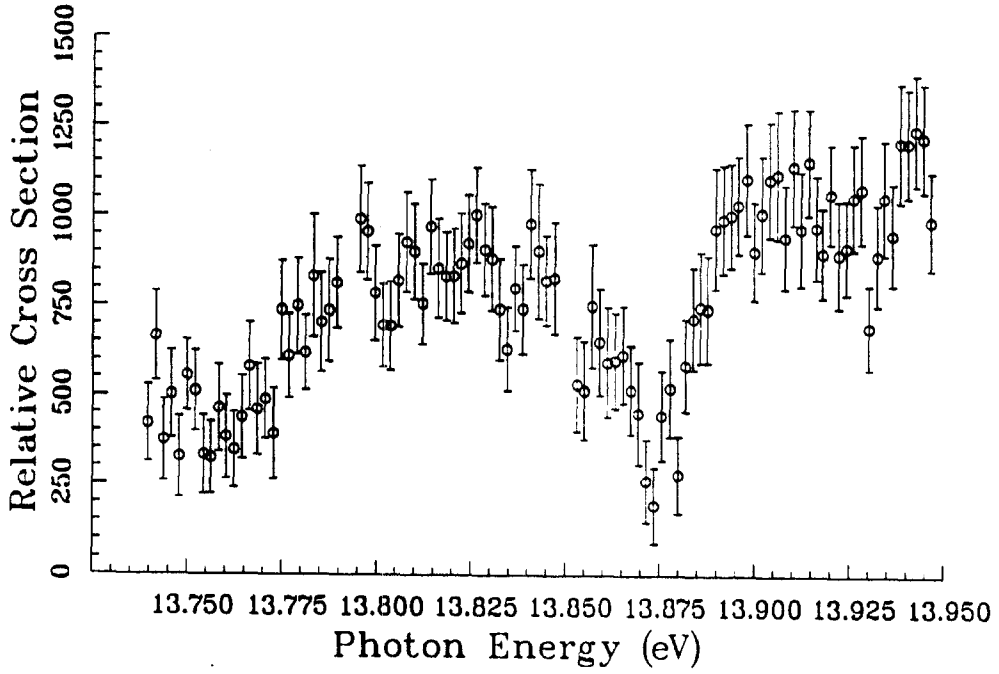

Figure J.68. Run 681: 63 kV/cm.

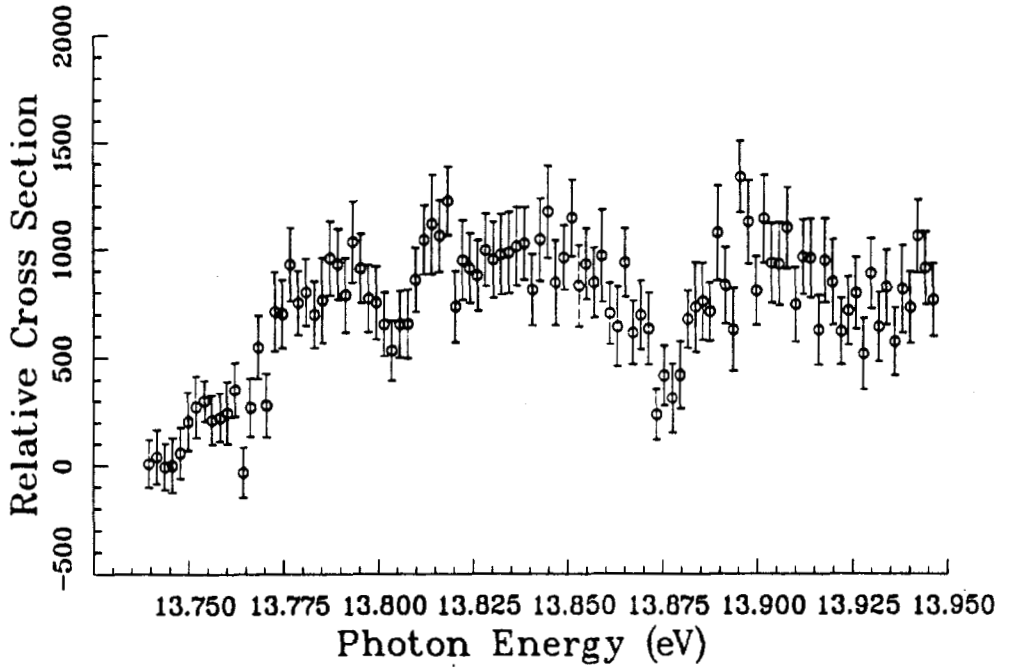

Figure J.69. Run 682: 63 kV/cm.

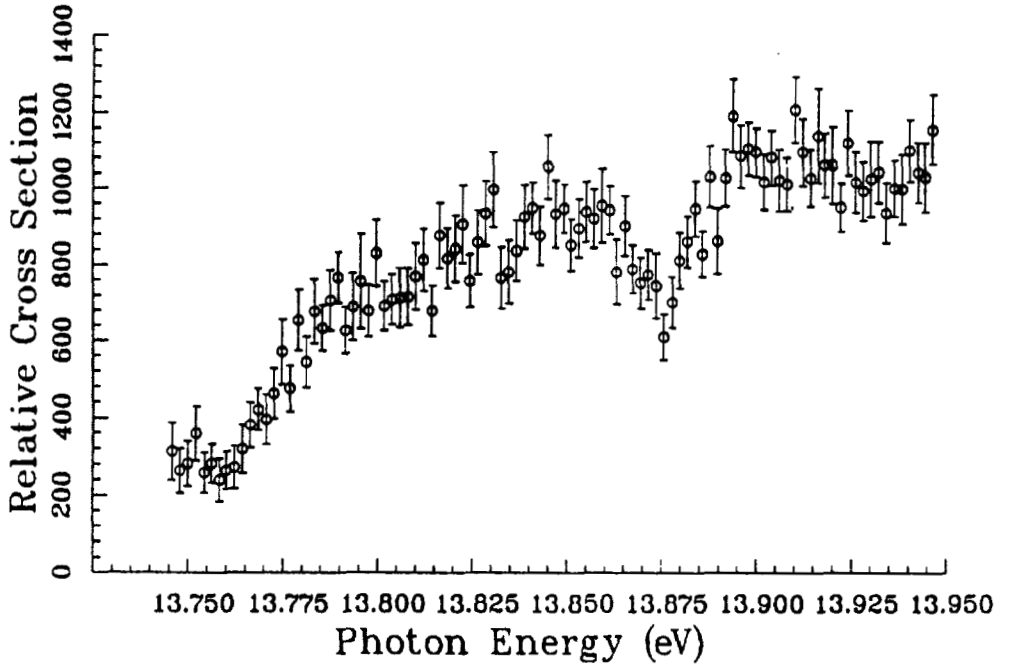

Figure J.70. Run 683: 63 kV/cm.

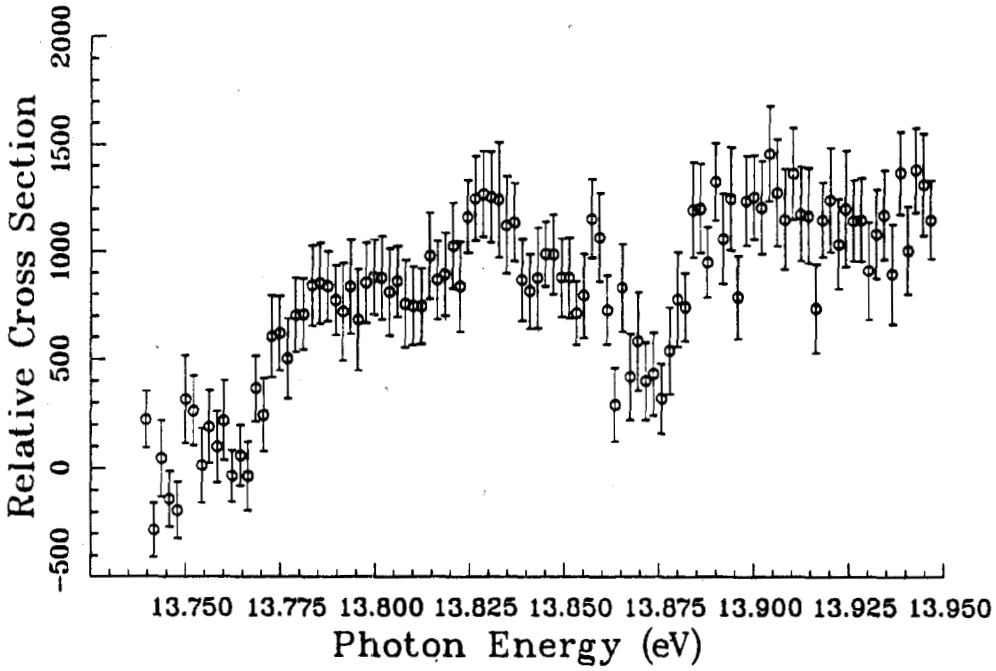

Figure J.71. Run 684: 63 kV/cm.

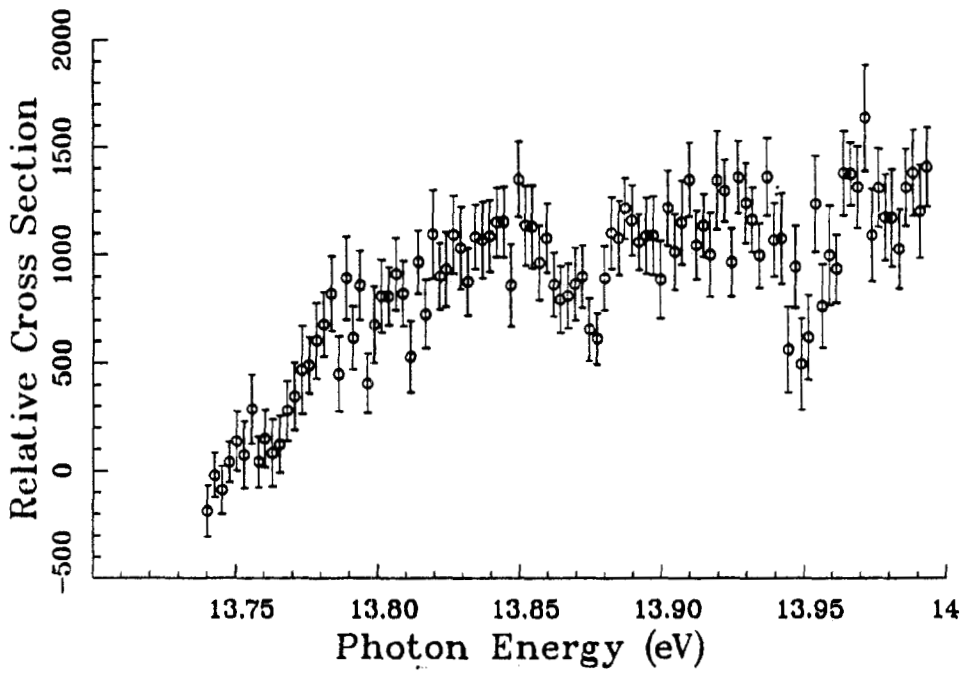

Figure J.72. Run 685: 75 kV/cm.

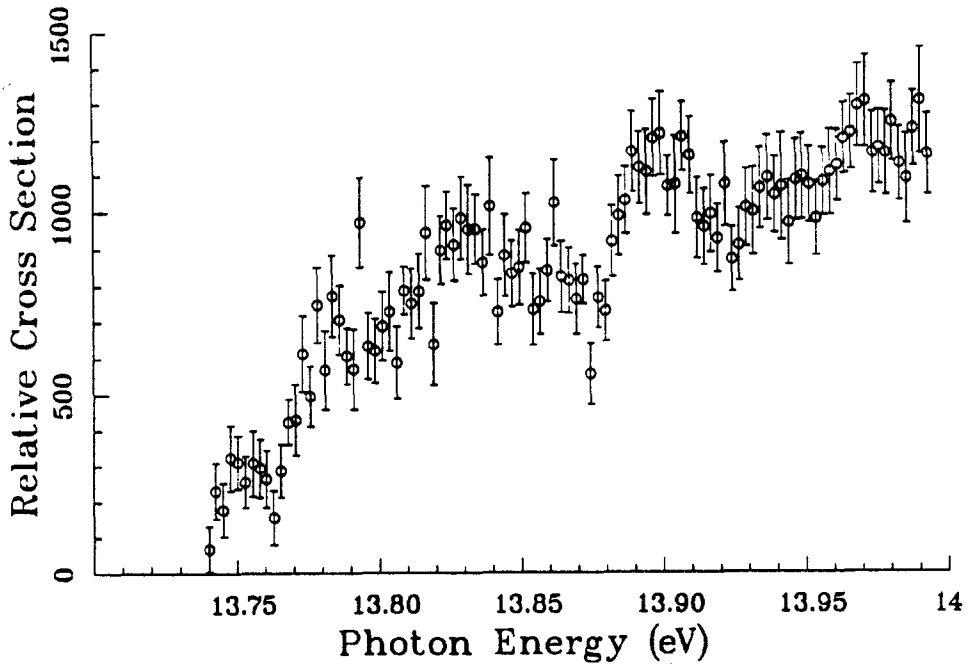

Figure J.73. Run 686: 75 kV/cm.

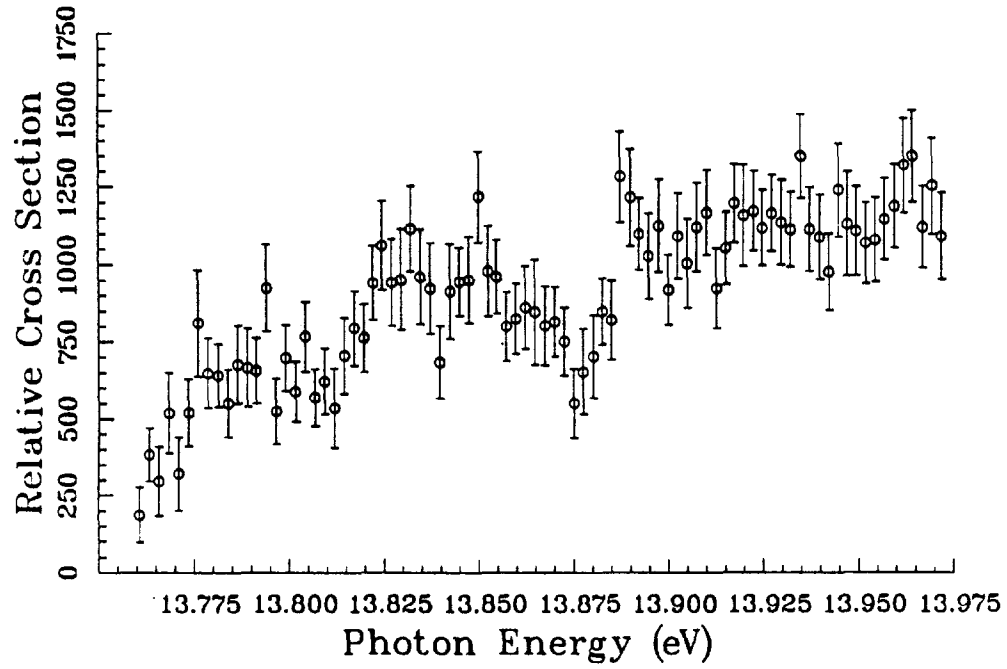

Figure J.74. Run 689: 75 kV/cm.

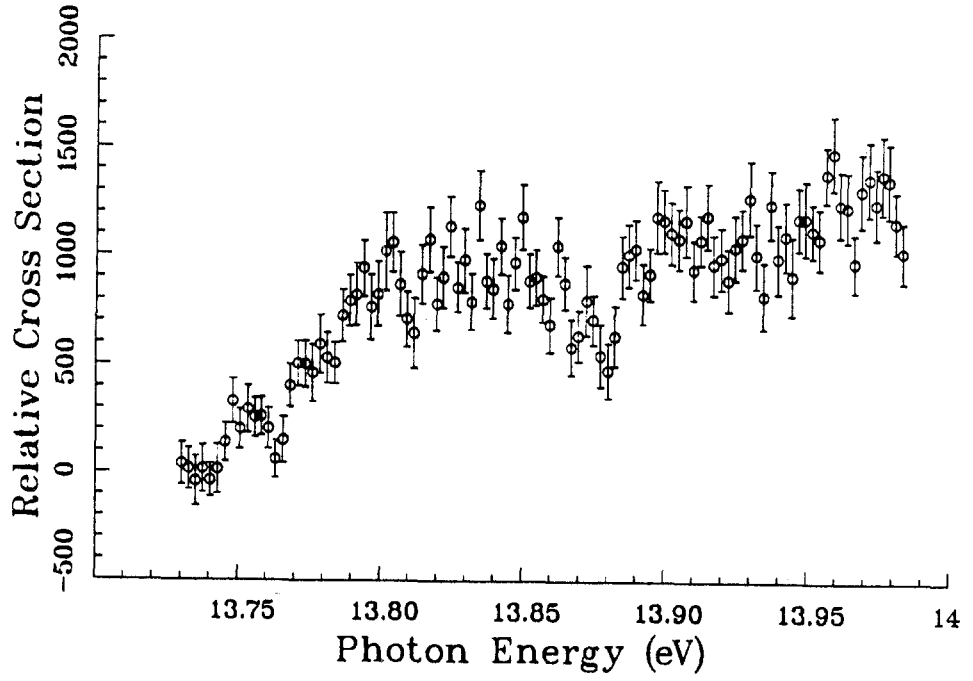

Figure J.75. Run 692: 75 kV/cm.

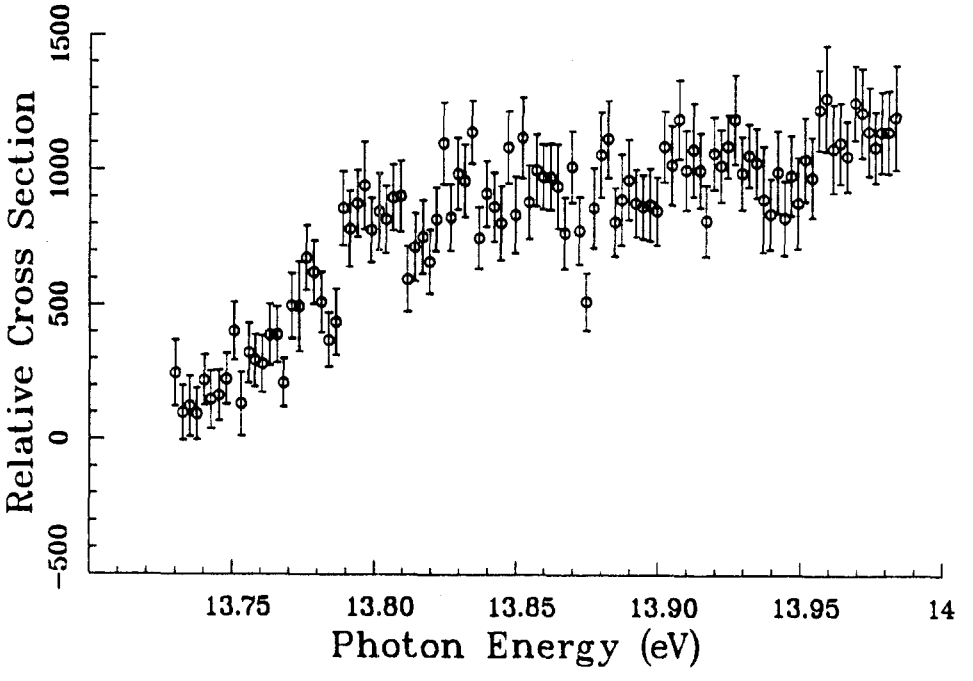

Figure J.76. Run 695: 87 kV/cm.

J.2.3 Resonances Converging on $n = 7$.

The following data show the production of H° in $n = 6$ (and above) as a function of photon energy, with various applied electric fields. The light was approximately 50% π polarized.

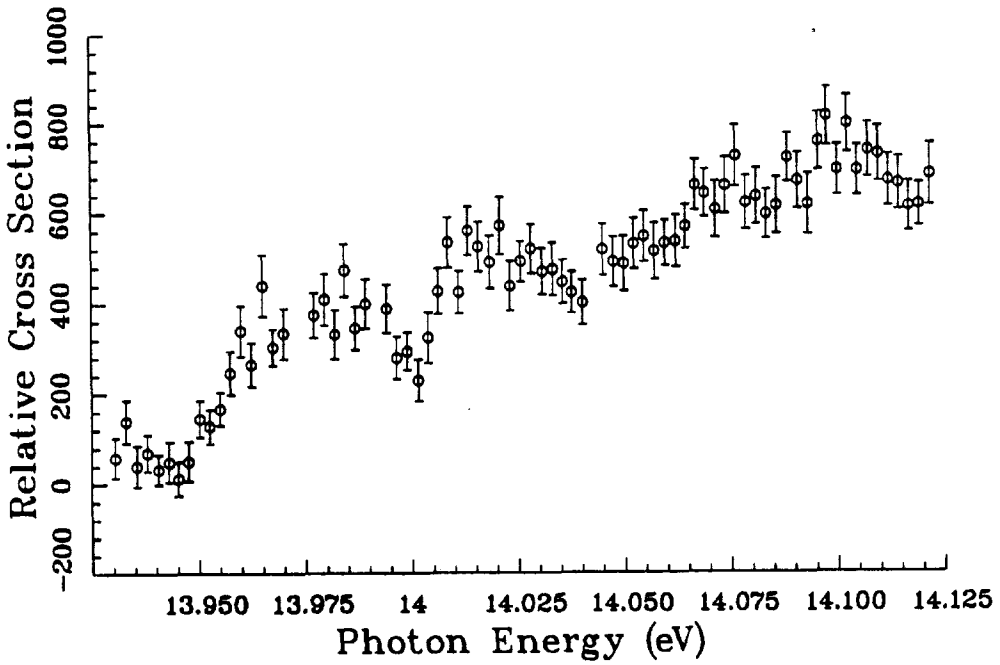

Figure J.77. Run 710: 13 kV/cm.

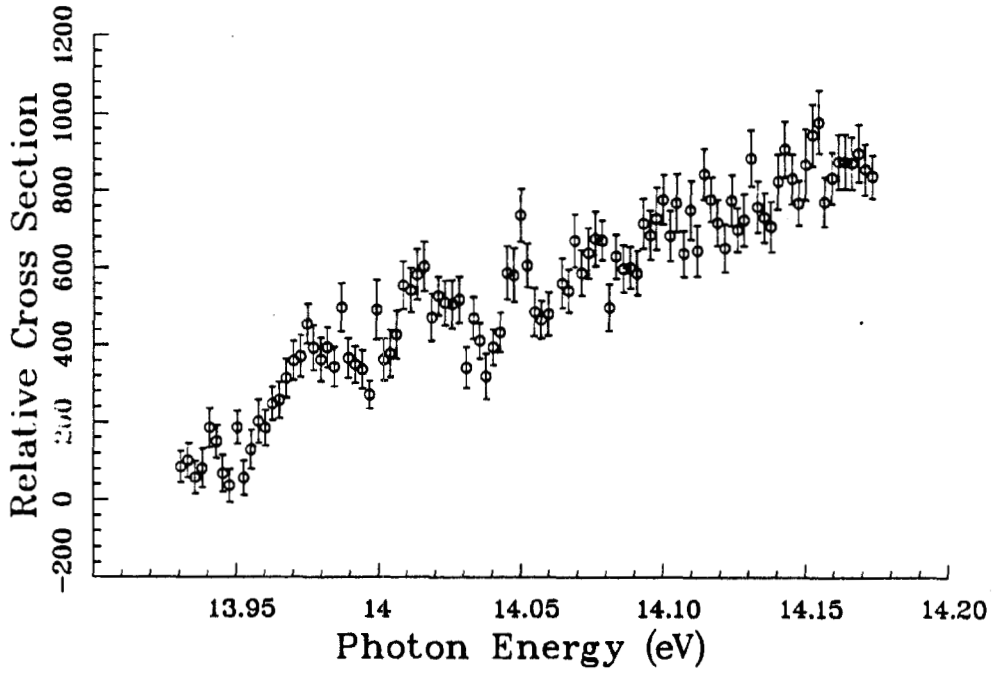

Figure J.78. Run 711: 13 kV/cm.

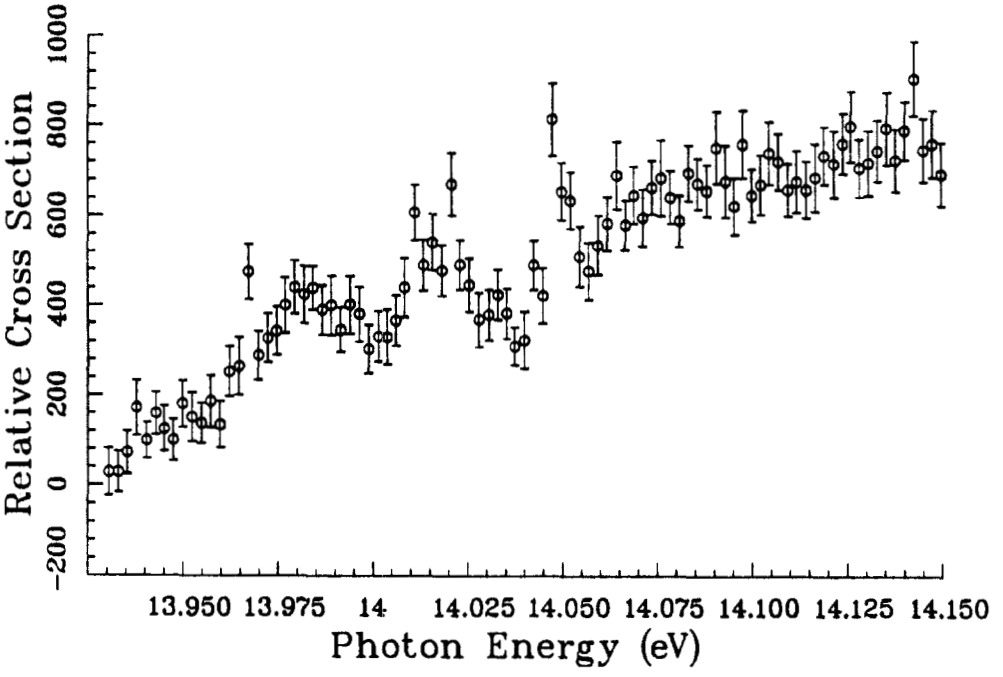

Figure J.79. Run 712: 13 kV/cm.

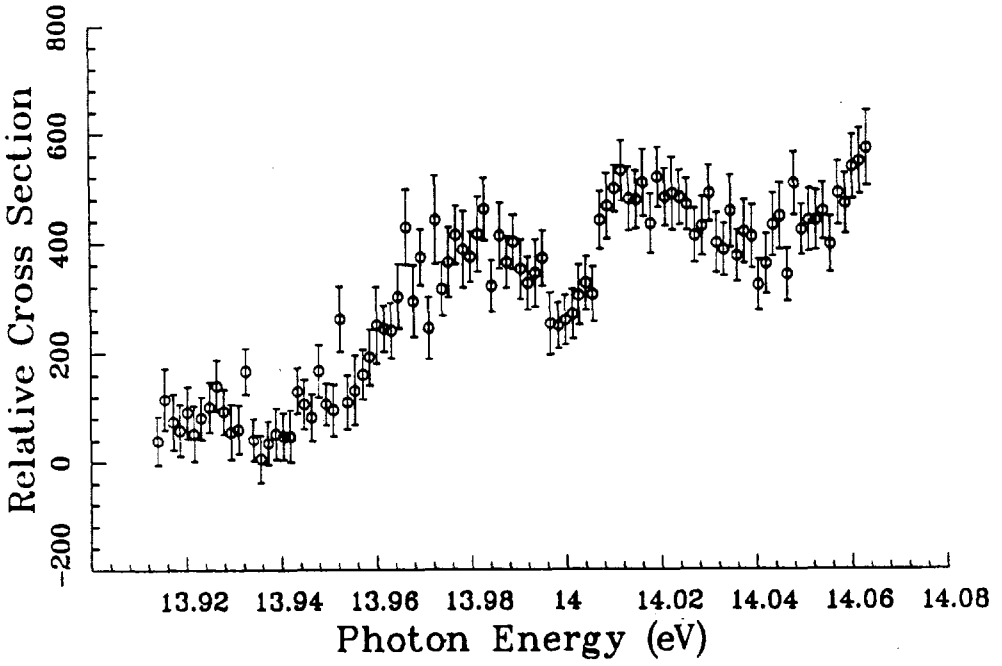

Figure J.80. Run 726: 13 kV/cm.

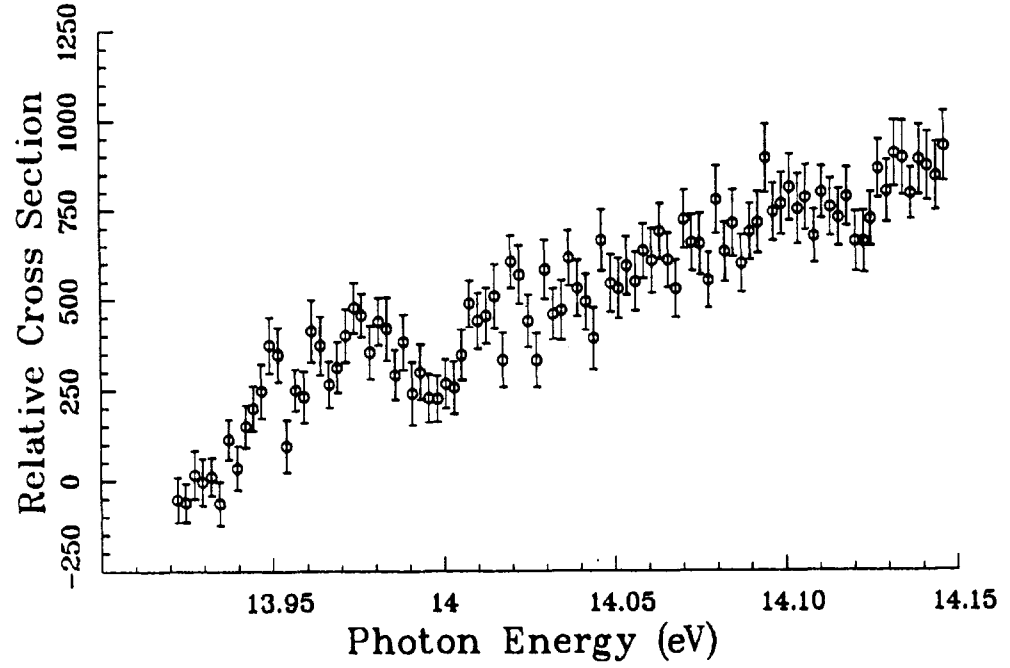

Figure J.81. Run 716: 25 kV/cm.

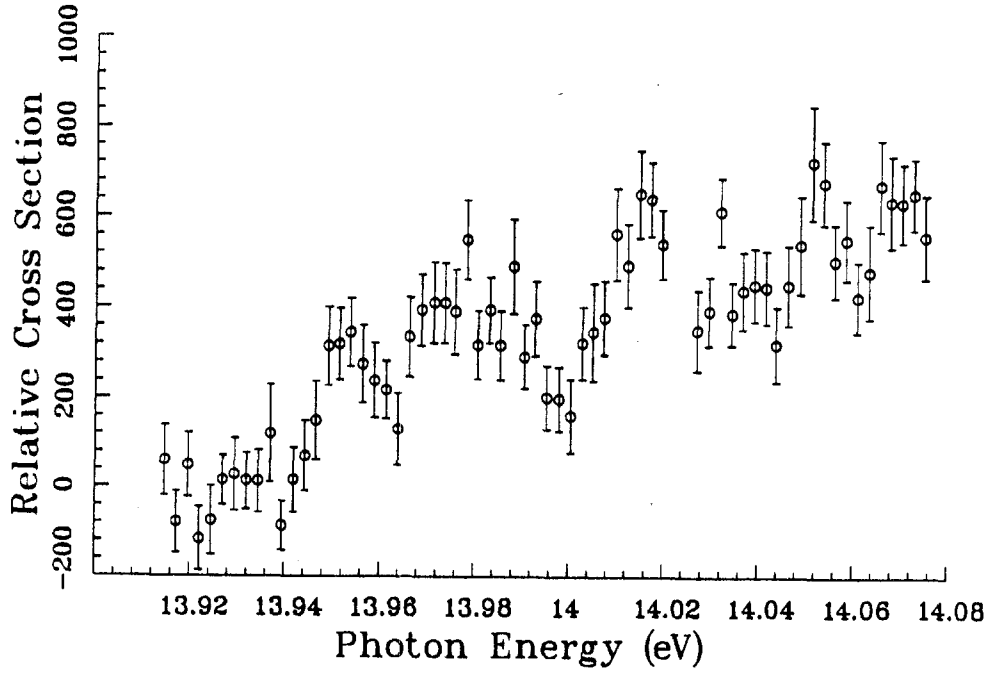

Figure J.82. Run 717: 25 kV/cm.

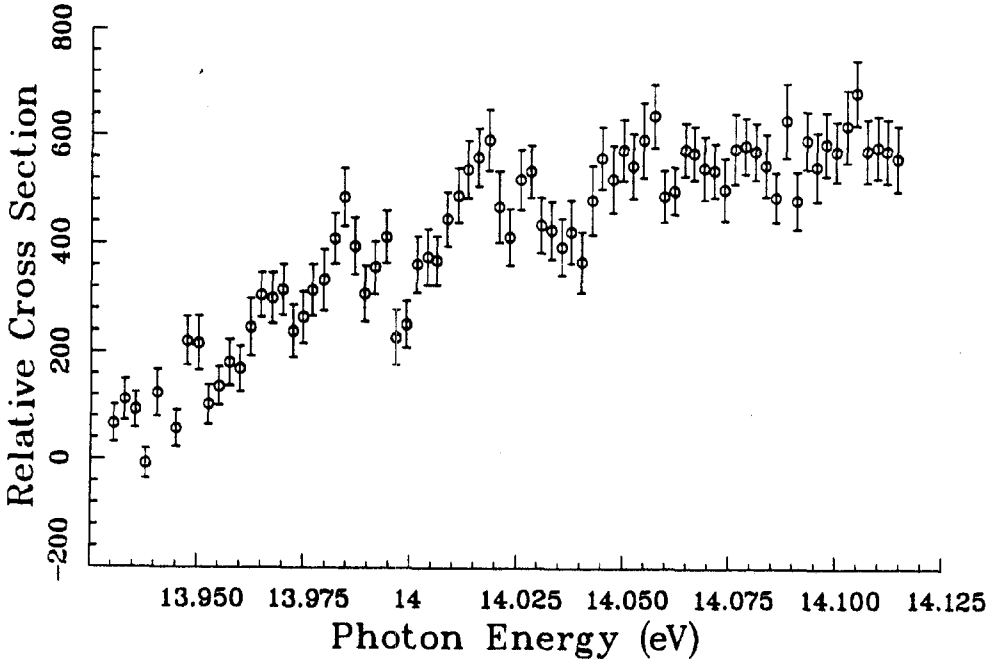

Figure J.83. Run 718: 25 kV/cm.

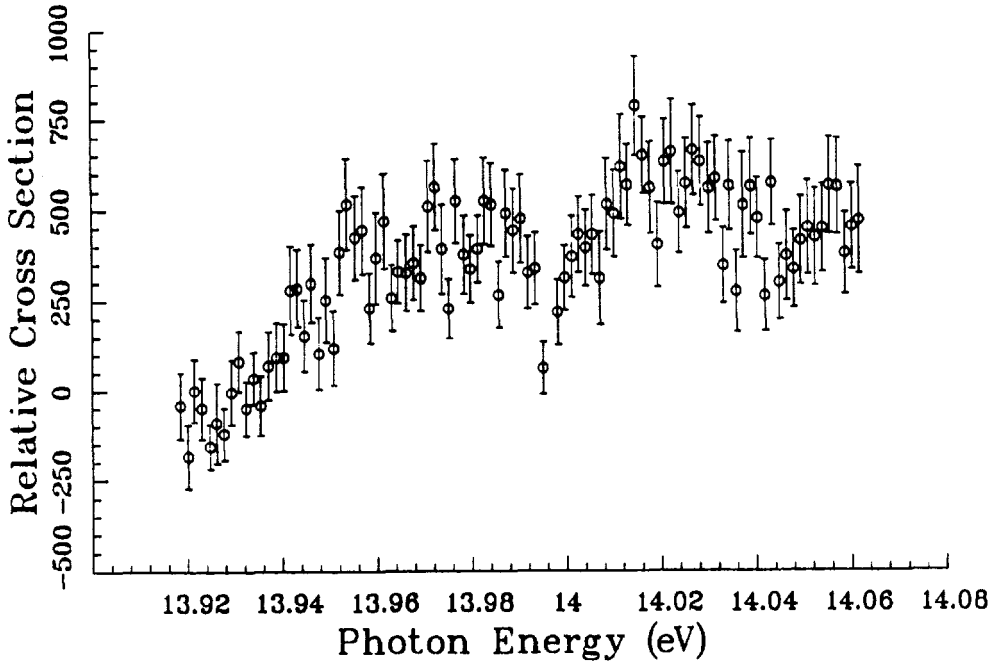

Figure J.84. Run 731: 25 kV/cm.

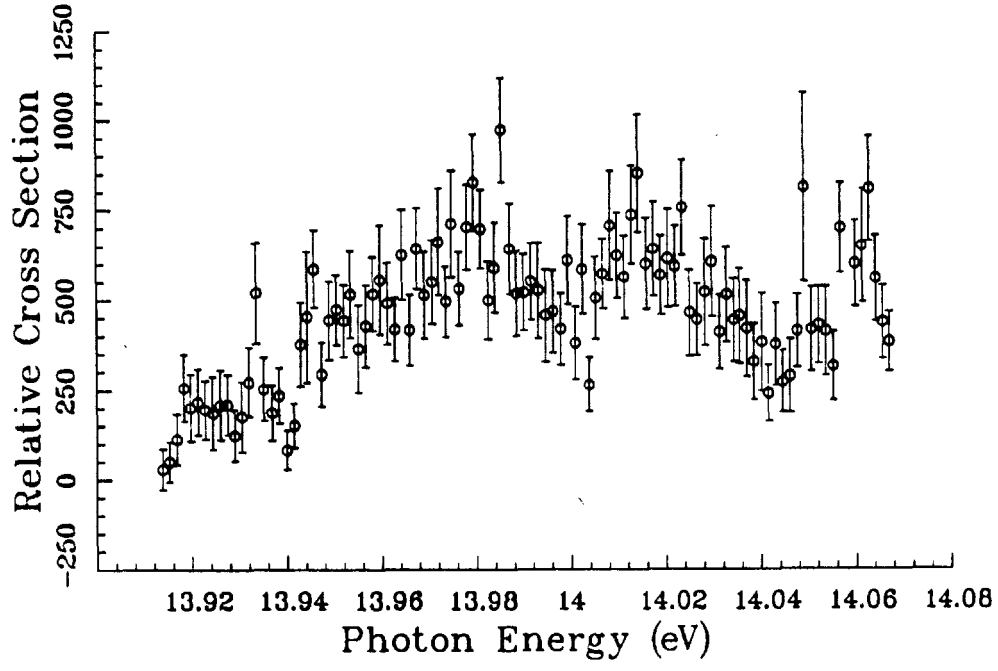

Figure J.85. Run 732: 25 kV/cm.

References

> To steal ideas from one person is plagiarism; to steal them from many is research.
>
> — Anon.

T. Altman, private communication, 1989.

Amperex Manual, Amperex Electronic Corporation, Hicksville, NY 11802.

B. H. Armstrong, *Phys. Rev.* **131**, 1132 (1963).

R. J. Barrett, B. D. Anderson, H. B. Willard, A. N. Anderson and N. Jarmie, *Nuc. Inst. Meth.* **129**, 441-445 (1975).

R. Bentley, private communication (December 1974).

K. Behringer and P. Thoma, *Phys. Rev. A* **17**, 1408 (1978).

BEI Motion Systems Co., Digital Products Division, Little Rock, Arkansas.

H. A. Bethe and E. E. Salpeter, *Quantum Mechanics of One- and Two-Elect ron Atoms*, Springer-Verlag, Berlin (1957).

P. R. Bevington, *Data Reduction and Error Analysis for the Physical Science s*, McGraw-Hill (1969).

J. P. Boutot, J. Nussli, D. Vallat, *Advances in Electronics and Electron Physics* **60**, 223.

J. T. Broad and W. P. Reinhardt, *Phys. Rev. A* **14**, 2159-2173 (1976).

J. T. Broad and W. P. Reinhardt, *Phys. Rev. A* **17**, 195 (1978).

H. C. Bryant, "*Studies of H^- Resonances in an Electric Field*", in *Electronic and Atomic Collisions*, North-Holland (1980).

References

H. C. Bryant, P. A. Lovoi and G. G. Ohlsen, *Phys. Rev. Lett.* **27**, 1628 (1971).

H. C. Bryant, B. D. Dieterlie, J. Donahue, H. Sharifian, H. Tootoonchi, D. M. Wolfe, P. A. M. Gram and M. A. Yates-Williams, *Phys. Rev. Lett.* **38**, 228 (1977).

H. C. Bryant, David A. Clark, Kenneth B. Butterfield, C. A. Frost, H. Sharifian, H. Tootoonchi, J. B. Donahue, P. A. M. Gram, M. E. Hamm, R. W. Hamm, J. C. Pratt, M. A. Yates and W. W. Smith, *Phys. Rev. A* **27**, 2889 (1983).

H. C. Bryant, A. Mohagheghi, J. E. Stewart, J. B. Donahue, C. R. Quick, R. A. Reeder, V. Yuan, C. R. Hummer, W. W. Smith, S. Cohen, W. Reinhardt and L. Overman, *Phys. Rev. Lett.* **58**, 2412 (1987).

K. B. Butterfield, Ph.D. Dissertation, University of New Mexico (1984); published as Los Alamos report LA-10149-T.

M. S. Caceci and W. P. Cacheris, *Fitting Curves to Data*, Byte, May 1984.

D. A. Clark, H. C. Bryant, K. B. Butterfield, C. A. Frost, J. B. Donahue, P. A. M. Gram, M. E. Hamm, R. W. Hamm and W. W. Smith, *Bull. Am. Phys. Soc.* **9**, 1137 (1980).

K. Crandall, SIMALAC (1970).

CVI Laser Corp., 200 Dorado Pl., Albuquerque, NM 87192.

J. Callaway, *Phys. Rev. A* **26**, 199 (1982).

Stanley Cohen, Ph.D. Dissertation, University of New Mexico (1985); published as Los Alamos report LA-10726-T.

Stanley Cohen, H. C. Bryant, C. J. Harvey, J. E. Stewart, K. B. Butterfield, D. A. Clark, J. B. Donahue, D. W. MacArthur, G. Comtet and W. W. Smith, *Phys. Rev. A* **36**, 4728 (1989).

K. T. Chung, *Phys. Rev. A* **6**, 1809 (1972).

G. Comtet, C. J. Harvey, J. E. Stewart, H. C. Bryant, K. B. Butterfield, D. A. Clark, J. B. Donahue, P. A. M. Gram, D. W. MacArthur, V. Yuan, W. W. Smith and Stanley Cohen, *Phys. Rev. A* **35**, 1547-1554 (1987).

J. W. Cooper, U. Fano, and F. Prats, *Phys. Rev. Lett.* **10**, 518 (1963).

D. M. Crowe, X. Q. Guo, M. S. Lubell, F. C. Tang, A. Vasilakis, J. Slevin and M Eminyan, "*Spin-Tagged Electron Hydrogen Scattering: Ionization in the Near Threshold Region*", submitted to *Phys. Rev. Lett.* (1989)

S. Cvejanovic and F. H. Read, *J. Phys. B* **7**, 1841 (1974).

N. B. Delone, I. Yu. Kiyan, V. P. Krainov, V. I. Tugushev, *Opt. Spectrosc. (U.S.S.R.)* **58**, 157 (1985) [*Opt. Spectrosk.* **58**, 262 (1985)].

Digital Equipment Corporation, Maynard, Massachusetts.

J. B. Donahue, P. A. M. Gram, M. V. Hynes, R. W. Hamm, C. A. Frost, H. C. Bryant, K. B. Butterfield, D. A. Clark and W. W. Smith, *Phys. Rev. Lett.* **48**, 1538-1541 (1982).

G. W. F. Drake, *Phys. Rev. Lett.* **24**, 126 (1970).

Du and Delos, *Phys. Rev. A* **38**, 5609 (1988).

I. I. Fabrikant, *Sov. Phys. JETP* **52**, 1045 (1980). [*Zh. Eksp. Teor. Fiz.* **79**, 2070 (1980)].

I. I. Fabrikant, *Near-Threshold Photodetachment from H^- Ions in Parallel Static Electric and Magnetic Fields*, Second International Workshop on the Physics of the Negative Hydrogen Ion, Albuquerque, NM (January 1990).

U. Fano, *Phys. Rev.* **124**, 1866 (1961).

U. Fano and J. W. Cooper, *Phys. Rev.* **137**, A1364 (1965).

U. Fano and A. R. P. Rau, *Atomic Collisions and Spectra*, Academic Press (1986).

James M. Feagin and Rafal D. Filipczyk, "*Generalized Coordinates for Wannier thresholds: Prediction of Multiple Power Laws for Triple Escape*", submitted to *Phys. Rev. A* (1989).

J. M. Feagin, *Generalized Coordinates for Wannier Thresholds: Prediction of Multiple Power Laws for Triple Escape*, Second International Workshop on the Physics of the Negative Hydrogen Ion, Albuquerque, NM (January 1990).

R. Fernow, *Introduction to Experimental Particle Physics*, Cambridge University Press (1986).

P. Frey, F. Breyer and H. Hotop, *J. Phys. B* **11**, L589 (1978).

C. A. Frost, Ph.D. Dissertation, University of New Mexico (1981); published as Los Alamos report LA-8976-T.

C. A. Frost, D. A. Clark, H. C. Bryant, J. B. Donahue, P. A. M. Gram, M. E. Hamm, R. W. Hamm, W. W. Smith, *Bull. Am. Phys. Soc.* **25**, 565 (1980).

M. Gailitis, *J. Phys. B* **13**, L479 (1980).

M. Gailitis and R. Damburg, *Sov. Phys. JETP* **17**, 1107 (1963a).

M. Gailitis and R. Damburg, *Proc. Phys. Soc.* **82**, 192 (1963b).

P. A. M. Gram, J. C. Pratt, M. A. Yates-Williams, H. C. Bryant, J. Donahue, H. Sharifian and H. Tootoonchi, *Phys. Rev. Lett.* **40**, 107 (1978).

C. H. Greene, *J. Phys. B* **13**, L39 (1980).

C. H. Greene, N. Rouze, *Zeitschrift für Physik* **9**, 219 (1988).

C. H. Greene, private communication, 1990.

M. E. Hamm, R. W. Hamm, J. Donahue, P. A. M. Gram, J. C. Pratt, M. A. Yates, R. D. Bolton, D. A. Clark, H. C. Bryant, C. A. Frost and W. W. Smith, *Phys. Rev. Lett.* **43**, 1715 (1979).

P. G. Harris, U.N.M. internal report (1986).

P. G. Harris, H. C. Bryant, A. Mohagheghi, C. Tang, J. B. Donahue, C. R. Quick, R. A. Reeder, S. Cohen, W. W. Smith and J. E. Stewart, LANL Report LA-UR-89-322 (1989a).

P. G. Harris, H. C. Bryant, A. H. Mohagheghi, C. Y. Tang, J. B. Donahue, C. R. Quick, R. A. Reeder, J. E. Stewart, T. Altman, D. Rislove, in *Abstracts of XVI ICPEAC*, New York (1989b).

P. G. Harris, H. C. Bryant, A. H. Mohagheghi, C. Y. Tang, J. B. Donahue, C. R. Quick, R. A. Reeder, J. E. Stewart, *High-Lying Resonances in the H^- Ion*, Second International Workshop on the Physics of the Negative Hydrogen Ion, Albuquerque, NM (1990a).

P. G. Harris, H. C. Bryant, A. H. Mohagheghi, C. Y. Tang, J. B. Donahue, C. R. Quick, R. A. Reeder, J. E. Stewart, T. Altman, D. Rislove, *Measurement and Reduction of Momentum Spread in the LAMPF Linac Beam*, to be published in *Nuc. Inst. Meth.* A (1990c).

P. G. Harris, H. C. Bryant, A. Mohagheghi, C. Tang, J. B. Donahue, C. R. Quick, R. A. Reeder, S. Cohen, W. W. Smith, J. E. Stewart and C. Johnstone, *Further Studies of H^- Photodetachment In Electric Fields*, to be published in *Phys. Rev. A* (1990d).

P. G. Harris, H. C. Bryant, A. H. Mohagheghi, R. A. Reeder, H. Tootoonchi, C. Y. Tang, C. R. Quick, Stanley Cohen, H. Sharifian, W. W. Smith, *Observation of High-Lying Resonances in the H^- Ion*, submitted to APS DAMOP meeting (1990e).

P. G. Harris, H. C. Bryant, A. H. Mohagheghi, R. A. Reeder, H. Sharifian, H. Tootoonchi, C. Y. Tang, J. B. Donahue, C. R. Quick, D. C. Rislove, W. W. Smith, *Observation of Doubly-Excited Resonances in the H^- Ion*, submitted to *Phys. Rev. Lett.* (1990f).

D. R. Herrick, *Phys. Rev. A* **12**, 413 (1975).

D. R. Herrick and Sinanoglu, *Phys. Rev. A* **11**, 97 (1975).

R. N. Hill, *Phys. Rev. Lett.* **38**, 643 (1976).

Y. K. Ho, *Physics Letters* **77A**, 147 (1980).

Y. K. Ho, *Phys. Rev. A* **41**, 1492 (1990).

Y. K. Ho and J. Callaway, *J. Phys. B* **18**, 3481 (1985).

Y. K. Ho and J. Callaway, *Phys. Rev. A* **34**, 130 (1986).

D. Holtkamp and C. R. Quick, *A New Method of H^- Beam Energy and Energy-Spread Diagnostics*, to be published in *Nuc. Inst. Meth. A* (1990).

International Foils, Alliance, Ohio.

F. James, *Function Minimization*, from the Proceedings of the 1972 CERN Computing and Data Processing School, Pertisau, Austria, 10-24 September 1972 (CERN 72-21).

F. James and M. Roos, *Comput. Phys. Commun.* **10**, 343 (1975).

Naoto Koyama, Atusko Takafuji and Michio Matsuzawa, *J. Phys. B* **22**, 553 (1989).

Lambda Physik, Hans-Böckler-Str. 12, D-3400 Göttingen, Federal Republic of Germany.

L. D. Landau, *Journal of Physics U.S.S.R.* **8**, 201 (1944).

L. D. Landau and E. M. Lifshitz, *Quantum Mechanics: Non-Relativistic Theory*, Addison-Wesley, Reading, Mass. (1965), 2nd edition.

C. D. Lin, *Phys. Rev. A* **10**, 1986 (1974).

C. D. Lin, *Phys. Rev. Lett.* **35**, 1150 (1975).

C. D. Lin, *Phys. Rev. Lett.* **51**, 1348 (1983).

C. D. Lin, *Phys. Rev. A* **29**, 1019 (1984).

C. D. Lin, *Adv. At. Mol. Phys.* **22**, 77 (1986).

C. D. Lin, *Novel Systematics of Autoionization Widths of Doubly Excited States of H^-*, Second International Workshop on the Physics of the Negative Hydrogen Ion, Albuquerque, NM (January 1990).

References

L. Lipsky and M. J. Conneely, *Phys. Rev. A* **14**, 2193 (1976).

Lotus-123, Copyright Lotus Development Corporation, 55 Cambridge Parkway, Cambridge, MA 02142.

M. Lubell, *Spin-tagged e-H Scattering Ionization Near The Threshold Region*, Second International Workshop on the Physics of the Negative Hydrogen Ion, Albuquerque, NM (January 1990).

D. W. MacArthur, K. B. Butterfield, D. A. Clark, J. B. Donahue, P. A. M. Gram, H. C. Bryant, C. J. Harvey, W. W. Smith and G. Comtet, *Phys. Rev. A* **32**, 1921 (1985).

D. W. MacArthur, K. B. Butterfield, D. A. Clark, J. B. Donahue, P. A. M. Gram, H. C. Bryant, C. J. Harvey, W. W. Smith and G. Comtet, *Phys. Rev. Lett.* **56**, 282 (1986).

J. Macek, *J. Phys. B* **1**, 831 (1968).

J. Macek and S. Watanabe, *Comments At. Mol. Phys.* **19**, 313-329 (1987).

R. P. Madden and K. Codling, *Phys. Rev. Lett.* **10**, 516 (1963).

M. Matsuzawa, *Ar-Impact Excitation of H^- in Doubly-Excited States*, Second International Workshop on the Physics of the Negative Hydrogen Ion, Albuquerque, NM (January 1990).

J. B. McClelland, D. A. Clark, J. L. Davis, R. C. Haight, R. W. Johnson, N. S. P. King, G. L. Morgan, L. J. Rybarcyik, John Ullmann, Paul Lisowski, W. R. Smythe, D. A. Lind, C. D. Zafiratos and J. Rapaport, *Nuc. Inst. Meth. A* **276**, 35 (1989).

John McGill, *Vibration Measurements at HiRAB*, private communication, in MP-5 file, Los Alamos National Laboratory, January 1989.

J. W. McGowan and E. M. Clarke, *Phys. Rev.* **167**, 43-51 (1968).

A. C. Melissinos, *Experiments in Modern Physics*, Academic Press (1966).

P. W. Milonni and J. H. Eberly, *Lasers*, Wiley Interscience (1988).

MINUIT Long Write-Up, CERN Computer, 7600 Interim Program Library; also see Rick Floyd, "*MINUIT under VAX/VMS*", LANL Office Memorandum MP-13/RAF/C79-01.

A. H. Mohagheghi, H. C. Bryant, P. G. Harris, R. A. Reeder, H. Tootoonchi, C. Y. Tang, C. R. Quick, H. Sharifian, W. W. Smith, *Interaction of Relativistic H^- Ions with Thin Foils*, Second International Workshop on the Physics of the Negative Hydrogen Ion, Albuquerque, NM (1990).

A. H. Mohagheghi, Ph.D. Dissertation, University of New Mexico, to be submitted for publication (1990).

Q. Molina, *Phys. Rev. A* **39**, 3298 (1989).

Lesley A. Morgan, M. R. C. McDowell and J. Calloway, *J. Phys. B* **10**, 3297 (1977).

MS-DOS, Copyright IBM Corporation, Boca Raton, FL 33429-1328.

C. A. Nicolaides, *The Two Electron Ionization Ladder for H^- of ^1S and ^1P Symmetry*, Second International Workshop on the Physics of the Negative Hydrogen Ion, Albuquerque, NM (January 1990).

R. S. Oberoi, *J. Phys. B* **5**, 1120 (1972).

S. K. O'Brien, *Turbo Pascal Advanced Programmer's Guide*, Osborne/McGraw-Hill (1988).

W. R. Ott, J. Slater, J. Cooper and G. Gieres, *Phys. Rev. A* **12**, 2009 (1975).

Oxford Minidictionary of Quotations, Oxford University Press (1983).

A. Pathak, A. E. Kingston, and K. A. Berrington, *J. Phys. B* **21**, 2939 (1988).

A. Pathak, P. G. Burke, and K. A. Berrington, *J. Phys. B* **22**, 2759 (1989).

Q documentation:
Introduction to Q, Los Alamos Document MP-1-3401-3.
Q-Programmer's Information Manual, Los Alamos Document MP-1-3401-5.
A Histogramming System Under RSX-11M and VMS, Los Alamos Document MP-1-3407-4.
Histogram Support System for RSX and VMS, Los Alamos Document MP-1-3403-4.
A Data Testing Package Under RSX-11 and VMS, Los Alamos Document MP-1-3412-3.
General Purpose Memory Management Region, Los Alamos Document MP-1-3409-1.
A Guide to Writing an RSX-11M or VMS Q Analyzer, Los Alamos Document MP-1-3417-1.

A. R. P. Rau, *Phys. Rev. A* **4**, 207-220 (1971).

A. R. P. Rau, *J. Phys. B* **16**, L699 (1983).

A. R. P. Rau, *States of an Atomic Electron Pair*, in *Atoms In Unusual Situations*, ed. J. P. Brown (Plenum, 1987).

A. R. P. Rau and H. Wong, *Phys. Rev. A* **37**, 632 (1988).

F. H. Read, *Aust. J. Phys.* **35**, 475 (1982).

R. A. Reeder, private communication (1989).

W. Reinhardt, private communication (April 16th 1979).

W. P. Reinhardt, in *Atomic Excitation and Recombination in External Fields*, M. H. Nayfeh and C. W. Clark, eds. (Gordon and Breach, 1985), p. 85.

Renco Corp., Goleta, California.

B. Rossi, *High Energy Particles*, Prentice-Hall, New Jersey.

H. R. Sadeghpour, private communication (1989a).

H. R. Sadeghpour, *Phys. Rev. A* **39**, 6048 (1989b).

H. R. Sadeghpour, *Highly Excited States of H^-*, Second International Workshop on the Physics of the Negative Hydrogen Ion, Albuquerque, NM (1990a).

H. R. Sadeghpour, private communication (1990b).

H. R. Sadeghpour and C. H. Greene, *Dominant Photodetachment Channels in H^-*, submitted to *Phys. Rev. Lett.* (1990).

T. Scholz, P. Scott and P. G. Burke, *J. Phys. B* **21**, L139 (1988).

H. Sharifian, Ph.D. Dissertation, University of New Mexico (1977).

W. W. Smith, C. R. Quick, J. B. Donahue, S. Cohen, C. Y. Tang, P. G. Harris, A. H. Mohagheghi, H. C. Bryant, R. A. Reeder, H. Toutounchi, J. E. Stewart and H. Sharifian, in *NICOLS '89.*

T. P. Snow, *Astrophys. J.* **198**, 361 (1975).

Spectra Physics, 1305 Terra Bella Avenue, P. O. Box 7013, Mountain View, California 94039-7013.

J. E. Stewart, Ph.D. Dissertation, University of New Mexico (1987); published as Los Alamos report LA-11152-T.

J. E. Stewart, H. C. Bryant, P. G. Harris, A. H. Mohagheghi, J. B. Donahue, C. R. Quick, R. A. Reeder, V. Yuan, C. R. Hummer, W. W. Smith, S. Cohen, *Phys. Rev. A* **38**, 5628 (1988).

C. Y. Tang, Ph.D. Dissertation, University of New Mexico, to be submitted for publication (1990).

References

C. Y. Tang, P. G. Harris, A. H. Mohagheghi, H. C. Bryant, C. R. Quick, J. B. Donahue, R. A. Reeder, Stanley Cohen, W. W. Smith, J. E. Stewart, *Phys. Rev. A* **39**, 6068 (1989).

C. Y. Tang, H. C. Bryant, P. G. Harris, A. H. Mohagheghi, R. A. Reeder, H. Tootoonchi, C. R. Quick, H. Sharifian, W. W. Smith, *Multiphoton Detachment of H^- Ions*, Second International Workshop on the Physics of the Negative Hydrogen Ion, Albuquerque, NM (January 1990).

A. Temkin and Y. Hahn, *Phys. Rev. A* **10**, 708 (1974).

A. Temkin, private communication (March 15th 1979).

A. Temkin, *Phys. Rev. A* **30**, 2737 (1984).

A. Temkin, *Inclusion of θ_{12} Dependence in the Coulomb-Dipole Theory of the Ionization Threshold*, Second International Workshop on the Physics of the Negative Hydrogen Ion, Albuquerque, NM (January 1990).

H. Tootoonchi Sarraf, Ph.D. Dissertation, University of New Mexico (1977).

Turbo Pascal version 5.0, Borland International, P. O. Box 660001, Scotts Valley, CA 95066-0001.

G. H. Wannier, *Phys. Rev.* **90**, 817-825 (1953).

John J. Wendoloski and William P. Reinhardt, *Phys. Rev. A* **17**, 195 (1978).

E. P. Wigner, *Phys. Rev.* **73**, 1002 (1948).

J. F. Williams, *J. Phys. B* **21**, 2107 (1988).

H. Wong, A. R. P. Rau and C. H. Greene, *Phys. Rev. A* **37**, 2393 (1988).

A. Yariv, *Optical Electronics*, 3rd ed., Holt, Rinehart and Winston, New York (1985).

V. Yuan, *Segmented Ion Chamber for HiRAB*, private communication, AT-2:87-342, Los Alamos National Laboratory (July 1987).

B. Zacharov, "*Camac Systems: A Pedestrian's Guide*", Daresbury Nuclear Physics Laboratory, UK (1972) (Extract from lecture series given at the CERN Computing and Data Processing School, Pertisau, Austria, 10-24 September 1972).

*U.S. GOVERNMENT PRINTING OFFICE: 1990-0-773-034/20034

This report has been reproduced directly from
the best available copy.

Available to DOE and DOE contractors from
the Office of Scientific and Technical Information
P.O. Box 62
Oak Ridge, TN 37831
prices available from
(615) 576-8401, FTS 626-8401

Available to the public from
the National Technical Information Service
U.S. Department of Commerce
5285 Port Royal Rd.
Springfield, VA 22161

Microfiche A01

Page Range	NTIS Price Code	Page Range	NTIS Price Code	Page Range	NTIS Price Code	Page Range	NTIS Price Code
001–025	A02	151–175	A08	301–325	A14	451–475	A20
026–050	A03	176–200	A09	326–350	A15	476–500	A21
051–075	A04	201–225	A10	351–375	A16	501–525	A22
076–100	A05	226–250	A11	376–400	A17	526–550	A23
101–125	A06	251–275	A12	401–425	A18	551–575	A24
126–150	A07	276–300	A13	426–450	A19	576–600	A25
						601-up*	A99

*Contact NTIS for a price quote.

Los Alamos Los Alamos National Laboratory
Los Alamos,New Mexico 87545